IMPURE SNOW AND ICE IN REMOTE AREAS: ARCTIC, ANTARCTICA AND HIGH MOUNTAINS

EDITED BY: Jing Ming, Khanghyun Lee, Feiteng Wang, Tong Zhang and Helle Astrid Kjær

PUBLISHED IN: Frontiers in Earth Science

frontiers Research Topics

Frontiers eBook Copyright Statement

The copyright in the text of individual articles in this eBook is the property of their respective authors or their respective institutions or funders. The copyright in graphics and images within each article may be subject to copyright of other parties. In both cases this is subject to a license granted to Frontiers.

The compilation of articles constituting this eBook is the property of Frontiers.

Each article within this eBook, and the eBook itself, are published under the most recent version of the Creative Commons CC-BY licence. The version current at the date of publication of this eBook is CC-BY 4.0. If the CC-BY licence is updated, the licence granted by Frontiers is automatically updated to the new version.

When exercising any right under the CC-BY licence, Frontiers must be attributed as the original publisher of the article or eBook, as applicable.

Authors have the responsibility of ensuring that any graphics or other materials which are the property of others may be included in the CC-BY licence, but this should be checked before relying on the CC-BY licence to reproduce those materials. Any copyright notices relating to those materials must be complied with.

Copyright and source acknowledgement notices may not be removed and must be displayed in any copy, derivative work or partial copy which includes the elements in question.

All copyright, and all rights therein, are protected by national and international copyright laws. The above represents a summary only. For further information please read Frontiers' Conditions for Website Use and Copyright Statement, and the applicable CC-BY licence.

ISSN 1664-8714
ISBN 978-2-88974-492-3
DOI 10.3389/978-2-88974-492-3

About Frontiers

Frontiers is more than just an open-access publisher of scholarly articles: it is a pioneering approach to the world of academia, radically improving the way scholarly research is managed. The grand vision of Frontiers is a world where all people have an equal opportunity to seek, share and generate knowledge. Frontiers provides immediate and permanent online open access to all its publications, but this alone is not enough to realize our grand goals.

Frontiers Journal Series

The Frontiers Journal Series is a multi-tier and interdisciplinary set of open-access, online journals, promising a paradigm shift from the current review, selection and dissemination processes in academic publishing. All Frontiers journals are driven by researchers for researchers; therefore, they constitute a service to the scholarly community. At the same time, the Frontiers Journal Series operates on a revolutionary invention, the tiered publishing system, initially addressing specific communities of scholars, and gradually climbing up to broader public understanding, thus serving the interests of the lay society, too.

Dedication to Quality

Each Frontiers article is a landmark of the highest quality, thanks to genuinely collaborative interactions between authors and review editors, who include some of the world's best academicians. Research must be certified by peers before entering a stream of knowledge that may eventually reach the public - and shape society; therefore, Frontiers only applies the most rigorous and unbiased reviews.
Frontiers revolutionizes research publishing by freely delivering the most outstanding research, evaluated with no bias from both the academic and social point of view. By applying the most advanced information technologies, Frontiers is catapulting scholarly publishing into a new generation.

What are Frontiers Research Topics?

Frontiers Research Topics are very popular trademarks of the Frontiers Journals Series: they are collections of at least ten articles, all centered on a particular subject. With their unique mix of varied contributions from Original Research to Review Articles, Frontiers Research Topics unify the most influential researchers, the latest key findings and historical advances in a hot research area! Find out more on how to host your own Frontiers Research Topic or contribute to one as an author by contacting the Frontiers Editorial Office: frontiersin.org/about/contact

IMPURE SNOW AND ICE IN REMOTE AREAS: ARCTIC, ANTARCTICA AND HIGH MOUNTAINS

Topic Editors:
Jing Ming, Beacon Science & Consulting, Australia
Khanghyun Lee, Korea Polar Research Institute, South Korea
Feiteng Wang, Chinese Academy of Sciences, China
Tong Zhang, Beijing Normal University, China
Helle Astrid Kjær, Niels Bohr Institute, Denmark

Citation: Ming, J., Lee, K., Wang, F., Zhang, T., Kjær, H. A., eds. (2022). Impure Snow and Ice in Remote Areas: Arctic, Antarctica and High Mountains. Lausanne: Frontiers Media SA. doi: 10.3389/978-2-88974-492-3

Table of Contents

frontiers in Earth Science

EDITORIAL
published: 20 January 2022
doi: 10.3389/feart.2021.780068

Editorial: Impure Snow and Ice in Remote Areas: Arctic, Antarctica and High Mountains

Jing Ming[1]*, *Khanghyun Lee*[2], *Feiteng Wang*[3], *Tong Zhang*[4] and *Helle Astrid Kjær*[5]

[1]Beacon Science & Consulting, Adelaide, SA, Australia, [2]Korea Polar Research Institute, Incheon, South Korea, [3]State Key Laboratory of Cryospheric Sciences, Chinese Academy of Sciences, Lanzhou, China, [4]Beijing Normal University (previously at Los Alamos Faculty of Geographical Science, National Laboratory, Los Alamos, United States), Beijing, China, [5]Physics for Ice, Climate and Earth, Niels Bohr Institute, University of Copenhagen, Copenhagen, Denmark

Keywords: snow, ice, impurities, remote areas, Arctic, Antarctica, high mountains

Editorial on the Research Topic

Impure Snow and Ice in Remote Areas: Arctic, Antarctica and High Mountains

Emissions of pollutants are transported to some of Earth's most remote areas. Increasingly intensified human activities into the industrial era, including industries, agriculture, transportation, and tourism continue to enhance pollutant depositions onto the surface. Snow and ice at these remote places are tainted with pollutants and are the carriers of such impurities. This topic issue, "*Impure Snow and Ice in Remote Areas: Arctic, Antarctica and High Mountains*," hosted by Frontiers in Earth Science, presents ten important papers to demonstrate the kinds of pollutants deposited as well as how, and where these pollutants get deposited and their impacts on the cryosphere.

The Arctic, home to snow and ice, is one of the most sensitive areas to climate change and a natural reflection of the environmental impacts from human activities. Matoba et al. found insoluble particles on the surface and in the deeper layers of the Qaanaaq Glacier, Greenland. The insoluble-particle concentration in the glacier ice at intermediate sites was approximately ten times larger than at low sites on this glacier. The resurfacing of the insoluble particles in ice due to ablation, and their coexistence in surface snow, enhanced the surface absorption of solar radiation and favoured the surface melting at the higher area of the glacier, an important climate feedback of such pollutants. Anthropogenic and natural metal and metalloid elements were found deposited in the snow of Svalbard (Koziol et al. and Spolaor et al.) via long-range transports. The on-site snow sampling in the Finish Arctic and the lab modelling work revealed a median black carbon (BC) concentration of 21–57 $\mu g\,kg^{-1}$ depending on the seasons deposited in the snow during 2009–2013.

In the mid-latitudes, the High Asian Mountains host a vast area of mountainous glaciers as the vital water resources to the livelihood of billions of people. These mountainous glaciers are rich in dust, BC, and debris in the surface snow and beneath ice. These impurities contribute to the surface absorption of solar radiation and hence to the melting of glaciers. On Urumqi Glacier No. 1, there were more than 300 $g\,m^{-2}$ of insoluble particles or dust covering the glacier on average, of which approximately 10% were organic matter. These particles largely darkened the glacier surface by reducing its albedo from 0.62 to 0.32 in summer (Yue et al.). The average concentration of BC mixed in the insoluble particles in snow reached as high as ~600 $\mu g\,kg^{-1}$, ten times more than that in the Arctic, and may reduce the surface albedo by 13–23% (Zhang et al.). A more eastern glacier, Yushugou Glacier No. 6, also preserved heavily dusty snow as Urumqi Glacier No. 1, and Ca^{2+} and SO_4^{2-} dominated the chemistry in the soluble components of the snow samples (Liu et al.). In the Hunza Valley of Karakoram, the supra-glacial debris showed an upward expansion during 1990–2019, suggesting the glaciers here would be more extensively covered by the heat-absorbed debris (Xie et al.).

OPEN ACCESS

Edited and reviewed by:
Michael Lehning,
Swiss Federal Institute of Technology Lausanne, Switzerland

***Correspondence:**
Jing Ming
petermingjing@hotmail.com

Specialty section:
This article was submitted to Cryospheric Sciences, a section of the journal Frontiers in Earth Science

Received: *20 September 2021*
Accepted: *29 November 2021*
Published: *20 January 2022*

Citation:
Ming J, Lee K, Wang F, Zhang T and Kjær HA (2022) Editorial: Impure Snow and Ice in Remote Areas: Arctic, Antarctica and High Mountains. Front. Earth Sci. 9:780068. doi: 10.3389/feart.2021.780068

There is evidence that the impurities also influence the snow albedo in Antarctica. However, the particle emissions from the biomass burning in the Southern Hemisphere swept across the peripheral snow-ice covered area only occasionally. The reconstruction of biomass burning history relies largely on deep ice cores, and the Chinese Taishan Station in East Antarctica showed stable glaciology and ideal meteorology for a super-deep ice core drilling (Tang et al.). The ice-core explorations here will provide an essential background to evaluate future climate and environmental changes in Antarctica.

AUTHOR CONTRIBUTIONS

All authors listed have made a substantial, direct, and intellectual contribution to the work and approved it for publication.

Conflict of Interest: Beacon Science and Consulting (ABN 28 737 731 238) is an academic consulting service providing relevant service to clients registered with Australian Securities and Investments Commission. Author JM is the founder and also the executive of this service.

The remaining authors declare that the research was conducted in the absence of any commercial or financial relationships that could be construed as a potential conflict of interest.

Publisher's Note: All claims expressed in this article are solely those of the authors and do not necessarily represent those of their affiliated organizations, or those of the publisher, the editors and the reviewers. Any product that may be evaluated in this article, or claim that may be made by its manufacturer, is not guaranteed or endorsed by the publisher.

Copyright © 2022 Ming, Lee, Wang, Zhang and Kjær. This is an open-access article distributed under the terms of the Creative Commons Attribution License (CC BY). The use, distribution or reproduction in other forums is permitted, provided the original author(s) and the copyright owner(s) are credited and that the original publication in this journal is cited, in accordance with accepted academic practice. No use, distribution or reproduction is permitted which does not comply with these terms.

frontiers in Earth Science

ORIGINAL RESEARCH
published: 19 May 2020
doi: 10.3389/feart.2020.00110

Variation in Albedo and Its Relationship With Surface Dust at Urumqi Glacier No. 1 in Tien Shan, China

Xiaoying Yue[1], Zhongqin Li[1,2], Jun Zhao[2], Jin Fan[3], Nozomu Takeuchi[4] and Lin Wang[1]*

[1] State Key Laboratory of Cryospheric Sciences/Tien Shan Glaciological Station, Northwest Institute of Eco-Environment and Resources, Chinese Academy of Sciences, Lanzhou, China, [2] College of Geography and Environmental Science, Northwest Normal University, Lanzhou, China, [3] College of Atmospheric Science, Chengdu University of Information Technology, Chengdu, China, [4] Department of Earth Sciences, Graduate School of Science, Chiba University, Chiba, Japan

Surface albedo is an important driver of surface processes that promote glacier melting and is a key variable influencing glacier surface melt. Despite much focus in the literature on variations in albedo and its influence on snow surfaces, little attention has been paid to dust and its impact on bare-ice albedo with respect to glacier melting surfaces. In this paper, spatial changes in glacier albedo were investigated using three Landsat images taken during the ablation season in 2006; temporal variations in albedo were measured by an automatic weather station (AWS) in the ablation zone between 26 June and 1 August 2007 at Urumqi Glacier No. 1 in Tien Shan. Ice and snow samples and reflection spectra at 325–1050 nm were collected in August, 2007 at Urumqi Glacier No. 1. The data suggested that spatial changes in glacier albedo are not prominent after snowfall; however, once ice becomes exposed, glacier albedo varies remarkably and generally increases with elevation, especially around the snow line. Temporal variations are characterized by a large range and high frequency, and most are induced by snowfall, changes in cloud conditions, and surface dust; snowfall and cloud increase glacier albedo. Furthermore, the response of snow albedo is more sensitive to cloud compared with the response of ice albedo. Over a bare ice surface, the albedo generally decreases as the concentration of surface dust increases. Organic matter is a primary factor in reducing the albedo over ice.

Keywords: albedo, temporal and spatial variations, surface dust, cloud, mountain glacier

OPEN ACCESS

Edited by:
Tong Zhang,
Los Alamos National Laboratory (DOE), United States

Reviewed by:
Yukihiko Onuma,
The University of Tokyo, Japan
Andrea Fischer,
Austrian Academy of Sciences (OAW), Austria

****Correspondence:***
Nozomu Takeuchi
ntakeuch@faculty.chiba-u.jp

Specialty section:
This article was submitted to Cryospheric Sciences, a section of the journal Frontiers in Earth Science

Received: *28 November 2019*
Accepted: *25 March 2020*
Published: *19 May 2020*

Citation:
Yue X, Li Z, Zhao J, Fan J, Takeuchi N and Wang L (2020) Variation in Albedo and Its Relationship With Surface Dust at Urumqi Glacier No. 1 in Tien Shan, China. Front. Earth Sci. 8:110. doi: 10.3389/feart.2020.00110

INTRODUCTION

An important source of freshwater, it is well known that mountain glaciers are seriously threatened by global climate change. A widespread decrease in the extent of glaciers and a continuous loss of glacier mass have been observed over the past 50 years (Zemp et al., 2019). These phenomena are particularly severe in semi-arid regions, where populations are heavily dependent on snow and glacier melt for their water supplies (Farinotti et al., 2015). Shortwave radiation provides the main energy source for glacial melting and consequently dominates the glacial surface melt magnitude (Hock, 2005; Sun et al., 2017). The shortwave radiation absorbed by glaciers is controlled by surface

albedo, which is highly variable in space and time. Therefore, surface albedo is a critical variable affecting the energy and mass balance at a melting glacier surface. The glacier surface mass balance (the sum of accumulation and ablation) is extremely sensitive to changes in albedo, varying, for example, by 36% when the albedo changed by 0.1 in the ablation zone of Laohugou Glacier No. 12 from 1 June to 30 September 2011 (Sun et al., 2017, 2014). On the Peyto Glacier, Munro (1991) reported that an increase of 0.05 in glacier albedo caused a change in mass balance of 0.66 m w.e., while mass balance changed −0.83 m w.e. with a decrease in glacier albedo of 0.05. This high sensitivity is linked to a positive feedback mechanism between glacier melt and surface albedo, involving enhanced melting and increased exposure of bare ice; aggregated impurities and meltwater on the glacier's surface; and reduced surface albedo and increased solar radiation absorption, consequently accelerating melt (Klok and Oerlemans, 2004; Moustafa et al., 2015). Driven by surface-atmosphere feedback, albedo reduction on a glacier's surface is considered responsible for accelerated recession (Li et al., 2011). Therefore, significant motivation exists to investigate the temporal and spatial variation in glacier albedo to reveal the response mechanism of glaciers to climate change.

To date, most long-term studies on spatiotemporal changes in glacier albedo have been generally based on point data recorded by an automatic weather station (AWS) set up on the glacier's surface (Oerlemans et al., 2009) or coarsely spatial resolution satellite data, such as that obtained by the Advanced Very High Resolution Radiometer (AVHRR) (Stroeve et al., 1997) or the Moderate Resolution Imaging Spectroradiometer (MODIS) (Sirguey et al., 2016; Mortimer and Sharp, 2018). However, for the limited size of mountain glaciers and the complex surrounding topography, the spatial resolution of MODIS data (500 m) and AVHRR data (1000 m) is not high enough, and no appropriate high-resolution albedo product is readily available (Naegeli et al., 2019). However, in order to capture the more detailed spatiotemporal changes in surface albedo on mountain glaciers, increasing numbers of researchers are focusing on the retrieval of glacier albedo from high spatial resolution satellite data. For example, Klok et al. (2003) first proposed in detail glacier albedo retrieval methods using Landsat images and found that, on average, satellite-derived albedos exceed measured surface albedos by 0.03 over a glacier with rugged topography. Fugazza et al. (2016) investigated the spatial distribution of surface albedo at the Forni Glacier, Stelvio National Park, Central Italian Alps, during the ablation season between 2011 and 2013 using four satellite images from the Landsat 7 ETM + images, and they showed that, over the ablation tongue, the albedo is typical of debris-rich ice. Conversely, over accumulation basins, albedo values were typical of old snow for all Landsat images. Naegeli et al. (2019) assessed the temporal evolution of shortwave, broadband albedo derived from 15 end-of-summer Landsat scenes for the bare-ice areas of 39 large glaciers in the western and southern Swiss Alps and declared that trends in bare-ice albedo crucially depend on spatial scales. They emphasized that no significant negative temporal trend in bare-ice albedo was found on a regional to glacier-wide scale, however, at grid cells scales of Landsat images, they discovered significant darkening for the study period of 1999–2016.

In addition, it is necessary to further quantify the dependence of albedo on its influencing factors for the accurate simulation of glacier energy and mass balance. Major factors affecting glacier albedo were related to the surface itself physical properties and the solar irradiance. The surface physical properties relate to the grain size, liquid water, impurities, surface roughness, snow depth, crystal orientation, and structure. The solar irradiance is dependent on the solar incidence angle, cloud optical thickness, cloud amount, aerosol extinction, and shadowing by terrain (Hock, 2005; Gardner and Sharp, 2010). An important factor driving change in glacier albedo is the occurrence of impurities or cryoconite (dark-colored spherical aggregates of mineral particles, organic matter, and microbes, including snow algae, cyanobacteria, and bacteria) at the glacier's surface (Takeuchi et al., 2010). The quantities and characteristics of these impurities vary spatially and temporally (Azzoni et al., 2016). For example, wind-blown dust is usually deposited in spring on Asian glaciers (Dong et al., 2009), and, on Alaskan glaciers, snow-algae bloom is generally aggregated near the snowline in summer (Takeuchi, 2009). Previous studies have revealed that impurities substantially decrease glacier surface albedo by absorbing incident radiation in the visible region (300–700 nm), where absorption by the glacier is weakest (Cutler and Munro, 1996; Yue et al., 2017; Li et al., 2019). For example, black carbon can strongly enhance absorption at visible and near-infrared wavelengths, whereas iron oxides, the primary light-absorbing component in mineral dust, reduce ultraviolet and visible waveband reflectance (Lafon et al., 2006; Zhang et al., 2015). Cong et al. (2018) found that organic materials in cryoconite were the most important light absorbers at wavelengths of 450 and 600 nm and that goethite played a stronger role than black carbon at shorter wavelengths for most glaciers on the Tibetan Plateau. Moreover, the albedo-reducing effect of biological impurities arises from their dark pigmentation – impurities such as xanthophyll, chlorophyll, and carotenoid, which absorb light with characteristic spectral profiles across ultraviolet and visible wavelengths; ice, typical in these areas, exhibits little absorption (Yallop et al., 2012).

Dust deposition on snowpacks has been well studied (Dumont et al., 2014; Ming et al., 2016; Skiles and Painter, 2016; Niu et al., 2017; Hu et al., 2018; Li et al., 2018). Variation in snow albedo results from light-absorbing impurities (i.e., black carbon, organic carbon, and mineral dust) and snow metamorphism. Temperature since previous snowfall events is deemed as a proxy for increasing grain size and impurity content, which leads to lower albedo (Klok and Oerlemans, 2004). Thus, snow albedo is best estimated from accumulated daily positive temperatures, since previous snowfall (Brock et al., 2000; Hock and Holmgren, 2005; Pellicciotti et al., 2005). However, little attention has been paid to the decreasing ice albedo caused by dust deposition on the glacier's melting surface. Moreover, in energy balance melt models, the ice albedo is usually treated as constant in time and space, about 0.3 (Oerlemans and Knap, 1998; Huintjes et al., 2015; Zhu et al., 2015). Brock et al. (2000) attempted to parameterize ice albedo using its relationship with elevation, and Azzoni et al. (2016) found that fine coverage values were directly

proportional to the natural logarithm of measured ice albedo in the Forni Glacier, Italy.

In general, albedo parameterization within energy and mass balance models cannot account for all spatial and temporal variations in surface albedo, especially for the surface of ice, and such parameterization is consequently regarded as a major source of error (Arnold et al., 1996; Klok and Oerlemans, 2002, 2004). Therefore, further studies are needed to combine measurements of the impurity characteristics with systematic measurements of ice albedo. Takeuchi et al. (2006, 2010) developed a field procedure and further standardized lab analysis to quantify the characteristics of surface dust and its effects on reflectance based on studies in the Alaska Range (2009), Qilian Mountain (2005), Altay (2006), the Himalayas (2000), Patagonia (2001), Russian Siberia (2015), and Greenland (2014). However, these studies were limited to monitoring changes based on several field points during the study period.

In the current study, Urumqi Glacier No. 1 was selected. Taking advantage of records provided by the AWS in the ablation zone, between 26 June and 1 August 2007, and three satellite images from the Landsat TM and ETM + in the warm season of 2006, high spatiotemporal resolution changes in surface albedo were investigated. Reflectance spectra in the wavelength range of 325–1050 nm were collected, and surface dust, as well as its organic matter content, was measured at six different elevations on 1 August 2007. The characteristics of surface dust and its role on ice albedo reduction are analyzed. In addition, the influence of cloud on surface albedo for snow and bare ice is discussed, in terms of physical properties. The principal purpose of this study was to investigate high spatiotemporal resolution variation in albedo and its influencing factors over glacier melting surfaces and to improve existing albedo parameterizations.

STUDY SITE DESCRIPTION

Urumqi Glacier No. 1 (UG1), located in an arid and semi-arid region of central Asia, is surrounded by vast desert areas (**Figure 1A**); it is a typical valley glacier with an area of 1.62 km^2 and an axis length of nearly 2.1 km, as of August 2012 (**Figure 1C**). It flows northeastward from the highest elevation of 4445 m.a.s.l to its terminal position of 3752 m.a.s.l. The latest radar echo-sounding measurement was carried out on the glacier in August 2012, indicating its maximum thickness to be 124 ± 5 m (WGMS, 2017).

Urumqi Glacier No. 1 is a reference glacier in the WGMS glacier monitoring network and has provided the longest and best glaciological and climatological monitoring records in China since 1959. The records show that the glacier has been in constant recession for the past 60 years, especially for the past 30 years – the glacier has experienced a rapid and accelerated shrinkage. Increased precipitation has not been sufficient to mitigate the impact of temperature increase in this area (Li et al., 2011). Consequently, the glacier divided itself into an eastern branch and a western branch in 1993. Recent measurements revealed that the cumulated mass balances of Urumqi Glacier No. 1 were -20 334 mm w.e. and that the ELA averaged approximately 4050 m a.s.l. over the period 1960–2018. The glacier experienced two accelerations in mass loss in the past 60 years, the first starting in 1985 and the second in 1996 (Li et al., 2011). Meanwhile, the ELA increased from 3940 to 4240 m a.s.l.

The study region of the paper is dominated by the westerly jet stream in the upper troposphere, the Siberian anticyclonic circulation, and the cyclonic disturbances of west wind circulation (Farinotti et al., 2015). The mean annual air temperature is about −5.0°C, and the annual precipitation is generally 460 mm, measured at the nearby meteorological station located at 3549 m.a.s.l (Daxigou Meteorological Station). Seventy-eight percent of the annual total precipitation occurs from May to August, predominantly as solid precipitation, as snow, hail, or sleet, at higher elevations (Yang et al., 1992). For Urumqi Glacier No. 1, accumulation and ablation both take place primarily during the warm season.

DATA AND METHODS

Measurements at Meteorological Station

Measurement of continuous albedo was carried out by an AWS in the ablation zone, between 26 June and 1 August 2007 (**Figure 1B**). The AWS was equipped with MS-402 pyranometers (EKO Instruments Co., Japan) to measure shortwave incoming (G_h) and shortwave reflected (R_h) radiation. The pyranometer was mounted horizontally, 1.5 m above the surface. The pyranometer error was about 5% in the wavelength range 0.3–2.8 μm. A data logger (CR1000) recorded half-hourly mean measurements taken every 10 s. During the measurement period, we visited the station and checked the sensors every 3–5 days to ensure the pyranometer remained at a height of 1.5 m.

In order to minimize the error introduced by installing the pyranometer horizontally instead of parallel to the sloping surface, the half-hourly albedo was corrected according to Jonsell et al. (2003). The corrected formula is as follows:

$$\alpha = \frac{R_h}{G_h(1-d)\frac{\cos\beta\cos Z+\sin\beta\sin Z\cos(\varphi-\theta)}{\cos Z} + G_h d} \quad (1)$$

Here, R_h is reflected shortwave radiation; G_h is incident shortwave radiation in the horizontal plane; Z is the solar zenith angle; φ is the solar azimuth angle; β is the slope angle of the surface with azimuth angle θ; and d is the diffuse portion of G_h, which is computed using an empirical relationship relating the ratio of incoming shortwave radiation (G_h) and extraterrestrial solar radiation (T). T can be calculated from solar geometric relationships, and G_h is approximately equal to the incoming shortwave radiation provided by AWS on the glacier.

In addition, the ratio G_h/T was taken as a measure of cloud cover (Cutler and Munro, 1996; Brock, 2004). In the current study, to quantify the effect of cloud on albedo, we related the change in albedo between two successive half-hourly measurements to the corresponding change in the diffuse portion of incoming shortwave radiation, $\Delta(G_h/T)$. The approach was used by Jonsell et al. (2003) on Storglaciaren, Sweden. As cloudiness increases, less solar radiation will reach the surface, the

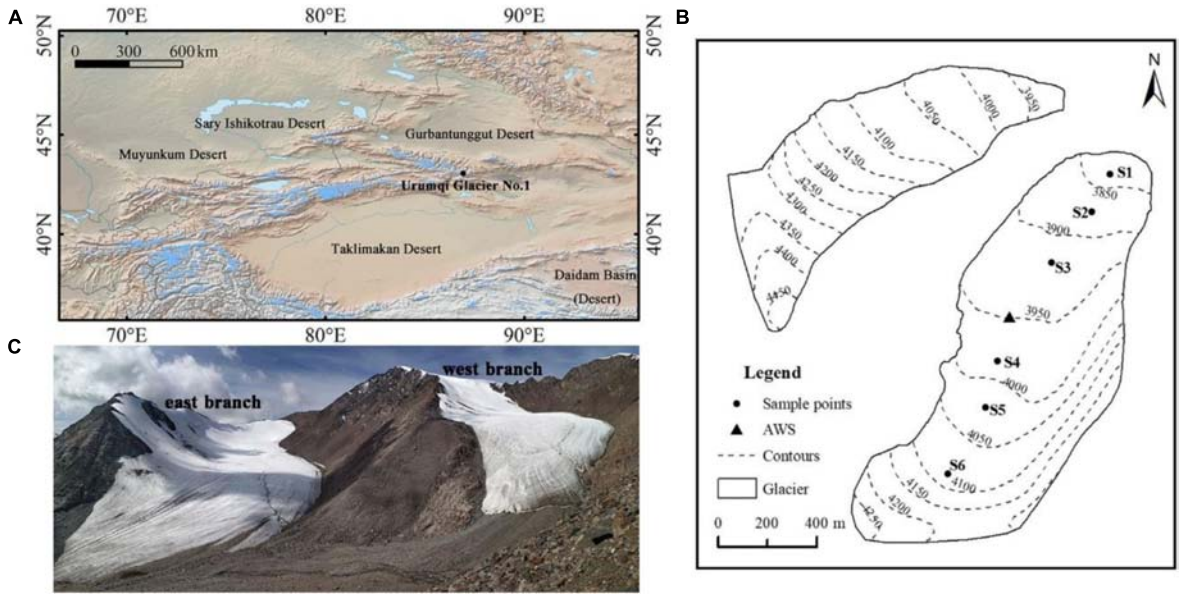

FIGURE 1 | Geographical location **(A)** and map **(B)** of Urumqi Glacier No. 1 in Tien Shan, China. Landscape photograph **(C)** of Urumqi Glacier No. 1 was taken on 20 July 2012.

ratio G_h/T will decrease, and d will tend to decrease. Thus, the ratio is generally higher under clear-sky conditions than under overcast-sky conditions. A positive change, $\Delta(G_h/T)$, indicates decreasing cloudiness, while a negative change corresponds to increasing cloudiness.

Half-hourly broadband albedo values derived from measured incoming shortwave radiation with values <4 W·m^{-2} and zenith angle $>65°$ were discarded, as instruments give unreliable responses for very low incoming shortwave radiation values and high zenith angles (Arendt, 1999). Moreover, albedo values that exceeded 0.98 (a value generally assumed for fresh snow) (Cuffey and Paterson, 2010) were also discarded.

Retrieval of the Surface Albedo

In this study, satellite images were used to investigate the spatial variation in albedo over the whole glacier. Unfortunately, there were no Landsat satellite images acquired of Urumqi Glacier No. 1 during the ablation period in 2007 because of cloud and timing. Thus, three Landsat satellite images were selected over this area between June and August 2006 (**Table 1**).

We adopted the methodology in Klok et al. (2003) to retrieve the glacier surface albedo from Landsat images. The methodology include geolocation, radiometric calibration, atmospheric correction, topographic correction, anisotropic correction, and narrow-to-broadband conversion. The process of deriving surface albedo is described in detail by Yue et al. (2017). The retrieval method considers all important processes that substantially influence the relationship between satellite signal and surface albedo. The method, therefore, has been widely applied for a number of mountain glaciers, such as Urumqi Glacier No. 1, China (Yue et al., 2017); Forni Glacier, Italy (Fugazza et al., 2016); Morteratschgletscher, Switzerland (Klok et al., 2003); and Haut Glacier, Switzerland (Knap et al., 1999). In these studies, good agreement between the Landsat-derived albedo and measured albedo suggests that the retrieval methodology generally produces accurate estimates of surface albedo and can be used quantitatively to research the spatiotemporal evolution of glacier albedo.

TABLE 1 | Landsat images were used to retrieve the surface albedo of glacier.

Path/ row	Data	Landsat Sensor	Sun azimuth	Sun elevation	Horizontal resolution
143/30	20060622	TM	131.23°	63.48°	30 m
	20060716	ETM +	130.80°	60.78°	30 m
	20060801	ETM +	134.39°	57.98°	30 m

Surface Dust Sample Collections and Field Spectroscopy Measurements

In order to quantify the effects of surface dust and its organic-matter content on albedo, field work was carried out on the east branch of Urumqi Glacier No. 1 in August 2007. Ice and snow samples on the surface layer were collected with a stainless-steel scoop in an area of approximately 15 cm × 15 cm to a depth of 1–3 cm at five sites in the bare ice area (S1–S5) and one site in the snow area (S6) (**Figure 1B**). Five samples were randomly selected from the surface at each study site. The chosen sites were visibly representative of the surface conditions around each site, in terms of surface roughness and the amount of rocky debris. In the laboratory, the samples were dried for 24 h at 60°C. Then, they were combusted for 3 h at 500°C. After each processing step, the samples were weighed to obtain the amount of surface dust and its organic matter content. The amount of dust per unit area of

the glacier was obtained based on measurements of the dry weight and the sampling area. All samples were analyzed in a laboratory of Chiba University, Japan. The process of sample collection and analysis has been described in detail by Takeuchi and Li (2008).

Reflectance spectra were collected at 325–1050 nm using a portable spectroradiometer (MS-720, Eiko Seiki, Japan), with a spectral resolution of 10 nm. Reflectances were obtained by dividing the surface radiances by the radiance acquired from a white reference panel that is nearly 100% reflective and diffuse. The distance between the sensor and the glacier surface was approximately 20 cm and had a region size of ∼8.9 cm diameter on surface. Under changing sky conditions, and before each measurement, the instrument was recalibrated. To minimize the influence of slope and solar zenith angle on albedo, all measurements were conducted on a surface-parallel plane, 11:00–14:00 local standard time in clear-sky conditions. At each measuring location, three consecutive spectral measurements were recorded and averaged.

The broadband albedo was calculated at wavelengths from 350 to 1050 nm. The associated expression is as follows:

$$\alpha_{broad} = \frac{\int_{350}^{1050} \alpha_{narrow}(\lambda) i(\lambda) d\lambda}{\int_{350}^{1050} i(\lambda) d(\lambda)} \quad (2)$$

where $\alpha_{narrow}(\lambda)$ denotes the measured spectral albedo using the spectroradiometer, and $i(\lambda)$ is incoming solar irradiance, which is provided by the American Society for Testing and Materials (ASTM G-173-03 data). A similar method was also adopted by Wright et al. (2014); Moustafa et al. (2015), and Li et al. (2019).

To obtain a high-quality albedo data set, rigorous quality controls were implemented. Outliers were removed – physically unrealistic spectral albedo values (>0.98) and raw spectra that were markedly different from other spectra across the entire spectral range (visible and near-infrared wavelengths) for the same sample.

RESULTS

Temporal Variation in Albedo

The half-hourly albedo recorded at the AWS in 2007 is shown in **Figure 2**, revealing a variety of diurnal patterns. In general, the half-hourly albedo value has a large range, from a maximum of 0.98 on 18 July to a minimum of 0.075 on 23 July. There are four "jumps" in the minimum albedo value between 1 day and the next – the most obvious increases in albedo occur on 30 June, 10 July, 17 July, and 29 July, likely to have resulted from fresh solid precipitation (**Figure 3**). Solid precipitation events were recognized according to the results of Kang and Atsumu (1993) on Urumqi Glacier No. 1. Specifically, when air temperature was lower than 2.8°C, the form of precipitation is classified as solid. In addition, the gradual decreasing trends of minimum albedo value are shown for during the day, from 10 July to 15 July, which reveal the transition in surface type from fresh snow to old snow and bare ice. Different magnitudes of the diurnal albedo cycle were observed, with little variation to considerable variation over the course of a day. The largest range was to be expected when the transitions between snow and ice happened because of snowfall and melting, and the diurnal variation of snow albedo was larger than that of ice (**Table 2**). Moreover, high frequency and small-to-medium magnitude albedo variability over all surfaces suggested that other factors were active, such as solar zenith angle and cloud. Generally, albedo is higher in the morning and afternoon than at noon, but asymmetry around solar noon is more pronounced; this phenomenon is likely to result from the change in solar zenith angle, while reduced afternoon values result from snow metamorphism and surface melt. However, minimal indications of diurnal albedo cycles were found between 22 and 27 July over ice surfaces, which implies that the effect of solar zenith angle <65° on ice albedo is negligible.

Spatial Variation in Albedo

Figure 4 shows the spatial variation in the retrieved albedo from the satellite snapshots over the whole glacier. Missing data in some of the Landsat ETM + images (due to the SLC failure, post May 2003) occur in our albedo retrievals. However, compared with the image on 22 June, the percentage of missing data is less than 10% over the whole glacier on 16 July and 1 August, which has a negligible impact.

On 22 June, spatial variation in the albedo was not obvious. The average albedo values for the glacier-wide scale was rather high, with a mean of 0.62 and a standard deviation of 0.13, indicating that the physical composition of the glacier surface was uniform. The frequency distribution of pixels has a peak around 0.70 (**Figure 5**). The glacier was, therefore, covered by snow, perhaps fresh snow or snow in an early stage of metamorphism.

On 16 July, the glacier albedo showed considerable spatial variation, markedly increasing with altitude. The mean of the albedo was 0.49 with a standard deviation of 0.20 over the whole glacier. Two distinct peaks corresponding to the albedo of ice and snow are present in **Figure 5** (Cuffey and Paterson, 2010). The snow albedo distribution is positively skewed around a value of 0.63, and the ice albedo is more normally distributed, with a strong peak at 0.17 (**Figure 5**). The glacier was clearly divided into a bare ice area and snow area by a snow line. The snow line altitude was around 3900 m a.s.l. on the eastern branch and 4000 m a.s.l. on the western branch. The pattern of spatial variation in albedo was slightly different between the eastern branch and the western branch. On the eastern branch, below the snow line, the albedo value was rather low, and variation with altitude was almost absent; the albedo value significantly increased above the snow line. On the western branch, the albedo fluctuated between low and high values below the snow line, while a gentle increase trend was shown above the snow line.

On 1 August, due to the expansion of ice surfaces, variation in albedo with altitude over the whole glacier was remarkable, while the mean albedo of the whole glacier decreased to 0.32 with a standard deviation of 0.19. The peaks corresponding to the albedos of ice and snow are very distinct, and low values occur more frequently than high values (**Figure 5**). The ice albedo decreased slightly by an average of 0.04, but the snow albedo decreased by an average of 0.18. The snow line retreated further and reached around 4000 m a.s.l. on the eastern branch and 4050 m a.s.l. on the western branch. Differences in spatial variation

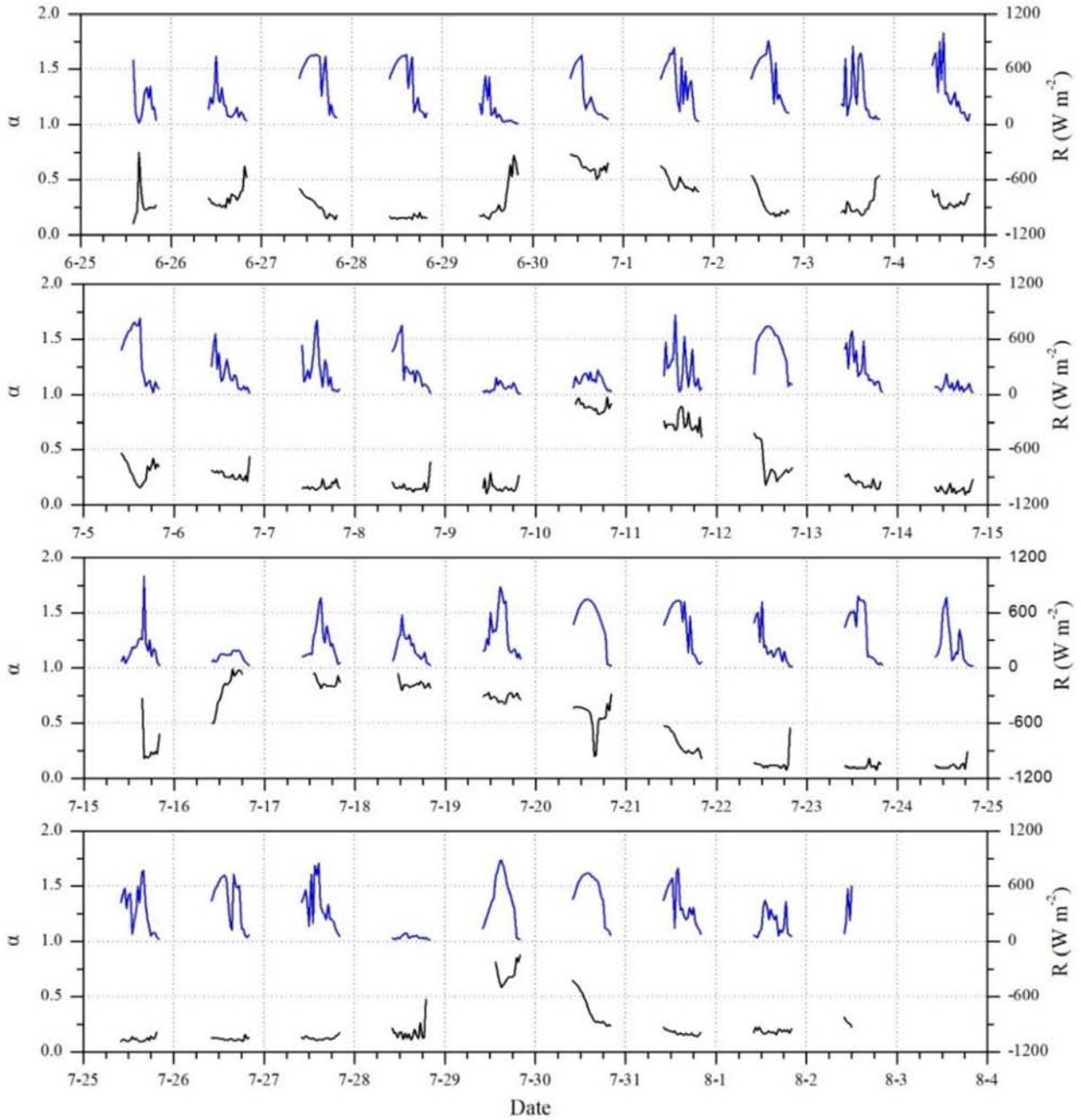

FIGURE 2 | Half-hourly albedo (α, black line) and incoming shortwave radiation (R, blue line) records by AWS between 26 June and 2 August 2007. Half-hourly values with solar zenith angle >65° were not considered.

in albedo remained between the eastern branch and the western branch. On the eastern branch, below the snow line, 70% of the albedo values were lower than 0.2, while above the snow line, the albedo increased weakly, ranging from 0.4 to 0.6. However, on the western branch, below the snow line, the fluctuations disappeared: high values only occurred on the terminal part of the glacier. Above the snow line, the albedo increased steadily and reached a maximum of 0.8 at 4400 m a.s.l.

It is notable that the surface albedo is generally higher on the western branch glacier than on the eastern branch glacier during the study period. This may be attributed to morpho-topographic variables, such as average altitude, slope and aspect, as well as surface dust abundance. In addition, on 1 August, in the same altitude zone, the albedo value was lower on the west side than on the east side, mainly resulting from the differential ablation due to terrain shadowing of

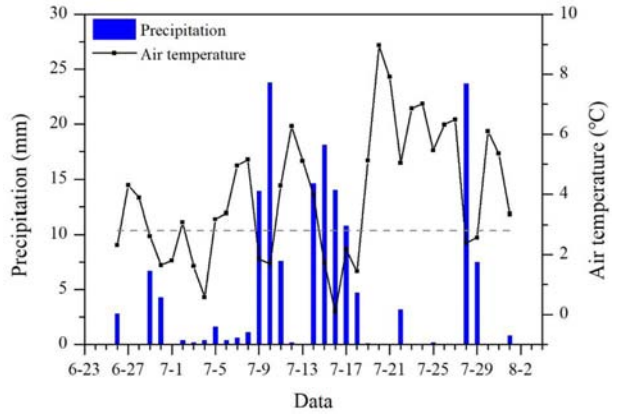

FIGURE 3 | Daily variation of the air temperature and precipitation on Urumqi Glacier No.1 between 26 June and 1 August 2007. The dashed line represented the air temperature threshold of snowfall, which was 2.8°C. The meteorological data was from the Daxigou station (86°50' E, 43°6' N, elevation: 3593 m a.s.l), which is located 3 km southeast of Urumqi Glacier No. 1.

the eastern mountain. However, the above difference between eastern and western sides is not shown on 22 June and 16 July, which may be linked to the retrieval accuracy of the Landsat albedo. On 22 June and 16 July, differences between the surface conditions of the eastern and western sides of the glacier were so small that the retrieval accuracy was not high enough to respond to the variation in albedo caused by different surface conditions.

Characteristics of Surface Dust

Across the sampling sites of snow and ice, the considerable variation in the dry weight of surface dust is shown in **Figure 6A**. For the bare ice sites, the dry weight of dust varies between 228 g m^{-2} and 414 g m^{-2}, with an average of 312 g m^{-2}. The altitudinal profile of such amounts shows that surface dust content is higher in middle of the glacier than at the upper (S5) and terminal (S1) of the study glacier, except for the snow area. Meanwhile, the heterogeneous distribution of the dust is revealed by large standard deviations of the mean dry weight at each ice site – the largest value appears at site S4. The variability in the dry weight of organic matter is similar to that of surface dust (**Figure 6B**). The organic matter content ranges from 16 g m^{-2} (S5) to 43 g m^{-2} (S4), and the mean is 30.2 g m^{-2}. However, on the bare ice surface, the altitudinal variation in the percentage of organic matter is slightly different from that the abundance of surface dust and organic matter (**Figure 6C**). The highest value is at site S2 (10.9%), gradually decreasing to site S5 (6.9%), with increasing altitude. Overall, for all ice sampling sites, the dry weight proportion of organic matter averages 9.4%.

The dry weight of surface dust and its organic matter abundance, as well as the altitudinal variation agreed with the results obtained in August 2006 for Urumqi Glacier No. 1 by Takeuchi and Li (2008). This implies that the results of the present study are reliable, and that variation in the characteristics of surface dust on Urumqi Glacier No. 1 are relatively weak on a short timescale.

TABLE 2 | Characteristics of variation in diurnal albedo records (Δα) in AWS between 26 June and 2 August 2007.

Surface type	n	Δ α range	Δ α mean	Standard deviation
Ice	20	0.027–0.295	0.119	0.066
Snow	7	0.112–0.229	0.180	0.048
Ice and snow	10	0.224–0.541	0.408	0.111

Statistics are based on diurnal variation in albedo (Δα) and given for snow surface, ice surface and the transition between snow and ice in terms of number of daily albedo available (n), the range in Δα, mean, and standard deviation.

Compared with glaciers in polar or sub-polar regions, the abundance of mineral particles and organic matter on Urumqi Glacier No. 1 was markedly high (**Figure 6D**). The average abundance of mineral matter on Urumqi Glacier No. 1 was about 16 times that on the Northwest Greenland (Takeuchi et al., 2014) and eastern Russian Siberian glaciers (Takeuchi et al., 2015), and the abundance of organic matter was approximately 24 times. However, the abundance of surface dust was comparable that on the Asian mountain glaciers. The amount of total surface dust has been reported to be 225 ± 121 g m^{-2} for the Himalayas (Takeuchi et al., 2000) and 291 ± 166 g m^{-2} for the Qilian Mountains in China (Takeuchi et al., 2005), indicating that Asian glaciers may be typically characterized by a high abundance of dust. High levels of mineral particles on these glaciers are probably caused by exposure to abundant wind-blown deposits of desert dust, while the organic components may be the result of intensive biological productivity on the glacial surface (Takeuchi and Li, 2008). In addition, the altitudinal variation in dust abundance on Urumqi Glacier No. 1 was also distinct from that of many other mountain glaciers, such as Gulkana Glacier, the Alaska Range (Takeuchi, 2009), and Xiaodongkemadi Glacier (Li et al., 2017). Generally, on an ablation surface, dust or debris is more abundant in the low part (or near the terminus) of the glacier because mineral particles are mainly supplied from above by glacial flow or from the basal bed by marginal shearing and concentrated on the surface layer as glacier ice melts (Takeuchi et al., 2014). However, compared with sites in the middle of the glacier (S2, S3, and S4), a small amount of dust was discovered in the area near the terminus of Urumqi Glacier No. 1 (S1). The altitudinal variation in surface dust abundance may be attributed to the removal of surface dust by meltwater in the lower part of the glacier (Brock, 2004; Azzoni et al., 2016). Moreover, in the middle of the glacier, the flatter surface terrain is beneficial for the concentration of windblown deposits of dust and microbial activity.

DISCUSSION

Surface Dust Effects

Recently, various research groups have revealed that surface dust significantly reduces glacier albedo, thus accelerating glacier

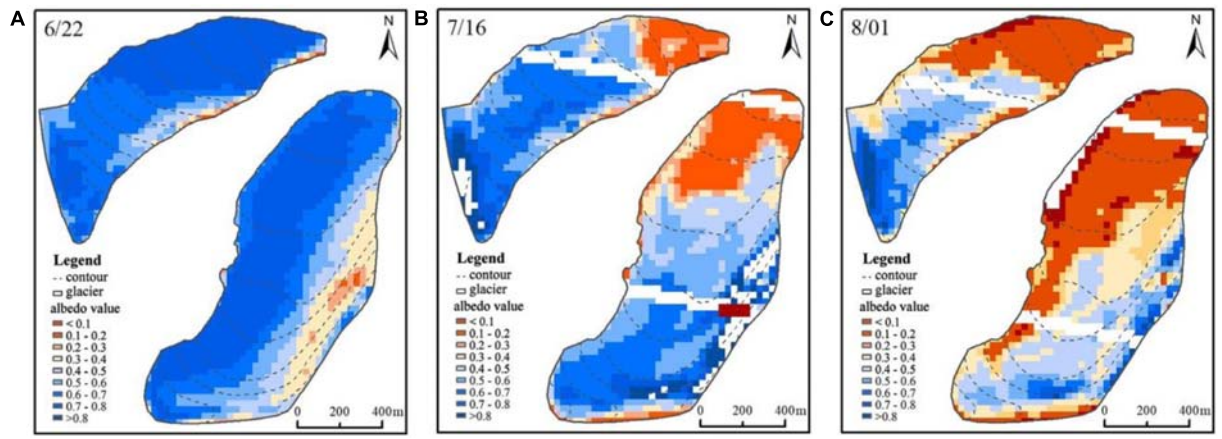

FIGURE 4 | Spatial distribution of the surface albedo of Urumqi Glacier No. 1 in the 2006 ablation season.

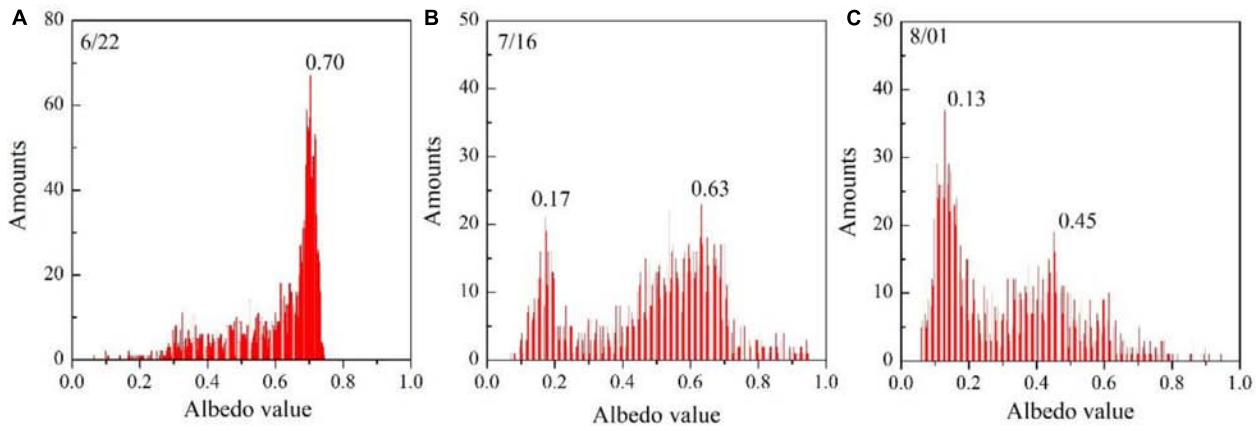

FIGURE 5 | The frequency distribution of the surface albedo over the whole Urumqi Glacier No. 1 in the 2006 ablation season.

melt (Takeuchi, 2002; Oerlemans et al., 2009; Gabbi et al., 2015; Wittmann et al., 2017). In addition, as shown in **Figure 4**, albedo values were higher in the low zone of the glacier than in the middle zone of the glacier for the west branch, which contradicts the general assumption that surface albedo increases with altitude in mid-latitude mountain glaciers (Wang et al., 2014; Fugazza et al., 2016). These distinctive albedo spatial distributions were mainly attributed to surface dust concentration.

In order to quantify the effects of surface dust on albedo, reflectance spectra were collected at ice and snow sampling sites (**Figure 1B**). The large amounts of surface dust at S4 coincided with a relatively low albedo (0.14), and small amounts of surface dust at S5 coincided with a high albedo (0.27) except for the snow area (S6). The albedo significantly decreases, and spectral curves flatten, as the concentration of surface dust increases (**Figure 7**). Thus, the amount of surface dust accounts for variation in glacier albedo. We analyzed the correlation between the dry weight of organic matter and mineral particles in surface dust and ice albedos, respectively (**Figure 8**). The results show that ice albedo follows a negative correlation relationship with the dry weight of mineral particles and organic matter. Organic matter had a much higher correlation with albedo than mineral particles (r = -0.94, p = 0.016, n = 5 vs. r = -0.87, p = 0.055, n = 5, respectively), although the mass proportion of organic matter was much less than that of mineral particles (6.9–11.5% for organic matter content). These relationships suggest that organic matter in the cryoconite decreases the glacier albedo more effectively than do mineral particles.

A microscopic study indicated that dust or cryoconite on the glacier surface is composed of wind-blown desert dust and organic matter. The latter is a product of microbial activity on the glacier itself, including the activity of filamentous cyanobacteria, dead bodies of microbes, and a dark-colored humic substance (Takeuchi et al., 2010). For the ice-surface spectrum, a valley at around 680 nm is clearly evident, which probably results from the chlorophyll of snow algae and cyanobacteria on the cryoconite (**Figure 7**).

For the snow albedo, the crude profile of the snow reflectance spectrum is determined by the complex refractive index of ice, which closely approximates that of liquid water at wavelengths

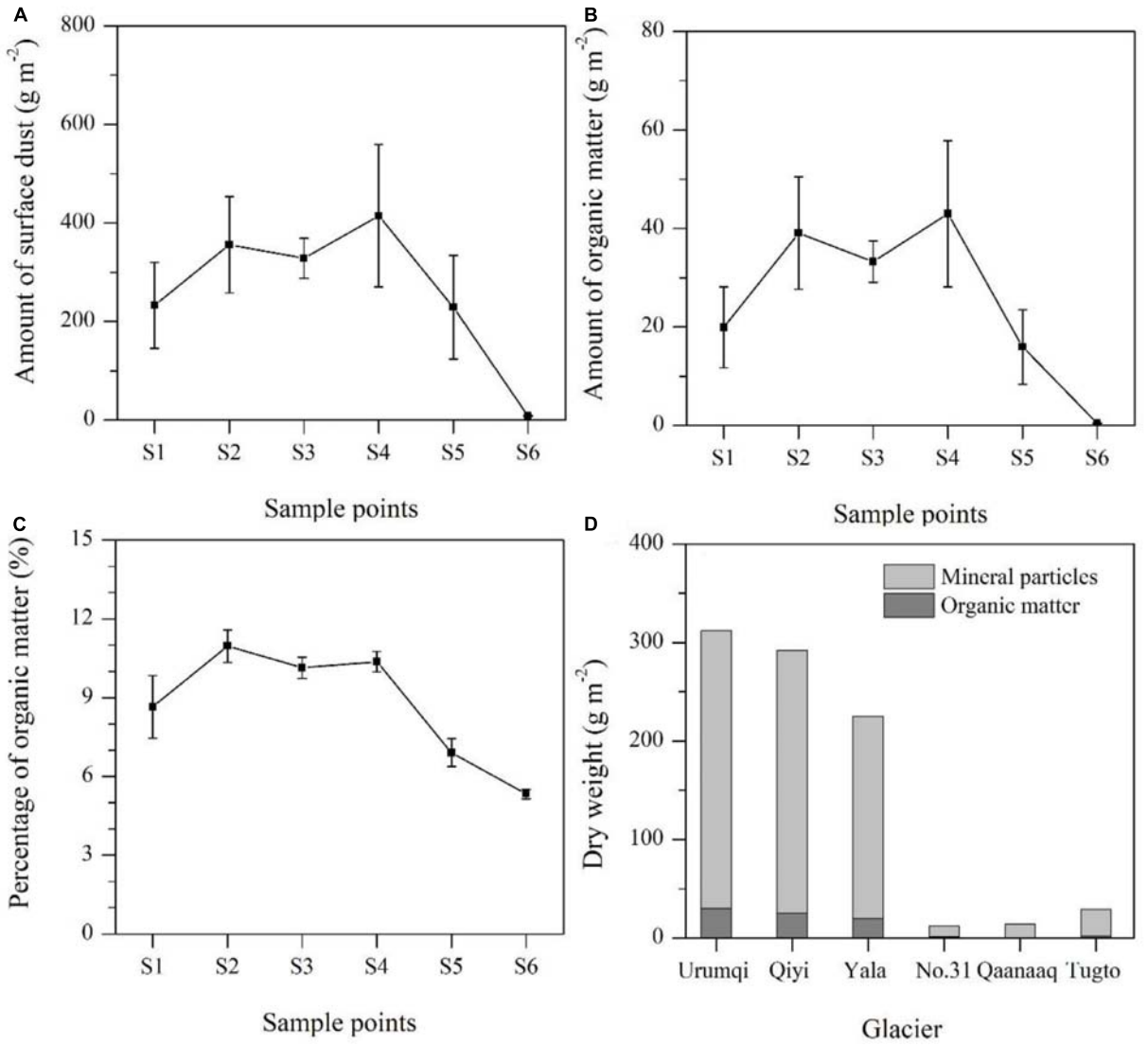

FIGURE 6 | Variations in amount of surface dust **(A)** and organic matter **(B)**, and percentage organic matter **(C)** on the Urumqi Glacier No. 1. Error bars indicates standard deviation. **(D)** Is the comparison of amounts of surface dust and their components among various glaciers around the world. Snow line located between site S5 and S6.

(λ) less than 5 μm (Wiscombe and Warren, 1980; Li et al., 2019). Valleys at wavebands of ∼770–830, 870–920, and 1000–1050 nm are shown, resulting from the strong absorption of ice and water. In general, snow reflectance increases for $\lambda < 600$ nm and decreases for $\lambda > 850$ nm (Li et al., 2019). Compared with pure aged snow (S0), dust reduces spectral reflectance at wavelengths shorter than 900 nm (**Figure 7**). According to the simulated results by Ming et al. (2016) in Urumqi Glacier No. 1, dust and black carbon contribute about 7% and 25% to the reduction in albedo in the accumulation zone, respectively.

Cloud Cover Effects

An important factor driving variations in albedo is cloud-cover fluctuations. Glacier albedo normally increases with increasing cloudiness, and the visible wavelengths (300–695 nm) are more sensitivity than the near-infrared wavelengths (695–2800 nm) to the presence of cloud (Gardner and Sharp, 2010; Abermann et al., 2014). Furthermore, there is a more sensitive response of snow reflectivity to variation in cloud compared with ice reflectivity (Jonsell et al., 2003; Brock, 2004).

In order to quantify the effect of cloud on glacier albedo, the linear relationship $\Delta\alpha$ to $\Delta(G_h/T)$ was fitted by scatter of points, and analyses were performed separately for snow and ice surfaces (**Figure 9**). A weak, but significant, negative correlation between albedo change and cloud-cover variation is evident. Furthermore, compared with snow surfaces, ice surfaces have a correlation that exhibits more scatter, with a lower slope of the linear fit. These results also suggest that the sensitivity of ice albedo to cloud is much weaker. When $\Delta(G_h/T) = 1$, the linear fit predicts a maximum $\Delta\alpha$ of 0.18

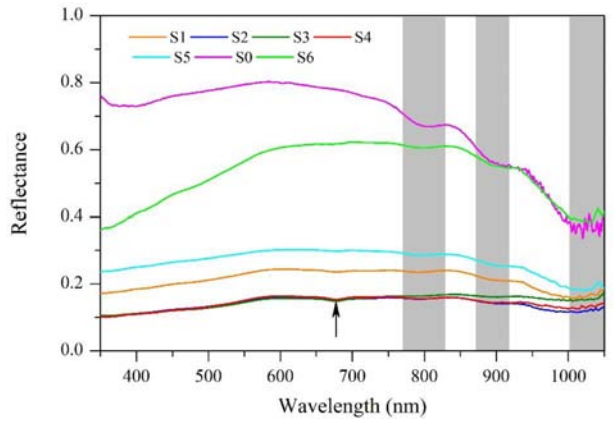

FIGURE 7 | The reflectance spectrum curves in wavelength ranged from 350 to 1050 nm on the surface of the Urumqi Glacier No. 1. S0 was collected over the pure aged snow surface of Urumqi Glacier No. 1 (Yue et al., 2017). The arrow shows absorption feature at 670–680 nm due to chlorophyll in the surface dust. The gray bands mark the known absorption wavelengths for ice/water.

that lies between 0.02 and 0.24 as a maximum value for cloud-induced albedo change according to previous studies (Table 3; Abermann et al., 2014).

The increase in reflectivity caused by clouds has several causes. Clouds, which have similar optical properties to snow, can alter the spectral distribution of incident shortwave radiation by preferentially absorbing near-IR wavelengths and returning near-UV and visible wavelengths. Consequently, this increases the fraction of total shortwave radiation incident at shorter wavelengths where the albedo of glacier is highest (Gardner and Sharp, 2010). Moreover, the weaker sensitivity of ice albedo to cloud due to the lower albedo of ice compared with that of snow, and creating multiple reflections between the surface and the cloud base to less efficient at increasing albedo (Jonsell et al., 2003). In addition, the weaker sensitivity of ice albedo to cloud may be related to the cloud base height, as observed at Haut Glacier d'Arolla by Brock (2004). Clouds also alter the effective solar zenith angle of the incident radiation due to an increase in its diffuse fraction (Abermann et al., 2014). In general, albedo increases with solar incident angle. This is because, at large angles of incidence, on average, a photon travels a path closer to the glacier surface, resulting in an increase in the probability that it is scattered, moving it out of the snowpack (Warren, 1982). However, diffuse radiation has an effective solar zenith angle of ∼50° over a horizontal snow surface (Warren, 1982; Gardner and Sharp, 2010). Below 50°, an increase in albedo is expected (as a result of an increased effective zenith angle), whereas above 50°, a decrease of albedo occurs (Abermann et al., 2014).

In addition, for the ice albedo, the sensitivity of a "clear" and "dark" ice albedo to clouds may be different. Theoretically, as mentioned above, the proportion of visible light is enhanced with the occurrence of clouds. However, impurities substantially decrease the glacier surface albedo in the visible region (300–700 nm) where absorption by the glacier is weakest, and albedo decreases. Thus, the effects of impurities on glacier albedo is contrary to the clouds. Under cloudy conditions, the presence of impurities may compromise the increase in albedo to some extent, and, as with the increase in the impurity abundance, the degree of its offset may be enhanced. In addition, because the degree of decrease of glacier albedo caused by impurities depends on the kinds of impurities, the sensitivity of dark ice albedo to cloud needs to take into account the kind of impurities. Of course, the above speculation requires a sufficiently large and accurate albedo measurement dataset to verify.

The Mechanism of Spatial Variation in Albedo and the Spatial Relationship With Dust

In a melting surface, the spatial distribution of surface albedo primarily depends on the area of snow and bare ice. The glacier is mainly covered by snow or firn in the accumulation zone, and glacier ice is exposed in the ablation zone. Hence, surface albedo generally increases with elevation. In particular, around the snow line, the transition of ice to snow or firn results in a rapid and distinct increase in albedo. Moreover, the spatial change in surface albedo is related to slope and aspect, which dominate the solar incident angle; glacier albedo clearly increases with solar incident angle, even for uniform surface coverage (Wang et al., 2014; Yue et al., 2017). In addition, there are high concentrations of dust over a bare ice surface and spatial variation in albedo is controlled by the abundance of surface dust; albedo significantly decreases as the abundance of surface dust increases.

In the current study, along the length of a glacier, the dust abundance is higher at the middle elevation sites (S2, S3, and S4) than at the higher elevation (S5) and lower elevation sites (S1) except for the snow area. In the transverse scale of the glacier, it is easy to accumulate dust or debris on the left and right sides of the glacier because these sides are close to bare soil surfaces. Thus, theoretically, the surface albedo should be lower in the middle elevation or near the left and right sides of the glacier. However, these spatial variations in albedo were not obvious in the retrieved surface albedo map taken from Landsat images. For a bare ice area, the altitudinal variation in satellite-derived albedo is slightly different from the measurement results of Takeuchi and Li (2008). These differences likely result from the retrieval accuracy of the Landsat albedo, which is not high enough to respond well to variation in the albedo caused by differences in dust abundance. In addition, it is probably due to a contrast of spatial resolution between the ground based and satellite-derived data (Yue et al., 2017). The measurement albedo and dust abundance can have high spatial variability over distances of only a few meters, evidenced by the high standard deviation. Thus, it is very probable that any abnormal sampling point has a significantly low or high dust abundance and albedo. However, the albedo

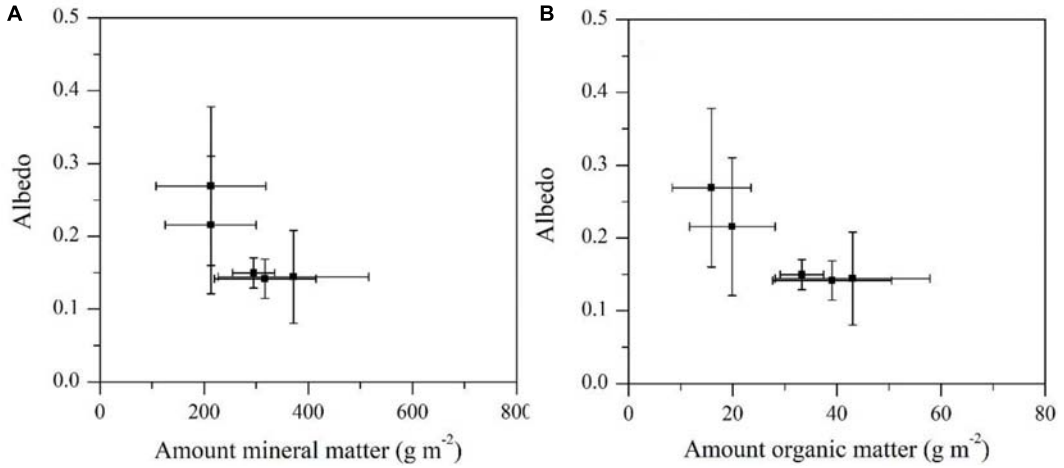

FIGURE 8 | Relationships between surface albedo and the number of mineral particles **(A)** and surface albedo and the amount of organic matter **(B)** on the ice surfaces.

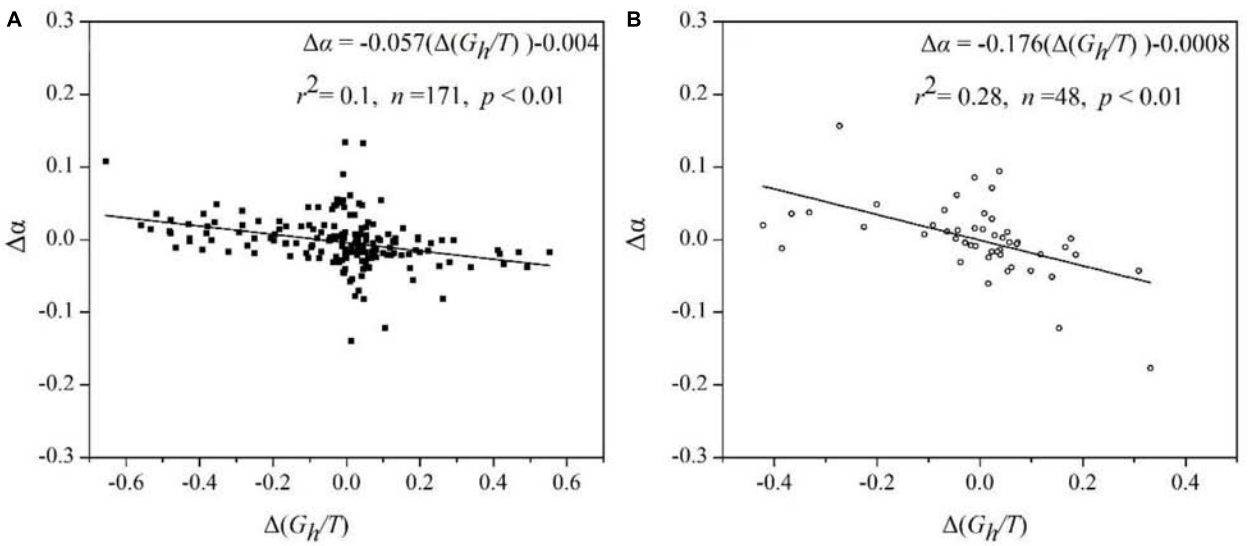

FIGURE 9 | The changes in albedo (Δα) between successive half hour vs. the corresponding changes in diffuse portion of shortwave incident radiation, $\Delta(G_h/T)$ over ice **(A)** and snow **(B)** between 26 June and 2 August 2007.

derived from the Landsat image is the average value for a 30 m × 30 m area.

CONCLUSION

In this study, the temporal variations in albedo were investigated using a data set of half-hour albedo measurements by AWS between 26 June and 1 August 2007 over the ablation area of Urumqi Glacier No. 1, a valley glacier in China. The data suggested that glacier albedo changes were characterized by a large range and very high frequency in the ablation season. Moreover, variations in surface albedo were generally more drastic for snow than ice, when solar zenith angle variations were less than 65°. The temporal variation in albedo emphasized that snow and ice surfaces must be treated separately. Over an ice surface, under the condition of more intense ablation, almost no variation in diurnal albedo cycles implied that the satellite-derived albedo represented short-term albedo values if there was no snowfall. However, rapid albedo variation caused by snowfall and snow metamorphism can quickly render satellite-derived albedo measurements out of date, even over the course of 1 day.

Spatiotemporal variation in albedo on a glacier-wide scale was also studied using three Landsat images taken during the ablation season in 2006. The retrieval results indicated that the mean of the glacier albedo gradually decreased as the ablation progressed, from 0.62 to 0.32. However, differences in the

physical composition of the glacier surface gradually increased, with a standard deviation of 0.13–0.20. Spatial variation in surface albedo was not obvious after snowfall. However, once ice was exposed, spatial variation became marked and generally increased with elevation, especially around the equilibrium line. Moreover, the patterns of spatial variation in the albedo on the eastern branch and the western branch were slightly different, which may be related to morpho-topographic variables, such as average altitude, slope, and aspect.

The characteristics of surface dust and their effect on glacier albedo were analyzed based on reflectance spectra and sampling snow and ice. The study glacier was mostly covered by fine brown dust in the ablation area. The dry weight of the surface dust ranged from 228 to 414 g m^{-2} with a mean of 312 g m^{-2}, which was within the normal range for Asian glaciers but significantly higher than that of glaciers of polar or sub-polar regions. Organic matter content in the dust ranged from 6.9 to 10.9% (with a mean value of 9.4%) on the ice surface. The abundances of dust and organic matter were greater in the middle parts of the glacier compared with the lower and upper parts of the glaciers. Glacier albedo was significantly reduced by surface dust, and organic matter was more effective than mineral particles in reducing albedo.

This study has discussed the influence of cloud on glacier albedo, in terms of physical properties, and attempted to quantify the dependence of variation in surface albedo on cloudiness over snow and ice surfaces using the diffuse portion of shortwave incoming radiation. The results indicated that a higher sensitivity of albedo to cloud was shown over snow surfaces.

DATA AVAILABILITY STATEMENT

The datasets for this article are not publicly available. Requests to access the datasets should be directed to XY, yuexiaoying@lzb.ac.cn or ntakeuch@faculty.chiba-u.jp.

AUTHOR CONTRIBUTIONS

XY, ZL, and NT designed research. XY performed the data analysis and wrote the manuscript. NT conducted field investigations and laboratory analyses. JZ and XY retrieved the glacier surface albedo from Landsat images. JF edited the English language of this manuscript. LW contributed to the figures drawing.

FUNDING

This work was supported by the Foundation for Excellent Youth Scholars of NIEER, CAS (FEYS2019003), the Strategic Priority Research Program of Chinese Academy of Sciences (XDA20020102 and XDA20020103), State Key Laboratory of Cryospheric Sciences (SKLCS-ZZ-2020), the National Natural Science Foundation of China (41761134093, 41771081, 41771077, and 41601076), the Grant-in-Aids of Japan Society for the Promotion of Science (23221004, 26247078, 26241020, and 16H01772), and the domestic visiting research program of Northwest Normal University.

ACKNOWLEDGMENTS

We would thank to the members of Tien Shan Glaciological Station, Northwest Institute of Eco-Environment and Resources of Chinese Academy of Sciences in Lanzhou, China, and Professor Takeuchi team of Department of Earth Sciences of Graduate School of Science of Chiba University, Japan, for supporting the data collection and laboratory analyses. We also thank the USGS (US Geological Survey) for the Landsat image data. In addition, we are very grateful to chief editor, scientific editor, and two reviewers for their comments on the manuscript.

REFERENCES

Abermann, J., Kinnard, C., and Macdonell, S. (2014). Albedo variations and impact of cloud on glaciers in the Chilean semi-arid Andes. *J. Glaciol.* 60, 183–191. doi: 10.3189/2014JoG13J094

Arendt, A. (1999). Approaches to modelling the surface albedo of a high arctic glacier. *Geogr. Ann.* 81A, 477–487. doi: 10.1111/j.0435-3676.1999.00077.x

Arnold, N. S. I., Willis, I. C., Sharp, M. J., Richards, K. S., and Lawson, W. J. (1996). A distributed surface energy-balance model for a small valley glacier. I. development and testing for Haut Glacier d'Arolla, Valais, Switzerland. *J. Glaciol.* 42, 77–89. doi: 10.1017/S0022143000030549

Azzoni, R., Antonella, S., Zerboni, A., Maugeri, M., Smiraglia, C., and Diolaiuti, G. A. (2016). Estimating ice albedo from fine debris cover quantified by a semi-automatic method the case study of Forni Glacier. *Italian Alps. Cryosphere* 10, 665–679. doi: 10.5194/tc-10-665-2016

Brock, B. W. (2004). An analysis of short-term albedo variations at Haut Glacier d'Arolla, Switzerland. *Geogr. Ann.* 86, 53–65. doi: 10.1111/j.0435-3676.2004.00213.x

Brock, B. W., Willis, I. C., and Sharp, M. J. (2000). Measurement and parameterization of albedo variations at Haut Glacier d'Arolla, Switzerland. *J. Glaciol.* 46, 675–688. doi: 10.3189/172756500781832675

Cong, Z., Gao, S., Zhao, W., Wang, X., Wu, G., Zhang, Y., et al. (2018). Iron oxides in the cryoconite of glaciers on the Tibetan Plateau: abundance, speciation and implications. *Cryosphere* 12, 3177–3186. doi: 10.5194/tc-12-3177-2018

Cuffey, K. M., and Paterson, W. S. B. (2010). *The Physics of Glaciers*, 4th Edn. Oxford: Butterworth-Heinemann/Elsevier.

Cutler, P. M., and Munro, D. S. (1996). Visible and near-infrared reflectivity during the ablation period on Peyto Glacier, Alberta, Canada. *J. Glaciol.* 42, 333–340. doi: 10.3189/S0022143000004184

Dong, Z., Li, Z., Wang, F., and Zhang, M. (2009). Characteristics of atmospheric dust deposition in snow on the glaciers of eastern Tian Shan, China. *J. Glaciol.* 55, 797–804. doi: 10.3189/002214309790152393

Dumont, M., Brun, E., Picard, G., Michou, M., Libois, Q., Petit, J.-R., et al. (2014). Contribution of light-absorbing impurities in snow to Greenland's darkening since 2009. *Nature Geosci.* 7, 509–512. doi: 10.1038/NGEO2180

Farinotti, D., Longuevergne, L., Moholdt, G., Duethmann, D., Molg, T., Bolch, T., et al. (2015). Substantial glacier mass loss in the Tian Shan over the past 50 years. *Nature Geosci.* 8, 716–722. doi: 10.1038/NGEO2513

Fugazza, D., Senese, A., Azzoni, R. S., Maugeri, M., and Diolaiuti, G. A. (2016). Spatial distribution of surface albedo at the Forni Glacier (Stelvio National Park, Central Italian Alpa). *Cold Reg. Sci. Technol.* 125, 128–137. doi: 10.1016/j.coldregions.2016.02.006

Gabbi, J., Huss, M., Bauder, A., Gao, F., and Schwikowski, M. (2015). The impact of Saharan dust and black carbon on albedo and long-term mass balance of an Alpine glacier. *Cryosphere* 9, 1385–1400. doi: 10.5194/tc-9-1385-2015

Gardner, A. S., and Sharp, M. J. (2010). A review of snow and ice albedo and the development of a new physically based broadband albedo parameterization. *J. Geophys. Res.* 115, 137–147. doi: 10.1029/2009JF001444

Hock, R. (2005). Glacier melt: a review of processes and their modeling. *Prog. Phys. Geogr.* 29, 362–391. doi: 10.1191/0309133305pp453ra

Hock, R., and Holmgren, B. (2005). A distributed surface energy balance model for complex topography and its application to Storglaciaren, Sweden. *J. Glaciol.* 51, 25–36. doi: 10.3189/172756505781829566

Hu, Z., Kang, S., Yan, F., Zhang, Y., Li, Y., Chen, P., et al. (2018). Dissolved organic carbon fractionation accelerates glacier-melting: a case study in the northern Tibetan Plateau. *Sci. Total Environ.* 627, 579–585. doi: 10.1016/j.scitotenv.2018.01.265

Huintjes, E., Sauter, T., Schroter, B., Maussion, F., Yang, W., Kropacek, J., et al. (2015). Evaluation of a coupled snow and energy balance model for Zhadang glacier, Tibetan Plateau, using glaciological measurements and time-lapse photography. *Arct. Antarct. Alp. Res.* 47, 573–590. doi: 10.1657/AAAR0014-073

Jonsell, U., Hock, R., and Holmgren, B. (2003). Spatial and temporal variations in albedo on Storglaciaren, Sweden. *J. Glaciol.* 49, 59–68. doi: 10.3189/172756503781830980

Kang, E., and Atsumu, O. (1993). Study on energy-water-mass balance and the hydrological flow model in a glacierized catchment of Tianshan mountain. *Chin. Sci. Bull.* 38, 925–929.

Klok, E. J., Greull, W., and Oerlemans, J. (2003). Temporal and spatial variation of the surface albedo of morteratschgletscher, Switzerland, as derived from 12 landsat images. *J. Glaciol.* 49, 491–502. doi: 10.3189/172756503781830395

Klok, E. J., and Oerlemans, J. (2002). Model study of the spatial distribution of the energy and mass balance of Morteratschgletscher, Switzerland. *J. Glaciol.* 48, 505–518. doi: 10.3189/172756502781831133

Klok, E. J., and Oerlemans, J. (2004). Modelled climate sensitivity of the mass balance of Morteratschgletscher and its dependence on albedo parameterization. *Int. J. Climatol.* 24, 231–245. doi: 10.1002/joc.994

Knap, W. H., Brock, B. W., Oerlemans, J., and Willis, I. C. (1999). Comparison of landsat TM-derived and ground-based albedos of Haut Glacier d'Arolla, Switzerland. *Int. J. Remote Sens.* 20, 3293–3310. doi: 10.1080/014311699211345

Lafon, S., Sokolik, I. N., Rajot, J. L., Caquineau, S., and Gaudichet, A. (2006). Characterization of iron oxides in mineral dust aerosols: implications for light absorption. *J. Eophys. Res. Atmos.* 111:D21207. doi: 10.1029/2005JD007016

Li, X., Kang, S., He, X., Qu, B., Tripathee, L., Jing, Z., et al. (2017). Light-absorbing impurities accelerate glacier melt in the Central Tibetan Plateau. *Sci. Total Environ.* 58, 482–490. doi: 10.1016/j.scitotenv.2017.02.169

Li, X., Kang, S., Zhang, G., Qu, B., Tripathee, L., Paudyal, R., et al. (2018). Light-absorbing impurities in a southern Tibetan Plateau glacier: variations and potential impact on snow albedo and radiative forcing. *Atmos. Res.* 200, 77–87. doi: 10.1016/j.atmosres.2017.10.002

Li, Y., Kang, S., Yan, F., Chen, J., Wang, K., Paudyal, R., et al. (2019). Cryoconite on a glacier on the northeastern Tibetan plateau light absorbing impurities albedo and enhanced melting. *J. Glaciol.* 65, 633–644. doi: 10.1017/jog.2019.41

Li, Z., Li, H., and Chen, Y. (2011). Mechanisms and simulation of accelerated shrinkage of continental glaciers: a case study of Urumqi Glacier No. 1 in eastern Tianshan, Central Asia. *J. Earth Sci.* 22, 423–430. doi: 10.1007/s12583-011-0194-5

Ming, J., Xiao, C., Wang, F., Li, Z., and Li, Y. (2016). Grey tienshan urumqi glacier No.1 and light-absorbing impurities. *Environ. Sci. Pollut. Res.* 23, 9549–9558. doi: 10.1007/s11356-016-6182-7

Mortimer, C. A., and Sharp, M. (2018). Spatiotemporal variability of Canadian high arctic glacier surface albedo from MODIS data, 2001–2016. *Cryosphere* 12, 701–720. doi: 10.5194/tc-12-701-2018

Moustafa, S. E., Rennermalm, K. A., Smith, L. C., Miller, M. A., Mioduszewski, J. R., Koenig, L. S., et al. (2015). Multi-modal albedo distributions in the ablation area of the southwestern Greenland Ice Sheet. *Cryosphere* 9, 905–923. doi: 10.5194/tc-9-905-2015

Munro, D. S. (1991). A surface energy exchange model of glacier melts and net mass balance. *Int. J. Climatol.* 11, 689–700. doi: 10.1002/joc.3370110610

Naegeli, K., Huss, M., and Hoelzle, M. (2019). Change detection of bare-ice albedo in the Swiss Alps. *Cryosphere* 13, 397–412. doi: 10.5194/tc-13-397-2019

Niu, H., Kang, S., Shi, X., Paudyai, R., He, Y., Li, G., et al. (2017). In-situ measurements of light-absorbing impurities in snow of glacier on Mt. Yulong and implications for radiative forcing estimates. *Sci. Total Environ.* 581–582, 848–856. doi: 10.1016/j.scitotenv.2017.01.032

Oerlemans, J., Giesen, R. H., and Van Den Broeke, M. R. (2009). Retreating alpine glaciers increased melt rates due to accumulation of dust (Vadret da Morteratsch, Switzerland). *J. Glaciol.* 55, 729–736. doi: 10.3189/002214309789470969

Oerlemans, J., and Knap, W. H. (1998). A 1 year record of global radiation and albedo in the ablation zone of Morteratscher, Switzerland. *J. Glaciol.* 44, 231–238. doi: 10.3189/s0022143000002574

Pellicciotti, F., Brock, B., Strasser, U., Burlando, P., Funk, M., and Corripoi, J. (2005). An enhanced temperature index glacier melt model including the shortwave radiation balance development and testing for Haut Glacier d'Arolla, Switzerland. *J. Glaciol.* 51, 573–587. doi: 10.3189/172756505781829124

Sirguey, P., Still, H., Cullen, N. J., Dumont, M., Arnaud, Y., and Conway, J. P. (2016). Reconstructing the mass balance of Brewster Glacier, New Zealand, using MODIS-derived glacier-wide albedo. *Cryosphere* 10, 2465–2484. doi: 10.5194/tc-10-2465-2016

Skiles, S. M., and Painter, T. (2016). Daily evolution in dust and black carbon content, snow grain size, and snow albedo during snowmelt, Rocky Mountains, Colorado. *J. Glaciol.* 63, 118–132. doi: 10.1017/jog.2016.125

Stroeve, J., Nolin, A., and Steffen, K. (1997). Comparison of AVHRR derived and in situ surface albedo over the Greenland ice sheet. *Remote Sens. Environ.* 62, 262–276. doi: 10.1016/s0034-4257(97)00107-7

Sun, W., Qin, X., Du, W., Liu, W., Liu, Y., Zhang, T., et al. (2014). Ablation modeling and surface energy budget in the ablation zone of Laohugou glacier No. 12, western Qilian Mountains, China. *Ann. Glaciol.* 55, 111–120. doi: 10.3189/2014aog66a902

Sun, W., Qin, X., Wang, Y., Chen, J., Du, W., Zhang, T., et al. (2017). The response of surface mass and energy balance of a continental glacier to climate variability, western Qilian Mountains, China. *Clim. Dyn.* 50, 3557–3570. doi: 10.1007/s00382-017-3823-6

Takeuchi, N. (2002). Optical characteristics of cryoconite (surface dust) on glacier the relationship between light absorbency and the property of organic matter contained in the cryoconite. *Ann. Glaciol.* 34, 409–414. doi: 10.3189/172756402781817743

Takeuchi, N. (2009). Temporal and spatial variations in spectral reflectance and characteristics of surface dust on Gulkana Glacier, Alaska range. *J. Glaciol.* 55, 701–709. doi: 10.3189/002214309789470914

Takeuchi, N., Fujisawa, Y., Kadota, T., Tanaka, S., Miyairi, M., Shirakawa, T., et al. (2015). The effect of impurities on the surface melt of a glacier in the suntar-khayata mountain range, Russian Siberia. *Front. Earth Sci.* 3:82.

Takeuchi, N., Kohshima, S., Yoshimura, Y., Seko, K., and Fujita, K. (2000). Characteristics of cryoconite holes on a Himalayan glacier, Yala Glacier central Nepal. *Bull. Glaciol. Res.* 17, 51–59.

Takeuchi, N., and Li, Z. (2008). Characteristics of surface dust on Ürümqi Glacier No. 1 in the Tien Shan Mountains, China. *Arct. Antarct. Alp. Res.* 40, 744–750. doi: 10.1657/1523-0430(07-094)[takeuchi]2.0.co;2

Takeuchi, N., Matsuda, Y., Sakai, A., and Fujita, K. (2005). A large amount of biogenic surface dust (cryoconite) on a glacier in the Qilian Mountains, China. *Bull. Glaciol. Res.* 22, 1–8.

Takeuchi, N., Nagatsuka, N., Uetake, J., and Shimada, R. (2014). Spatial variations in impurities (cryoconite) on glaciers in northwest Greenland. *Bull. Glaciol. Res.* 32, 85–94.

Takeuchi, N., Nishiyama, H., and Li, Z. (2010). Structure and formation process of cryoconite granules on Urumqi glacier No. 1, Tien Shan, China. *Ann. Glaciol.* 51, 9–14. doi: 10.3189/172756411795932010

Takeuchi, N., Uetake, J., Fujita, K., Aizen, V., and Nikitin, S. (2006). A snow algal community on Akkem Glacier in the Russian Altai Mountains. *Ann. Glaciol.* 43, 378–384. doi: 10.3189/172756406781812113

Wang, J., Ye, B., Cui, Y., He, X., and Yang, G. (2014). Spatial and temporal variations of albedo on nine glaciers in western China from 2000 to 2011. *Hydrol. Process.* 28, 3454–3465. doi: 10.1002/hyp.9883

Warren, S. G. (1982). Optical properties of snow. *Rev. Geophys. Space Phys.* 20, 67–89.

WGMS (2017). *Global Glacier Change Bulletin No. 2 (2014–2015)*. CSU(WDS)/IUGG (IACS)/UNEP/UNESCO/WMO. Zurich: World Glacier Monitoring Service.

Wiscombe, W. J., and Warren, S. G. (1980). A model for the spectral albedo of snow. I: pure snow. *J. Atmos. Sci.* 37, 2712–2733.

Wittmann, M., Zwaaftink, C. D. G., Schmidt, L. S., Guðmundsson, S., Pálsson, F., Arnalds, O., et al. (2017). Impact of dust deposition on the albedo of Vatnajökull ice cap, Iceland. *Cryosphere* 11, 741–754. doi: 10.5194/tc-11-741-2017

Wright, P., Bergin, M., Dibb, J., Lefer, B., Domine, F., Carman, T., et al. (2014). Comparing MODIS daily snow albedo to spectral albedo field measurements in Central Greenland. *Remote Sens. Environ.* 140, 118–129. doi: 10.1016/j.rse.2013.08.044

Yallop, M. L., Alexandre, A. M., Perkins, R. G., Cook, J., Telling, J., Fagan, D., et al. (2012). Photophysiology and albedo-changing potential of the ice algal community on the surface of the Greenland ice sheet. *ISME J.* 6, 2302–2313.

Yang, D., Kang, E., and Felix, B. (1992). Characteristics of precipitation in the source area of the Urumqi river basin. *J. Glaciol. Geocryol.* 14, 258–266.

Yue, X., Zhao, J., Li, Z., Zhang, M., Fan, J., Wang, L., et al. (2017). Spatial and temporal variations of the surface albedo and other factors influencing Urumqi Glacier No. 1 in Tien Shan, China. *J. Glaciol.* 63, 899–911. doi: 10.1017/jog.2017.57

Zemp, M., Huss, M., Thibert, E., McNabb, R., Huber, J., Barandun, M., et al. (2019). Global glacier mass changes and their contributions to sea-level rise from 1961 to 2016. *Nature* 568, 382–386. doi: 10.1038/s41586-019-1071-0

Zhang, X., Wu, G., Zhang, C., Xu, T., and Zhou, Q. (2015). What is the real role of iron oxides in the optical properties of dust aerosols? *Atmos. Chem. Phys.* 15, 12159–12177.

Zhu, M., Yao, T., Yang, W., Maussion, F., Huintjes, E., and Li, S. (2015). Energy- and mass-balance comparison between Zhadang and Parlung No. 4 glaciers on the Tibetan plateau. *J. Glaciol.* 61, 595–607. doi: 10.3189/2015JoG14J206

Conflict of Interest: The authors declare that the research was conducted in the absence of any commercial or financial relationships that could be construed as a potential conflict of interest.

Copyright © 2020 Yue, Li, Zhao, Fan, Takeuchi and Wang. This is an open-access article distributed under the terms of the Creative Commons Attribution License (CC BY). The use, distribution or reproduction in other forums is permitted, provided the original author(s) and the copyright owner(s) are credited and that the original publication in this journal is cited, in accordance with accepted academic practice. No use, distribution or reproduction is permitted which does not comply with these terms.

frontiers in Earth Science

ORIGINAL RESEARCH
published: 12 June 2020
doi: 10.3389/feart.2020.00153

Snow Samples Combined With Long-Range Transport Modeling to Reveal the Origin and Temporal Variability of Black Carbon in Seasonal Snow in Sodankylä (67°N)

Outi Meinander[1]*, *Anna Kontu*[2], *Rostislav Kouznetsov*[1,3] and *Mikhail Sofiev*[1]

[1] Atmospheric Composition Research Unit, Climate Research Programme, Finnish Meteorological Institute, Helsinki, Finland, [2] Earth Observation Research Unit, Space and Earth Observation Centre, Finnish Meteorological Institute, Sodankylä, Finland, [3] Obukhov Institute for Atmospheric Physics, Moscow, Russia

In the Arctic areas, the influence of global climate change is enhanced. Enabling a better understanding of the changes in the Arctic environment is of the utmost importance. The deposition of local and long-range transported air pollutants includes light-absorbing aerosols, such as black carbon (BC), which darken bright surfaces and induce snow melt. In 2009–2013, surface snow was sampled on a weekly basis during autumn, winter and spring at the Arctic Space Center of the Finnish Meteorological Institute in Sodankylä, which is located north of the Arctic Circle (67.37° N, 26.63° E). Snow samples were analyzed for BC with an Organic/Elemental Carbon Aerosol (OCEC) analyzer. These data were combined with SILAM modeling (System for Integrated modeLing of Atmospheric coMposition) to reveal the origin and temporal (weekly, monthly, and seasonal) variability of black carbon in seasonal snow. Quantitative footprint calculations for the BC observations were performed with the SILAM-model considering emission sources at all heights and including also the sensitivity to the local and near-surface sources. The median BC concentration in snow was 25 μg/kg (number of samples $n = 107$, skewness $\gamma_1 = 0.12$, 75th percentile $Q3 = 42$ μg/kg), determined as [μg-EC/L-H_2O]. During snow accumulation season, the median surface snow black carbon concentration was 21 μg/kg ($n = 78$, $\gamma_1 = 1.5$, $Q3 = 33$ μg/kg), and during melt season, it was 57 μg/kg ($n = 29$, $\gamma_1 = 2.2$, $Q3 = 85$ μg/kg). The melt period was identified using snow depth data from the Sodankylä station. The highest values in spring represented the enrichment of BC to the snow surface due to seasonal snow melt. The spring melt BC enrichment ratio was 2.7 (calculated as the ratio of median spring melt season concentration to median accumulation season snow concentration). The results showed that increased surface snow BC concentrations (>30 μg/kg) were due to air masses originating from the Murmansk region in Russia, where smelting and mining industries are located. The temporal variability of BC in snow was high and depended on atmospheric and cryospheric processes, mostly the origin of BC due to atmospheric transport and dry and wet deposition processes, as well as post-depositional snow processes.

Keywords: Arctic, BC, deposition, long-range transport, origin, seasonal, snow melt, thermal-optical OCEC analysis

OPEN ACCESS

Edited by:
Jing Ming,
Independent Researcher, Melbourne, Australia

Reviewed by:
Maria Shahgedanova,
University of Reading, United Kingdom
Xiaobin Xu,
Chinese Academy of Meteorological Sciences, China
Mark Flanner,
University of Michigan, United States

***Correspondence:**
Outi Meinander
outi.meinander@fmi.fi

Specialty section:
This article was submitted to Cryospheric Sciences, a section of the journal Frontiers in Earth Science

Received: *17 January 2020*
Accepted: *22 April 2020*
Published: *12 June 2020*

Citation:
Meinander O, Kontu A, Kouznetsov R and Sofiev M (2020) Snow Samples Combined With Long-Range Transport Modeling to Reveal the Origin and Temporal Variability of Black Carbon in Seasonal Snow in Sodankylä (67°N). Front. Earth Sci. 8:153. doi: 10.3389/feart.2020.00153

INTRODUCTION

The influence of climate change is enhanced in the Arctic in comparison to other areas (Serreze and Barry, 2011). Enabling a better understanding of the changes in the Arctic climate and environment is of the utmost importance. In addition to temperature feedbacks, other feedbacks such as ice-albedo feedback contribute to Arctic amplification (Boy et al., 2019), i.e., greater warming in the region. Ice-albedo feedback is greatly influenced by the deposition of local pollution and pollution transported over long distances. This includes light-absorbing aerosols, such as black carbon (BC), which darken bright surfaces, induce snow melt, and enhance Arctic climate change (IPCC, 2019). Black carbon is a light-absorbing aerosol originating mainly from the incomplete combustion of carbonaceous materials like fossil fuels and biomass. Various cryospheric and climatic impacts of BC in snow and ice have been widely investigated (e.g., Forsström et al., 2009; Doherty et al., 2010; Meinander et al., 2014; Peltoniemi et al., 2015), and detailed scientific assessments have been presented in Bond et al. (2013), in the Arctic Monitoring Assessment Programme report (AMAP, 2015) and in the Intergovernmental Panel on Climate Change report (IPCC, 2019).

Long-range transported industrial and biofuel burning emissions, mostly outside the Arctic, i.e., from Europe, East Asia, the former Soviet Union, and North America, contribute to the black carbon observed in the Arctic region (Sharma et al., 2013; Jiao et al., 2014). Half of the BC originating from biomass in the Arctic is estimated to have come from Europe, North America, and Russia, each contributing 10–15% (Koch and Hansen, 2005). Also, Europe, Russia, and South Asia each contribute about 20–25% of BC to the low-altitude springtime "Arctic haze," which consists primarily of anthropogenic particles with high sulfur concentrations and other components such as soot, with a contribution from BC released in the atmosphere via gas flaring (Stohl et al., 2013).

Black carbon is a short-lived climate forcer (SLCF) that undergoes regional and intercontinental transport from source regions during its short atmospheric lifetime. When emitted, BC is mostly hydrophobic (Laborde et al., 2013) but can become coated with water-soluble components through atmospheric aging processes in which it changes from hydrophobic to hydrophilic. The atmospheric removal of BC occurs within a few days to weeks via precipitation and contact with surfaces (Bond et al., 2013). The atmospheric lifetime of BC can be largely determined by factors that control local deposition rates, e.g., precipitation (Zhang et al., 2015), turbulence (Emerson et al., 2018), and breakdown of temperature inversions in spring (Stohl, 2006). Wet-scavenging processes (in-cloud and below-cloud scavenging) are a major source of uncertainty in predicting atmospheric BC concentrations over remote regions (Schwarz et al., 2010). Arctic climate response has been found to be sensitive to the vertical distribution and deposition efficiency of black carbon reaching the Arctic (Flanner, 2013). Normalized to the mass of emissions, BC emissions within the Arctic have been shown to induce warming about five times greater than emissions from middle latitudes because there is a higher fraction of within-Arctic emissions deposited in snow and sea ice than mid-latitude emissions (Sand et al., 2013). A significantly longer BC impact takes place through deposition and accumulation in the cryosphere, continuing until snow or ice has melted. The deposition of BC in snow or ice reduces surface albedo and contributes to earlier and more rapid snow and ice melt (Warren and Wiscombe, 1980; Hansen and Nazarenko, 2004; Flanner et al., 2007; Xu et al., 2009; Bond et al., 2013; Peltoniemi et al., 2015). The widest Arctic data set for BC snow content is presented in Doherty et al. (2010), with a pan-Arctic network of observations using one sampling and analysis protocol for all the sites. The origin of black carbon in snow has been studied, e.g., in Wang et al. (2011), Eckhardt et al. (2017) and Mori et al. (2019).

Simple backward trajectories can be used for a qualitative analysis of the origins of pollution in the air. The pollution origin in the current study has been computed using the adjoint dispersion formalism, which, unlike the often-used back-trajectory approach, accounts for the full list of relevant processes rather than a back-transport of the mean wind. In application to the BC snow samples, the crucial processes were scavenging with snow, dry deposition and sedimentation (for coarse aerosols). The outcome of the adjoint computations, the footprints, allow for quantitative analysis of the sources of pollution that affected the specific observation. The observations were performed in Sodankylä (67°36 N, 26°62 E), Finland, north of the Arctic Circle, with week-long sampling over inters 2009–2013 and subsequent sprint-time snow-melt seasons. The SILAM-model (System for Integrated modeLing of Atmospheric coMposition) was subsequently applied to each sample computing its footprint. The results were grouped and processed statistically thus revealing the sources affecting the monitoring site.

MATERIALS AND METHODS

Site Description

Sodankylä is situated north of the Arctic Circle, in the boreal forest zone (**Figure 1**). The Arctic Space Center in Sodankylä is located at 67.37° N, 26.63° E, 7 km south of the Sodankylä town center. The station area consists of coniferous forests and open areas on mineral soil, as well as an open peat bog (Leppänen et al., 2016). Snow falls in Sodankylä in October, and snowpack reaches its maximum depth (79 cm on average) in late March and melts in mid-May (Pirinen et al., 2012). The monthly average air temperature is below 0°C from November to April, and the average annual precipitation is 527 mm. The snow conditions belong to the taiga class (Sturm and Holmgren, 1995). The station sites include regular manual and automatic snow measurements. Manual snow measurements cover snow depth and snow water equivalent (SWE), as well as snow macro- and microstructures at several sites for temperature, density, stratigraphy, grain size, specific surface area (SSA), and liquid water content (LWC), as detailed in Leppänen et al. (2016). Automatic observations include, for example, snow height, SWE, broadband albedo, and a snow temperature profile. More details about instrumentation (description, coordinates, sensor types, and data availability) can be found at http://litdb.fmi.fi. Snow-related Sodankylä measurements also include the automatic weather station (AWS)

FIGURE 1 | Map of the sampling location in Sodankylä, north-up map orientation. All the snow samples represented one location, shown in the photograph. The sampling site is inside the FMI Sodankylä Space and Earth Observation Center area, 67.37° N, 26.63° E. (National Land Survey open data Attribution CC 4.0 license).

data, the micrometeorological mast (Kangas et al., 2016), the road weather station (Sukuvaara et al., 2016), the UV measurement field (Meinander et al., 2013; Mäkelä et al., 2016), the distributed soil moisture and frost stations (Ikonen et al., 2015), and the optical laboratory (Lakkala et al., 2016). The area is characterized with very low wind speeds, e.g., with a monthly wind speed average of 2.5–2.9 m s^{-1} above the treetops and a 2-year average during the snow season at 1.5 m height in a forest opening of 1.17 +/− 0.56 m/s^{-1} (Pirinen et al., 2012). The station is part of the World Meteorological Organization (WMO) Global Cryosphere Watch (GAW) network. Synoptic weather observations have been made in Sodankylä since 1908; the first measurements were taken in the town center, and since 1913, they have been taken at the current research station area (Tietäväinen et al., 2010). In this study, the daily snow depth measured at the Sodankylä Tähtelä station during 2009–2013 was used (FMI-ARC database, 2020). These data are available from http://litdb.fmi.fi, under the Creative Commons Attribution 4.0 International License (CC BY 4.0).

Snow Sampling and OCEC Analysis

Between 21 January, 2009, and 3 May, 2013, during snow season, surface snow was sampled on a weekly basis at the Finnish Meteorological Institute's Arctic Space Center in Sodankylä (67.37° N, 26.63° E), 67 km north of the Arctic Circle (**Table 1**). A total of 107 weekly samples of BC in snow were collected from one location. These data were used to study the origin and temporal variability of black carbon in surface snow. The samples were collected at the end of the work week (Thursday–Friday) to avoid contamination from wood-stove saunas, the main local sources of BC in the air. First, two to three centimeters of surface snow was collected, always from the same sampling field (**Figure 1**) dedicated to weekly BC sampling, using the same sampling tool and plastic container each time. The field was located inside a fenced area in order to prohibit reindeer from destroying or contaminating the snow pack. Sampling started at the beginning of snow season in one spot in the sampling field, and each week, the sampling spot progressed along a line, one side after another, creating a path in the field. The site is in the vicinity of the Arctic Space Center sounding station, where the sample was taken immediately after sampling. The snow sample was then melted in a microwave oven, after which the meltwater was filtered through sterilized micro-quartz filters (Munktell, 55 mm diameter) using a hand pump attached to the filtering system to create a vacuum during filtering. Filters were dried and analyzed with a Thermal-Optical Carbon Aerosol Analyzer (OCEC) [Sunset Laboratory Inc. (2018) Forest Grove, USA] for their elemental carbon (EC), organic carbon (OC), and total carbon (TC) concentrations. The volume of meltwater was used for concentration conversions into μg/kg, which is equal to parts per billion by mass (ppb), and is determined as μg-EC/L-H_2O in the OCEC method. The thermal-optical OCEC method is the current European standard for determining atmospheric BC (Brown et al., 2017; CEN-TC264, 2017). Here, the NIOSH 5040 protocol developed by Birch (2003) was used. The thermal-optical method was created by Birch and Cary (1996), in which a more detailed description of the method can be found.

SILAM Modeling

Possible origins of the snow sample impurities were estimated through analyses of so-called footprints of the observations. This approach is based on solving the adjoint dispersion equation (Sofiev et al., 2015), which is done separately for each observation. The problem is solved backwards in time; it starts from the end of the observational interval so that the resulting field represents the sensitivity distribution of that particular observation to the emission sources located within the area covered by the footprint and emits at the corresponding time period. In particular, the observed values can be affected only by the emission fluxes from the area when and where the footprint is non-zero. This sensitivity field has certain analogies with the spatial-temporal density of a continuum of backward trajectories. It should be stressed, however, that the footprint is not a probability distribution for the possible source locations: a higher sensitivity to some area evidently does not imply a higher probability for the source to be located in this area.

The simulations were performed with the System for Integrated modeling of Atmospheric coMposition (SILAM, http://silam.fmi.fi, accessed 24.03.2020; Galperin, 2000; Sofiev, 2002; Sofiev et al., 2015), which is an offline global-to-meso-scale chemistry transport model. The operational evaluation of SILAM had been performed on a regular basis for many years within the scope of the Copernicus Atmospheric Monitoring Service (CAMS) and its predecessors (http://atmosphere.copernicus.eu, accessed 24.03.2020), as well as within several research projects

TABLE 1 | Summary of snow and black carbon data for 2009–2013 around the Sodankylä Arctic Space Center area.

Year	Snow on	Snow off	Day of h^a_{max}	$BC_{enhanced}$ spring melt observations	Md_{BC}; Q3	*n*
2009	8 Oct	5 May	31 March	19, 24, and 30 April	34; 45	22
2010	24 Oct	15 May	30 March	23 and 30 April; 7 and 14 May	25; 37	30
2011	17 Nov	2 May	22 March	8, 15, and 22 April	25; 42	21
2012	24 Oct	19 May	11 April	13 April; 4 and 11 May	16; 29	22
2013	23 Oct	9 May	29 March	19 and 26 April	31; 50	12

BC concentrations in snow are parts per billion in mass [μg/kg], which equals [μg/L], determined as [μg-EC/L-H_2O]. Snow depth data are from the FMI Tähtelä weather station. The day of snow height maximum, h_{max}, refers to the end of snow accumulation and the beginning of the melt, after which the snow depth decreases as a function of time, n = number of weekly samples in 1 year, n_{tot} = 107, Md_{BC} = BC concentration median, Q3 = 75th percentile of BC concentrations.
[a]During snow accumulation periods in 2009–2013, Md_{BC} was 21 μg/kg (n = 78), and during the melt period, it was 57 μg/kg (n = 29).

all over the world (Huijnen et al., 2010; Brasseur et al., 2019; Petersen et al., 2019). In the current study, SILAM was used for the footprint calculations following the approach we developed and applied for source apportionment tasks (in, e.g., Saarikoski et al., 2007; Siljamo et al., 2008; Prank et al., 2010; Veriankaite et al., 2010).

Three-hourly meteorological fields from short-term operational forecasts of the European Center for Medium-Range Weather Forecasts (ECMWF) were used as a driver for SILAM. The adjoint simulations were performed with a resolution of 0.5 × 0.25 degrees on a domain of 10–60°E, 55–75°N with eight stacked layers of thickness (30, 70, 100, 200, 500, 1,000, 2,000, 2,000 m) covering a height range from the surface to 5.9 km. The simulations were separately run for each observation 5 days back in time, with an internal time step of 30 min and hourly output. Note, however, that the precision of the snowfall timing in the simulations is controlled by the time step of the driving meteorology.

To minimize the effect of dry deposition and to ensure consistency between observed and modeled snowfalls, only such cases were selected in which snowfall was reported by both the weather station at Sodankylä and the meteorological driver to be more than 1 mm snowfall within 24 h before sample collection and in which the amount of precipitation agreed within a factor of two between them (**Figure 2**). The uptake of the soot by snow was parameterized in a simple way: the in-snow BC content was used as a proxy for the in-air concentration within the scavenging height range. Two scenarios for scavenging were considered. The first was "below-cloud," where the in-snow BC was assumed to be representative of the in-air concentration average within the height range from the ground to 0.8 h_{cloud}, the second was "in-cloud," 0.8–1.2 h_{cloud}, where h_{cloud} was the height of the center of mass of the condensed cloud water from the meteorological model. The temporal distribution of the sensitivity was weighted according to the snowfall intensity from the meteorological model so that the total sensitivity is unity.

To reduce the impact of uncertainty in the vertical distribution of the sources of black carbon, the 3D adjoint-sensitivity distribution was processed into the 2D footprint by taking maximum of the vertical profile of the sensitivity in each grid cell at each time. With such processing, all emission sources emitting at all heights within the footprint were included and accounted for their (potential) contribution to the observations.

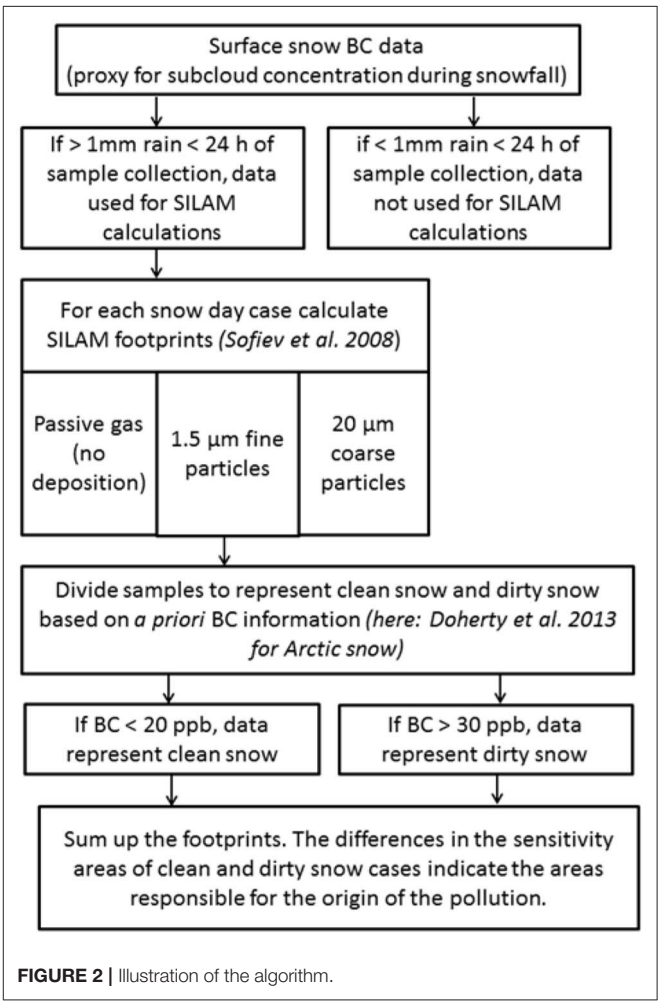

FIGURE 2 | Illustration of the algorithm.

The volumetric content of black carbon was used as a tracer of anthropogenic pollution. With the above criteria, "clean" (<20 μg/kg of BC based on Doherty et al., 2010, 2013) and "dirty" (>30 μg/kg of BC) samples were selected, and the in-cloud and sub-cloud footprints for both classes were calculated. Since the size of airborne black carbon is unknown, the footprints were calculated for passive gas with no deposition for 1.5 μm (fine) particles and for 20 μm (coarse) particles. Since uncertainties in

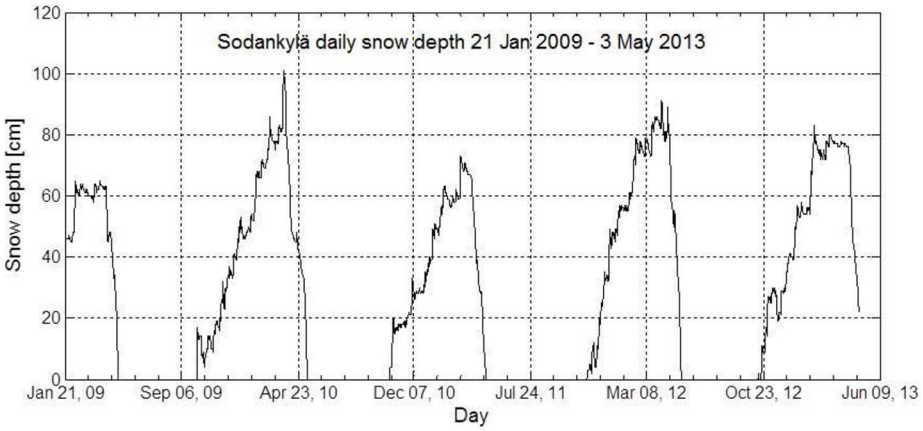

FIGURE 3 | Daily snow depth at Sodankylä during 21 January, 2009–3 May, 2013.

the input data and the parametrizations are very large, we limit our considerations to comparisons of average "clean" and "dirty" footprints, giving equal weight to the footprints in each class.

RESULTS

Snow Concentrations

The distribution of black carbon values was found to be positively skewed (number of samples $n = 107$, skewness $\gamma_1 = 0.12$). Therefore, the results are reported using median and 75th percentile, instead of average and standard deviation which are valid for normally distributed data. From 21 January, 2009, to 3 May, 2013, the median BC concentration ($n = 107$) in surface snow in Sodankylä was 25 μg/kg, and the 75th percentile was $Q3 = 42$ μg/kg (**Table 1**). In spring, increased BC concentrations (ranging from 53 to 293 μg/kg) in seasonal snow melt (**Figure 3**) were observed during each of the five consecutive springs (**Figure 4**). The highest values represented the enrichment of BC to the snow surface due to post-depositional snow processes. The spring BC enrichment ratio was 2.7, calculated as the ratio of 50th percentile (median) of spring melt season concentration to accumulation season snow concentration, $n_{tot} = 107$. The melt period was identified using snow depth data from the FMI Tähtelä weather station and was defined as the period in spring starting from the day when snow depth begins to decrease as a function of time (**Table 1**, snow accumulation period = from "snow on" to "day of h_{max};" snow melt period = from "day of h_{max}" to "snow off"). The differences (d) in concentrations between consecutive weeks (x) were calculated for each week as $d_i = |x_i - x_{i+1}|$. The maximum difference was 252 μg/kg in late spring and the minimum difference was 0 μg/kg, meaning that the same concentration of BC was observed during two consecutive weeks. The original black carbon concentration data are presented in (**Table 2**).

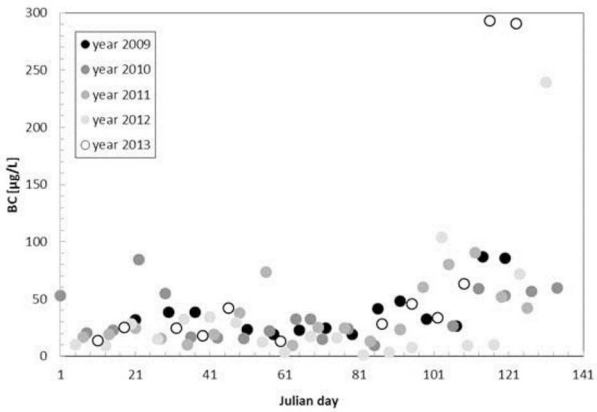

FIGURE 4 | Black carbon in snow [μg/L] in Sodankylä during five snow melt seasons, taken each spring during 2009–2013, Julian day 1–141 (day of the year).

SILAM Model Results

Figure 5 shows average footprints for in-cloud and sub-cloud scavenging for "clean" and "dirty" snow for (i) passive gas, i.e., substance with no deposition, decay; (ii) fine aerosol that has little deposition; and (iii) coarse aerosol that is subject to intensive wet and dry deposition. The deposition rate controls the extent of a footprint for each species. The comparison of "clean" and "dirty" patterns clearly reveals a sensitivity area at the Kola Peninsula for "dirty" footprints that correspond to a gap in sensitivity for "clean samples." The gap is most pronounced for fine aerosol particles (middle panels), which are likely to be responsible for the snow pollution.

Hence, the modeling results showed that increased surface snow BC concentrations (>30 μg/kg) were due to air masses originating from the Murmansk region, Kola Peninsula, Russia, where smelting and mining industries are located (**Figure 5**). The passive in-cloud and fine-particle sub-cloud results also suggest that Helsinki (Finland), St. Petersburg (Russia), and Western Russia could also contribute to increased black carbon observed in snow in Sodankylä during 2009–2013. These areas, however, are covered by one or two individual dirty footprints, so no solid conclusion can be made for these locations.

TABLE 2 | Sodankylä observations in 2009–2013 on BC concentrations in snow [μg/kg], which equals [μg/L], determined as [μg-EC/L-H_2O].

2009	2010	2011	2012	2013
21.1.2009 31,6	1.1.2010 52,8	7.1.2011 16,7	5.1.2012 20,9	11.1.2013 13,5
30.1.2009 38,2	8.1.2010 20,4	14.1.2011 19,2	5.1.2012 10,0	18.1.2013 25,5
6.2.2009 17,3	15.1.2010 22,6	21.1.2011 24,7	13.1.2012 9,1	1.2.2013 24,8
20.2.2009 23,6	22.1.2010 84,2	28.1.2011 15,8	20.1.2012 28,3	8.2.2013 17,7
27.2.2009 19,1	29.1.2010 54,7	4.2.2011 10,3	27.1.2012 15,0	15.2.2013 41,8
6.3.2009 22,7	5.2.2010 16,82	11.2.2011 18,8	3.2.2012 32,5	1.3.2013 12,8
13.3.2009 20,6	12.2.2010 16,1	18.2.2011 37,6	10.2.2012 34,1	28.3.2013 28,0
13.3.2009 38,5	19.2.2010 15,7	25.2.2011 73,8	17.2.2012 29,2	5.4.2013 45,8
17.3.2009 38,3	26.2.2010 22,0	4.3.2011 9,5	24.2.2012 12,4	12.4.2013 33,4
18.3.2009 31,6	5.3.2010 32,6	11.3.2011 25,2	2.3.2012 3,1	19.4.2013 63,3
18.3.2009 27,2	12.3.2010 15,1	18.3.2011 24,7	9.3.2012 17,4	26.4.2013 292,9
20.3.2009 18,8	19.3.2010 24,1	25.3.2011 13,1	16.3.2012 16,2	3.5.2013 291,0
27.3.2009 41,5	26.3.2010 9,4	2.4.2011 23,6	23.3.2012 1,00	
3.4.2009 48,1	2.4.2010 23,2	8.4.2011 60,2	30.3.2012 3,5	
10.4.2009106,3	9.4.2010 32,3	15.4.2011 79,9	5.4.2012 7,9	
17.4.2009 15,7	16.4.2010 26,7	22.4.2011 90,4	13.4.2012 103,8	
24.4.2009 87,1	23.4.2010 59,3	29.4.2011 51,5	20.4.2012 9,2	
30.4.2009 85,7	30.4.2010 52,9	6.5.2011 42,1	27.4.2012 9,9	
4.12.2009 16,9	7.5.2010 56,8	9.12.2011 33,0	4.5.2012 71,8	
12.12.2009 46,3	14.5.2010 59,7	16.12.2011 9,6	11.5.2012 239,3	
18.12.2009 55,0	29.10.2010 14,6	23.12.2011 12,0	2.11.2012 16,2	
25.12.2009 36,9	5.11.2010 37,3		7.12.2012 21,6	
	12.11.2010 34,4			
	3.12.2010 36,6			
	19.11.2010 29,8			
	26.11.2010 35,0			
	10.12.2010 14,4			
	17.12.2010 12,4			
	24.12.2010 15,5			
	31.12.2010 20,5			

The data are presented as day.month.year c_{BC}. The detection limit of the OCEC method is 0.2 ugC and the Uncertainty (UNC) = c(EC) x 0.05 + 0.1 [Sunset Laboratory Inc. (2018) Forest Grove, USA, https://www.sunlab.com/]. The relative portion (± 5%) is composed not only of the instrument variation itself but also of slight variations of sample deposit in-homogeneity and sample handling.

DISCUSSION AND CONCLUSIONS

Light-absorbing impurities in snow darken the surface and enhance snow melt. The BC in Arctic snow can originate from local, regional, or long-range transported BC aerosols, which deposit as dry and wet deposition. Here, the aim was to investigate the origin and temporal variability of black carbon observed in surface snow in Sodankylä, north of the Arctic Circle. For this purpose, BC observations were coupled with a quantitative long-range transport modeling approach. The data consisted of 107 weekly observations at one location in 2009–2013 during the snow season, including five consecutive seasonal spring melt periods. BC in the snow samples was analyzed using the European Union standard for atmospheric black carbon analysis, the thermal-optical OCEC.

SILAM-model was the key used to explain where the detected black carbon can originate from. In this study, the model-observation coupled approach included the sensitivity to the local and near-surface sources for the first time. The modeling results showed that increased surface snow BC concentrations (>30 μg/kg) were due to air masses originating from the Murmansk region, Kola Peninsula, Russia, e-particle sub-cloud results suggested that Helsinki (Finland), St. Petersburg (Russia) and Western Russia could also contribute to increased BC observed in snow in Sodankylä during 2009–2013. The modeling result of the origin of increased BC concentrations in snow is valid for the period of time investigated here, i.e., 2009–2013. A new investigation is needed for any other period to detect a possible change in emission sources. Direct quantification of the footprint uncertainties is not possible because footprint is not a measured quantity. However, SILAM model itself is a very extensively evaluated tool, both in operational and research context. The following uncertainties and means of mitigation of their impact are identified here:

i) The observed snow black carbon concentrations may vary largely with snowfall intensity. In other words, higher BC concentrations do not necessarily mean higher contributions of BC sources. However, the intensity of the snowfall is explicitly treated by SILAM as a part of adjoint dispersion equation. The issue however remains because the intensity of individual snowfalls has comparatively low accuracy. This could influence the results and interpretation of the results. Therefore, the consideration was limited to qualitative comparison of the mean footprints.

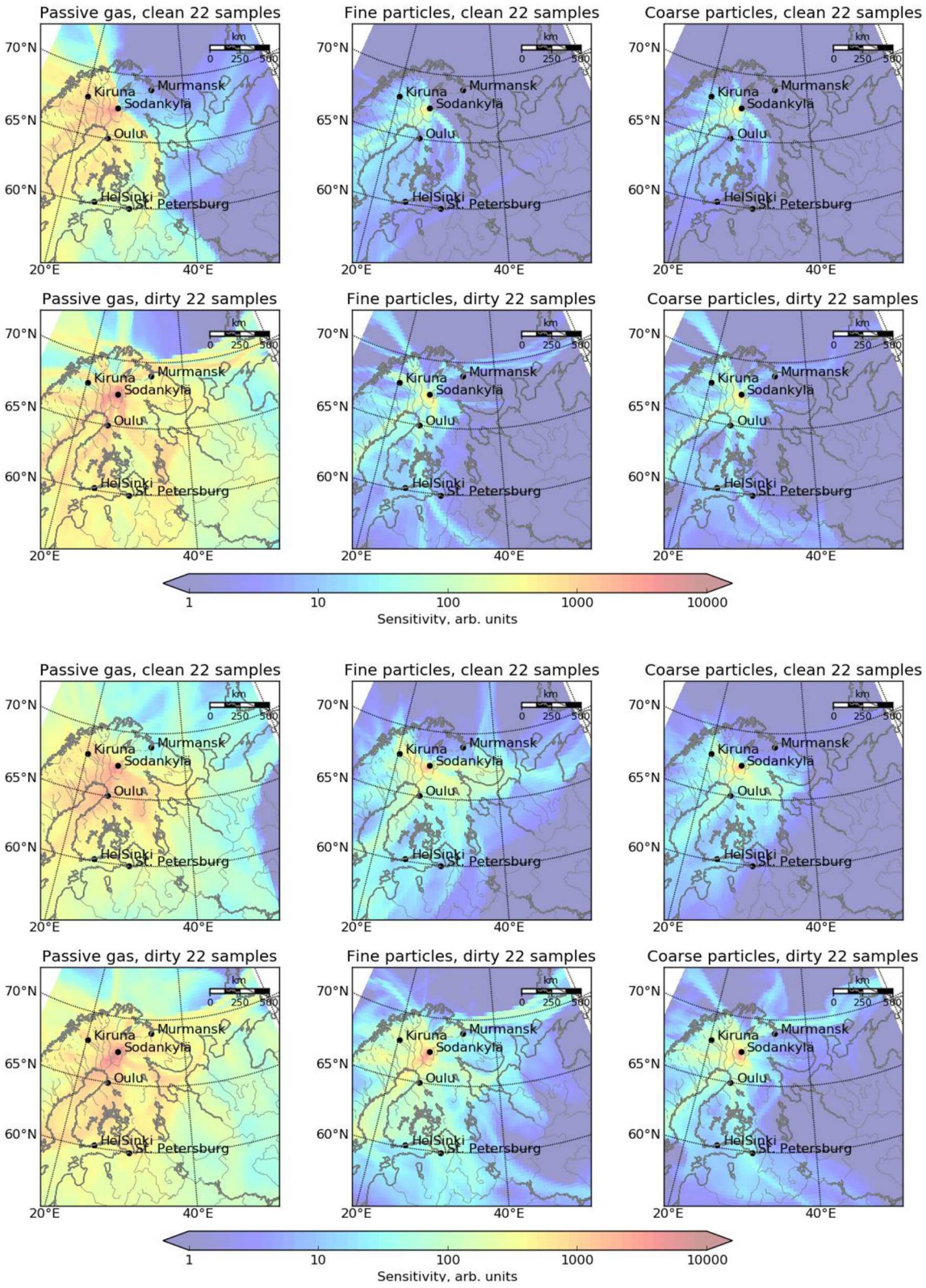

FIGURE 5 | (A) In-cloud and **(B)** sub-cloud SILAM footprint calculations. The footprints where smelting and mining industries are located. The passive in-cloud and fin for "clean" (upper) and "dirty" snowfall (lower), on the basis of measured BC mixing ratio in surface-snow samples, for (i) passive gas (no deposition, decay, etc., left), (ii) fine aerosol (middle), and (iii) coarse aerosol (right). Arbitrary unit (arb.unit) refers to procedure defined unit (abbreviated p.d.u.) of sensitivity.

ii) Due to uncertainties in the parametrizations. The primary contributor is the scavenging with snow, which is comparatively less accurate than that with rain. However, the operational evaluation of Copernicus Atmospheric Monitoring Service (http://atmosphere.copernicus.eu) shows that SILAM skills do not degrade in winter, confirms the balanced parameterizations.

iii) To additionally reduce the impact of uncertainties in the meteorology and scavenging processes, as well as of the limited number of samples, the observed samples were split to two groups—"clean" and "dirty." Corresponding footprints were also grouped and considerations were then focused on these averaged footprints, giving equal weight to the footprints in each class, which allowed more robust statistical processing.

Earlier, with the focus on explaining the measured low snow albedo values, a shorter and smaller data set of black carbon in snow in Sodankylä was used to calculate the average footprints with SILAM (Meinander et al., 2013), not including modeling of local sources. Here, with two times more observational cases fulfilling the footprint calculation criteria, the longer and bigger data set allowed for separate calculations of in-cloud and sub-cloud footprints and including also the sensitivity to the local and near-surface sources. Hence, a more reliable analysis of the origin of black carbon in snow was gained. The pattern found using the footprint calculations agreed not only that the location of the main air pollution sources in the region (Prank et al., 2010) are smelting, mining and refining industries located on the Kola Peninsula, but also with our earlier average footprint results using a smaller data set (Meinander et al., 2013). These SILAM model results can be further compared with the annual total EC emission data of **Figure 6** (CAMS-REG v3.1 for 2016, Granier et al., 2019). These emission results also confirm that the area around Murmansk is the major emitter in the region.

The observed snow BC concentrations may vary largely with snowfall intensity. In other words, higher BC concentrations do not necessarily mean higher contributions of BC sources. To avoid the influence of this on the results and the interpretation of results, our consideration was limited to a qualitative comparison of the mean footprints. The idea of the method is to compare the footprints in areas where they differ. Large uncertainties in the meteorology and scavenging processes, as well as the limited number of samples, make quantitative analysis hardly possible. Yet, statistics were calculated using the current threshold values. Given that the total number of footprints is 22 for each class, the percentages would be more likely to represent the particular data set rather than the contribution of different areas to local pollution in general.

During snow accumulation, the median surface snow BC concentration was 21 μg/kg, and during melt, it was 57 μg/kg. The melt period was identified using snow depth data from Sodankylä station. The median BC in surface snow concentration in Sodankylä in 2009–2013 ($n = 107$) was 25 μg/kg. This is the same magnitude reported by Svensson et al. (2018) for Pallas in March–April 2015 ($n = 10$) and March 2016 ($n = 2$), with an average of 40 μg/kg, and with Doherty et al. (2010) who

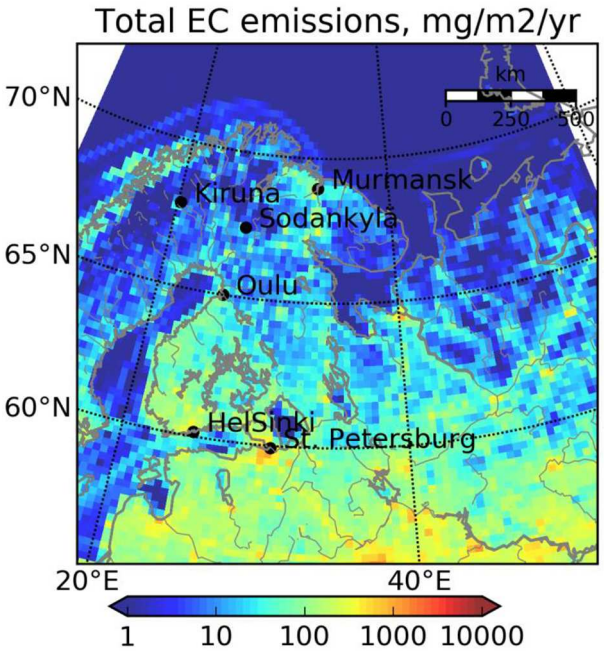

FIGURE 6 | Annual total EC emissions according to the CAMS-REG v3.1 for 2016 (Granier et al., 2019).

reported BC in European Arctic snow in Tromso, Norway, with an average of ∼20 μg/kg and increasing to ∼60 μg/kg during melt. Here, black carbon concentrations increased from 53 to 293 μg/kg during seasonal snow melt. The maximum concentrations were found in spring, influenced by the combination of long-range transported black carbon and spring melt. The highest concentrations were observed in 2013 (two data points, **Figure 4**) and 2012 (one data point, **Figure 4**). These highest values represent the largest enrichment of BC to the snow surface due to post-depositional snow processes. The multiannual data showed that black carbon concentrations in surface snow in one location can vary from 1 week to the next, from 0 μg/kg, i.e., concentration remaining the same for consecutive weeks, up to a maximum of 252 μg/kg, as detected in 2013 during intensive spring melt.

In this paper, it was also identified that these Sodankylä BC in snow concentration data did not follow the normal distribution. The distribution was skewed, and instead of using average and standard deviation values in reporting the data, median values were used together with 75th percentile values. The detection limit of the OCEC method is 0.2 ugC and the Uncertainty (UNC) = c(EC) × 0.05 + 0.1. The relative portion (± 5%) is composed not only of the instrument variation itself but also of slight variations of sample deposit in-homogeneity and sample handling (Sunset Laboratory Inc., 2018; Sunset Laboratory Inc., Forest Grove, USA, https://www.sunlab.com).

Our data showed that the temporal variability of black carbon in snow depends on atmospheric and cryospheric processes, such as the origin of BC due to atmospheric transport and dry and wet

deposition processes, as identified in the footprint calculations. Black carbon concentrations are also dependent on snow melt, which is evident in the data as a repeating pattern of the spring enhancement of BC contents during each of the five springs. These processes, in turn, are affected by meteorological factors, such as rain, temperature, wind, cloudiness, solar irradiance conditions, and other environmental factors, such as topography and ground properties. The effects of meteorological factors on Sodankylä snow albedo were studied earlier in Meinander et al. (2008). Sodankylä is an ideal place for the approach presented here, as it is characterized with flat terrain and low wind speeds, where new falling snow easily remains on top of the existing seasonal snowpack during the accumulation period. In addition, when snow melt starts in Sodankylä, the snow height declines almost monotonically through the spring melt season, making it easy to sample new surface snow.

The quantitative observations modeling approach presented here can be similarly applied to any location or period without *a priori* knowledge of the pollution source. New surface snow samples (sampled within 24 h of snow fall) are the main requirement. Then, any unknown pollution sources can be identified, and any later changes in emissions or in long-range transport or deposition processes can be detected by applying the coupled observations modeling method presented here.

DATA AVAILABILITY STATEMENT

The datasets generated for this study are available on request to the corresponding author.

AUTHOR CONTRIBUTIONS

OM conceived the idea of the work and was the main author of the paper and the A4 research plan. AK was responsible for the Sodankylä snow sampling, provided the BC data and contributed to the writing of the paper. RK and MS were responsible for the SILAM modeling calculations and for developing the coupled observations model method, and they contributed significantly to the writing of the paper.

FUNDING

Funding for the original work came from the Academy of Finland's A4 Project (No. 254195). OM was also supported by the Academy of Finland's NABCEA project, the Novel Assessment of Black Carbon in the Eurasian Arctic (No. 296302); the Ministry for Foreign Affairs of Finland's IBA project, Black Carbon in the Eurasian Arctic and Significance Compared to Dust Sources (No. PC0TQ4BT-25); the EU-Interact-BLACK-project, Black Carbon in Snow and Water (H2020 Grant Agreement No. 730938); the Academy of Finland's Centers of Excellence program, The Center of Excellence in Atmospheric Science—From Molecular and Biological Processes to the Global Climate (No. 272041); and the Nordic Center of Excellence's CRAICC project, Cryosphere–Atmosphere Interactions in a Changing Arctic Climate. RK was partially supported by the Russian Foundation for Basic Research (project 19-05-01008). RK and MS were supported by the Nordic Ministry of Research's CarboNord project (KOL-1406), the Academy of Finland's A4 Project, and NordForsk under the Nordic Programme on Health and Welfare (#75007 NordicWelfAir project).

ACKNOWLEDGMENTS

Sodankylä personnel are acknowledged for snow sampling and filtering. OM's Ph.D. dissertation (Meinander, 2016), Effect of black carbon and Icelandic dust on snow albedo, melt and density, University of Helsinki, is acknowledged and cited accordingly. ECCAD is acknowledged for EC emission data.

REFERENCES

AMAP (2015). *Blasck Carbon and Ozone as Arcticclimate forcers, Arctic Monitoring and Assessment Programme Arctic Monitoring and Assessment Programme (AMAP)* Oslo. p. 116. Available online at: www.amap.no.

Birch, M. E. (2003). *Diesel Particulate Matter (as Elemental carbon)Method 5040, in NIOSH Manual of Analytical Methods, National Institute of Occupational Safety and Health*. Cincinnati, Ohio.

Birch, M. E., and Cary, R. A. (1996). Elemental carbon-based method for monitoring occupational exposures to particulate diesel exhaust. *Aerosol. Sci. Technol.* 25, 221–241. doi: 10.1080/02786829608965393

Bond, T. C., Doherty, S. J., Fahey, D. W., Forster, P. M., Berntsen,T., and DeAngelo, B. J., et al. (2013). Bounding the role of black carbon in the climate system: a scientific assessment. *J. Geophys. Res.* 118, 5380–5552. doi: 10.1002/jgrd.50171

Boy, M., Thomson, E. S., Acosta Navarro, J.-C., Arnalds, O., Batchvarova, E., Bäck, J., et al. (2019). Interactions between the atmosphere, cryosphere, and ecosystems at northern high latitudes. *Atmos. Chem. Phys.* 19, 2015–2061. doi: 10.5194/acp-19-2015-2019

Brasseur, G. P., Xie, Y., Petersen, A. K., Bouarar, I., Flemming, J., Gauss, M., et al. (2019). Ensemble forecasts of air quality in eastern China – part 1: model description and implementation of the marcopolo–panda prediction system, version 1. *Geosci. Model Dev.* 12, 33–67. doi: 10.5194/gmd-12-33-2019

Brown, R. J. C., Beccaceci, S., and Butterfield, D. M., et al. (2017). Standardisation of a European measurement method for organic carbon and elemental carbon in ambient air: results of the field trial campaign and the determination of a measurement uncertainty and working range. *Environ. Sci. Process Impacts* 19, 1249–1259. doi: 10.1039/C7EM00261K

CEN-TC264 (2017). *European Committee for Standardisation, EN 16909:2017, Ambient Air – Measurement of Elemental Carbon (EC) and Organic Carbon (OC) Collected on Filters.* CEN, Brussels.

Doherty, S. J., Grenfell, T. C., Forsström, S., Hegg, D. L., Brandt, R. E., and Warren, S.G. (2013). Observed vertical redistribution of black carbon and other insoluble light-absorbing particles in melting snow. *J. Geophys. Res. Atmos.* 118. doi: 10.1002/jgrd.50235

Doherty, S. J., Warren, S. G., Grenfell, T. C., Clarke, A. D., and Brandt, R. E. (2010). Light-absorbing impurities in Arctic snow. *Atmos. Chem. Phys.* 10, 11647–11680. doi: 10.5194/acp-10-11647-2010

Eckhardt, S., Cassiani, M., Evangeliou, N., Sollum, E., Pisso, I., and Stohl, A. (2017). Source–receptor matrix calculation for deposited mass with the Lagrangian particle dispersion model FLEXPART v10.2 in backward mode. *Geosci. Model Dev.* 10, 4605–4618. doi: 10.5194/gmd-10-4605-2017

Emerson, E. W., Katich, J. M., Schwarz, J. P., McMeeking, G. R., and Farmer, D. K. (2018). Direct measurements of dry and wet deposition of

black carbon over a grassland. *J. Geophys. Res. Atmos.* 123, 12277–12290. doi: 10.1029/2018JD028954

Flanner, M. G. (2013). Arctic climate sensitivity to local black carbon. *J. Geophys. Res.* 118, 1840–1851. doi: 10.1002/jgrd.50176

Flanner, M. G., Zender, C. S., Randerson, J. T., and Rasch, P. T. (2007). Present day climate forcing and response from black carbon in snow. *J. Geophys. Res.* 112:D11202. doi: 10.1029/2006JD008003

FMI-ARC database (2020). Available online at: http://litdb.fmi.fi./luo0015_data.php (accessed 27 March, 2020).

Forsström, S., Ström, J., Pedersen, C. A., Isaksson, E., and Gerland, S. (2009). Elemental carbon distribution in svalbard snow. *J. Geophys. Res.* 114:D19112. doi: 10.1029/2008JD011480

Galperin, M. V. (2000). "The approaches to correct computation of airborne pollution advection," in *Problems of Ecological Monitoring and Ecosystem Modelling. XVII (in Russian)* (St.Petersburg: Gidrometeoizdat), 54–68.

Granier, C. S., Darras, H., Denier van der Gon, J., Doubalova, N., Elguindi, B., Galle, M., et al. (2019). *The Copernicus Atmosphere Monitoring Service Global and Regional Emissions (April 2019 Version)*. Copernicus Atmosphere Monitoring Service (CAMS) Report. doi: 10.24380/d0bn-kx16

Hansen, J., and Nazarenko, L. (2004). Soot climate forcing via snow and ice albedos. *Proc. Natl. Acad. Sci. U. S. A.* 101, 423–428. doi: 10.1073/pnas.2237157100

Huijnen, V., Eskes, H. J., Poupkou, A., Elbern, H., Boersma, K. F., Foret, G., et al. (2010). Comparison of OMI NO2 tropospheric columns with an ensemble of global and European regional air quality models. *Atmospheric Chem. Phys.* 10, 3273–3296. doi: 10.5194/acp-10-3273-2010

Ikonen, J., Vehviläinen, J., Rautiainen, K., Smolander, T., Lemmetyinen,J., Bircher, S., et al. (2015). The sodankylä *in situ* soil moisture observation network: an example application to earth observation data product evaluation. *Geosci. Instrum.Method Data Syst. Discuss.* 5, 599–629. doi: 10.5194/gid-5-599-2015

IPCC (2019). IPCC special report on the ocean and cryosphere in a changing climate. Eds H.-O. Pörtner, D.C. Roberts, V. Masson-Delmotte, P. Zhai, M. Tignor, E. Poloczanska, K. Mintenbeck, A. Alegría, M. Nicolai, A. Okem, J. Petzold, B. Rama, N.M. Weyer. In press, Available online at: https://www.ipcc.ch/srocc/ (accessed May 13, 2020).

Jiao, C., Flanner, M. G., Balkanski, Y., Bauer,S. E., Bellouin,N.,Berntsen,T. K., et al. (2014). An aerocom assessment of black carbon in Arctic snow and sea ice. *Atmos. Chem. Phys.* 14, 2399–2417. doi: 10.5194/acp-14-2399-2014

Kangas, M., Rontu, L., Fortelius, C., Aurela, M., and Poikonen, A. (2016). Weather model verification using Sodankylä mast measurements. *Geosci. Instrum. Method. Data Syst.* 5, 75–84. doi: 10.5194/gi-5-75-2016

Koch, D., and Hansen, J. (2005). Distant origins of arcticblack carbon, a goddard institute for space studies modeleexperiment. *J. Geophys. Res.* 110:D04204. doi: 10.1029/2004JD005296

Laborde, M., Crippa, M., Tritscher, T., Jurányi, Z., Decarlo, P. F.,Temime-Roussel, B., et al. (2013). Black carbon physical properties and mixing state in the European megacity Paris. *Atmos. Chem. Phys.* 13, 5831–5856. doi: 10.5194/acp-13-5831-2013

Lakkala, K., Suokanerva, H., Karhu, J. M., Aarva, A., Poikonen, A., Karppinen, T., et al. (2016). Optical laboratory facilities at the Finnish Meteorological Institute—Arctic Research Centre. *Geosci. Instrum. Method, Data Syst.* 5, 315–320. doi: 10.5194/gi-5-315-2016

Leppänen, L., Kontu, A., Hannula, H.-R., Sjöblom, H., and Pulliainen, J. (2016). Sodankylä manual snow survey program. *Geosci. Instrum. Method. Data Syst.* 5, 163–179. doi: 10.5194/gi-5-163-2016

Mäkelä, J. S., Lakkala, K., Koskela, T., Karppinen, T., Karhu, J. M., Savastiouk, V., et al. (2016). Data flow of spectral UV measurements at Sodankylä and Jokioinen, Geosci. *Instrum. Method. Data Syst.* 5, 193–203. doi: 10.5194/gi-5-193-2016

Meinander, O. (2016). *Effect of black carbon and Icelandic dust on snow albedo, melt and density*. (Ph.D. dissertation thesis), Belongs to series: finnish meteorological Institute Contributions—URN:ISSN:0782-6117, University of Helsinki, Helsinki (Finland): Available online at: http://urn.fi/URN:ISBN:78-951-697-896-6 (accessed March 27, 2020).

Meinander, O., Kazadzis, S., Arola, A., Riihelä, A., Räisänen, P., Kivi, R., et al. (2013). Spectral albedo of seasonal snow during intensive melt period at Sodankylä, beyond the Arctic Circle. *Atmos. Chem. Phys.* 13, 3793–3810. doi: 10.5194/acp-13-3793-2013

Meinander, O., Kontu, A., Lakkala, K., Heikkilä, A., Ylianttila, L., and Toikka, M. (2008). Diurnal variations in the UV albedo of arctic snow. *Atmos. Chem. Phys.* 8, 6551–6563. doi: 10.5194/acp-8-6551-2008

Meinander, O., Kontu, A., Virkkula, A., Arola, A., Backman, L., DagssonWaldhauserová, P., et al. (2014). Brief communication: Light-absorbing impurities can reduce the density of melting snow. *Cryosphere.* 8, 991–995. doi: 10.5194/tc-8-991-2014

Mori, T., Goto-Azuma, K., Kondo, Y., Ogawa-Tsukagawa, Y., Miura, K., Hirabayashi, M., et al. (2019). Black carbon and inorganic aerosols in Arctic snowpack. *J. Geophys. Res. Atmos.* 124, 13325–13356. doi: 10.1029/2019JD030623

Peltoniemi, J. I., Gritsevich, M., Hakala, T., Dagsson-Waldhauserová, P., Arnalds, Ó., Anttila, K., et al. (2015). Soot on Snow experiment: bidirectional reflectance factor measurements of contaminated snow. *Cryosphere* 9, 2323–2337. doi: 10.5194/tc-9-2323-2015

Petersen, A. K., Brasseur, G. P., Bouarar, I., Flemming, J., Gauss, M., Jiang, F., et al. (2019). Ensemble forecasts of air quality in eastern China–Part 2: evaluation of the MarcoPolo–Panda prediction system, version 1. *Geosci Model Dev* 12, 1241–1266. doi: 10.5194/gmd-12-1241-2019

Pirinen, P., Simola, H., Aalto, J., Kaukoranta, J.-P., Karlsson, P., and Ruuhela, R. (2012). *Climatological Statistics of Finland 1981–2010, Finnish Meteorological Institute* Reports. 2012:96. Available online at: www.fmi.fi

Prank, M., Sofiev, M., Denier van der Gon, H. A. C., Kaasik, M.,Ruuskanen, T. M., and Kukkonen, J. (2010). A refinement of the emission data for Kola Peninsula based on inverse dispersion modeling. *Atmos. Chem. Phys.* 10, 10849–10865. doi: 10.5194/acp-10-10849-2010

Saarikoski, S., Sillanpaa, M., Sofiev, M., Timonen, H., Saarnio, K., Teinela, K., et al. (2007). Chemical composition of aerosols during a major biomass burning episode over northern Europe in spring 2006: experimental and modelling assessments. *Atmos. Environ.* 41, 3577–3589. doi: 10.1016/j.atmosenv.2006.12.053

Sand, M., Berntsen, T., Kay, J. E., Lamarque, J. F., Seland, O., and Kirkevag, A. (2013). The Arctic response to remote and local forcing of black carbon. *Atmos. Chem. Phys.* 13, 211–224 doi: 10.5194/acp-13-211-2013

Schwarz, J. P., Spackman, J. R., Gao, R. S., Watts, L., Stier, P., Schulz, M., et al. (2010). Global-scale black carbon profiles observed in the remote atmosphere and compared to model. *Geophys. Res. Lett.* 37:L18812. doi: 10.1029/2010GL044372

Serreze, M. C., and Barry, R. G. (2011). Processes and impacts of arctic amplification: a research synthesis. *Global Planet. Change* 77, 85–96. doi: 10.1016/j.gloplacha.2011.03.004

Sharma, S., Ishizawa, M., Chan, D., Lavoué, D., Andrews, E., Eleftheriadis, K., et al. (2013). 16-years simulation of Arctic black carbon: transport, source contribution, and sensitivity analysis on deposition. *J. Geophys. Res.* 118, 1–22. doi: 10.1029/2012JD017774

Siljamo, P., Sofiev, M., Severova, E., Ranta, H., Kukkonen, J., Polevova, S., et al. (2008). Sources, impact and exchange of early-spring birch pollen in the Moscow region and Finland. *Aerobiologia* 24, 211–230. doi: 10.1007/s10453-008-9100-8

Sofiev, M. (2002). Extended resistance analogy for construction of the vertical diffusion scheme for dispersion models. *J. Geophys. Res. Atmos.* 107:4159. doi: 10.1029/2001JD001233

Sofiev, M., Vira, J., Kouznetsov, R., Prank, M., Soares, J., and Genikhovich, E. (2015). Construction of the SILAM Eulerian atmospheric dispersion model based on the advection algorithm of Michael Galperin. *Geosci. Model Dev.* 8, 3497–3522. doi: 10.5194/gmd-8-3497-2015

Stohl, A. (2006). Characteristics of atmospheric transport into the Arctic troposphere. *J. Geophys. Res.* 111:D11306. doi: 10.1029/2005JD006888

Stohl, A., Klimont,Z., Eckhardt, S., Kupiainen, K., Shevchenko, V. P., Kopeikin,V. M., et al. (2013). Black carbon in the Arctic:the underestimated role of gas flaring and residential combustion emissions. *Atmos. Chem. Phys.* 13, 8833–8855. doi: 10.5194/acp-13-8833-2013

Sturm, M., and Holmgren, J. (1995). A seasonal snow cover classification system for local to global applications. *J. Climate* 8, 1261–1283. doi: 10.1175/1520-0442(1995)008<1261:ASSCCS>2.0.CO;2

Sukuvaara, T., Mäenpää, K., and Ylitalo, R. (2016). Vehicular-networking- and road-weather-related research in Sodankylä. *Geosci. Instrum. Method. Data Syst*. 5, 513–520. doi: 10.5194/gi-5-513-2016

Sunset Laboratory Inc. (2018). *Organic Carbon / Elemental Carbon (OCEC) Laboratory Instrument Manual*. Sunset Laboratory Inc, Forest Grove. Available online at: www.sunlab.com (accessed April 8, 2020).

Svensson, J., Ström, J., Kivekäs, N., Dkhar, N. B., Tayal, S., et al. (2018). Light-absorption of dust and elemental carbon in snow in the Indian Himalayas and the Finnish Arctic. *Atmos. Meas. Tech*. 11, 1403–1416. doi: 10.5194/amt-11-1403-2018

Tietäväinen, H., Tuomenvirta, H., and Venäläinen, A. (2010). Annual and seasonal mean temperatures in Finland during the last 160 years based on gridded temperature data. *Int. J. Climatol*. 30, 2247–2256. doi: 10.1002/joc.2046

Veriankaite, L., Siljamo, P., Sofiev, M., Sauliene, I., and Kukkonen, J. (2010). Modelling analysis of source regions of long-range transported birch pollen that influences allergenic seasons in Lithuania. *Aerobiologia* 26, 47–62. doi: 10.1007/s10453-009-9142-6

Wang, Q., Jacob, D. J., Fisher, J. A., Mao, J., Leibensperger, E. M., Carouge, C. C., et al. (2011). Sources of carbonaceous aerosols and deposited black carbon in the Arctic in winter-spring: implications for radiative forcing. *Atmos. Chem. Phys*. 11, 12453–12473. doi: 10.5194/acp-11-12453-2011

Warren, S. G., and Wiscombe, W. J. (1980). A model for the spectral albedo of snow. II: snow containing atmospheric aerosols. *J. Atmos. Sci*. 37, 2734–2745. doi: 10.1175/1520-0469(1980)037<2734:AMFTSA>2.0.CO;2

Xu, B., Cao, J., Hansen, J.,Yao, T., Joswia, D. R., Wang, N., et al. (2009). Black soot and the survival of Tibetan glaciers. *Proc. Natl. Acad. Sci. U. S. A*. 106, 22114–22118. doi: 10.1073/pnas.0910444106

Zhang, J., Liu, J., Tao, S., and Ban-Weiss, G. A. (2015). Long-range transport of black carbon to the Pacific Ocean and its dependence on aging timescale. *Atmos. Chem. Phys*. 15, 11521–11535. doi: 10.5194/acp-15-11521-2015

Conflict of Interest: The authors declare that the research was conducted in the absence of any commercial or financial relationships that could be construed as a potential conflict of interest.

Copyright © 2020 Meinander, Kontu, Kouznetsov and Sofiev. This is an open-access article distributed under the terms of the Creative Commons Attribution License (CC BY). The use, distribution or reproduction in other forums is permitted, provided the original author(s) and the copyright owner(s) are credited and that the original publication in this journal is cited, in accordance with accepted academic practice. No use, distribution or reproduction is permitted which does not comply with these terms.

frontiers in Earth Science

ORIGINAL RESEARCH
published: 23 July 2020
doi: 10.3389/feart.2020.00308

Upward Expansion of Supra-Glacial Debris Cover in the Hunza Valley, Karakoram, During 1990 ~ 2019

Fuming Xie[1,2], Shiyin Liu[1,2,3], Kunpeng Wu[1,2], Yu Zhu[1,2], Yongpeng Gao[1,2], Miaomiao Qi[1,2], Shimei Duan[1,2], Muhammad Saifullah[2,4] and Adnan A. Tahir[5]*

[1] Yunnan Key Laboratory of International Rivers and Transboundary Eco-Security, Yunnan University, Kunming, China, [2] Institute of International Rivers and Eco-Security, Yunnan University, Kunming, China, [3] State Key Laboratory of Cryospheric Sciences, Northwest Institute of Eco-Environment and Resources, Chinese Academy of Sciences, Lanzhou, China, [4] Department of Agricultural Engineering, Muhammad Nawaz Shareef University of Agriculture, Multan, Pakistan, [5] Department of Environmental Sciences, COMSATS University Islamabad, Abbottabad Campus, Abbottabad, Pakistan

OPEN ACCESS

Edited by:
Tong Zhang, Los Alamos National Laboratory (DOE), United States

Reviewed by:
Leigh A. Stearns, The University of Kansas, United States
Aparna Shukla, Ministry of Earth Sciences, India
Takayuki Nuimura, Tokyo Denki University, Japan

***Correspondence:**
Shiyin Liu
shiyin.liu@ynu.edu.cn

Specialty section:
This article was submitted to Cryospheric Sciences, a section of the journal Frontiers in Earth Science

Received: *17 January 2020*
Accepted: *30 June 2020*
Published: *23 July 2020*

Citation:
Xie F, Liu S, Wu K, Zhu Y, Gao Y, Qi M, Duan S, Saifullah M and Tahir AA (2020) Upward Expansion of Supra-Glacial Debris Cover in the Hunza Valley, Karakoram, During 1990 ~ 2019. Front. Earth Sci. 8:308. doi: 10.3389/feart.2020.00308

Supra-glacial debris cover is key to glacier ablation through increasing (thin debris layer) or decreasing (thick debris layer) melt rates, thereby regulating the mass balance of a glacier and its meltwater runoff. The thickening or lateral expansion of supra-glacial debris cover correlates with a reduction of glacier ablation and, consequently, runoff generation, which is also considered to be an influential factor on the rheology and dynamics of a glacierized system. Studies on supra-glacial debris cover have recently attracted wide attention especially for glaciers in the Himalayas and Karakoram, where the glaciers have heterogeneously responded to climate change. In this study, we used 32 images from the Landsat Thematic Mapper, Enhanced Thematic Mapper Plus, and Operational Land Imager archive, going back to 1990, which are available on the Google Earth Engine cloud-computing platform, to map the supra-glacial debris cover in the Hunza Valley, Karakoram, Pakistan, based on a band ratio segmentation method (normalized difference snow index [NDSI] < 0.4), Otsu thresholding, and machine learning algorithms. Compared with manual digitization, the random forest (RF) model was found to have the greatest accuracy in identifying supra-glacial debris, with a Kappa coefficient of 0.94 ± 0.01 and an overall accuracy of $95.5 \pm 0.9\%$. Overall, the supra-glacial debris cover in the study area showed an increasing trend, and the total area expanded by 8.1–21.3% for various glaciers from 1990 to 2019. The other two methods (Otsu thresholding and NDSI < 0.4) generally overestimated the supra-glacial debris covered area, by 36.3 and 18.8%, respectively, compared to that of the RF model. The supra-glacial debris cover has migrated upward on the glaciers, with intensive variation near the equilibrium-line altitude zone (4,500–5,500 m a.s.l.). The increase in ice or snow avalanche activity at high altitudes may be responsible for this upward expansion of supra-glacial debris cover in the Hunza Valley, which is attributed to the combined effect of temperature decrease and precipitation increase in the study area.

Keywords: supra-glacial debris, Hunza Valley, machine learning, Otsu, Google Earth Engine

INTRODUCTION

Glaciers are not only a diminishing natural freshwater resource but also a sensitive indicator of global climate change (Yang, 1995; Kaab et al., 2012; Kraaijenbrink et al., 2017; Zemp et al., 2019). However, due to global warming, global glaciers are showing a trend of retreat and thinning. Recent studies on mass balance (Rowan et al., 2015; Lynch et al., 2016; Dehecq et al., 2018; Wu et al., 2018; Wang et al., 2019a; Wouters et al., 2019; Zemp et al., 2019), glacial area change (Paul et al., 2013; Patel et al., 2019; Reinthaler et al., 2019), surface velocity (Wang et al., 2018; Altena et al., 2019; Garg et al., 2019), glacio-hydrological modeling (Shrestha et al., 2015), and glaciers' response to climate change (Scherler et al., 2011; Rowan et al., 2015) have revealed that changes in glaciers are exerting an impact on socioeconomic development in their downstream areas through changes in glacial water resources in High Mountain Asia (Immerzeel et al., 2010). Climate change may force geomorphological processes on high mountain slopes (Tipper et al., 2012; Cook et al., 2020) by accelerating the disintegration of rocks and increasing the accumulation of debris on glaciers and mountain slopes. As a result, the alpine glaciers widely distributed in the Pamir, Karakorum, Kunlun, Nyainqentangula, and Himalaya Mountains (Scherler et al., 2011; Khan et al., 2015; Zhang et al., 2016; Shukla and Garg, 2019) have widespread supra-glacial debris cover. Some studies have referred to glacier areas with sporadic debris cover as "dirty ice" (Robson et al., 2015; Fyffe et al., 2019a,b). The debris cover on glaciers affects the energy exchange at the ice surface and therefore has an impact on the surface mass balance of glaciers. It is therefore possible for glaciers to gain more heat from the environment, increasing the melt rate and causing the mass loss of glaciers.

Compared with clean ice or snow, the debris layer has a unique thermal process due to differences in physical properties such as reflectance, particle size, and color, which results in different ablation processes in the underlying ice (Østrem, 1959; Nicholson and Benn, 2006). Also, the differential ablation caused by an uneven distribution of debris thickness makes it easy for glaciers to form cliffs (Kindermann et al., 2008; Herreid and Pellicciotti, 2018) and ponds (Miles et al., 2016; Chand and Watanabe, 2019) in the ablation zone. Notably, these cliffs and ponds are not only factors that affect the hydrological process but also home to numerous glacial lakes, which can pose a serious threat to downstream communities and lead to catastrophic socioeconomic disasters in cases of glacial lake outburst flood (Benn et al., 2012; Dubey and Goyal, 2020). Therefore, obtaining information about the spatial distribution and temporal variation of supra-glacial debris cover would enhance the understanding of debris-covered glaciers and the glacial hydrological model. Some studies have shown that the area of debris cover is increasing as, overall, glaciers shrink and lose mass. For example, the supra-glacial debris cover in the Greater Caucasus increased from 48.3 ± 3.1 km^2 in 1986 to 79.0 ± 4.9 km^2 in 2014, based on Landsat and images from the years 1986, 2000, and 2014 (Tielidze et al., 2020). Furthermore, the glaciers in Pamir, Karakoram, and West Kunlun have moved forward or backward, either in equilibrium or showing an increase in mass ("Karakoram anomaly") in recent years (Salerno et al., 2017; Farinotti et al., 2020; Gao et al., 2020), and it is of great interest to know whether this debris cover increase phenomenon exists for glaciers in anomaly areas, such as the Hunza Valley. Although some studies have mapped the spatial distribution of supra-glacial debris cover in this area (Khan et al., 2015, 2020; Mölg et al., 2018; Gao et al., 2020), they were limited to the extraction of spatial distribution information and lack any analysis on the temporal dynamic changes of supra-glacial debris.

Since the reflectance of supra-glacial debris is similar to that of non-glaciated slopes (Paul et al., 2004) and there is a lack of continuous, large-scale, high-quality cloud and shadow-free optical images, obtaining the long-term supra-glacial debris variations based on remote imagery is challenging. Previous studies have attempted to distinguish clean ice from debris-covered ice by using individual parameters such as the normalized difference vegetation index (NDVI), normalized difference snow index (NDSI), normalized difference water index (NDWI), and spectral band ratio thresholds [e.g., near-infrared (NIR)/short-wave infrared (SWIR)] or their combination from optical remote sensing images (Bolch et al., 2010; Alifu et al., 2015, 2016; Mölg et al., 2018). These methods can robustly delineate clean ice or snow, but they cannot accurately and automatically classify debris-covered ice as distinct from clean ice and the surrounding land surface (Robson et al., 2015). This has stimulated studies on the use of other parameters, such as geomorphic parameters derived from digital elevation models (DEMs) (Paul et al., 2004; Frey and Paul, 2012; Patel et al., 2019) and thermal characteristics from the infrared band (Singh and Goyal, 2018), as well as utilizing the coherence change between two successive synthetic aperture radar (SAR) images (Janke et al., 2015; Robson et al., 2015; Yang et al., 2016; Lippl et al., 2018), and the recognition accuracy was improved. However, complex preprocessing and severe terrain noise from SAR data make large-scale applications difficult. In conclusion, especially for the long-time series involved in debris monitoring, optical images, with decades of continuous observations, such as the Landsat archive, are more practical.

In recent years, machine-learning-based classification methods have been applied to mapping glacier facies (Racoviteanu and Williams, 2012; Shukla and Yousuf, 2016; Zhang et al., 2019; Yousuf et al., 2020). Studies have shown that machine learning has advantages in extracting land-surface information from remote sensing images, which can effectively improve the accuracy of object recognition (Lary et al., 2017; Maxwell et al., 2018). However, mining large-scale and time series land information from high spatiotemporal resolution remote sensing data was found to be a computationally intensive task, requiring powerful computing platforms for analysis. Fortunately, some geospatial cloud-computing platforms are emerging that meet this demand, such as Google Earth Engine GEE, Amazon Web Services, Earth Server, and the Earth Observation Data Centre (Guo et al., 2020). Among these, GEE has advantages because it is an open-source, cloud-based platform for planetary-scale geospatial analysis that integrates mainstream free satellite data, such as the Landsat archive, Sentinel series imagery, and other terrain products and climate

data (Gorelick et al., 2017). It can remove the parts of cloud, cloud shadow, and terrain shadow that affect each scene at the pixel scale, compared with the local image processing and analysis software, which takes the scene as a processing unit. The GEE platform has been widely used for various high-impact societal issues such as forest resources (Hazel et al., 2016), water resources (Pekel et al., 2016; Wang et al., 2019b), and land-use classification (Dong et al., 2016; Midekisa et al., 2017; Hao et al., 2019_ENREF_18) and has achieved remarkable results.

The aim of this study was to develop an automatic algorithm to identify debris-covered ice and map its spatiotemporal distribution in order to explore the dynamic process of supra-glacial debris cover by combining glacier inventory data and remotely sensed images on the GEE geospatial analysis platform. The study focused on glaciers in the Hunza Valley in the Karakorum Mountains of Pakistan. Otsu's method was utilized to optimize thresholds of NDSI, and three machine learning algorithms [random forest (RF), support vector machine (SVM), and classification and regression tree (CART)] were used to classify supra-glacial features, including debris-covered ice, at the pixel level. Raw spectral information, band ratios, and color-to-grayscale conversion from Landsat 5/8 optical satellite imagery and the topographical components derived from DEM products were extracted as feature variables in the machine learning models. The same scheme was used to generate a time series of the debris-covered and clean ice areas in the study area. Finally, the results were comprehensively analyzed and discussed together with other data derived at the same time.

STUDY AREA

The Hunza Valley is an area measuring ∼11,000 km^2, located in the western Karakoram, northern Pakistan (36°00′15″ ∼ 37°05′23″ N, 74°02′57″ ∼ 75°46′48″ E) (**Figure 1**). The topography across the Hunza Valley is characterized by large altitudinal variations, from 1,341 to 7,831 m above sea level (a.s.l.). The valley is home to glaciers with a total area of ∼3,600 km^2 (1,878 glaciers, with ∼12% of them being larger than 0.5 km^2) that accounts for ∼33% of the basin area based on the Randolph Glacier Inventory (RGI) 6.0 dataset (RGI Consortium, 2017). Most of the glaciers (e.g., Hispar, Batura, and Barpu) are debris-covered and in a state of surging and advancing (Bhambri et al., 2017). Debris-covered glaciers are potential factors driving glacial lake outburst floods (Bhambri et al., 2019), which represent a major threat to local people, their property, and infrastructure such as the Karakoram Highway in the Hunza Valley. Climatologically, the study area is arid to semi-arid, situated in the subtropical climate zone and experiences significant variations in precipitation and temperature (Immerzeel et al., 2012). Based on the Moderate Resolution Imaging Spectroradiometer (MODIS) 1-km land-surface temperature daily products, the mean land-surface temperature for the entire region is −12.9°C in January and 20.1°C in July. Precipitation is mainly controlled by Indian monsoons and the westerlies, and the average annual precipitation is between 180 and 690 mm (Qureshi et al., 2017). Snow cover occupies approximately 80% of the basin's land surface in the winter, decreasing to 30% in the summer (Tahir et al., 2011). The types of land cover in the basin include forest (0.4%), shrubland (16.1%), farmland (0.7%), and barren land (82.8%). The main soil types include Leptosols (type LP), rock outcrop soil (type RK), and glaciated soil (type GG). The primary soil component in the region is highly active clay, followed by rock outcrops and glacial soil (Garee et al., 2017; Ali et al., 2018).

DATA AND METHODS

Landsat Imagery and Preprocessing

The Hunza Valley is covered by three WRS2 path/rows (149/034, 149/035, and 150/034) of Landsat images. We collected all the available standard level 1 terrain-corrected products of the Landsat raw scenes that were consistent in geometry and radiometry on the GEE platform, representing the years 1990–2019, including 10 Landsat TM images, four Landsat Enhanced Thematic Mapper Plus (ETM+) images, and 18 Landsat Operational Land Imager (OLI) images (see **Table 1**). The selection of images was constrained by the acquisition time during the ablation season (e.g., during July, or 200–270 days) when the images showed minimum snow cover, with little or no cloud cover. Mosaics of three path-row images within the same year in the research domain has been processed ready for debris extraction except for 2010 which were the mosaic from TM images acquired in 2008 (149/034), 2009 (149/035), and 2011 (150/034), respectively, due to wide snow cover of images in 2010. The Landsat 7 ETM+ data from 2000 only were used because of data gaps caused by scan line corrector failure since June 2003. Spectral bands with 30-m resolution were used in this study. All the data were publicly available, for free, on the United States Geological Survey (USGS) website.[1] We applied a standard top-of-atmosphere calibration, which is available on the GEE platform, to all the USGS Landsat Raw Scenes, converting the pixel digital number values to top-of-atmosphere reflectance (Chandera et al., 2009). Then, we assigned a cloud score to each pixel, using the Landsat simple cloud score algorithm,[2] which computes a simple cloud-likelihood score from 0 (not cloudy) to 100 (most cloudy), using a combination of brightness, temperature, and NDSI. We used a <10 threshold on the cloud score to mask cloudy pixels and took the per-band median values from the accepted pixels. Whole-image data preprocessing and the subsequent classification process were implemented by coding on the GEE platform.

Supra-Glacial Debris Extraction

Debris-Covered Ice Extraction

In this work, we used three algorithms to map the debris-covered outlines of glaciers. A detailed framework for debris-covered ice extraction is presented in **Figure 2**. The first algorithm was a machine-learning algorithm including SVM (Suykens and Vandewalle, 1999), RF (Liaw and Wiener, 2002), and CART

[1]https://www.usgs.gov/land-resources/nli/landsat

[2]https://developers.google.com/earth-engine/landsat

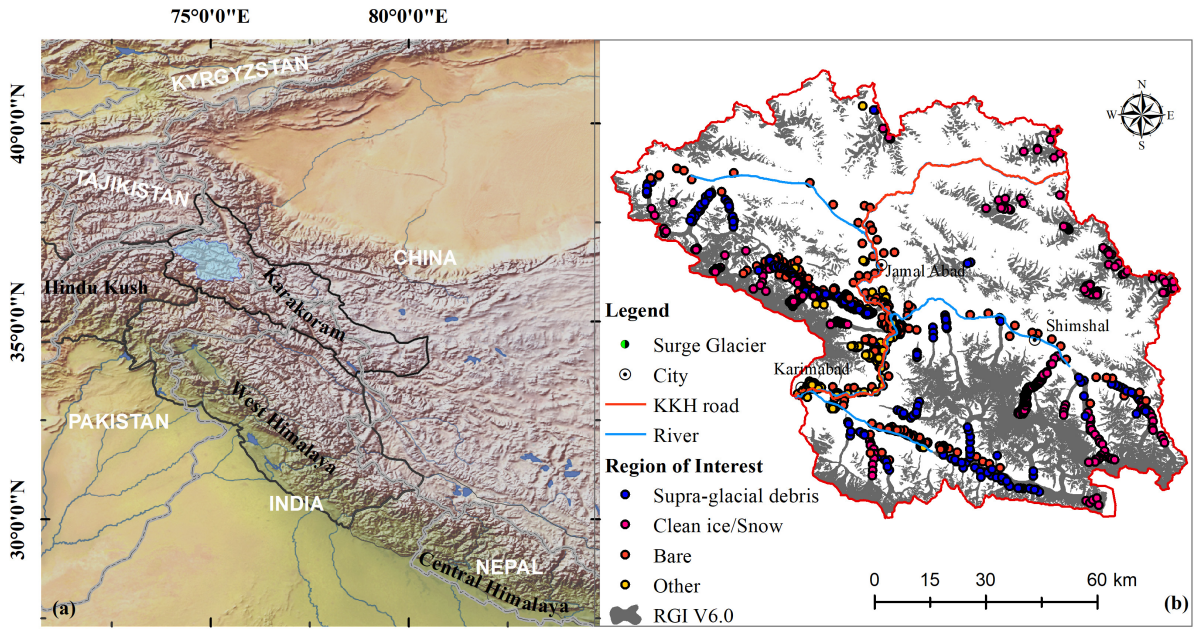

FIGURE 1 | (a) Location of the Hunza Valley (blue area) in the Karakoram. **(b)** Major cities, rivers, and road (Karakoram Highway) in the Hunza Valley, RGI 6.0 glaciers, and region-of-interest sample sites for various land types used in the machine-learning classification model (2019).

(Breiman et al., 1984). Default parameters were used, but 500 trees were set for the RF classification model, and the kernel type of radial basis function that is suitable for the case of linear inseparability was applied in the SVM model. It is obvious that a single spectrum cannot fully solve the problem of the similarity of ice covered with debris to the surrounding terrain. We generated 14 feature variables: original spectrum (Band 1 ~ 7); band ratios (NIR/SWIR1); NDVI ([NIR − Red]/[NIR + Red]); NDSI ([Green − SWIR1]/[Green + SWIR1]); NDWI ([Green − NIR]/[Green + NIR]); and luminance (0.3∗Red + 0.59∗Green + 0.11∗Blue); and geomorphic parameters (slope and aspect). The training data were visually sampled, based on Landsat images at coincident times, combined with high-resolution images from Sentinel-2 and Google Maps. Samples in the regions of interest were divided into clean ice or snow, debris-covered ice (or supra-glacial debris), bare land, and other (e.g., vegetation, villages, rivers, lakes, and shadows), according to the land cover types pertaining to the Hunza Valley (Ali et al., 2018). For example, for 2019, 1,024 samples (shown in **Figure 1**) were selected, including 373 debris, 356 ice/snow, 270 bare land, and 205 other. The second method was a band ratio segmentation method (NDSI < 0.4) (Dozier, 1989) for eliminating the clean ice/snow part, under the restrictions of the RGI 6.0 outlines. However, a fixed NDSI threshold of 0.4 may not have been applicable to all periods. Therefore, we developed an optimization method based on Otsu algorithms to optimize the NDSI threshold to better distinguish between clean ice/snow and debris-covered ice in different periods. The Otsu algorithm is an automatic non-parametric and unsupervised method for thresholding that is used to automatically detect targets in computer vision and image-processing fields (Ng, 2006). It is a global threshold method, and its principles are the following: assume that the gray value of an image is 1 ~ N, divide it into two groups at value k, $G_0 = [1 \sim k]$, and $G_1 = [k+1 \sim N]$, and calculate the probability of the two groups, ω_0 and ω_1, the average values for each group (μ_0 and μ_1), and the entire image (μ). Then, the variance of the two groups can be calculated by the following equation:

$$\sigma^2(k) = \omega_0(\mu_0 - \mu)^2 + \omega_1(\mu_1 - \mu)^2$$

where $\sigma^2(k)$ is a threshold selection function. By changing the k-value in 1 ~ N, the k-value at which $\sigma^2(k)$ is maximized is the required threshold.

Slope Delimitation and "Salt and Pepper Effect" Removal

Topographic parameters are a key factor in delineating glacier areas with debris cover. The spatial distribution of supra-glacial debris depends on the geomorphology and elevation gradient (Paul et al., 2004). Thus, parameters such as slope, aspect, and plan curvature derived from DEM were applied to improve the accuracy of classification of the debris cover and clean ice on the glacier surfaces. Some previous studies proposed various thresholds for the slope; for example, a slope < 24° (Paul et al., 2004) or smaller values [<12° (Alifu et al., 2015) or <14 ~ 16° (Robson et al., 2015)] were used to distinguish debris-covered glaciers from the surrounding terrain. We hypothesized that the slope threshold would show spatial heterogeneity for various glacierized mountains. We used the slope gradient derived from the Shuttle Radar Topography Mission DEM void-filled version, known as "SRTM Plus," at a resolution of 1 arc-second (approximately

TABLE 1 | List of Landsat scenes used to map the dynamics of supra-glacial debris.

Time stage	WRS2 path-row	Date	LANDSAT_SCENE_ID	Sensor	Cloud cover (%)
1990s	150–034	July 05, 1993	LT51500341993186ISP00	TM	5
	149–034	August 07, 1990	LT51490341990219ISP00	TM	1
	149–035	August 07, 1990	LT51490351990219ISP00	TM	1
1998s	149–035	August 13, 1998	LT51490351998225XXX01	TM	4
	149–034	August 29, 1998	LT51490341998241BIK03	TM	4
	150–034	August 20, 1998	LT51500341998232BIK00	TM	3
	149–035	August 16, 1999	LT51490351999228AAA02	TM	8
2000s	149–035	September 11, 2000	LE71490352000255SGS00	ETM+	5
	149–034	September 11, 2000	LE71490342000255SGS00	ETM+	3
	150–035	September 16, 1999	LE71500351999259SGS00	ETM+	1
	149–034	September 02, 2000	LE71500342000246SGS01	ETM+	4
2010s	149–034	September 25, 2008	LT51490342008269KHC01	TM	2
	150–034	August 24, 2011	LT51500342011236KHC00	TM	1
	149–035	August 27, 2009	LT51490352009239KHC00	TM	3
2013s	149–035	September 07, 2013	LC81490352013250LGN01	OLI	2
	149–034	September 07, 2013	LC81490342013250LGN01	OLI	4
	150–034	July 28, 2013	LC81500342013209LGN02	OLI	3
2014s	150–034	September 17, 2014	LC81500342014260LGN01	OLI	2
	149–035	July 24, 2014	LC81490352014205LGN01	OLI	3
	149–034	September 26, 2014	LC81490342014269LGN01	OLI	2
2015s	150–034	August 19, 2015	LC81500342015231LGN01	OLI	2
	149–034	September 13, 2015	LC81490342015256LGN01	OLI	2.5
	149–035	September 13, 2015	LC81490352015256LGN01	OLI	12.5
2017s	150–034	September 09, 2017	LC81500342017252LGN00	OLI	1.6
	149–034	August 01, 2017	LC81490342017213LGN00	OLI	4.7
	149–035	August 01, 2017	LC81490352017213LGN00	OLI	3.6
2018s	150–034	September 12, 2018	LC81500342018255LGN00	OLI	1.7
	149–035	August 04, 2018	LC81490352018216LGN00	OLI	2.6
	149–034	August 04, 2018	LC81490342018216LGN00	OLI	10
2019s	149–034	September 24, 2019	LC81490342019267LGN00	OLI	0.5
	149–035	September 24, 2019	LC81490352019267LGN00	OLI	1.1
	150–034	September 12, 2018	LC81500342018255LGN00	OLI	1.7

30 m), which was available from the National Aeronautics Space Administration Jet Propulsion Laboratory. To obtain a typical slope threshold for this region, we evenly selected 713 slope samples from the glacier areas covered by debris in the Hunza Valley using visual interpretation. Our statistical results indicated that slopes of <25° dominated 99% of the debris-covered glacier areas with an average slope of 6.7° (**Figures 3A,B**). Therefore, a slope threshold of 25°, which is consistent with suggestions in Paul et al. (2004), was used to distinguish the glacier debris areas from the surrounding debris areas.

The "salt-and-pepper" effect is a common noise problem in pixel-based remotely sensed imagery classification, occurring when the same features (adjacent pixels) on the image are divided into different categories. Usually, median or morphological filtering is considered as a method for noise reduction (Serra and Vincent, 1992; Jassim, 2013). To remove this noise (also known as island pixels), we applied a morphological reducer filter to classified images using a custom kernel. We found that a 5 × 5 square kernel, with 50 connected pixels, was the best format for removing this effect, after a comparison of different kernel sizes (kernel radii of 3 × 3, 5 × 5, 7 × 7, 9 × 9, 11 × 11, 13 × 13, 15 × 15, and 25 × 25) (**Figure 3C**) and types (square, circle, octagon, diamond, cross, and plus) and maximum number of connected pixels (5, 10, 20, 30, 40, 50, 100, 200, 300, 400, 500, and 1000).

Definition of Glacier Outlines

At present, there are several datasets defining glacier outlines of the world including Global Land Ice Measurements from Space (GLIMS) (Raup et al., 2007), RGI (Pfeffer et al., 2014), Glacier Area Mapping for Discharge from the Asian Mountains (GAMDAM) (Nuimura et al., 2015), and the Second Glacier Inventory of China (Liu et al., 2015). In our study, the glacier outlines consisted of clean ice and supra-glacial debris outlines. We automatically extracted the clean ice outlines robustly using the classification algorithm, while relying on the existing RGI 6.0 outlines for the supra-glacial debris outlines, as in previous studies (Mölg et al., 2018; Scherler

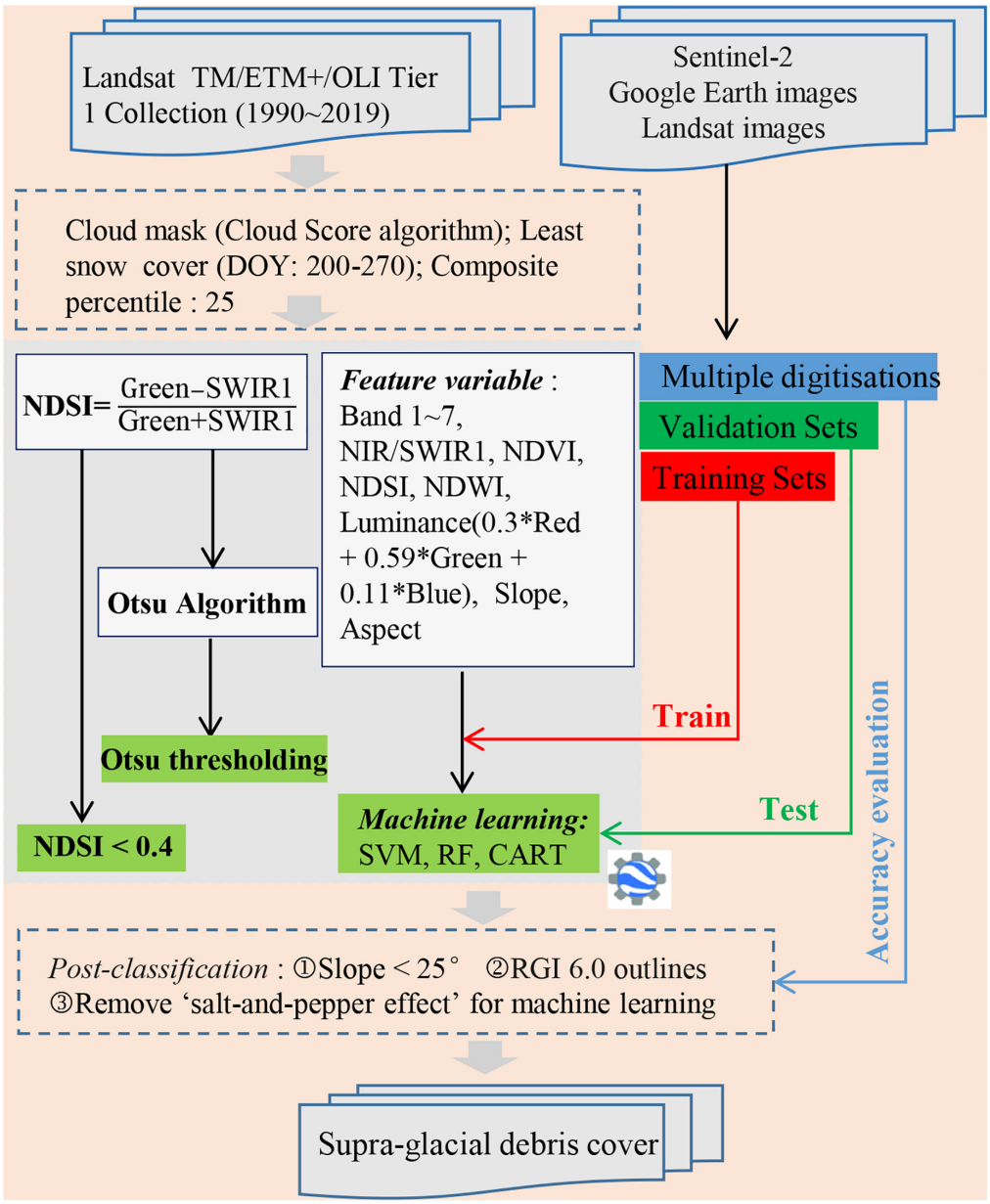

FIGURE 2 | Framework used for mapping debris cover on the GEE platform.

et al., 2018; Tielidze et al., 2020). For terminus-advancing or retreating glaciers, however, it is not reasonable to use a fixed glacier outline in time series of supra-glacial debris mapping. Therefore, we manually improved the RGI 6.0 outlines by visually interpreting glacier boundaries based on historical images of Landsat, Sentinel-2, and Google Maps, especially for the surging glaciers proposed by Bhambri et al. (2017) (**Figure 1**) and debris-covered glaciers. A total of six glacial outlines were modified based on the historical images of 1990, 1998, 2014, 2018, and 2019. We found that although the Karakoram contains a large number of surge-type glaciers (Quincey et al., 2011; Bhambri et al., 2017), there were no significant terminus-advancing or retreating glaciers in our study area. Thus, we assumed that the limiting effect of RGI outlines did not affect the dynamic analysis of supra-glacial debris. Nevertheless, there were voids or missing data in the glacier outlines mapped by RF modeling, possibly due to some darker pixels on the glaciers being misclassified, with so much attention being paid to these in the process during "salt and pepper effect" removal. Also, we found that the clean ice/snow automatically mapped by NDSI < 0.4 and Otsu thresholding contained some water pixels located outside the glacier area, so the results were masked using a 500-m buffer of the RGI 6.0 outlines.

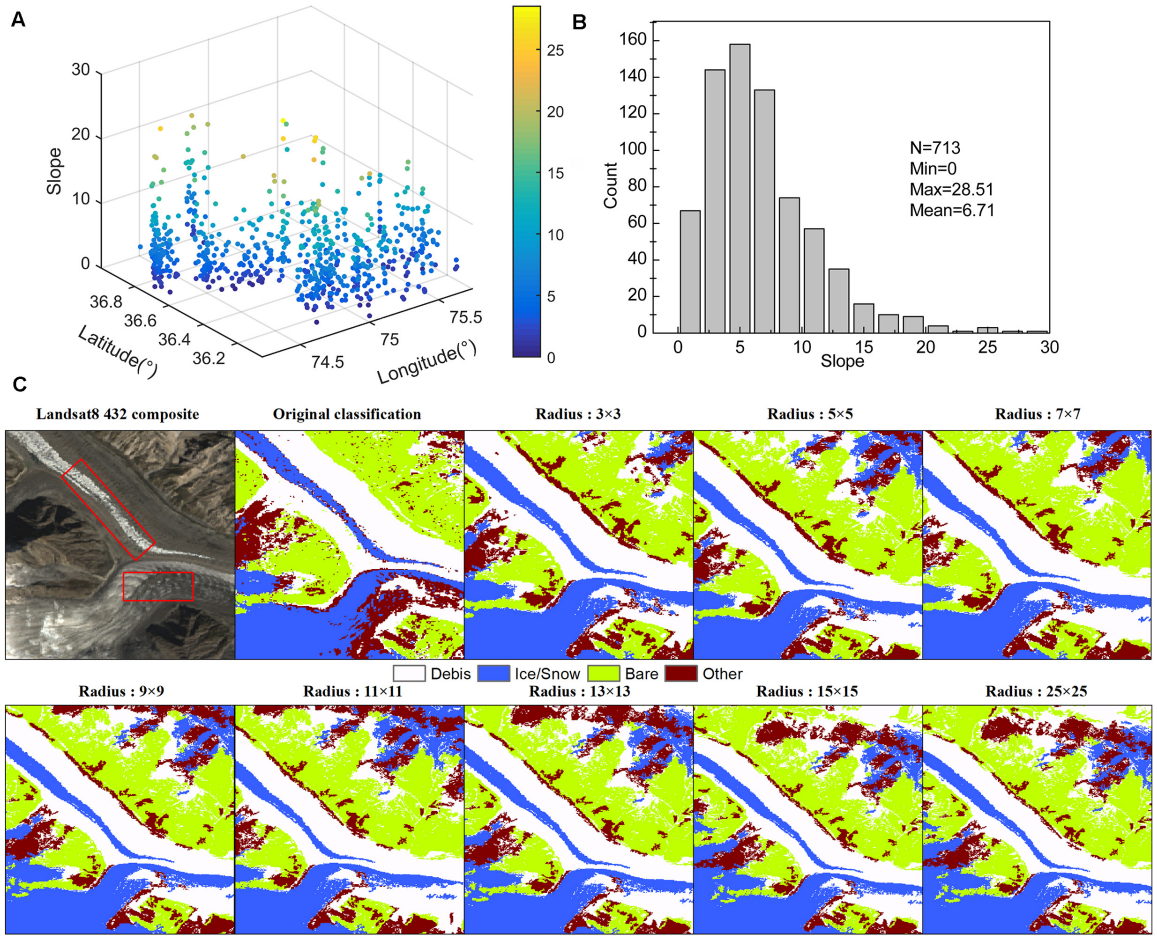

FIGURE 3 | (A) 3D distribution of slopes in the debris-covered areas of the glaciers. **(B)** Histogram of slope statistics. **(C)** Comparison of removal effects (e.g., red rectangles) under different kernel radius and square kernel types. A 5 × 5 square type and 50 connected pixels were selected for this study.

TABLE 2 | Comparison of debris cover area values (2019) derived from automatic extraction algorithms and manual digitization.

Glacier	Multiple digitizations (km^2)							RF	NDSI < 0.4	Otsu thresholding
	1	2	3	4	5	Std.	Mean			
Kukki Jerab	15.7	16.1	15.0	15.1	14.0	0.8	15.2	12.8	14.3	14.6
Virjerab	21.7	21.9	21.5	21.0	21.6	0.4	21.5	20.1	25.9	27.1
Yashkuk Yaz	25.9	27.3	26.2	30.2	24.3	2.2	26.8	25.2	27.5	28.5

Evaluation of Classification Accuracy

We used two methods to assess the accuracy of the classification results. For machine learning, a cross-validation method was used, where the total sample was divided into two parts, and 70% of the sample points from each class were randomly selected to train the model while 30% were withheld to form a validation dataset. Using the validation dataset, a confusion matrix was generated to assess the accuracy of the predictions across the classes, and the overall accuracy through the Kappa coefficient. The confusion matrix prediction versus the validation data based on the RF model and 2019 Landsat 8 OLI image are shown in **Table 2**. The prediction accuracy of the RF model for different land types exceeded 89%, especially for clean ice/snow with user and producer accuracy of 100%. Therefore, for this study, we used the RF model because it had the greatest accuracy compared with the SVM and CART models. Another evaluation tool is the "round robin" method proposed by Paul et al. (2017), which is based on multiple manual digitizations. Based on high-resolution Sentinel-2 and Google Earth images, we selected three glaciers (Kukki Jerab, Virjerab, and Yashkuk Yaz) and performed manual digitization five times, using the average value for evaluating the automatically derived extent and standard deviation for digitization accuracy. **Table 3** shows the debris-covered area

on three debris-covered glaciers derived by machine learning algorithms and by manual digitization.

RESULTS

Changes in Supra-Glacial Debris Cover From 1990 to 2019

Overall, the supra-glacial debris-covered area in the Hunza Valley showed a trend of slowly increasing from 1990 to 2019. This increasing trend has been seen in other major glaciers during the same period, as indicated in **Figure 4**. Considering the accuracy of the RF model for satellite data acquired at different times, the Kappa coefficient of the RF model was within a range of 0.92–0.96 (0.94 ± 0.01), the overall accuracy was 95.5 ± 0.9, and the estimated debris coverage was 410.9 ± 25.9 km^2. The debris cover estimated by the Otsu thresholding method was 559.1 ± 23.4 km^2, with an optimized threshold of 0.53 ± 0.04. The NDSI < 0.4 method gives a value of 487.1 ± 16.9 km^2. The detailed estimates of supra-glacial debris cover are shown in **Table 4** and **Figure 5**. The total area of supra-glacial debris cover in the Hunza Valley has expanded by about 8.1–21.3% from 1990 to 2019. In comparing the estimated values from the three methods, we found that those based on Otsu thresholding were the largest, followed by the NDSI < 0.4 method and the RF model, while the estimated standard deviation based on the RF model was the largest, with a value of 25.9 km^2. The results indicated that the supra-glacial debris cover in this region has been expanding slowly since the 1990s, due to an increasing number of clean ice areas being covered by impurities, such as rock and dust, which reduce the *albedo*, resulting in a debris-covered ice classification.

In order to further explore the variations in supra-glacial debris cover, we drew the spatial distribution of supra-glacial debris in the Hunza Valley from 1990 to 2019 using spatial overlay analysis, as shown in **Figure 6A**. The supra-glacial debris has migrated up-glacier, and the main area of change is located in the middle and upper regions of the glacier, close to the altitude of the equilibrium line (4,500–5,500 m a.s.l.). The variation in debris on the slopes showed a normally skewed distribution, with ∼60% of the variation in coverage being located in the area below a slope of 10° (**Figure 6B**). The maximum variation in supra-glacial debris was at an altitude of 5,000 m a.s.l. (**Figure 6C**) and with a northeast aspect. Also, We mapped the distribution of supra-glacial debris and clean ice/snow cover in the Hunza Valley at elevation gradient and aspect based on the estimation results by RF model on images acquired in 2019. More than 78% of the clean ice/snow area lies higher than 5,500 m a.s.l., while about 80% of the debris-covered ice was distributed between 4,000 and 5,000 m a.s.l. The median elevations were approximately 5,365 m for clean ice/snow and 4,075 m for debris-covered ice (**Figure 7A**). The median elevation of glaciers is 5,230 m a.s.l., which is sometimes referred to as the equilibrium line altitude of glaciers in the Hunza basin (Qureshi et al., 2017). This means that supra-glacial debris is extensively distributed in the lower part of the ablation area of glaciers. Most glaciers have a north (N) and northeast (NE) aspect, accounting for 38.7% of the glaciers' area, with only a few glaciers having a west-facing aspect (**Figure 7B**).

TABLE 3 | Confusion matrix for random forest model classification in 2019 [model prediction (top) and validation data (left)].

	Debris	Ice/snow	Bare	Other	Total	Producer accuracy
Debris	101	0	5	0	106	95.3%
Ice/snow	0	104	0	0	104	100%
Bare	2	0	65	1	68	95.6%
Other	3	0	3	66	72	91.7%
Total	106	104	73	67	350	Overall accuracy: 96.0%
User accuracy	95.3%	100%	89.0%	98.5%	–	Kappa: 0.95

Status of Glaciers in the Hunza Valley

Over the past 30 years, the glacier area in the Hunza Valley has shown a downward trend. The glacier area estimated by the NDSI < 0.4, Otsu thresholding, and the RF model is 4,355.5 ± 210.2 km^2, 4,104.8 ± 167.6 km^2, and 3,810.8 ± 321.7 km^2, respectively. The clean ice/snow and supra-glacial debris areas of the Hunza Valley for the years 1990, 1998, 2000, 2010, 2013, 2014, 2015, 2017, 2018, and 2019 are included in **Table 4** and **Figure 5**. The results presented in this study indicate a 9.311.6% decrease in clean ice/snow area in this region between 1990 and 2019. This decrease may be due to the retreat of glaciers and the overall expansion of debris-covered areas on glaciers (8.1–21.3%). According to the estimates from the RF model, the total glacier area of the Hunza Valley was 3,497.1 km^2 in 1990 and 3,286.6 km^2 in 2019. Overall, there was a 6.0% decrease in glacier area from 1990 to 2019.

DISCUSSION

Uncertainty Analysis

Uncertainty, including that stemming from measurement errors, models, and scale effects, is an important step in validating the mapping results of supra-glacial debris. In this study, the quality of the satellite imagery was the most important factor, as this directly determined the classification results, especially in the high mountain areas with clouds and steep terrain. To exclude the impact of fresh snow, images from previous and subsequent years were used for some periods when there were few cloud-free images, such as in 2010, and this may inevitably have added to the uncertainty. Besides, the uncertainty mainly stemmed from the ground observational data (such as the counts and spatial distribution of the samples for the machine learning model), the classification methods, including the model types, the selected feature variables, model parameters or thresholds, and the postprocessing process. We analyzed this uncertainty from the following two aspects.

Uncertainties in Mapping Glacier Outlines

Uncertainty of supra-glacial debris extraction is a major source of uncertainty in mapping glacier outlines compared with the uncertainty from the extraction of the clean ice/snow part. The mapping uncertainty for the clean-ice areas was mainly affected by the seasonal snow cover. Seasonal snow cover has

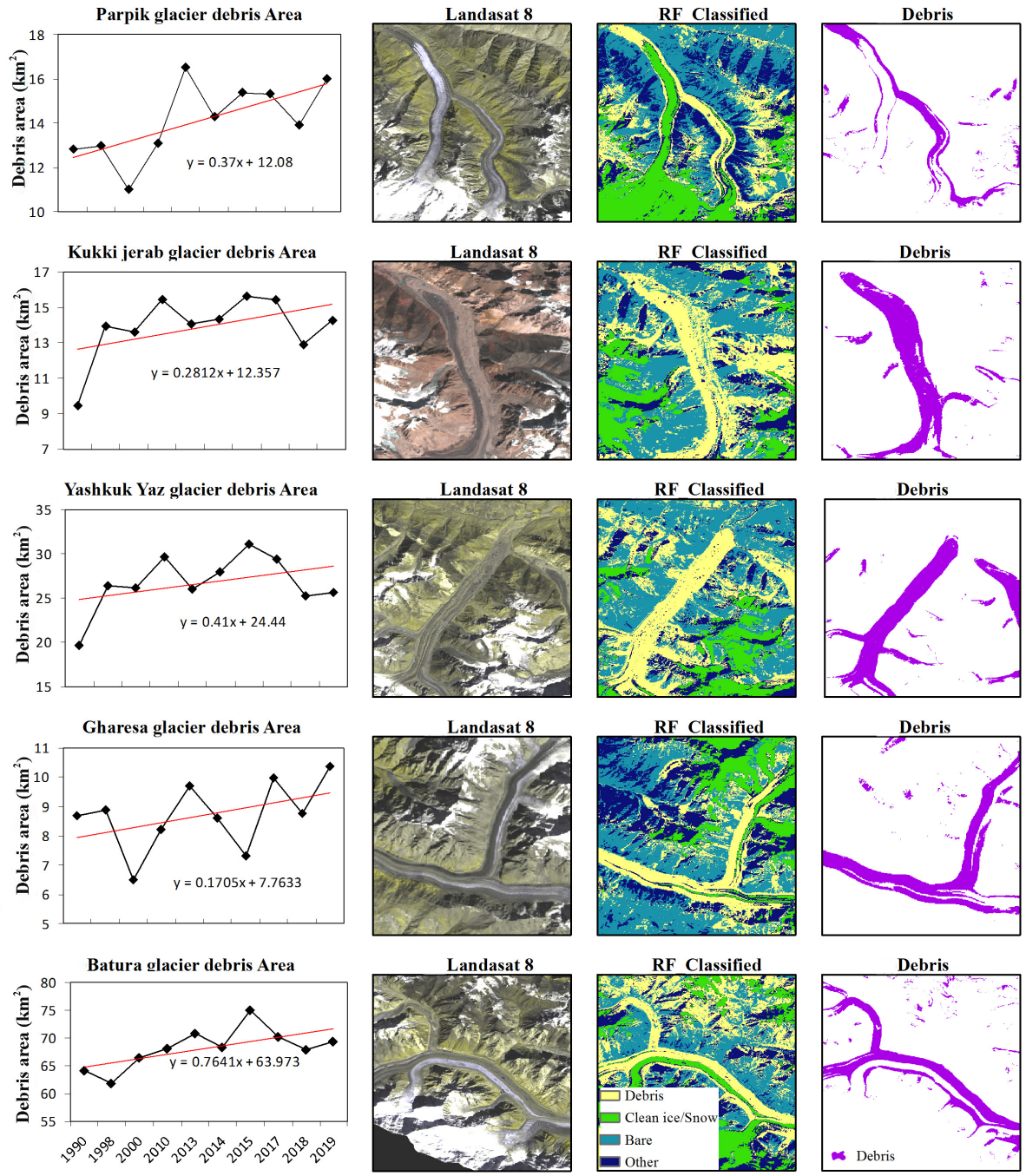

FIGURE 4 | RF-classifier-based supra-glacial debris mapping of five typical debris-covered glaciers. Column 1 (left) illustrates the variation curves for the supra-glacial debris area, indicating the expansion of supra-glacial debris cover from 1990 to 2019. The next columns show examples of supra-glacial debris extraction for each glacier, including the Landsat 8 OLI image from 2019 (Column 2), the RF classified results (Column 3), and the debris extent passed through post-classification processing (Column 4).

a greater impact on small glaciers, and the uncertainty may exceed 50% or even more (Mölg et al., 2018). From 2010 to 2014, the clean ice/snow area estimated by the three methods was on the high side, which may be caused by seasonal snow cover. In addition, we compared the glacier area estimated by Mölg et al. (2018), hereafter called the Mölg dataset, with our inventory to determine the main differences between them. The RF-based classification accuracy for clean ice/snow was 100% with an estimated glacier area of 3,810.8 ± 321.7 km^2, which is ∼6% larger than the Mölg dataset (3,617.1 km^2). The glacier area estimated by NDSI < 0.4 and Otsu thresholding tended to be overestimated, being 738.4 km^2 and 487.8 km^2 higher

TABLE 4 | Debris cover area change in Hunza valley between 1990 and 2019.

Time stage	NDSI < 0.4		Otsu thresholding		RF model				
	Clean ice/snow (km^2)	Supra-glacial debris (km^2)	Thresholds	Clean ice/snow (km^2)	Supra-glacial debris (km^2)	Kappa	Overall accuracy (%)	Clean ice/snow (km^2)	Supra-glacial debris (km^2)
1990	3951.7 ± 220.7	483.9 ± 16.9	0.52	3629.0 ± 179.5	542.0 ± 23.4	0.93	95.2	3118.0 ± 330.0	379.2 ± 25.9
1998	3694.0 ± 220.7	486.9 ± 16.9	0.49	3442.3 ± 179.5	540.7 ± 23.4	0.94	95.6	3175.0 ± 330.0	439.1 ± 25.9
2000	3722.7 ± 220.7	487.9 ± 16.9	0.49	3502.8 ± 179.5	534.1 ± 23.4	0.94	95.8	3344.3 ± 330.0	390.0 ± 25.9
2010	3992.9 ± 220.7	481.9 ± 16.9	0.49	3744.2 ± 179.5	529.6 ± 23.4	0.93	94.9	3738.7 ± 330.0	405.4 ± 25.9
2013	4086.0 ± 220.7	483.2 ± 16.9	0.57	3717.2 ± 179.5	548.4 ± 23.4	0.93	94.9	3704.8 ± 330.0	434.4 ± 25.9
2014	4267.0 ± 220.7	484.7 ± 16.9	0.60	3822.9 ± 179.5	559.8 ± 23.4	0.96	96.7	3853.2 ± 330.0	397.6 ± 25.9
2015	3788.0 ± 220.7	515.3 ± 16.9	0.51	3447.0 ± 179.5	582.7 ± 23.4	0.95	96.3	3675.2 ± 330.0	394.7 ± 25.9
2017	3804.0 ± 220.7	518.9 ± 16.9	0.55	3457.6 ± 179.5	593.0 ± 23.4	0.92	93.8	3307.7 ± 330.0	416.1 ± 25.9
2018	3782.2 ± 220.7	503.6 ± 16.9	0.55	3466.7 ± 179.5	574.7 ± 23.4	0.95	96.1	3255.8 ± 330.0	392.1 ± 25.9
2019	3493.0 ± 220.7	524.8 ± 16.9	0.53	3227.8 ± 179.5	586.0 ± 23.4	0.95	96.0	2826.7 ± 330.0	459.9 ± 25.9
Average	3858.4 ± 220.7	487.1 ± 16.9	0.53 ± 0.04	3545.7 ± 179.5	559.1 ± 23.4	0.94 ± 0.01	95.5 ± 0.9	3399.9 ± 330.0	410.9 ± 25.9

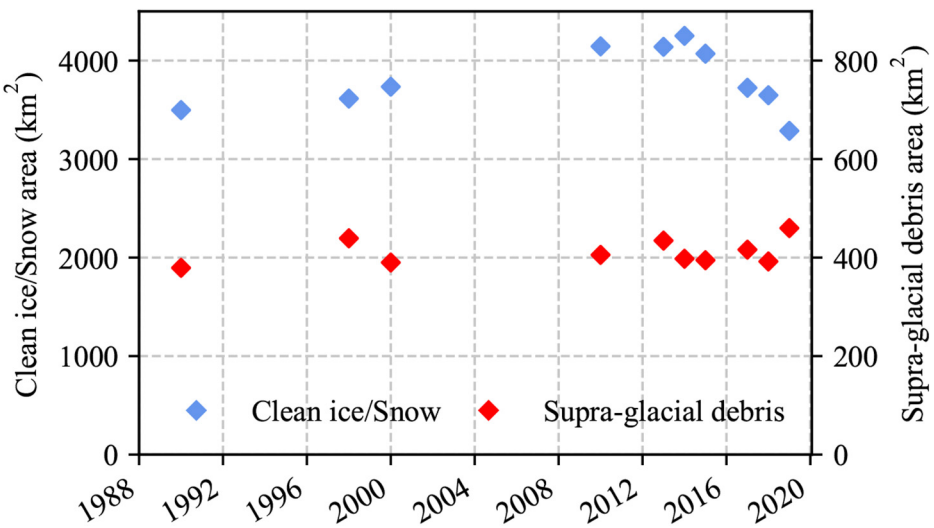

FIGURE 5 | Time-varying trend of the clean ice/snow and supra-glacial debris area estimated by the random forest model.

than the Mölg dataset, respectively. Unfortunately, there were still voids or missing data in the glacier outlines mapped by the RF model, which also lead to the underestimation of glacier area in some years.

Uncertainties in Mapping Supra-Glacial Debris

Figure 8A shows that the results from the machine learning algorithms generally had high accuracy, with Kappa coefficients ranging from 0.82 to 0.95. In comparison, the classification accuracy for the SVM model was slightly lower than for the RF model, where the Kappa coefficient was 0.9 and the overall accuracy was 96.0%. The manual digitization for each glacier by five professionals showed decreasing standard deviations from the largest to the smallest glaciers, specifically Yashkuk Yaz (26.8 ± 2.2 km^2), Kukki Jerab (15.2 ± 0.8 km^2), and Virjerab (21.6 ± 0.4 km^2) glaciers. The linear fit between the mean of the digitizations and the automatic estimates indicated that all the machine learning algorithms could produce results close to reality but that the RF model was better than the other two, in terms of the determination of an R^2 coefficient of 0.99 for the RF model, 0.87 for the NDSI <0.4 method and 0.86 for the Otsu thresholding algorithm (**Figure 8B**).

As shown in the results, there were differences in the supra-glacial debris cover area estimated by the three methods, with the Otsu thresholding tending to overestimate the debris coverage, while the RF model gave the smallest estimated value. To verify the reliability of these estimates, we compared the results with those from other works. For example, the supra-glacial debris area extracted from the 2007 and 2009 ALOS-1 PALSAR-1 coherence images in the Mölg dataset was 583.6 km^2, which was larger than the debris area estimated by our study for 2010–481.9 km^2 (NDSI < 0.4), 529.6 km^2 (Otsu thresholding) and 405.4 km^2 (RF model). Another comparative dataset is one obtained by extracting regions with NDSI < 0.4 and clipping them with RGI 6.0 outlines (Scherler et al., 2018), the same as method 2 of this study. In this work, the automatically

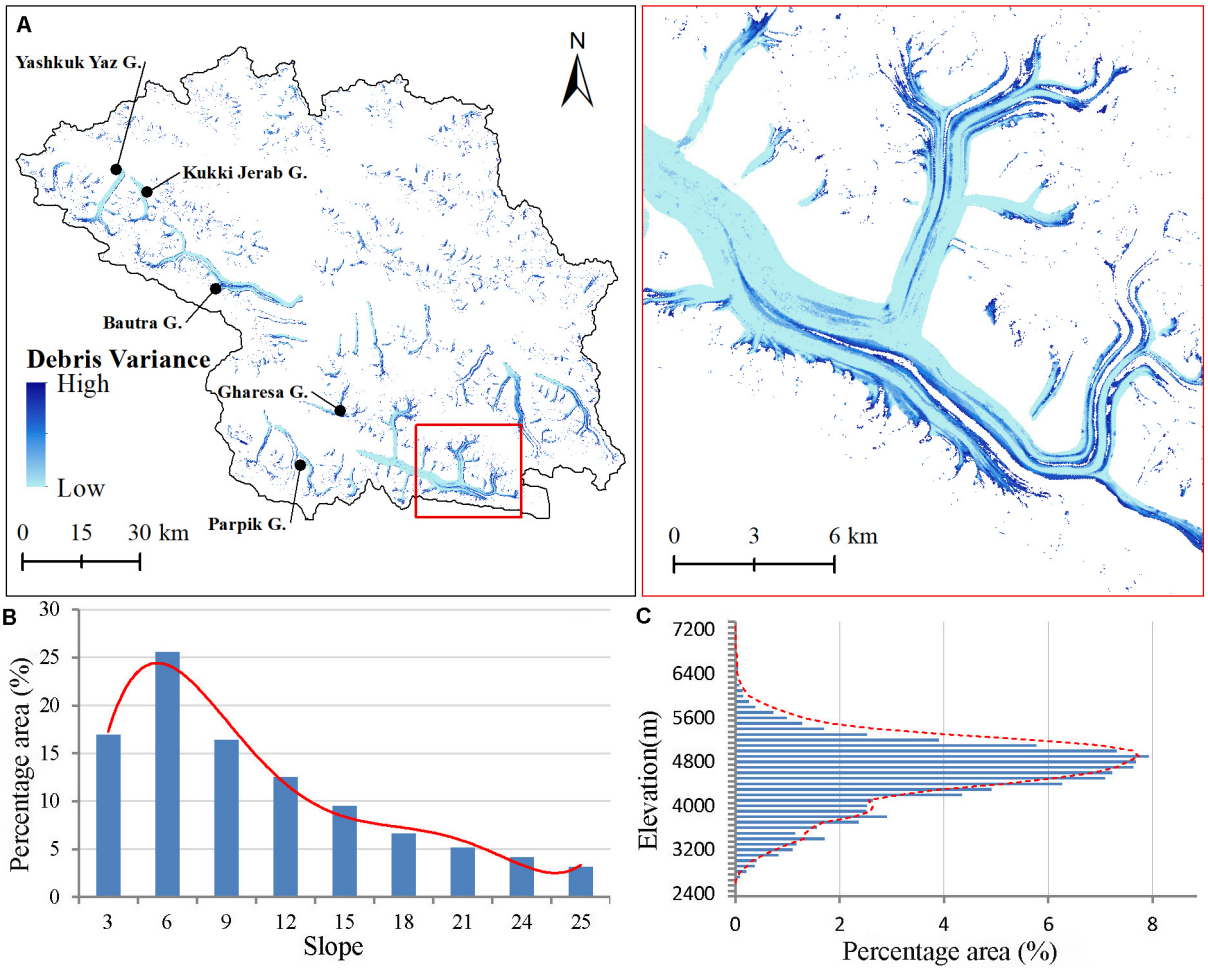

FIGURE 6 | (A) Spatial distribution of supra-glacial debris cover variance from 1990 to 2019. **(B,C)** Variations in supra-glacial debris cover area (%) at different slopes and for different elevations, respectively.

extracted areas, using Landsat 8 composite images from 2013 to 2017 and Sentinel-2 composite images from 2015 to 2017, were 465.1 and 453.3 km^2, respectively. For the same period, the estimated results from the RF model in this study were comparable (408.9 ± 22.2 and 405.4 ± 13.2 km^2, respectively). However, the supra-glacial debris results for the NDSI < 0.4 and Otsu thresholding were higher than those of Scherler et al. (2018). It is difficult to evaluate the estimated results from this study in terms of previous results because they derive from different remote sensing data, and the methods used for data processing and classification are different; however, the supra-glacial debris-covered area falls within a reasonable range, in terms of magnitude.

Uncertainty from complex surfaces debris-covered glaciers, such as stagnant ice in glacier tongue areas, cliffs, and ponds on the surfaces of debris-covered areas, and boulders and dirty ice, have extensive effects on pixel-based classification. The supra-glacial ponds or lakes widely distributed on glaciers such as Batura, Hispar, Yashkuk Yaz, and Kukki Jerab frequently emerge or disappear, demonstrating obvious supra-glacial characteristics with time. We used salt-and-pepper-effect removal, as described above, to compare these effects. By comparison, we found that convolution kernel and maximum-connected pixel counts have to be properly decided in order to avoid the removal of correctly classified patches, or vice versa. In this study, a 5 × 5 kernel with 50 connected pixels was used, but this may not have been optimal. The problem of the salt-and-pepper effect is unavoidable in pixel-based classification. Although some studies have pointed out that the object-based classification method can effectively solve this problem and improve the accuracy (Rastner et al., 2014; Robson et al., 2015; Kraaijenbrink et al., 2016; Sahu and Gupta, 2018), its universality and operability on a large scale need to be further considered. Also, the stagnant ice at glacier tongues, such as the Batura and Hispar Glaciers, tend to have thick overlying debris layers with signs of vegetation (shrub) growth on their surfaces. Parts of these regions are classified as non-debris cover regions, which increases the uncertainty of estimating supra-glacial debris coverage, especially for RF models. Vezzola et al. (2016) showed that the number of debris-covered glaciers featuring supra-glacial trees is increasing globally as a response

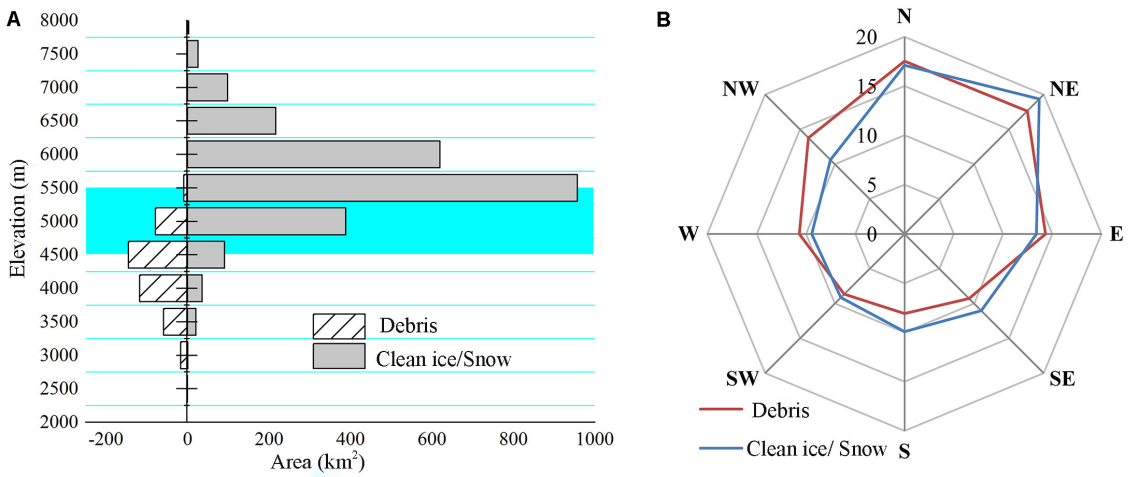

FIGURE 7 | (A) Distribution of supra-glacial debris and clean ice/snow areas by altitude, based on the 2019 random forest model classified result. The light blue area represents the equilibrium-line altitude of glaciers in the Hunza Valley (4,500–5,500 m a.s.l.). **(B)** Percentage of supra-glacial debris and clean ice/snow distribution by aspect.

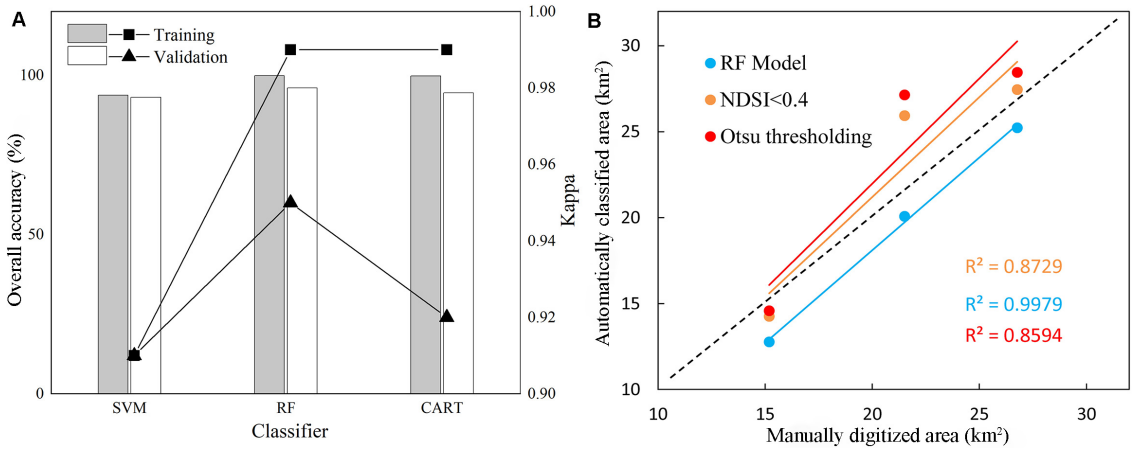

FIGURE 8 | (A) Model accuracy of three machine-learning algorithms (the bar plot shows the overall accuracy; the lines link the Kappa coefficients). **(B)** Linear fit of estimated values to manually digitized values. The black dashed line represents the 1:1 line.

of the alpine environment to climate warming. They found supra-glacial trees present on the Miage Glacier when a debris thickness threshold (≥19 cm) was exceeded, and where there was a gentle slope (≤10°) and a low glacier surface velocity (≤7.0 m yr^{-1}) and where the vertical changes due to glacier dynamics were positive.

Additionally, although the image acquisition time was limited to 200–270 days, there may still be snow cover at high altitude, which is one of the significant uncertainties in mapping debris-covered ice. Due to the annual difference in temperature and precipitation, the melting limits of seasonal snow on the upper part of glaciers in summer are different each year, which may lead to an underestimation of the supra-glacial debris area. Similarly, the effects of shadows and cloud coverage inevitably pose challenges to the mapping of supra-glacial debris.

Characteristics and Possible Causes for Supra-Glacial Debris Cover Changes

Overall, the supra-glacial debris cover migrated up-glacier. Similar patterns of up-glacier migration have also been described for the Zmutt Glacier, Swiss Alps (Mölg et al., 2019) and the Greater Caucasus (Tielidze et al., 2020). Variations in supra-glacial debris cover were mainly observed in the middle and upper parts of the glacier, while the distribution of supra-glacial debris from the lower part to the glacier tongue remained stable. In the middle of the glacier, the area showing the most intensive variation was at the junction between the clean ice and the debris-covered ice. We found that the expansion of debris-cover over clean ice was slow. Due to the characteristics of glacier movements, the spatial distribution of supra-glacial debris cover in the downstream part of the glacier changes with time, while the

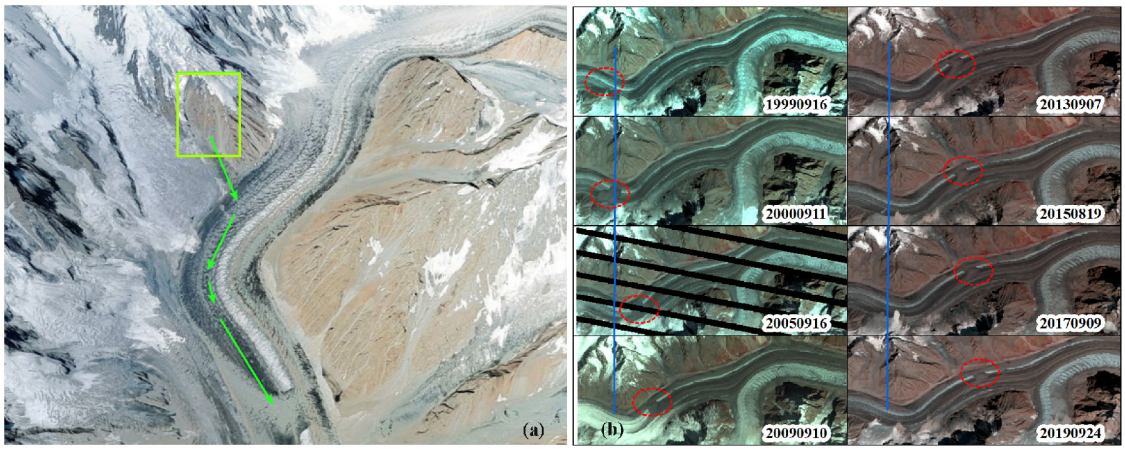

FIGURE 9 | (a) Location of the landslide area (green rectangle), shown on Google Earth images. **(b)** Emergence of landslide sediments and its position changes on the glacier from 1999 to 2019. The base image is from the Landsat TM, ETM+ and OLI sensors.

area changes slightly. This redistribution of the surface moraine is a key factor in the diversification of glacier surface types, and it also changes the debris coverage. Recycled material from lateral moraines may be the source of this debris. As the glacier lowers and the permafrost melts, the lateral moraines become unstable, causing moraine material to fall onto the glacier (Nakawo et al., 1986). Debris eroded from the glacier bed may also be entangled in the ice. The degree of under-ice entrainment mainly depends on the thermal conditions at the base of the glacier and the substrate erodibility.

Previous studies have indicated that the main sources of debris are mass movements such as rockfalls, rock avalanches, debris-laden ice, and snow avalanches from the surrounding slopes (Hambrey et al., 2008). These sudden and sometimes massive debris migration/relocation events are common in alpine areas. For example, between September 1999 and June 2000, a landslide occurred in the upper region of the Batura Glacier, possibly as a result of slope failure. The accumulated rock fragments covered the glacier surface and moved downstream with the glacier ice, following a dynamic change in their shapes and sizes (**Figure 9**). Such phenomena play a key role in the increase and fluctuation of supra-glacial debris-covered areas.

Figure 10 shows the hypsometry of the supra-glacial debris coverage, and the five representative debris-covered glaciers, in 1990, 1998, 2010, 2014, and 2019. The zone at 4,500 ∼ 5,500 m a.s.l. displayed the greatest variation in supra-glacial debris (**Figure 10A**) and is within the altitude equilibrium line zone of glaciers in the Hunza Valley (Scherler et al., 2011; Kaab et al., 2012; Gardelle et al., 2013). These areas have steep topography and are prone to rockfalls and rock avalanches, in which there is an abundant release of supra-glacial debris. The amount of debris reaching a given glacier depends on the characteristics and extent of the catchment area, and especially its weathering and erosion rates (Haeberli et al., 2006). These are also affected by the lithology of the bedrock (Singh et al., 2011). Not all glaciers have experienced an increase in supra-glacial debris cover, with minor changes in supra-glacial debris having been recorded for the Batura, Parpik, and Gharesa glaciers (**Figures 10B,C,E**), which differ significantly from the obvious increases reported for the Kukki Jerab and Yashkuk Yaz glaciers (**Figures 10D,F**), especially between 1990 and 1998. In addition to subjective factors, the apparent increase in supra-glacial debris cover on Kukki Jerab and Yashkuk Yaz glaciers is mainly attributed to the evolution of ice ponds and cliffs and the upward expansion of surface moraines.

Impact of Climate Change

Thinning of glaciers and a warming atmosphere can lead to permafrost melting and slope instability at higher altitudes (Deline et al., 2015). Glacier changes in the Karakoram Mountains have been attributed to the dynamics of the Indian monsoon and the westerlies (Qureshi et al., 2017). To demonstrate the relationship between supra-glacial debris and climate change, we analyzed temperature, *albedo*, and precipitation datasets taken from MODIS products and Terra Climate Monthly[3] and Climate Hazards Group InfraRed Precipitation with Station data (CHIRPS) products.[4] The temporal changes in temperature, *albedo*, and precipitation derived from this data are shown in **Figure 11**. It is clear that warming and wetting have been a dominant phenomenon in the Hunza Valley in recent decades (**Figures 11A,C,D**). Temperature had a downward trend in 1990–1998; however, since 2000, the temperature derived from both MODIS and the Terra Climate products have shown a slight increase. *Albedo* on the ice surface is decreasing (**Figure 11B**)—-a sign of supra-glacial debris increase. The amount of absorbed solar radiation on a glacier's surface increases where the ice is covered by supra-glacial debris or discontinuous debris (dirty ice); such debris causes an increase in glacier surface temperature and a decrease in *albedo* (Singh et al., 2011). As shown in **Figures 11E,F**, we also analyzed the relationships

[3]http://www.climatologylab.org

[4]https://chc.ucsb.edu/data/chirps

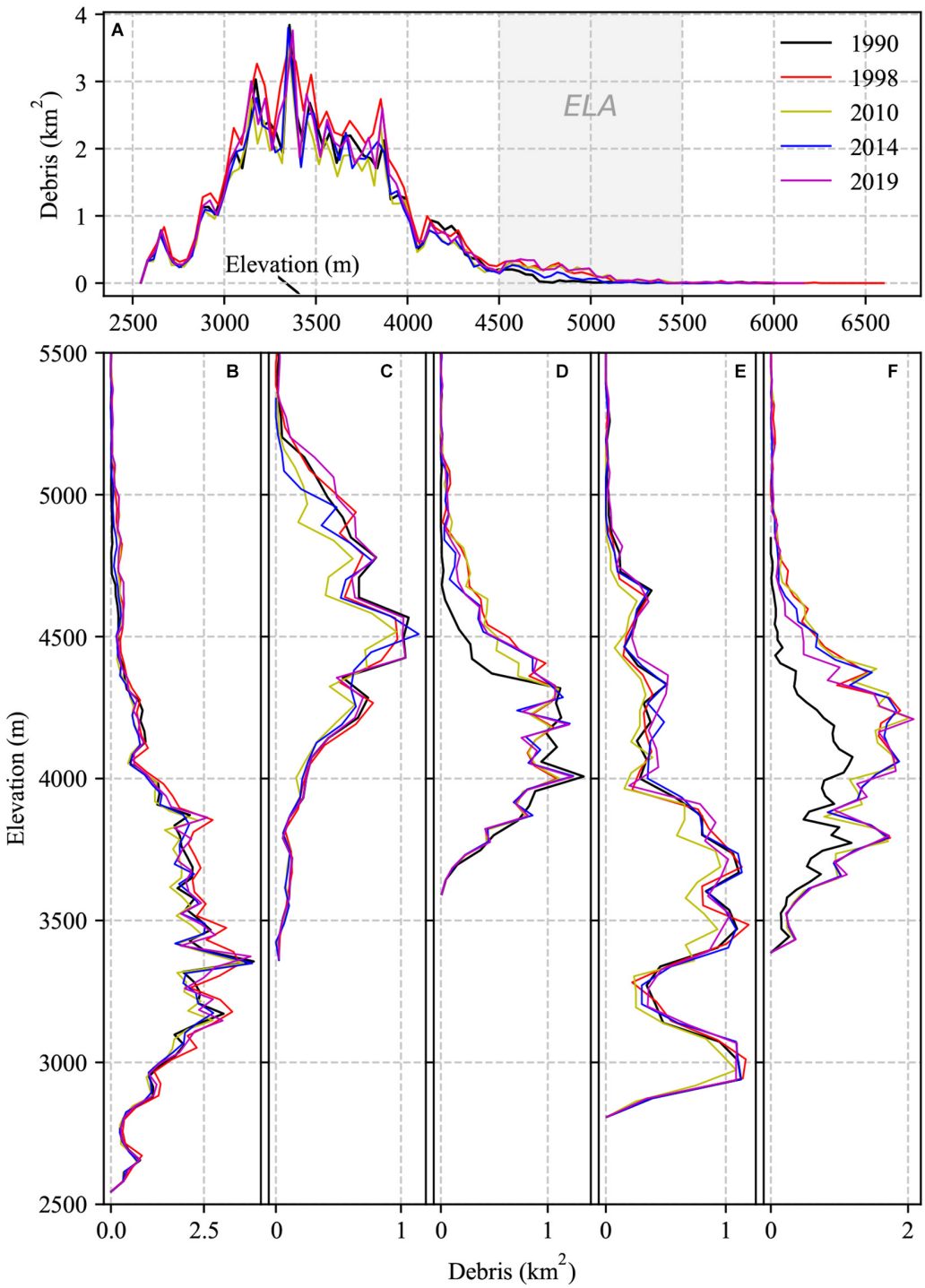

FIGURE 10 | Hypsometry of the supra-glacial debris cover in the studied regions, alongside data from five typical debris-covered glaciers in 1990, 1998, 2010, 2014, and 2019. **(A)** Study area. **(B)** Batura Glacier. **(C)** Gharesa Glacier. **(D)** Kukki Jerab Glacier. **(E)** Parpik Glacier. **(F)** Yashkuk Yaz Glacier. The locations of the five glaciers are indicated in **Figure 6A**.

between temperature or precipitation and supra-glacial debris cover. Decreasing temperature and increasing precipitation have a positive relation with supra-glacial debris increase. This is particularly evident in the period 1990–1998. Global warming has accelerated the melting of glaciers resulting in changes in ice surface morphology and the redistribution of surface moraine material. A positive mass balance under decreasing temperatures and increasing precipitation may be caused by an

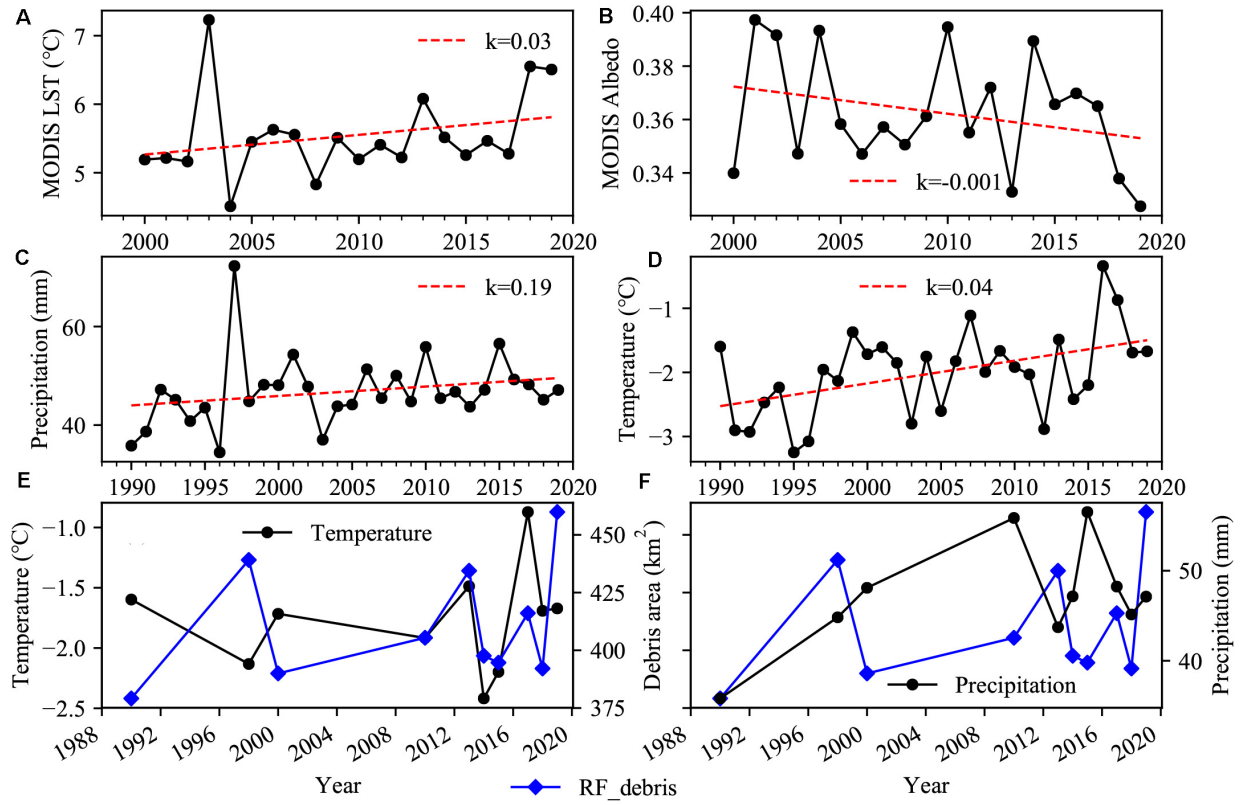

FIGURE 11 | Average land-surface temperatures **(A)** and *albedo* **(B)** for 200 ~ 270 days per year, derived from MODIS products (MOD11A2006 and MCD43A3006, respectively) in the glacier areas from 2000 to 2019 [*k*-value refers to the slope of the trend line (red dashed line), the same below]. **(C)** Precipitation for 200–270 days per year in the glacier area, generated from CHIRPS Pentad product data. **(D)** Trend map of average annual maximum temperatures in the Hunza River Basin, derived from the TerraClimate dataset, with a monthly temporal resolution and ~4-km (1/24th of a degree) spatial resolution. Correlation of the supra-glacial debris area estimated by the RF model with temperature **(E)** and precipitation **(F)** [for a description of the data used, see **(C,D)**] in the Hunza Valley.

increase in the production of material triggered by snow/ice avalanches or rockfalls.

CONCLUSION

The expansion of supra-glacial debris and decrease of glacier surface *albedo* have been reported widely in several parts of the word (Ming et al., 2012; Jiang et al., 2018; Fugazza et al., 2019; Tielidze et al., 2020). In this study, we mapped the dynamics of supra-glacial debris cover in the Hunza Valley, using 34 Landsat images (10 TM, four ETM+, and 18 OLI) acquired from 1990 to 2019. Firstly, an image composite method was applied, and sequential Landsat images with less cloud and snow cover at the pixel level were used to generate annual images of supra-glacial debris on glaciers. Then, the Otsu algorithm was utilized to optimize thresholds of NDSI segmentation, and the supra-glacial features (e.g., clean ice/snow and debris-covered ice) were classified on the state-of-the-art GEE cloud computing platform together with three machine learning algorithms (RF, SVM, and CART). All the training and validation datasets were derived from the visual inspection of freely available, high-spatial-resolution satellite imagery (Landsat, Sentinel-2, and Google Earth). Among these, the RF model produced the best classification accuracy, with a Kappa coefficient of 0.94 ± 0.01 and an overall accuracy of 95.6 ± 0.9%. Based on these estimates, we found that significant increases in areal supra-glacial debris cover had occurred during the last 30 years. The total area of supra-glacial debris cover in the Hunza Valley has expanded by about 8.1–21.3% from 1990 to 2019. It has migrated up-glacier, and the main area of change is located in the middle and upper regions of the glacier, close to the altitude of the equilibrium line (4,500–5,500 m a.s.l.). We also found that the interannual temperature decrease and precipitation increase had positive relations with the supra-glacial debris increase. This supra-glacial debris areal change information can also be used in mass balance, glacier hydrology, glacier hazard, and glacier response to climate change models.

The identification of debris is a fundamental, and yet still challenging field in studying glacier change and water resources. With the effects of global warming, clean glaciers in the high mountains of Asia are increasingly changing into debris-covered glaciers, which leads to changed discharge in rivers mainly supplied by glacial meltwater, resulting in the water resources in basins, and their future trends, likely to be greatly affected.

To explore the response of debris-covered glaciers to climate change, and their effect on hydrology and water resources, future work should focus on extracting information about debris thickness and other surface features (e.g., glacial ponds and cliffs) using high-resolution aerial or satellite imagery and deep-learning techniques.

DATA AVAILABILITY STATEMENT

All datasets generated for this study are included in the article/supplementary material.

AUTHOR CONTRIBUTIONS

The study was designed by SL and FX. FX ran models and performed the data analysis. FX and SL performed the analysis and drafted the first manuscript. KW, YZ, YG, MQ, SD, MS, and AT discussed and improved the manuscript. All authors contributed to the article and approved the submitted version.

FUNDING

This project has received funding from the National Natural Science Foundation of China (Grant Nos. 41761144075 and 41801031), the Second Tibetan Plateau Scientific Expedition and Research Program (STEP, Grant No. 2019QZKK0208), the Research Fund for Introducing Talents of Yunnan University (No. YJRC3201702), and the initiative for the promotion of Yunnan University in the development of a world-class university. FX was also supported by the Innovation Fund Designated for Graduate Students of Yunnan University (Grant No. 2019226).

ACKNOWLEDGMENTS

We thank the Google Earth Engine Science team for the freely available cloud-computing platform and USGS for Landsat imagery and SRTM DEM. We thank Sidou Zhang, Xinxin Qiang, and Ying Yi at the Institute of International Rivers and Eco-Security, Yunnan University, who involved in the conception of the manuscript. Finally, we thank the editor TZ and three reviewers for their constructive comments on the manuscript.

REFERENCES

Ali, A. F., Xiao, C., Zhang, X., Adnan, M., Iqbal, M., and Khan, G. (2018). Projection of future streamflow of the Hunza River Basin, Karakoram Range (Pakistan) using HBV hydrological model. *J. Mt. Sci.* 15, 2218–2235. doi: 10.1007/s11629-018-4907-4

Alifu, H., Johnson, B. A., and Tateishi, R. (2016). Delineation of debris-covered glaciers based on a combination of geomorphometric parameters and a TIR/NIR/SWIR band ratio. *IEEE J. Sel. Top. Appl. Earth Observ. Remote Sens.* 9, 781–792. doi: 10.1109/JSTARS.2015.2500906

Alifu, H., Tateishi, R., and Johnson, B. (2015). A new band ratio technique for mapping debris-covered glaciers using Landsat imagery and a digital elevation model. *Int. J. Remote Sens.* 36, 2063–2075. doi: 10.1080/2150704x.2015.1034886

Altena, B., Scambos, T., Fahnestock, M., and Kääb, A. (2019). Extracting recent short-term glacier velocity evolution over southern Alaska and the Yukon from a large collection of Landsat data. *Cryosphere* 13, 795–814. doi: 10.5194/tc-13-795-2019

Benn, D. I., Bolch, T., Hands, K., Gulley, J., Luckman, A., Nicholson, L. I., et al. (2012). Response of debris-covered glaciers in the Mount Everest region to recent warming, and implications for outburst flood hazards. *Earth Sci. Rev.* 114, 156–174. doi: 10.1016/j.earscirev.2012.03.008

Bhambri, R., Hewitt, K., Kawishwar, P., Kumar, A., Verma, A., Tiwari, S., et al. (2019). Ice-dams, outburst floods, and movement heterogeneity of glaciers, Karakoram. *Glob. Planet. Change* 180, 100–116. doi: 10.1016/j.gloplacha.2019.05.004

Bhambri, R., Hewitt, K., Kawishwar, P., and Pratap, B. (2017). Surge-type and surge-modified glaciers in the Karakoram. *Sci. Rep.* 7:15391. doi: 10.1038/s41598-017-15473-8

Bolch, T., Menounos, B., and Wheate, R. (2010). Landsat-based inventory of glaciers in western Canada, 1985–2005. *Remote Sens. Environ.* 114, 127–137. doi: 10.1016/j.rse.2009.08.015

Breiman, L., Friedman, J. H., Olshen, R. A., and Stone, C. J. (1984). *Classification and Regression Trees*. (Belmont, CA: Wadsworth Inc). doi: 10.1201/9781315139470

Chand, M. B., and Watanabe, T. (2019). Development of Supraglacial Ponds in the Everest Region, Nepal, between 1989 and 2018. *Remote Sens.* 11:1058. doi: 10.3390/rs11091058

Chandera, G., Markham, B. L., and Helder, D. L. (2009). Summary of current radiometric calibration coefficients for Landsat MSS, TM, ETM+, and EO-1 ALI Sensors. *Remote Sens. Environ.* 113, 893–903. doi: 10.1016/j.rse.2009.01.007

Cook, S. J., Swift, D. A., Kirkbride, M. P., Knight, P. G., and Waller, R. I. (2020). The empirical basis for modelling glacial erosion rates. *Nat. Commun.* 11:759. doi: 10.1038/s41467-020-14583-8

Dehecq, A., Gourmelen, N., Gardner, A. S., Brun, F., Goldberg, D., Nienow, P. W., et al. (2018). Twenty-first century glacier slowdown driven by mass loss in High Mountain Asia. *Nat. Geosci.* 12, 22–27. doi: 10.1038/s41561-018-0271-9

Deline, P., Gruber, S., Delaloye, R., Fischer, L., Geertsema, M., Giardino, M., et al. (2015). "Ice loss and slope stability in high-mountain regions, in *Snow and Ice-Related Hazards, Risks and Disasters*. eds W. Haeberli, and C. Whiteman (Amsterdam: Elsevier), 521–561. doi: 10.1016/b978-0-12-394849-6.00015-9

Dong, J., Xiao, X., Menarguez, M. A., Zhang, G., Qin, Y., Thau, D., et al. (2016). Mapping paddy rice planting area in northeastern Asia with Landsat 8 images, phenology-based algorithm and Google Earth Engine. *Remote Sens. Environ.* 185, 142–154. doi: 10.1016/j.rse.2016.02.016

Dozier, J. (1989). Spectral signature of Alpine snow cover from the Landsat thematic mapper. *Remote Sens. Environ.* 28, 9–22. doi: 10.1016/0034-4257(89)90101-6

Dubey, S., and Goyal, M. K. (2020). Glacial lake outburst flood hazard, downstream impact, and risk over the Indian Himalayas. *Water Resour. Res.* 56:e2019WR026533. doi: 10.1029/2019wr026533

Farinotti, D., Immerzeel, W. W., and Dehecq, A. (2020). Manifestations and mechanisms of the Karakoram glacier anomaly. *Nat. Geosci.* 13, 8–16. doi: 10.1038/s41561-019-0513-5

Frey, H., and Paul, F. (2012). On the suitability of the SRTM DEM and ASTER GDEM for the compilation of topographic parameters in glacier inventories. *Int. J. Appl. Earth Obs. Geoinf.* 18, 480–490. doi: 10.1016/j.jag.2011.09.020

Fugazza, D., Senese, A., Azzoni, R. S., Maugeri, M., Maragno, D., and Diolaiuti, G. A. (2019). New evidence of glacier darkening in the Ortles-Cevedale group from Landsat observations. *Glob. Planet. Change* 178, 35–45. doi: 10.1016/j.gloplacha.2019.04.014

Fyffe, C. L., Brock, B. W., Kirkbride, M. P., Black, A. R., Smiraglia, C., and Diolaiuti, G. (2019a). The impact of supraglacial debris on proglacial runoff and water chemistry. *J. Hydrol.* 576, 41–57. doi: 10.1016/j.jhydrol.2019.06.023

Fyffe, C. L., Brock, B. W., Kirkbride, M. P., Mair, D. W. F., Arnold, N. S., Smiraglia, C., et al. (2019b). Do debris-covered glaciers demonstrate distinctive

hydrological behaviour compared to clean glaciers? *J. Hydrol.* 570, 584–597. doi: 10.1016/j.jhydrol.2018.12.069

Gao, H., Zou, X., Wu, J., Zhang, Y., Deng, X., Hussain, S., et al. (2020). Post-20(th) century near-steady state of Batura Glacier: observational evidence of Karakoram Anomaly. *Sci. Rep.* 10:987. doi: 10.1038/s41598-020-57660-0

Gardelle, J., Berthier, E., Arnaud, Y., and Kääb, A. (2013). Region-wide glacier mass balances over the Pamir-Karakoram-Himalaya during 1999-2011. *Cryosphere* 7, 1263–1286. doi: 10.5194/tc-7-1263-2013

Garee, K., Chen, X., Bao, A., Wang, Y., and Meng, F. (2017). Hydrological modeling of the upper Indus Basin: a case study from a high-altitude glacierized catchment Hunza. *Water* 9:17. doi: 10.3390/w9010017

Garg, P. K., Shukla, A., and Jasrotia, A. S. (2019). On the strongly imbalanced state of glaciers in the Sikkim, eastern Himalaya, India. *Sci. Total Environ.* 691, 16–35. doi: 10.1016/j.scitotenv.2019.07.086

Gorelick, N., Hancher, M., Dixon, M., Ilyushchenko, S., Thau, D., and Moore, R. (2017). Google Earth Engine: planetary-scale geospatial analysis for everyone. *Remote Sens. Environ.* 202, 18–27. doi: 10.1016/j.rse.2017.06.031

Guo, H., Goodchild, M. F., and Annoni, A. (2020). *Manual of Digital Earth*. Singapore: Springer. doi: 10.1007/978-981-32-9915-3

Haeberli, W., Hallet, B., Arenson, L., Elconin, R., Humlum, O., Kääb, A., et al. (2006). Permafrost creep and rock glacier dynamics. *Permafr. Periglac. Process.* 17, 189–214. doi: 10.1002/ppp.561

Hambrey, M. J., Quincey, D. J., Glasser, N. F., Reynolds, J. M., Richardson, S. J., and Clemmens, S. (2008). Sedimentological, geomorphological and dynamic context of debris-mantled glaciers, Mount Everest (Sagarmatha) region, Nepal. *Quat. Sci. Rev.* 27, 2361–2389. doi: 10.1016/j.quascirev.2008.08.010

Hao, B., Ma, M., Li, S., Li, Q., Hao, D., Huang, J., et al. (2019). Land use change and climate variation in the three gorges reservoir catchment from 2000 to 2015 based on the Google Earth Engine. *Sensors* 19:2118. doi: 10.3390/s19092118

Hazel, J., Krutkramelis, K., Mooney, P., Tomschik, M., Gerow, K., Oakey, J., et al. (2016). High-resolution global maps of 21st-century forest cover change. *Science* 342, 850–853. doi: 10.1126/science.1244693

Herreid, S., and Pellicciotti, F. (2018). Automated detection of ice cliffs within supraglacial debris cover. *Cryosphere* 12, 1811–1829. doi: 10.5194/tc-12-1811-2018

Immerzeel, W. W., Pellicciotti, F., and Shrestha, A. B. (2012). Glaciers as a proxy to quantify the spatial distribution of precipitation in the Hunza Basin. *Mt. Res. Dev.* 32, 30–38. doi: 10.1659/MRD-JOURNAL-D-11-00097.1

Immerzeel, W. W., van Beek, L. P., and Bierkens, M. F. (2010). Climate change will affect the Asian water towers. *Science* 328, 1382–1385. doi: 10.1126/science.1183188

Janke, J. R., Bellisario, A. C., and Ferrando, F. A. (2015). Classification of debris-covered glaciers and rock glaciers in the Andes of central Chile. *Geomorphology* 241, 98–121. doi: 10.1016/j.geomorph.2015.03.034

Jassim, F. A. (2013). Kriging interpolation filter to reduce high density salt and pepper noise. *World Comput. Sci. Inf. Technol. J.* 3, 8–14.

Jiang, S., Nie, Y., Liu, Q., Wang, J., Liu, L., Hassan, J., et al. (2018). Glacier change, supraglacial debris expansion and glacial lake evolution in the Gyirong river basin, Central Himalayas, between 1988 and 2015. *Remote Sens.* 10:986. doi: 10.3390/rs10070986

Kaab, A., Berthier, E., Nuth, C., Gardelle, J., and Arnaud, Y. (2012). Contrasting patterns of early twenty-first-century glacier mass change in the Himalayas. *Nature* 488, 495–498. doi: 10.1038/nature11324

Khan, A., Naz, B. S., and Bowling, L. C. (2015). Separating snow, clean and debris covered ice in the Upper Indus Basin, Hindukush-Karakoram-Himalayas, using Landsat images between 1998 and 2002. *J. Hydrol.* 521, 46–64. doi: 10.1016/j.jhydrol.2014.11.048

Khan, A. A., Jamil, A., Hussain, D., Taj, M., Jabeen, G. and Malik, M. K. (2020). Machine-learning algorithms for mapping debris-covered glaciers: the hunza basin case study. *IEEE Access* 8, 12725–12734. doi: 10.1109/access.2020.2965768

Kindermann, G. E., McCallum, I., Fritz, S., and Obersteiner, M. (2008). A global forest growing stock, biomass and carbon map based on FAO statistics. *Silva Fenn.* 42, 387–396. doi: 10.14214/sf.244

Kraaijenbrink, P. D. A., Bierkens, M. F. P., Lutz, A. F., and Immerzeel, W. W. (2017). Impact of a global temperature rise of 1.5 degrees celsius on Asia's glaciers. *Nature* 549, 257–260. doi: 10.1038/nature23878

Kraaijenbrink, P. D. A., Shea, J. M., Pellicciotti, F., Jong, S. M. D., and Immerzeel, W. W. (2016). Object-based analysis of unmanned aerial vehicle imagery to map and characterise surface features on a debris-covered glacier. *Remote Sens. Environ.* 186, 581–595. doi: 10.1016/j.rse.2016.09.013

Lary, D. J., Alavi, A. H., Gandomi, A. H., and Walker, A. L. (2017). Machine learning in geosciences and remote sensing. *Geosci. Front.* 7, 3–10. doi: 10.1016/j.gsf.2015.07.003

Liaw, A., and Wiener, M. (2002). Classification and regression by randomForest. *R News* 2, 18–22.

Lippl, S., Vijay, S., and Braun, M. (2018). Automatic delineation of debris-covered glaciers using InSAR coherence derived from X-, C- and L-band radar data: a case study of Yazgyl Glacier. *J. Glaciol.* 64, 811–821. doi: 10.1017/jog.2018.70

Liu, S., Yao, X., Shangguan, D., Guo, W., Wei, J., Xu, J., et al. (2015). The contemporary glaciers in China based on the second Chinese glacier inventory. *Acta Geogr. Sin.* 70, 3–16. doi: 10.11821/dlxb201501001

Lynch, C. M., Barr, I. D., Mullan, D., and Ruffell, A. (2016). Rapid glacial retreat on the Kamchatka Peninsula during the early 21st century. *Cryosphere* 10, 1809–1821. doi: 10.5194/tc-10-1809-2016

Maxwell, A. E., Warner, T. A., and Fang, F. (2018). Implementation of machine-learning classification in remote sensing: an applied review. *Int. J. Remote Sens.* 39, 2784–2817. doi: 10.1080/01431161.2018.1433343

Midekisa, A., Holl, F., Savory, D. J., Andrade-Pacheco, R., Gething, P. W., Bennett, A., et al. (2017). Mapping land cover change over continental Africa using Landsat and Google Earth Engine cloud computing. *PLoS One* 12:e0184926. doi: 10.1371/journal.pone.0184926

Miles, E. S., Willis, I. C., Arnold, N. S., Steiner, J., and Pellicciotti, F. (2016). Spatial, seasonal and interannual variability of supraglacial ponds in the Langtang Valley of Nepal, 1999–2013. *J. Glaciol.* 63, 88–105. doi: 10.1017/jog.2016.120

Ming, J., Du, Z., Xiao, C., Xu, X., and Zhang, D. (2012). Darkening of the mid-Himalaya glaciers since 2000 and the potential causes. *Environ. Res. Lett.* 7:014021. doi: 10.1088/1748-9326/7/1/014021

Mölg, N., Bolch, T., Rastner, P., Strozzi, T., and Paul, F. (2018). A consistent glacier inventory for Karakoram and Pamir derived from Landsat data: distribution of debris cover and mapping challenges. *Earth Syst. Sci. Data* 10, 1807–1827. doi: 10.5194/essd-10-1807-2018

Mölg, N., Bolch, T., Walter, A., and Vieli, A. (2019). Unravelling the evolution of Zmuttgletscher and its debris cover since the end of the Little Ice Age. *Cryosphere* 13, 1889–1909. doi: 10.5194/tc-13-1889-2019

Nakawo, M., Iwata, S., Watanabe, O., and Yoshida, M. (1986). Processes which distribute supraglacial debris on the Khumbu glacier, Nepal Himalaya. *Ann. Glaciol.* 8, 129–131. doi: 10.3189/S0260305500001294

Ng, H.-F. (2006). Automatic thresholding for defect detection. *Pattern Recognit. Lett.* 27, 1644–1649. doi: 10.1016/j.patrec.2006.03.009

Nicholson, L., and Benn, D. I. (2006). Calculating ice melt beneath a debris layer using meteorological data. *J. Glaciol.* 52, 463–470. doi: 10.3189/172756506781828584

Nuimura, T., Sakai, A., Taniguchi, K., Nagai, H., Lamsal, D., Tsutaki, S., et al. (2015). The GAMDAM glacier inventory: a quality-controlled inventory of Asian glaciers. *Cryosphere* 9, 849–864. doi: 10.5194/tc-9-849-2015

Østrem, G. (1959). Ice melting under a thin layer of moraine, and the existence of ice cores in moraine ridges. *Geogr. Ann.* 41, 228–230. doi: 10.2307/4626805

Patel, A., Prajapati, R., Dharpure, J. K., Mani, S., and Chauhan, D. (2019). Mapping and monitoring of glacier areal changes using multispectral and elevation data: a case study over Chhota-Shigri glacier. *Earth Sci. Inform.* 12, 489–499. doi: 10.1007/s12145-019-00388-x

Paul, F., Barrand, N. E., Baumann, S., Berthier, E., Bolch, T., Casey, K., et al. (2017). On the accuracy of glacier outlines derived from remote-sensing data. *Ann. Glaciol.* 54, 171–182. doi: 10.3189/2013AoG63A296

Paul, F., Bolch, T., Kääb, A., Nagler, T., Nuth, C., Scharrer, K., et al. (2013). The glaciers climate change initiative: methods for creating glacier area, elevation change and velocity products. *Remote Sens. Environ.* 162, 408–426. doi: 10.1016/j.rse.2013.07.043

Paul, F., Huggel, C., and Kääb, A. (2004). Combining satellite multispectral image data and a digital elevation model for mapping debris-covered glaciers. *Remote Sens. Environ.* 89, 510–518. doi: 10.1016/j.rse.2003.11.007

Pekel, J. F., Cottam, A., Gorelick, N., and Belward, A. S. (2016). High-resolution mapping of global surface water and its long-term changes. *Nature* 540, 418–422. doi: 10.1038/nature20584

Pfeffer, W. T., Arendt, A. A., Bliss, A., Bolch, T., Cogley, J. G., Gardner, A. S., et al. (2014). The Randolph Glacier Inventory: a globally complete inventory of glaciers. *J. Glaciol.* 60, 537–552. doi: 10.3189/2014JoG13J176

Quincey, D. J., Braun, M., Glasser, N. F., Bishop, M. P., Hewitt, K., and Luckman, A. (2011). Karakoram glacier surge dynamics. *Geophys. Res. Lett.* 38:L18504. doi: 10.1029/2011gl049004

Qureshi, M. A., Yi, C., Xu, X., and Li, Y. (2017). Glacier status during the period 1973-2014 in the Hunza Basin, Western Karakoram. *Quat. Int.* 444, 125–136. doi: 10.1016/j.quaint.2016.08.029

Racoviteanu, A., and Williams, M. W. (2012). Decision tree and texture analysis for mapping debris-covered glaciers in the Kangchenjunga area, Eastern Himalaya. *Remote Sens.* 4, 3078–3109. doi: 10.3390/rs4103078

Rastner, P., Bolch, T., Notarnicola, C., and Paul, F. (2014). A comparison of pixel- and object-based glacier classification with optical satellite images. *IEEE J. Sel. Top. Appl. Earth Observ. Remote Sens.* 7, 853–862. doi: 10.1109/JSTARS.2013.2274668

Raup, B., Racoviteanu, A., Khalsa, S. J. S., Helm, C., Armstrong, R., and Arnaud, Y. (2007). The GLIMS geospatial glacier database: a new tool for studying glacier change. *Glob. Planet. Change* 56, 101–110. doi: 10.1016/j.gloplacha.2006.07.018

Reinthaler, J., Paul, F., Granados, H. D., Rivera, A., and Huggel, C. (2019). Area changes of glaciers on active volcanoes in Latin America between 1986 and 2015 observed from multi-temporal satellite imagery. *J. Glaciol.* 65, 542–556. doi: 10.1017/jog.2019.30

RGI Consortium (2017). *Randolph Glacier Inventory – A Dataset of Global Glacier Outlines: Version 6.0: Technical Report, Global Land Ice Measurements from Space*. Colorado: Digital Media.

Robson, B. A., Nuth, C., Dahl, S. O., Hölbling, D., Strozzi, T., and Nielsen, P. R. (2015). Automated classification of debris-covered glaciers combining optical, SAR and topographic data in an object-based environment. *Remote Sens. Environ.* 170, 372–387. doi: 10.1016/j.rse.2015.10.001

Rowan, A. V., Egholm, D. L., Quincey, D. J., and Glasser, N. F. (2015). Modelling the feedbacks between mass balance, ice flow and debris transport to predict the response to climate change of debris-covered glaciers in the Himalaya. *Earth Planet. Sci. Lett.* 430, 427–438. doi: 10.1016/j.epsl.2015.09.004

Sahu, R., and Gupta, R. D. (2018). Conceptual framework of combined pixel and object-based method for delineation of debris-covered glaciers. *ISPRS Ann. Photogramm. Remote Sens. Spat. Inf. Sci.* IV-5, 173–180. doi: 10.5194/isprs-annals-IV-5-173-2018

Salerno, F., Thakuri, S., Tartari, G., Nuimura, T., Sunako, S., Sakai, A., et al. (2017). Debris-covered glacier anomaly? Morphological factors controlling changes in the mass balance, surface area, terminus position, and snow line altitude of Himalayan glaciers. *Earth Planet. Sci. Lett.* 471, 19–31. doi: 10.1016/j.epsl.2017.04.039

Scherler, D., Bookhagen, B., and Strecker, M. R. (2011). Spatially variable response of Himalayan glaciers to climate change affected by debris cover. *Nat. Geosci.* 4, 156–159. doi: 10.1038/ngeo1068

Scherler, D., Wulf, H., and Gorelick, N. (2018). Global assessment of supraglacial debris-cover extents. *Geophys. Res. Lett.* 45, 798–11,805. doi: 10.1029/2018gl080158

Serra, J., and Vincent, L. (1992). An overview of morphological filtering. *Circuits Syst. Signal Process.* 11, 47–108. doi: 10.1007/bf01189221

Shrestha, M., Koike, T., Hirabayashi, Y., Xue, Y., Wang, L., Rasul, G., et al. (2015). Integrated simulation of snow and glacier melt in water and energy balance-based, distributed hydrological modeling framework at Hunza River Basin of Pakistan Karakoram region. *J. Geophys. Res. Atmos.* 120, 4889–4919. doi: 10.1002/2014jd022666

Shukla, A., and Garg, P. K. (2019). Evolution of a debris-covered glacier in the western Himalaya during the last four decades (1971–2016): a multiparametric assessment using remote sensing and field observations. *Geomorphology* 341, 1–14. doi: 10.1016/j.geomorph.2019.05.009

Shukla, A., and Yousuf, B. (2016). Evaluation of multisource data for glacier terrain mapping: a neural net approach. *Geocarto Int.* 32, 569–587. doi: 10.1080/10106049.2016.1161078

Singh, V., and Goyal, M. K. (2018). An improved coupled framework for Glacier classification: an integration of optical and thermal infrared remote-sensing bands. *Int. J. Remote Sens.* 39, 6864–6892. doi: 10.1080/01431161.2018.1468104

Singh, V. P., Singh, P., and Haritashya, U. K. (2011). *Encyclopedia of Snow, Ice and Glaciers*. Berlin: Springer. doi: 10.1007/978-90-481-2642-2

Suykens, J. A. K., and Vandewalle, J. (1999). Least squares support vector machine classifiers. *Neural Process. Lett.* 9, 293–300.

Tahir, A. A., Chevallier, P., Arnaud, Y., Neppel, L., and Ahmad, B. (2011). Modeling snowmelt-runoff under climate scenarios in the Hunza River basin, Karakoram Range, Northern Pakistan. *J. Hydrol.* 409, 104–117. doi: 10.1016/j.jhydrol.2011.08.035

Tielidze, L. G., Bolch, T., Wheate, R. D., Kutuzov, S. S., Lavrentiev, I. I., and Zemp, M. (2020). Supra-glacial debris cover changes in the Greater Caucasus from 1986 to 2014. *Cryosphere* 14, 585–598. doi: 10.5194/tc-14-585-2020

Tipper, E. T., Lemarchand, E., Hindshaw, R. S., Reynolds, B. C., and Bourdon, B. (2012). Seasonal sensitivity of weathering processes: hints from magnesium isotopes in a glacial stream. *Chem. Geol.* 312-313, 80–92. doi: 10.1016/j.chemgeo.2012.04.002

Vezzola, L. C., Diolaiuti, G. A., D'Agata, C., Smiraglia, C., and Pelfini, M. (2016). Assessing glacier features supporting supraglacial trees: a case study of the Miage debris-covered Glacier (Italian Alps). *Holocene* 26, 1138–1148. doi: 10.1177/0959683616632883

Wang, P., Li, Z., Li, H., Wang, W., Wu, L., Zhang, H., et al. (2018). Recent evolution in extent, thickness, and velocity of Haxilegen glacier no. 51, Kuytun River Basin, Eastern Tianshan Mountains. *Arct. Antarct. Alp. Res.* 48, 241–252. doi: 10.1657/aaar0014-079

Wang, R., Liu, S., Shangguan, D., Radić, V., and Zhang, Y. (2019a). Spatial heterogeneity in glacier mass-balance sensitivity across High Mountain Asia. *Water* 11:776. doi: 10.3390/w11040776

Wang, Y., Ma, J., Xiao, X., Wang, X., Dai, S., and Zhao, B. (2019b). Long-term dynamic of Poyang lake surface water: a mapping work based on the Google Earth Engine cloud platform. *Remote Sens.* 11:313. doi: 10.3390/rs11030313

Wouters, B., Gardner, A. S., and Moholdt, G. (2019). Global glacier mass loss during the GRACE satellite mission (2002-2016). *Front. Earth Sci.* 7:96. doi: 10.3389/feart.2019.00096

Wu, K., Liu, S., Jiang, Z., Xu, J., Wei, J., and Guo, W. (2018). Recent glacier mass balance and area changes in the Kangri Karpo Mountains from DEMs and glacier inventories. *Cryosphere* 12, 103–121. doi: 10.5194/tc-12-103-2018

Yang, Y., Li, Z., Huang, L., Tian, B., and Chen, Q. (2016). Extraction of glacier outlines and water-eroded stripes using high-resolution SAR imagery. *Int. J. Remote Sens.* 37, 1016–1034. doi: 10.1080/01431161.2016.1145365

Yang, Z. (1995). Glacier meltwater runoff in China and its nourishment to river. *Chin. Geogr. Sci.* 5, 66–76. doi: 10.1007/bf02664344

Yousuf, B., Shukla, A., Arora, M. K., Bindal, A., and Jasrotia, A. S. (2020). On drivers of subpixel classification accuracy—an example from glacier facies. *IEEE J. Sel. Top. Appl. Earth Observ. Remote Sens.* 13, 601–608. doi: 10.1109/jstars.2019.2955955

Zemp, M., Huss, M., Thibert, E., Eckert, N., McNabb, R., Huber, J., et al. (2019). Global glacier mass changes and their contributions to sea-level rise from 1961 to 2016. *Nature* 568, 382–386. doi: 10.1038/s41586-019-1071-0

Zhang, J., Jia, L., Menenti, M., and Hu, G. (2019). Glacier facies mapping using a machine-learning algorithm: the Parlung Zangbo basin case study. *Remote Sens.* 11:452. doi: 10.3390/rs11040452

Zhang, Z., Liu, S., Wei, J., Xu, J., Guo, W., Bao, W., et al. (2016). Mass change of glaciers in Muztag Ata-Kongur Tagh, Eastern Pamir, China from 1971/76 to 2013/14 as Derived from Remote Sensing Data. *PLoS One* 11:e0147327. doi: 10.1371/journal.pone.0147327

Conflict of Interest: The authors declare that the research was conducted in the absence of any commercial or financial relationships that could be construed as a potential conflict of interest.

Copyright © 2020 Xie, Liu, Wu, Zhu, Gao, Qi, Duan, Saifullah and Tahir. This is an open-access article distributed under the terms of the Creative Commons Attribution License (CC BY). The use, distribution or reproduction in other forums is permitted, provided the original author(s) and the copyright owner(s) are credited and that the original publication in this journal is cited, in accordance with accepted academic practice. No use, distribution or reproduction is permitted which does not comply with these terms.

frontiers in Earth Science

ORIGINAL RESEARCH
published: 07 August 2020
doi: 10.3389/feart.2020.00250

Glaciological and Meteorological Conditions at the Chinese Taishan Station, East Antarctica

Xueyuan Tang[1], Jingxue Guo[1], Yinke Dou[2], Yuzhong Zhang[1,2], Siyuan Cheng[1,3], Kun Luo[1,3], Lejiang Yu[1], Xiangbin Cui[1], Lin Li[1], Shengkai Zhang[4] and Bo Sun[1]*

[1] Polar Research Institute of China, Shanghai, China, [2] College of Electrical and Power Engineering, Taiyuan University of Technology, Taiyuan, China, [3] College of Geo-Exploration Science and Technology, Jilin University, Changchun, China, [4] Chinese Antarctic Center of Surveying and Mapping, School of Geodesy and Geomatics, Wuhan University, Wuhan, China

The glacio-meteorological characteristics of Princess Elizabeth Land in East Antarctica are poorly known due to a lack of measurement. This is problematic given the importance of this area for understanding ice sheet dynamics and climate change. We present a comprehensive approach (including field surveys, reanalysis data, remote sensing, and ice flow models) to investigate the glaciological and meteorological conditions in the vicinity of the new Chinese Taishan Station (73.864°S, 76.974°E) in Princess Elizabeth Land. We collected the datasets of satellite-derived ice surface velocities, surface mass balance, and wind field; mapped the ice thickness and internal layers around the Taishan Station site; and constructed profiles of the surface snow temperature and snow density. Also, we used a transient 1-D thermodynamical model to simulate the age of ice and the basal temperature with surface meteorological data and subglacial topography as boundary conditions. These investigations showed that Taishan Station is subject to a relatively high wind velocity, low temperatures (about −36°C), and simple ice flow. The well-behaved internal layer stratigraphy implies that the ice flow of Taishan Station has been relatively stable, possibly for a long time. The fact that the internal layers are conformal with bed topography—there is a relatively old basal age from ice modeling—and that the site lies over a bed depression filled with ice 1,900 m thick, suggests that Taishan Station may be a good location for obtaining undisturbed old ice at depth. The combination of glacio-meteorological parameters suggests that Taishan Station is a potential drill site for the Chinese Antarctic Research Expedition and an ideal logistical support location for proposed scientific field activities in the East Antarctic ice sheet (e.g., Dome A, Grove Mountains, and Princess Elizabeth Land).

Keywords: Chinese Taishan Station, glaciological and meteorological conditions, internal layer, mass balance, age-depth profile

OPEN ACCESS

Edited by:
Tong Zhang,
Los Alamos National Laboratory (DOE), United States

Reviewed by:
Masaki Kanao,
National Institute of Polar Research, Japan
Alexey Ekaykin,
Arctic and Antarctic Research Institute, Russia

****Correspondence:***
Xueyuan Tang
tangxueyuan@pric.org.cn

Specialty section:
This article was submitted to Cryospheric Sciences, a section of the journal Frontiers in Earth Science

Received: *03 January 2020*
Accepted: *08 June 2020*
Published: *07 August 2020*

Citation:
Tang X, Guo J, Dou Y, Zhang Y, Cheng S, Luo K, Yu L, Cui X, Li L, Zhang S and Sun B (2020) Glaciological and Meteorological Conditions at the Chinese Taishan Station, East Antarctica. Front. Earth Sci. 8:250. doi: 10.3389/feart.2020.00250

INTRODUCTION

The Antarctic ice sheet has been losing ice mass to glacier dynamic thinning in recent decades, and the mass losses in 2012–2016 were likely greater than those from 2002 to 2011 (Meredith et al., 2019). Surface and subglacial processes transport mass and energy underneath continental ice sheets and influence ice sheet structure. Changes in surface and basal conditions are responsible

for a wide range of dynamic ice sheet behaviors (Cuffey and Paterson, 2010). However, the extent to which the mass loses is affected by the dynamic processes on the surface and under the ice sheet remains uncertain.

Princess Elizabeth Land (64.93°–90°S, 73.58°–87.72°E) is located in East Antarctica with an area of about 4.37 km × 10^5 km and an overall fan shape extending outwards from the South Pole. It is bounded in the west by the Amery ice shelf, in the southwest by the Lambert glacier, in the east by Wilhelm II Land, and in the south by Dome A. The Lambert basin-Amery ice shelf is one of the largest glacial drainage systems in Antarctica (**Figure 1**), and the impact of Princess Elizabeth Land in this system is clearly significant. However, at present, little is known about the local and large-scale surface glaciological conditions and meteorological parameters (Li et al., 2009), especially subglacial topography and dynamics in this region (Fretwell et al., 2013; Tang et al., 2016).

The Chinese Taishan Station (**Figures 1**, **2**) was established during the 30th Chinese Antarctic Research Expedition (CHINARE 30) in the middle of Princess Elizabeth Land in East Antarctica in 2013/2014. The station is about 522 km from Zhongshan Station and 715 km from Kunlun Station at Dome A (Tang et al., 2016). As the Chinese component of the ITASE (International Trans-Antarctic Scientific Expedition), Princess Elizabeth Land was first investigated by the CHINARE in the 1996/1997 austral summer (Qin et al., 2000). The CHINARE transect goes from Zhongshan Station to Kunlun Station at Dome A, the summit of the East Antarctic ice sheet, with a distance of ∼1,250 km (**Figure 3**). Taishan Station is located at the transect.

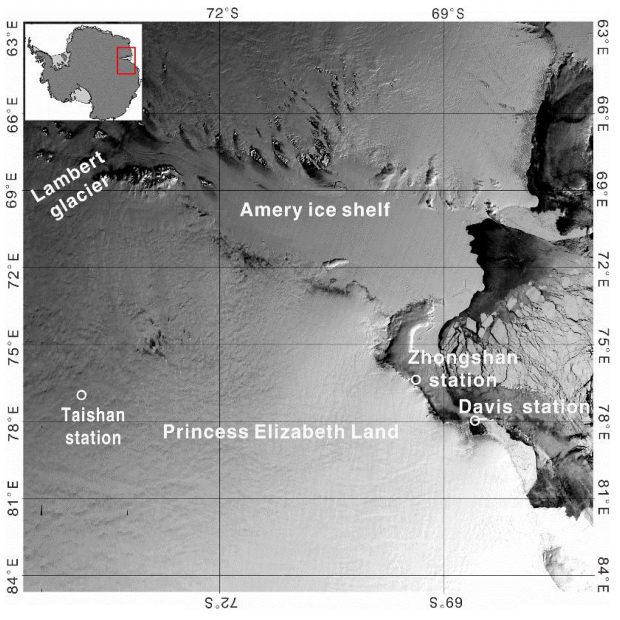

FIGURE 1 | The Moderate Resolution Imaging Spectroradiometer (MODIS) image of the new Chinese Taishan Station (73°51′50″S, 76°58′28″E), including the drainage system of the Lambert glacier–Amery ice shelf, Princess Elizabeth Land, the Chinese Zhongshan Station, and the Australian Davis Station.

FIGURE 2 | Aerial view of the Taishan Station site, January 2013.

Along the transect, some glaciological and meteorological parameters have been collected, e.g., shallow snow stratigraphy, snow accumulation rate (Ren et al., 2001), ice velocity (Zhang et al., 2008), surface mass balance (Ding et al., 2015), shallow ice cores (Li et al., 2013; Ding et al., 2015), chemical elements, and particles (Li et al., 2009, 2014). By summarizing these published data, we can obtain a better understanding of the basic characteristics of environmental information. Zhang et al. (2008) showed that the ice of Taishan Station flows downward into the Amery ice shelf along the altitude gradient with a surface speed of ∼20 m $year^{-1}$. Ding et al. (2011) measured the surface snow temperature at Taishan Station. Ma et al. (2010) measured the annual average wind speed (∼8 m s^{-1}) near the station site. Tang et al. (2016) mapped a radar profile of the internal layer, and suggested that the ice sheet under Taishan Station may have undergone a complex deposition process. Wu et al. (2017) found that the intensity of optical turbulence in the near-surface atmosphere of Taishan Station has obvious diurnal variation characteristics, which are stronger at night than during the day, and the minimum values appear around sunrise and sunset. However, in addition to the few parameters mentioned above, due to the lack of systematic research around the site, we have little knowledge of the glaciological and meteorological characteristics in the area of Taishan Station.

Here, we collect and analyze the data from field observations by CHINARE and present the glaciological and meteorological results obtained at Taishan Station. The glacio-meteorological parameters allow us to establish the fundamental environment characteristics at the site.

SURFACE MASS BALANCE AND ICE FLOW

Surface mass balance is usually used to represent snow accumulation on the Antarctic ice sheet. Along the transect from Zhongshan to Dome A, CHINARE have installed a series of stakes, which were used to measure the surface mass balance during the expeditions in 1999, 2005, 2008, 2011, and 2013. Ding et al. (2011, 2015) discussed the temporal trend of the surface mass balance based on the morphological, geographical, and meteorological conditions of the CHINARE transect. Their studies showed that the average surface mass balance values

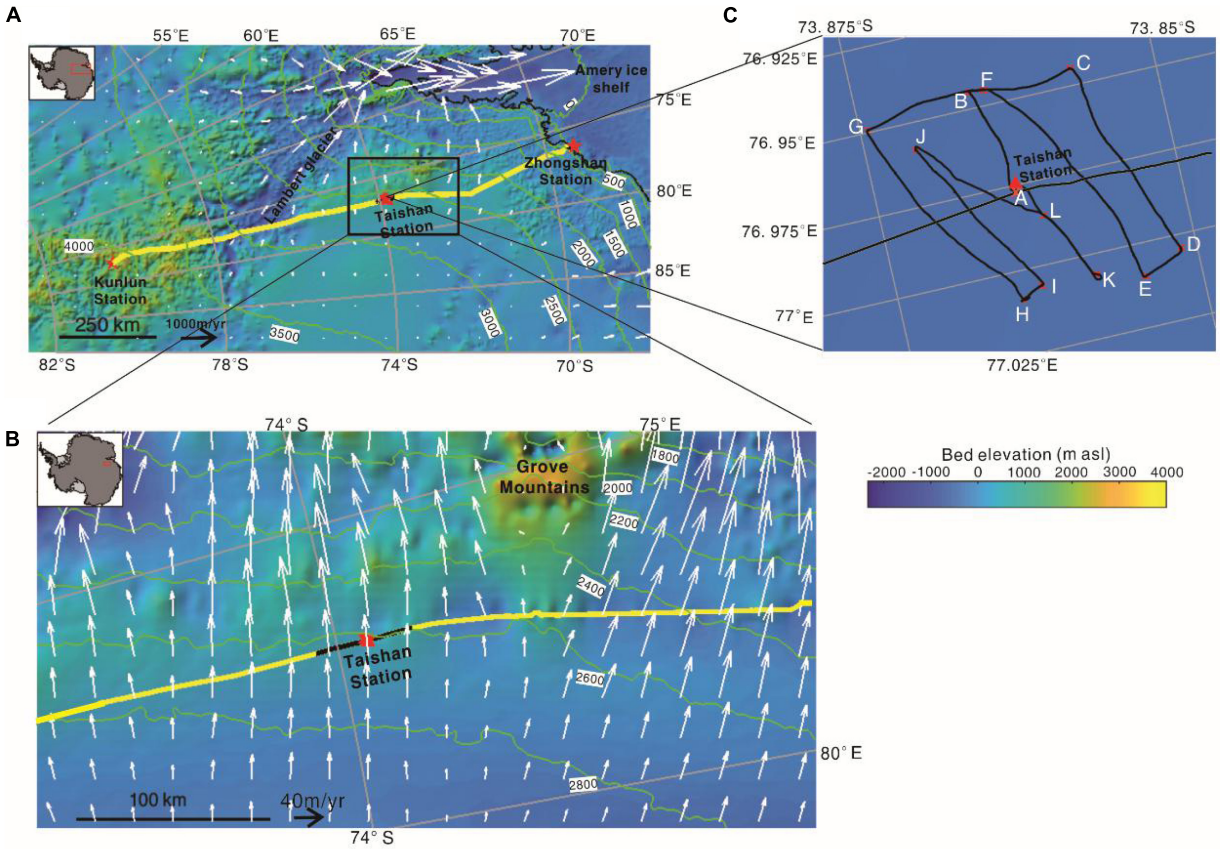

FIGURE 3 | (A) Area map showing the transect routes from Zhongshan to Dome A, East Antarctica. **(B)** Location of Taishan Station (the red triangle) and orientation of the radar line (black) around the Taishan Station site. **(C)** Radar profiles in a 2 km × 2 km square area centered on the Taishan Station. The yellow line denotes the radar line from Zhongshan Station to Dome A. Bed elevation (background image), surface elevation (green line), and grounding line (black line) are from Bedmap2 (Fretwell et al., 2013; Tang et al., 2016; Greene et al., 2017). The white arrows represent the vector of the surface ice velocity which was derived from the interferometric synthetic aperture radar (InSAR) data (Rignot et al., 2011; Shepherd et al., 2018).

in 1999–2013 in a section with a length of 300 km covering the Taishan Station site was 65.5 kg m^{-2} a^{-1}, and wind-driven processes had a great impact on surface mass balance.

Here, the regional surface ice velocity data are collected in the satellite-derived MEaSUREs database from the National Snow and Ice Data Center (NSIDC; Rignot et al., 2011; Shepherd et al., 2018). The ice flow of Princess Elizabeth Land and Dome A of the East Antarctic ice sheet moves toward the Lambert glacier and finally enters the Amery ice shelf (**Figure 3A**). The ice flow directions along a radar line across the Taishan Station site are approximately perpendicular to the ice surface elevation contours (**Figure 3B**), and the ice velocities are 12.5–18 m $year^{-1}$. The average ice flow speed near Taishan Station is 16 m $year^{-1}$ (**Figure 3C**).

RADAR SURVEYS

Previous radar measurements along Zhongshan Station to Dome A were performed in 2004/2005 using an ice penetrating radar system with a center frequency of 60 MHz (Cui et al., 2010; Tang et al., 2011), which produced detailed maps of the ice thickness and bed topography along the traverse (close to the Taishan Station site) (**Figure 3C**). Subsequent radar measurements were made in 2012/2013 on an ice-penetrating radar (IPR) traverse from Zhongshan Station (69.449°S, 76.311°E) to Dome A covering Taishan Station (**Figure 3A**). The main technical parameters of deep IPR are given in **Table 1**. The ice-penetrating radar was designed as a linear frequency modulated pulse system by the Institute of Electronics of the Chinese Academy of Sciences with a center frequency of 150 MHz and a bandwidth of 100 MHz. For deep ice measurements over 3,000 m, the radar operates with long 8 μs chirped pulses, a pulse repetition frequency (PRF) of 8 kHz, and a peak transmitting power of 500 W. The data acquisition system digitizes the received signal at a sampling frequency of 500 MHz and simultaneously acquires the GPS signal. Two logarithmic period antennas were mounted 2 m above the ice surface on the specialized versatile mobile observation cabin. The spacing between the antennas was 20–30 dB. The specialized cabin was carried by a snow vehicle at a speed of 12–15 km h^{-1} (Tang et al., 2016; Liu et al., 2018). To evaluate the subglacial

TABLE 1 | The parameters of the ice-penetrating radar.

Parameter name	Value	Units
Radar style	Linear frequency modulated (LFM) pulse	–
Antenna	Log-periodical	–
Center frequency	150	MHz
Transmitted pulse duration	2/4/8	μs
Signal bandwidth	100	MHz
Peak power	500	W
PRF	8	kHz
Sampling frequency	500	MHz
Dynamic range	>110	dB
Antenna gain	9	dBi
Antenna beamwidth	60	deg

PRF, pulse repetition frequency.

internal stratigraphy at Taishan Station, we selected a radar profile of about 50 km on the cross section near Taishan Station, which is from (73.7228°S, 76.9671°E) to (74.1683°S, 77.0075°E) (**Figure 3B**). We also selected four radar profiles (G–H, B–K, C–D, and C–G) in a 2 km × 2 km square area centered around Taishan Station (**Figure 3C**).

For radar data processing, we first removed 2,000 sampling points of the raw data, which is the blind area caused by the receiver-blanking switch in order to avoid data receiver saturation. Then, the processes, including eliminating redundant traces, coherently stacking 150 traces, pulse compression, and mean filtering, were conducted. Finally, the conversion of time to depth was used to estimate the ice thickness by the electromagnetic wave speed of 0.168 m ns^{-1} within the ice sheet (Zhang et al., 2006).

Ice Thickness and Bed Topography

High-resolution ice radar profiles can effectively evaluate the subglacial topography, ice thickness, and internal structure of ice sheets (**Figures 4**, **5**). Those profiles allowed us to establish the fundamental glaciological characteristics of the ice surface and bedrock in the vicinity of Taishan Station (**Figures 4A**, **5A**). **Figure 4A** shows a profile through Taishan Station. The profile reveals that the ice surface is flat, with an elevation of 2,620 m a.s.l. at Taishan Station. In the first 25 km, the bed elevation difference of the undulating subglacial topography is about 300 m, and the ice thickness is between 1,400–1,700 m. Within 25–50 km, the bed elevation is between 600 and 900 m a.s.l., and the average ice thickness is 1,900 m (**Figure 5B**). Along the radar profile, the ice-surface speed is about 15 m $year^{-1}$ (**Figure 5C**), which is in good agreement with the previous estimation from stake observations (Zhang et al., 2008). The average ice thickness of the echo free zone is about 400 m, where echo free zone is a layer in the lowest hundreds of meters above bedrock more or less free of radar echoes. Around the station site, the variation of the ice thickness along the profiles is between 1,860 and 1,953 m, and the bed topography varies from 664 to 773 m a.s.l. and is about 750 m a.s.l. at the Taishan Station site, revealing a subglacial mountainous landscape. Compared with the previous study of the ice thickness and bed elevation, Tang et al. (2016) used a ground-based radar dataset over this area from 2004/2005 to 2012/2013 and GPS measurements to establish a two-dimensional map of ice thickness and bed topography. However, due to the poor denoising of the radar data, the radar profiles only show part of the subglacial bedrock and fail to identify the internal layer around Taishan Station. Therefore, they can only obtain a low-resolution map of the ice thickness by interpolation.

Internal Layers

Internal layers recorded in radar images can provide additional local information about bed, surface and internal reflections, and inform ice-flow modeling (Cavitte et al., 2016). The profile reveals that the ice surface is flat (**Figure 5A**), and the ice deformation pattern of the internal layer changes with the subglacial bed topography. As the internal layer is closer to the surface, the amplitude of the undulation gradually decreases. Excluding the blind zone data that is cut off near the ice surface, we can pick up about 60% of the visible isochronic layers. **Figure 4B** shows a bright isochronous layer with a minimum thickness interval of 5 m between adjacent layers. It can be seen from the four profiles in **Figure 4C** that the topography near Taishan Station is flat and the internal layering structure is intact. The ice thickness is 1,900 m, and the thickness of the visible isochronous layers is about 1,150 m. The bright layers of the radar profile are important for future ice core age estimation.

Modeling the Age–Depth Relationship and Ice Temperature

The dynamics process of the ice flow below Taishan Station is unknown. To determine the temperature–depth profile and the age distribution, we use different flux shape functions to simulate the ice flow. In principle, it is assumed that the mass balance of ice flow is given based on the incompressibility condition. The flux shape function depends on a non-dimensional vertical coordinate and is the combination of one sliding term and one deformation term (Parrenin et al., 2007). It can be expressed in the following form:

$$\omega(\xi) = s\xi + (1-\xi)\,\omega_D\,(\xi) \tag{1}$$

$$\omega_D(\xi) = \frac{1}{n+1}\left[(1-\xi)^{n+2} + (n+2)\xi - 1\right] \tag{2}$$

where $\omega_D(\xi)$ is the deformation term, $\xi = \frac{z-B}{H}$ is the normalized vertical coordinate (oriented toward the ice surface, $\xi = 0$ denotes the bedrock), B is bedrock elevation, H is the ice thickness elevation, z is the vertical coordinate of the ice particle, and n is the exponent of Glen Law.

Assuming the basal ice is not melting, the flux shape function approximately represents the vertical compression, which describes the ratio of the layer thickness to its initial thickness at the surface (Parrenin et al., 2007). We can calculate the age of the ice by integrating along the particle trajectories of the vertical compression. The age at ξ (at depth z) is given by

$$A(\xi) = \int_{\xi}^{1} \frac{H}{\omega(x)a(x)}dx \tag{3}$$

where $a(x)$ is the accumulation.

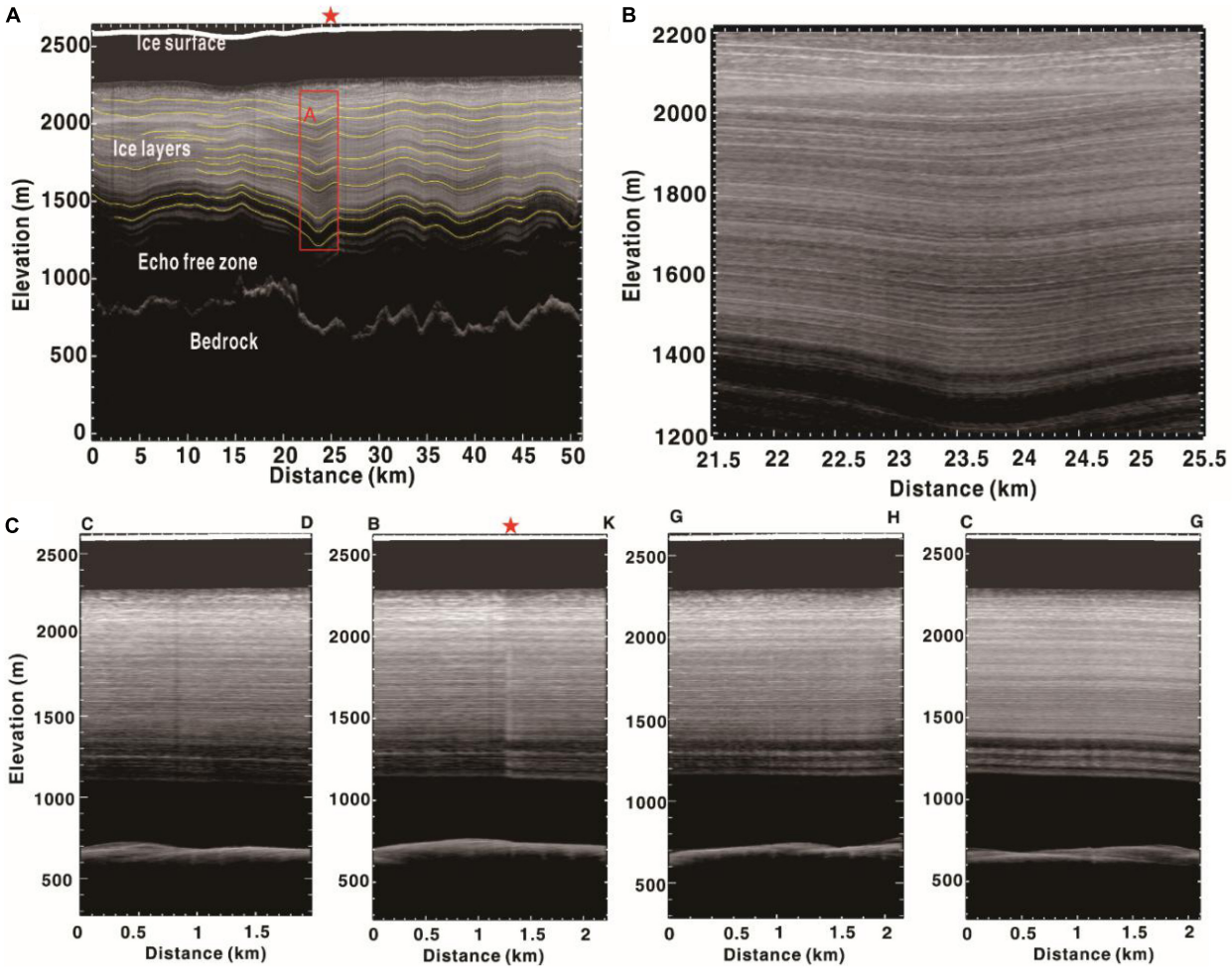

FIGURE 4 | Radargrams of ice-penetrating radar from CHINARE (Chinese Antarctic Research Expedition) 29. The red star marks the position of Taishan Station. **(A)** Profile of high resolution (150 MHz) corresponding to the black line though Taishan Station in **Figure 3B**. **(B)** Radar profile of the selected red rectangles in **(A)**. **(C)** Radar profiles around Taishan Station (corresponding to **Figure 3C**).

In the following text, we use three flux shape functions to estimate the temperature-depth and age-depth relationship. The three functions are described as (1) the exponent of the value $n = 3$ in Glen's flow where the ice fabric was induced by isothermal internal deformation under the shallow-ice approximation, i.e., no sliding $\omega(\xi) = \omega_D(\xi)$ (s = 0, n = 3) (Glen, 1952); (2) the plug flow, i.e., all sliding $\omega(\xi) = \xi$ (Parrenin et al., 2007); and (3) the non-linear rheology of ice (Raymond–Reeh model), i.e., a parabolic profile for the plug flux shape function ω ($n = 3$), where shear stresses are negligible (Raymond, 1983; Reeh, 1988). The melting point of ice decreases linearly as a function of the depth (Huybrechts and Payne, 1996).

The input data for the models were the accumulation rates, surface temperature, and geothermal heat flux in the region of Taishan Station. The temperature string data shows that the annual mean temperature is −35.5°C. The average accumulation rate is 53 kg m^{-2} a^{-1} (13 cm depth of snow), and the average snow density is 389 kg m^{-3}, as determined from the measurements of the stake arrays estimating the surface mass balance along the traverse route from Zhongshan to Dome A (Ding et al., 2011). For solid ice, the density is 917 kg m^{-3} (Cuffey and Paterson, 2010). Then, present day accumulation rates are estimated as about 58 mm ice equivalents every year. The largest uncertainty in calculating the temperature profiles is the value of the geothermal heat flux (G). No direct measurements for G exist in this area, and from the studies by Van Liefferinge and Pattyn (2013), we consider the values for G to be 50, 55, or 60 mW m^{-2}. From the radar profiles, the ice thickness of the site at Taishan Station is shown to be 1,870 m.

The age–depth, and temperature–depth relationships derived from the model results with the input data are shown in **Figure 6**. The result of the ice flow modeling makes it possible to estimate the age and temperature of the ice in the bottom part of Taishan Station, where no age markers are yet available. All three age–depth profiles from the three flux shape functions closely agree about the basal age of the ice: approximately 50–150 kyr (kiloyear). Note that the "Raymond–Reeh" model is valid for the ice-divide region, where longitudinal stress gradients cannot

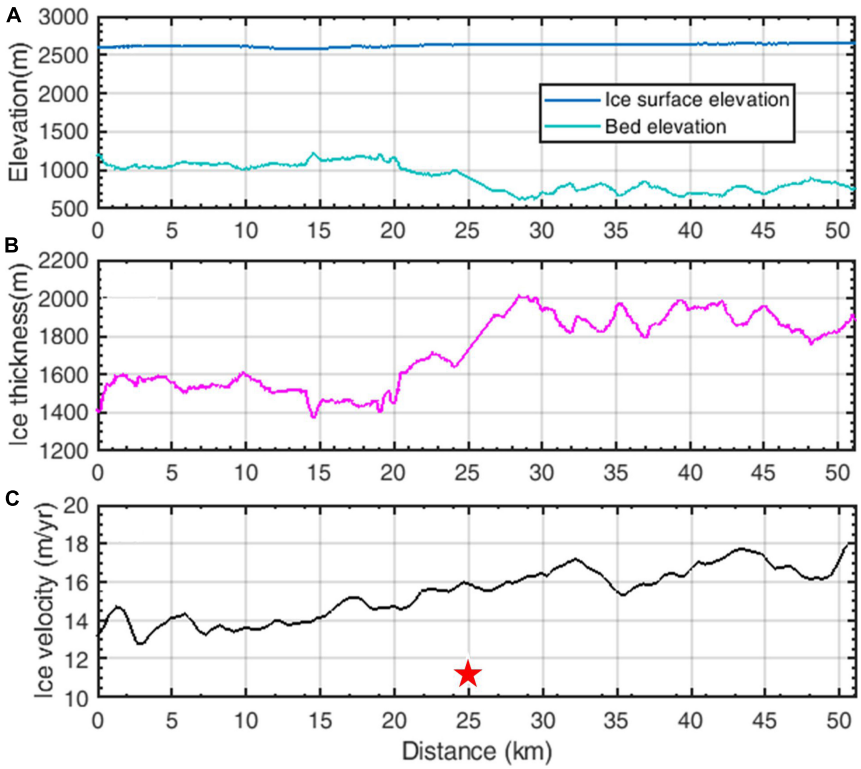

FIGURE 5 | (A) Surface and subglacial topography elevation, **(B)** ice thickness, and **(C)** ice velocity, from Rignot et al. (2011). The radar profile is shown in **Figure 4A**. The red star marks the position of Taishan Station.

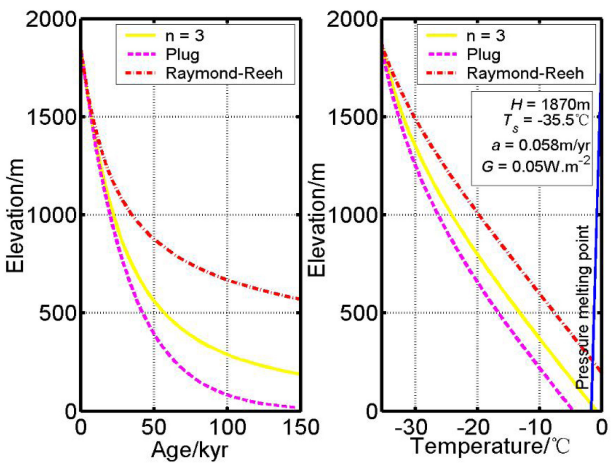

FIGURE 6 | Profiles of age depth and temperature depth at Taishan Station calculated for the input parameters of the ice thickness *H*, surface temperature T_S, and accumulation *a*, and geothermal heat flux values *G* of 50 mW m^{-2} from modeling using three flux shape functions in the ice model.

be ignored (Raymond, 1983), and Taishan Station is clearly not located in a region of ice divide. Thus, in the age–depth profile of this model, at the same depth, the age may be overestimated. The temperature profiles (**Figure 6**) predict that the basal ice may reach the melting point (Raymon–Neeh model), or the basal ice freezing point (Plug flow model). While no basal melting corresponding to the bright reflector was found in radar profiles and because the region of Taishan Station is not an ice divide, the one-dimensional assumption of the Raymon–Neeh model is probably invalid in this region. For the temperature profile, it should be noted that below the threshold of zero melting, a slight decrease in the geothermal flux has no impact on the basal melting.

SNOW TEMPERATURE

Accurate and reliable near-surface ice temperature is an important factor in numerical models for assessing the mass balance and energy balance of polar ice sheets. Because the ice flow of Taishan Station is relatively stable and preserves the complete layered structure, to analyze its vertical variation along the temperature profile is of great value.

A 10 m temperature chain was installed at a site with initial coordinates of (73°51′50″S, 76°58′28″E) at Taishan Station (**Figure 2**) during CHINARE 32nd on January 31, 2016. The string of temperature sensors was used to monitor the temperature change in the shallow near-surface snow layer. **Figure 7** shows the daily average snow temperatures at six typical depths (0.1, 2, 4, 6, 8, and 10 m) from February 2016 to January 2017 at Taishan Station. The daily average temperature was

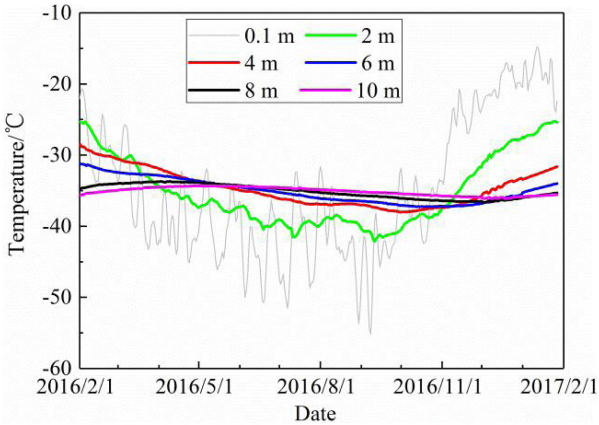

FIGURE 7 | Daily average snow temperatures at different depths at Taishan Station from February 2016 to January 2017.

chosen as the average of four representative times (2:00, 8:00, 14:00, and 20:00).

Figure 7 shows that the high frequency change from the surface to the snow layer gradually disappears when heat is conducted in the snow layer. The amplitude of snow layer temperature fluctuation from the surface decreases with depth, and the phase of snow layer temperature fluctuation from the surface lags with depth.

The snow temperature at a depth of 0.1 m from the surface is greatly affected by changes in the surface temperature, and the high frequency of the surface temperature wave decreases sharply from the surface downwards. At the depth of 2 m, the snow temperature has clear seasonal fluctuations, and the daily temperature variation is weak. The seasonal fluctuations of snow temperature at depths of 4, 6, and 8 m decrease gradually and the seasonal fluctuation of snow temperature at the depth of 10 m basically disappears. From a phase point of view, the temperature at the surface reached the lowest value on September 8, 2016, and the date that the temperature at various depths from the surface downwards reached the lowest value lagged behind slightly. The temperature at the depth of 10 m reached the lowest value on December 19, 2016, 101 days behind from the date at the surface.

The snow temperature at the depth of 10 m is an important indicator in glaciology. It is commonly accepted that the snow temperature at the depth of 10 m is equivalent to the mean annual air temperature at the surface in the dry-snow zone (Chen et al., 2010). It can be seen from **Figure 7** that the snow temperature at the depth of 10 m is almost constant—it is maintained at the −35.5°C baseline. The value is close to the annual average snow temperature at the depth of 10 m at LT790 (−36.1°C) which is 46 km away from Taishan Station (Ding et al., 2010).

SNOW DENSITY PROFILES

The surface temperature of the Antarctic ice sheet is extremely low, and the surface of the ice sheet does not melt, even in summer. It is named as the dry-snow zone in glaciology. The Taishan Station is a cold-type densification zone (Qin, 1987). We drilled a 10 m snow core at Taishan Station during the 2012/2013 CHINARE field season. The snow density at each depth was calculated by the length and weight data. The result is shown in **Figure 8**, and the fitting curve of the snow density data is also shown. The fitting curve of the snow density data was constructed by referring to the densification model (Cuffey and Paterson, 2010):

$$\rho = \rho_i - (\rho_i - \rho_s)\, exp\,(-Cz)\,, \tag{4}$$

where ρ is the snow (firn) density at depth z, ρ_i is the pure ice density, and ρ_s is the snow density at the surface. According to the fitting curve, it can be seen that the density shows an exponential change with depth. The density fluctuation range of the 10 m snow core is 0.35–0.60 g cm^{-3}, and the surface snow density at Taishan Station is 0.381 g cm^{-3}.

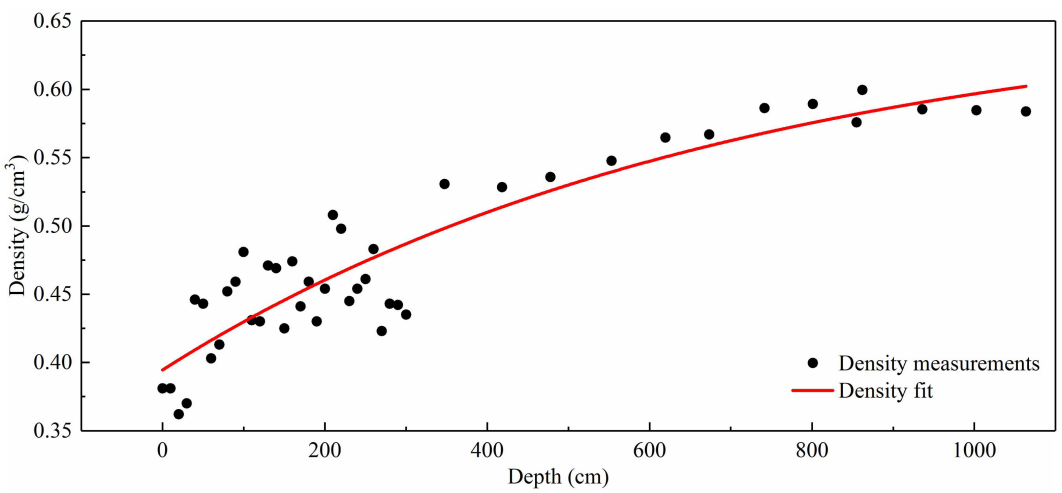

FIGURE 8 | Snow density profile of Taishan Station from a 10 m shallow snow core.

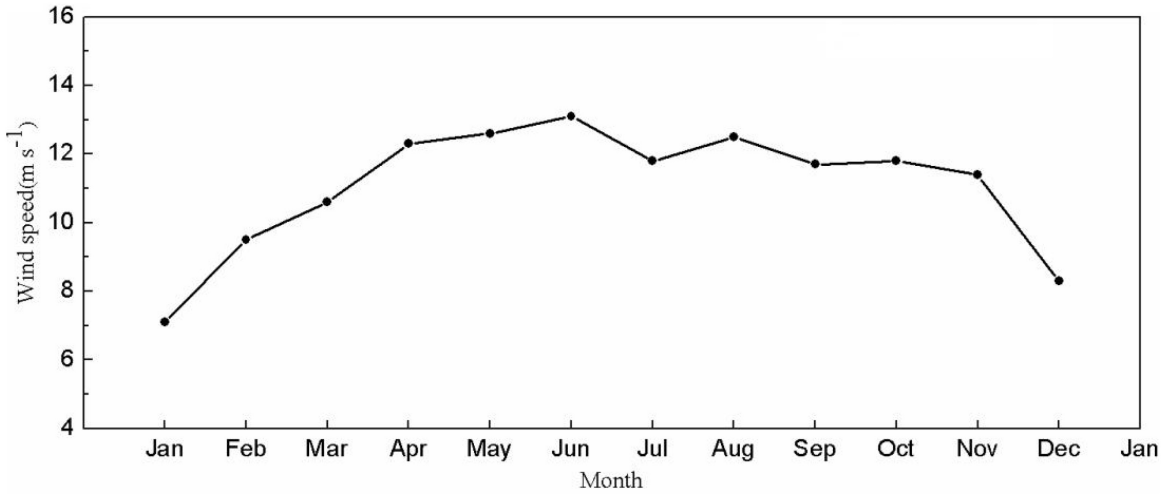

FIGURE 9 | Monthly variation of the average wind speed at Taishan Station from an Automatic Weather Station at Taishan Station from February 2016 to February 2017.

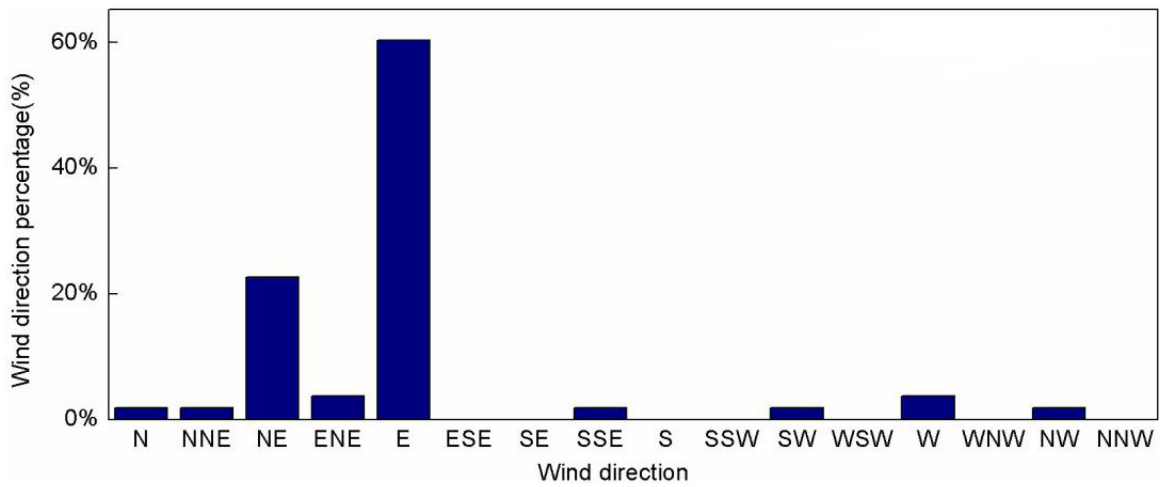

FIGURE 10 | Frequencies of the average wind direction at Taishan Station.

Previous studies have suggested one (ρ = 0.55 g cm^{-3}) or even two (ρ = 0.83 g cm^{-3}) critical values to proclaim different densification processes that occur in the snow column (Salamatin and Lipenkov, 2008). In the upper part (ρ < 0.55 g cm^{-3}), the dominant densification processes are the grain settling and packing of snow grains. Thereafter, the densification process is slower and is mainly due to sublimation, diffusion and deformation processes until the density reaches the pore close-off depth (ρ = 0.83 g cm^{-3}). From **Figure 8**, we can conclude that the depth corresponding to the first critical value of ice density in Taishan Station is 5.8 m. This result is similar to that shown in the simulation results (Ligtenberg et al., 2011).

From the characteristics of the snow profile, the composition of the 10 m snow core has experienced the transition from firn (wind panels) to fine snow, hard fine snow, medium snow, coarse snow, and then snow with an ice lens from top to bottom. The snow profile of Taishan Station is more complex and the hardness of the snow is greater than at other sampling points.

METEOROLOGICAL CONDITIONS

From February 2016 to February 2017, an Automatic Weather Station (AWS) was operational at Taishan Station. **Figure 9** shows the monthly variation in the average wind speed observed from the AWS. It can be seen that the maximum monthly average wind speed occurs in June, up to 13.1 m s^{-1}, and the minimum of monthly average wind speed occurs in January, up to 7.1 m s^{-1}. The annual average wind speed of Taishan Station is about 11 m s^{-1}. It is clear that there are notable seasonal changes in wind speed at Taishan Station, and the wind speed in winter is significantly higher than that in summer.

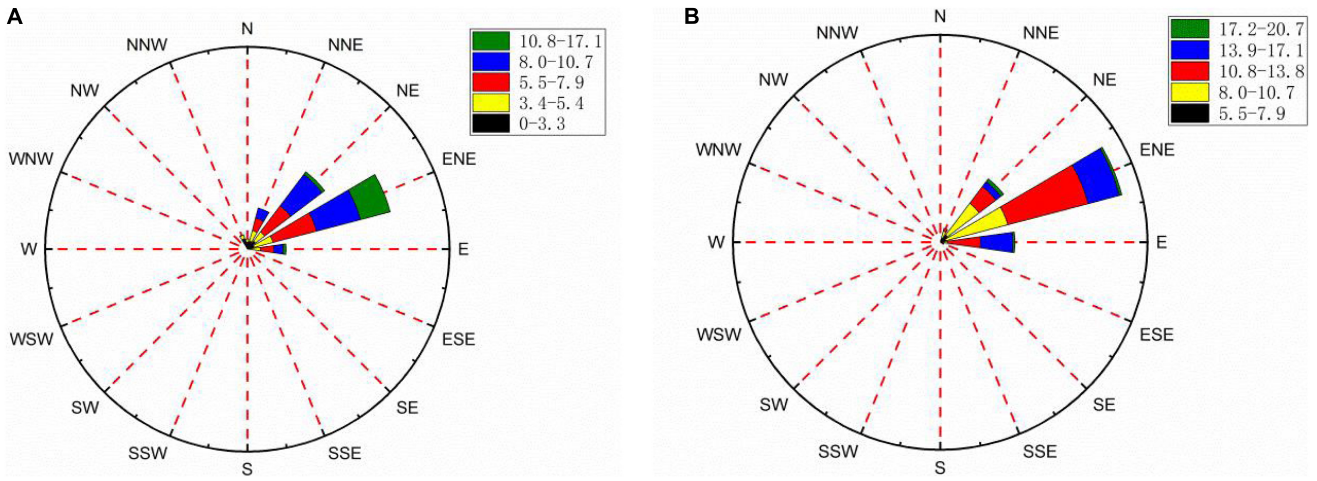

FIGURE 11 | Seasonal variation of wind speed (Unit: m s^{-1}) and wind direction from the Automatic Weather Station at Taishan Station, **(A)** January 2016, **(B)** July 2016.

Figure 10 shows the frequency of the average wind direction at Taishan Station. The dominant wind direction at Taishan Station is east with a frequency of 60.37%. The secondary wind directions are north-east and east-north-east winds, accounting for 22.64 and 3.77%, respectively. The wind direction is relatively concentrated, and the frequency of easterly winds can reach 86.78% of the total.

Rose diagrams of the wind direction at Taishan Station are shown against both wind direction and wind speed in **Figure 11**. **Figure 11A** shows the wind direction in January, and **Figure 11B** shows the wind direction in July. It can be seen that the main wind force is at levels 3–5 (Beauford scale) in January, accounting for nearly 80% of the wind force. The frequency of wind force at levels 1–5 is close to 90%, and the lower wind speed is conducive to the safety of summer observations at Taishan Station.

In July, the main wind force is at levels 5–7, accounting for more than 90% of the wind force. It is difficult to work outdoors in such windy weather. Wind speeds are significantly different in winter and summer, and the wind force in January (Southern hemisphere summer) is significantly lower than that in July (Southern hemisphere winter). The seasonal difference in wind speed at Taishan Station may be related to its positioning as a summer scientific expedition station.

In January, the dominant wind direction at Taishan Station is east-north-east winds, with a frequency of 41.99%. The secondary wind directions are north-east winds and north-east-north winds. The sum of these three wind directions can reach 81.70% of the total. In July, the dominant wind direction at Taishan Station is also east-north-east winds with a frequency of 60.37%. The secondary wind directions are north-east winds and east winds. The sum of these three wind directions can reach 94.89% of the total. The distribution of the wind direction in July is relatively concentrated; the frequency of east winds in July increases significantly compared with that in January, and the wind direction in July has an obvious shift toward east relative to that in January. This is similar to the conclusion reached by Yang et al. (2007) at the LGB69 station (70°50′S, 77°04′E) in East Antarctica. Strong winds can carry a large amount of surface snow, and the stability of the wind direction determines the surface topography, which has a great influence on the credibility of local observation.

The annual average wind direction stability of Taishan Station is 0.89, which is higher than that of 0.78 in Dome A, which is related to the slope of Taishan Station being higher than that of Dome A (Ma et al., 2010). The large wind direction stability appears in the strong descending wind area with a large surface slope. In general, the wind at Taishan Station is obviously affected by the katabatic wind, and the wind direction is prevailing easterly winds. The observations of wind speed and wind direction provide a theoretical support for further analysis of the replenishment capacity at Taishan Station.

The spatial pattern of the surface pressure shows minimum values over the plateau of East Antarctica and maximum values over the Ross Sea (**Figure 12A**). The spatial pattern is mainly attributed to the Antarctic topography. The surface pressure at Taishan Station is approximately 700 hPa. In contrast to the surface pressure, the mean sea level pressure (MSLP) can reflect the realistic surface circulation. A high-pressure ridge occurs over the plateau of East Antarctica where the maximum value exceeds 1025 hPa (**Figure 12B**). Two low pressure troughs occur over the Amundsen Sea and the Southern Indian Ocean (120°E). The former usually corresponds to an Amundsen low. Taishan Station has a MSLP of 1000 hPa. Corresponding to the high pressure over East Antarctica, the surface wind field here shows a large anticyclonic circulation (**Figure 12C**). The steep topography over coastal regions drives a strong katabatic wind. The anticyclonic circulation enables the prevailing wind at Taishan Station to be an easterly wind. The surface air temperature over the Antarctic continent shows a similar pattern to the topography (**Figure 12D**). Namely, the higher terrain corresponds to the lower temperature and vice versa. The surface air temperature

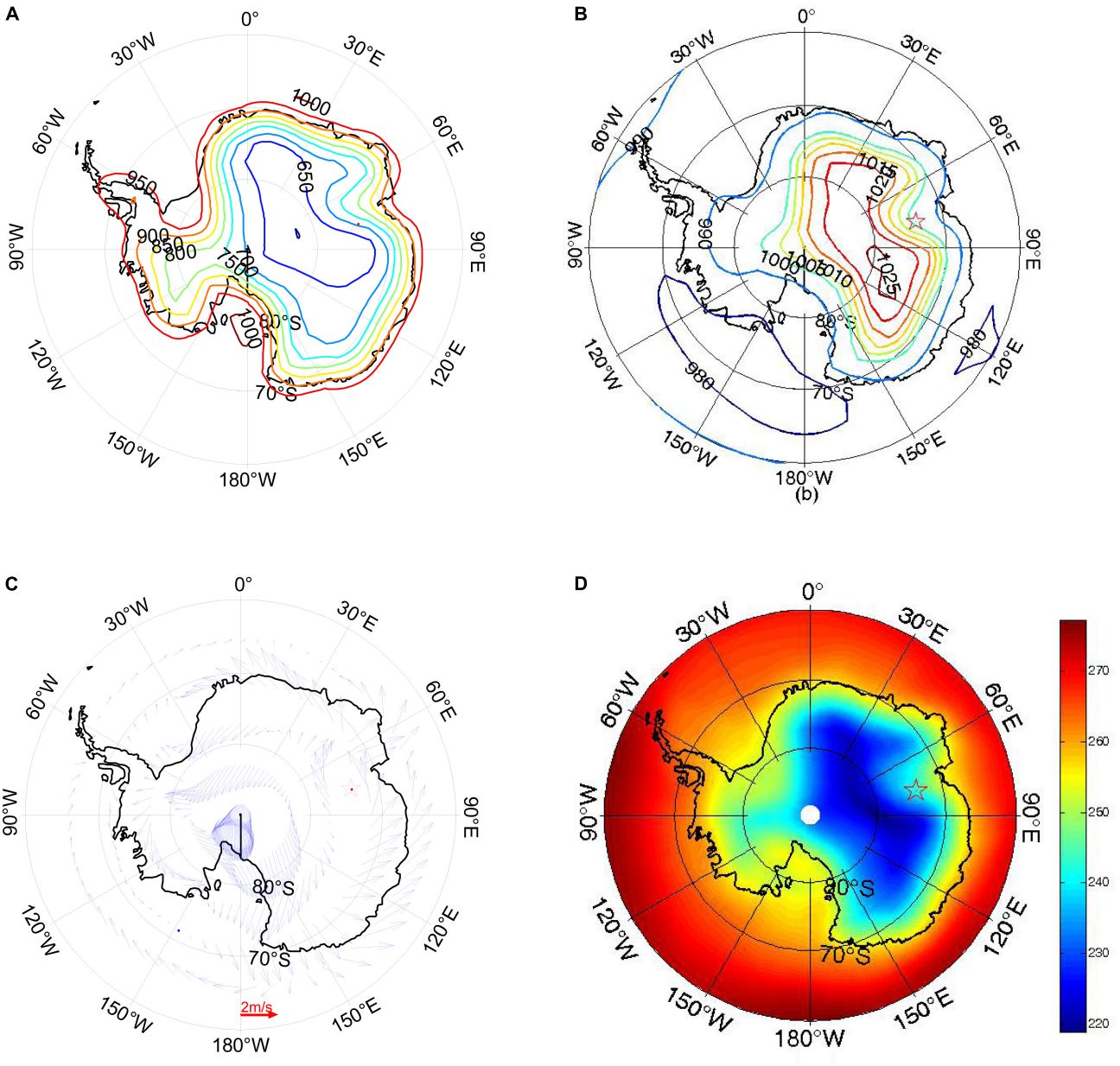

FIGURE 12 | (A) Spatial patterns of the averaged surface pressure (Unit: hpa), **(B)** mean sea level pressure (Unit: hpa), **(C)** 10 m wind field, and **(D)** 2 m air temperature (Unit: K). The asterisk denotes the site of Taishan Station. All data are derived from the National Center for Environmental Prediction (NCEP)-DOE (Department of Energy) Reanalysis II dataset (ftp.cdc.noaa.gov/Projects/Datasets/necp.reanalysis2.derived/).

at Taishan Station is nearly 250 K (−23°C), which is apparently higher than the observational value (−36°C). It indicates that the reanalysis data overestimate the surface air temperature at Taishan Station.

SNOW ISOTOPES

The stable isotopes of water (δD and $\delta^{18}O$) are important climate proxies that are commonly interpreted in terms of temperature. The measured results from the surface snow along a section from Zhongshan Station to Dome A during the 31st CHINARE show that the spatial variation range of $\delta^{18}O$ at Taishan Station is around −35 to −45‰, and the δD variation range is −260 to −360‰ (Ma et al., 2017). The δD record exhibits detectable seasonal cycles through ice core, providing a method to obtain a timescale by annual layer counting. Nitrate (NO^{3-}) is one of the main chemical ions in Antarctic snow ice, which can account for more than 40% of the total ions in snow ice. The isotopic fractionation associated with nitrate

volatilization at Taishan Station was minor. The snow mass, concentration, and isotopic composition of NO^{3-} ($\delta^{15}N$ and $\delta^{18}O$) near the site are constant during a 16-day experiment, and volatilization of NO^{3-} is estimated to decrease $\delta^{15}N$ and $\delta^{18}O$ in the snowpit by 0–3‰ and 0–6‰, respectively (Shi et al., 2019).

CONCLUSION

We conducted an integrated glaciological and meteorological investigation around the site of the Chinese Antarctic Taishan Station, focusing on the potential deep ice core drilling and supporting field activities in the East Antarctic plateau. We deduced the surface mass balance and ice velocity from the published data and derived the surface topography, ice thickness, internal layers and bed topography from radar data. The age control and englacial temperature from the internal layers seen in the radar data and ice modeling suggested a range of 50–150 kyr (kiloyear) and no melting over the basal ice. The internal layer structure also indicated that the ice around the Taishan Station site has been stable, with smaller undulations and disturbances at the shallower depth. The stratigraphical character of the internal layers offers an outstanding opportunity to improve our understanding of ice dynamics and to accurately infer the ice sheet history with the accompanying climatic change.

The snow temperature at the depth of 10 m was determined to be −35.5°C from a 10 m temperature chain, which can provide an estimate of the mean annual air temperature at the surface. The 10 m snow density profiles showed that different densification processes occur in the snow column. The annual average wind speed of Taishan Station is about 11 m s^{-1} from an AWS, and the wind direction is relatively concentrated and can redistribute the surface snow. The atmospheric reanalysis data showed that the site has a prevailing easterly wind and is sensitive to the strong katabatic wind over coastal regions. Furthermore, the surface air temperature around the station showed a similar pattern to the topography.

A significant way of selecting drilling locations is to trace the continuous internal layers along the radar profiles. Of interest in site selection is the smoothness of continuous internal layers and the geometric lengths of ice column (Tang et al., 2012). The properties that internal layers are relatively stable and conformal with bed topography and that the site has an ice thickness of 1,900 m suggest that Taishan Station may be a good location for drilling older and undisturbed ice. A deep ice core at Taishan Station would be expected to improve our understanding of past East Antarctic climate. It would be a better complement to the existing records (e.g., Dome A, Dome Fuji, Dome C) from the East Antarctic ice sheet. Taishan Station is considered as ideal logistical base because of the uniqueness of its location and glacio-meteorological conditions. Taishan Station can provide strong support for proposed ground-based and airborne investigations in the Antarctic ice sheet (e.g., Grove Mountains, Dome A, Ridge B, and Vostok, etc.). In fact, CHINARE has used Taishan station as its logistics base to investigate a large-scale area from the coastal to the interior of the East Antarctic ice sheet, including Prydz Bay, Amery Ice Shelf, Grove Mountains, Princess Elizabeth Land, Ridge B, Vostok and Dome A (Cui et al., 2018). Our study is potentially valuable for an ice dynamics investigation associated with the East Antarctic ice sheet in response to sea level and climate forcing.

Potential climate proxy data from ice cores at the Taishan Station site would be helpful for understanding changes in the East Antarctic climate variability and may provide new information for the evolution of the Antarctic ice sheet. In the future, to date the ice column of Taishan Station, it will be necessary to obtain a more continuous and direct stratigraphic link between the site and the Antarctic ice cores. However, our radar surveys failed to detect some deeper layers, possibly because the ice stream of Lambert glacier flowing into the Amery ice shelf disturbs the deeper layers and removes the surface troughs and their effects, affecting the layer geometries as the ice flows over them. It requires additional ground-based or airborne geophysical observations and modeling studies to aid in englacial structure mapping and determination of ice–bedrock interactions in the vicinity of Taishan Station. Additional glaciological and meteorological data on the present and past environment are also needed to evaluate the field work around the site.

DATA AVAILABILITY STATEMENT

All the data presented in the paper are available for scientific purposes upon request to the corresponding author (XT, tangxueyuan@pric.org.cn).

AUTHOR CONTRIBUTIONS

XT: methodology and formal analysis. XT and YZ: software. XT, YD, and JG: validation. XT, JG, XC, LL, SZ, and BS: resources. XT, YZ, SC, KL, and LY: writing – original draft preparation. XT, YZ, SC, and KL: writing – review and editing. XT, YD, and BS: supervision. All authors contributed to the article and approved the submitted version.

FUNDING

This study was supported by the National Natural Science Foundation of China (Nos. 41876230, 41876227, 41941006, and 41776199) and the Chinese Polar Environmental Comprehensive Investigation and Assessment Programs (CHIANRE 2017-01-01).

ACKNOWLEDGMENTS

We thank the Chinese National Antarctic Research Expedition for their help in the field data collection, an English editor of MDPI for improving the language of this text, and Richard C. Hindmarsh for providing the ice model.

REFERENCES

Cavitte, M. G., Blankenship, D. D., Young, D. A., Schroeder, D. M., Parrenin, F., Lemeur, E., et al. (2016). Deep radiostratigraphy of the East Antarctic plateau: connecting the Dome C and Vostok ice core sites. *J. Glaciol.* 62, 323–334. doi: 10.1017/jog.2016.11

Chen, B., Zhang, R., Xiao, C., Bian, L., and Zhang, T. (2010). Analyses on the air and snow temperatures near ground with observations of an AWS at Dome A, the summit of Antarctic Plateau. *Chin. Sci. Bull.* 55, 1430–1436. doi: 10.1007/s11434-010-0099-1

Cuffey, K. M., and Paterson, W. S. (2010). *The Physics of Glaciers*. Cambridge, MA: Academic Press, doi: 10.1063/1.2915138

Cui, X., Greenbaum, J. S., Beem, L. H., Guo, J., Gregory, N. G., Li, L., et al. (2018). The First Fixed-wing Aircraft for Chinese Antarctic Expeditions: Airframe modifications. Scientific Instrumentation and Applications. *J. Environ. Eng. Geophys.* 23, 1–13. doi: 10.2113/JEEG23.1.1

Cui, X., Sun, B., Tian, G., Tang, X., Zhang, X., Jiang, Y., et al. (2010). Preliminary results of ice radar investigation along the traverse between Zhongshan and Dome A in East Antarctic ice sheet: Ice thickness and subglacial topography. *Chin. Sci. Bull.* 55, 2715–2722. doi: 10.1007/s11434-010-3238-9

Ding, M., Xiao, C., Jin, B., Ren, J., Qin, D., and Sun, W. (2010). Distribution of δ 18 O in surface snow along a transect from Zhongshan Station to Dome A. East Antarctica. *Chin. Sci. Bull.* 55, 2709–2714. doi: 10.1007/s11434-010-3179-3

Ding, M., Xiao, C., Li, C., Qin, D., Jin, B., Shi, G., et al. (2015). Surface mass balance and its climate significance from the coast to Dome A. East Antarctica. *Sci. China Earth Sci.* 58, 1787–1797. doi: 10.1007/s11430-015-5083-9

Ding, M., Xiao, C., Li, Y., Ren, J., Hou, S., Jin, B., et al. (2011). Spatial variability of surface mass balance along a traverse route from Zhongshan station to Dome A. Antarctica. *J. Glaciol.* 57, 658–666. doi: 10.3189/002214311797409820

Fretwell, P. T., Pritchard, H. D., Vaughan, D. G., Bamber, J. L., Barrand, N. E., Bell, R. E., et al. (2013). Bedmap2: Improved ice bed, surface and thickness datasets for Antarctica. *Cryosphere* 7, 375–393. doi: 10.5194/tc-7-375-2013

Glen, J. W. (1952). Experiments on the deformation of ice. *J. Glaciol.* 2, 111–114. doi: 10.1017/S0022143000034067

Greene, C. A., Gwyther, D. E., and Blankenship, D. D. (2017). Antarctic Mapping Tools for Matlab. *Computers Geosci.* 104, 151–157. doi: 10.1016/j.cageo.2016.08.003

Huybrechts, P., and Payne, T. (1996). The EISMINT benchmarks for testing ice-sheet models. *Ann. Glaciol.* 23, 1–12. doi: 10.1017/S0260305500013197

Li, C., Kang, S., Shi, G., Huang, J., Ding, M., Zhang, Q., et al. (2014). Spatial and temporal variations of total mercury in Antarctic snow along the transect from Zhongshan Station to Dome A. *Tellus B Chem. Phys. Meteorol.* 66:25152. doi: 10.3402/tellusb.v66.25152

Li, C., Ren, J., Qin, D., Xiao, C., Hou, S., Li, Y., et al. (2013). Factors controlling the nitrate in the DT-401 ice core in eastern Antarctica. *Sci. China Earth Sci.* 56, 1531–1539. doi: 10.1007/s11430-012-8888-9

Li, Y., Cole-Dai, J., and Zhou, L. (2009). Glaciochemical evidence in an East Antarctica ice core of a recent (AD 1450–1850) neoglacial episode. *J. Geophys. Res.* 114:D08117. doi: 10.1029/2008jd011091

Ligtenberg, S. R. M., Helsen, M. M., and Van Den Broeke, M. R. (2011). An improved semi-empirical model for the densification of Antarctic firn. *Cryosphere* 5, 809–819. doi: 10.5194/tc-5-809-2011

Liu, X., Lang, S., Zhao, B., Zhang, F., Liu, Q., Tang, C., et al. (2018). High-resolution ice-sounding radar measurements of ice thickness over East Antarctic Ice Sheet as a part of Chinese National Antarctic Research Expedition. *IEEE Trans. Geosci. Remote Sens.* 56, 3657–3666. doi: 10.1109/TGRS.2018.2804384

Ma, T., Xie, Z., Li, Y., An, C., Shi, G., Yu, J., et al. (2017). The spatial changes and impact factors of water stable isotope in surface snow along Zhongshan Station-Dome A. *Chin. J. Polar Res.* 29, 210–217.

Ma, Y., Bian, L., Xiao, C., Allison, I., and Zhou, X. (2010). Near surface climate of the traverse route from Zhongshan Station to Dome A. East Antarctica. *Antarct. Sci.* 22, 443–459. doi: 10.1017/s0954102010000209

Meredith, M., Sommerkorn, M., Cassotta, S., Derksen, C., Ekaykin, A., Hollowed, G., et al. (2019). "Polar Regions," in: *IPCC Special Report on the Ocean and Cryosphere in a Changing Climate*, eds H.-O. Pörtner et al. (Geneva: IPCC)

Parrenin, F., Dreyfus, G., Durand, G., Fujita, S., Gagliardini, O., Gillet, F., et al. (2007). 1-D-ice flow modelling at EPICA Dome C and Dome Fuji, East Antarctica. *Clim. Past.* 3, 243–259. doi: 10.5194/cp-3-243-2007

Qin, D. (1987). The densification process of snow in the surface layer of the Antarctic ice sheet. *J. Glaciol. Geocryol.* 9, 190–204.

Qin, D., Ren, J., Kang, J., Xiao, C., Li, Z., Li, Y., et al. (2000). Primary results of glaciological studies along an 1100 km transect from Zhongshan station to Dome A, East Antarctic ice sheet. *Ann. Glaciol.* 31, 198–204. doi: 10.3189/172756400781819860

Raymond, C. F. (1983). Deformation in the vicinity of ice divides. *J. Glaciol.* 29, 357–373. doi: 10.1017/S0022143000030288

Reeh, N. (1988). A flow-line model for calculating the surface profile and the velocity, strain-rate, and stress fields in an ice sheet. *J. Glaciol.* 34, 46–55. doi: 10.3189/s0022143000009059

Ren, J., Qin, D., and Xiao, C. (2001). Preliminary results of the inland expeditions along a transect from the Zhongshan Station to Dome A, East Antarctica. *J. Glaciol. Geocryol.* 23, 51–56.

Rignot, E., Mouginot, J., and Scheuchl, B. (2011). *MEaSUREs InSAR-Based Antarctica Ice Velocity Map*. Boulder, CL: NASA DAAC at the National Snow and Ice Data Center, doi: 10.5067/MEASURES/CRYOSPHERE/nsidc-0484.001

Salamatin, A., and Lipenkov, V. (2008). Simple relations for the close-off depth and age in dry-snow densification. *Ann. Glaciol.* 49, 71–76. doi: 10.3189/172756408787814889

Shepherd, A., Ivins, E., Rignot, E., Smith, B., Van Den Broeke, M., Velicogna, I., et al. (2018). Mass balance of the Antarctic Ice Sheet from 1992 to 2017. *Nature* 558, 219–222. doi: 10.1038/s41586-018-0179-y

Shi, G., Chai, J., Zhu, Z., Hu, Z., Chen, Z., Yu, J., et al. (2019). Isotope fractionation of nitrate during volatilization in snow: a field investigation in Antarctica. *Geophys. Res. Lett.* 46, 3287–3297. doi: 10.1029/2019GL081968

Tang, X., Sun, B., Li, Y., Li, X., and Cui, X. (2012). Dome Argus: ideal site for deep ice drilling. *Adv. Polar Sci.* 23, 47–54. doi: 10.3724/SP.J.1085.2012.00047

Tang, X., Sun, B., Zhang, Z., Zhang, X., Cui, X., and Li, X. (2011). Structure of the internal isochronous layers at Dome A, East Antarctica. *Sci. China Earth Sci.* 54, 445–450. doi: 10.1007/s11430-010-4065-1

Tang, X. Y., Guo, J. X., Sun, B., Wang, T. T., and Cui, X. B. (2016). Ice thickness, internal layers, and surface and subglacial topography in the vicinity of Chinese Antarctic Taishan station in Princess Elizabeth Land. East Antarctica. *Appl. Geophys.* 13, 203–208. doi: 10.1007/s11770-016-0540-6

Van Liefferinge, B. V., and Pattyn, F. (2013). Using ice-flow models to evaluate potential sites of million year-old ice in Antarctica. *Clim. Past* 9, 2335–2345. doi: 10.5194/cp-9-2335-2013

Wu, X., Tian, Q., Jin, X., Jiang, P., Qing, C., Cai, J., et al. (2017). Estimating optical turbulence of atmospheric surface layer at Antarctic Taishan station from meteorological data. *Acta Phys. Sin.* 66, 380–388. doi: 10.7498/aps.66.039201

Yang, Q., Yin, T., Zhang, L., and Jiang, D. (2007). Analyses of surface winds along the track from Zhongshan Station to Dome A, Antarctica. *Chin. J. Polar Res.* 19, 295–304.

Zhang, S., Eaa, D., Wang, Z., Li, Y., Jin, B., and Zhou, C. (2008). Ice velocity from static GPS observations along the transect from Zhongshan station to Dome A, East Antarctica. *Ann. Glaciol.* 48, 113–118. doi: 10.3189/172756408784700716

Zhang, X., Sun, B., Wang, B., Tang, X., and Tian, G. (2006). "Radar detection of ice characteristics and distribution in the Antarctic ice sheet," in *Proceedings of the Annual Meeting of the Chinese Geophysical Society*, Beijing.

Conflict of Interest: The authors declare that the research was conducted in the absence of any commercial or financial relationships that could be construed as a potential conflict of interest.

Copyright © 2020 Tang, Guo, Dou, Zhang, Cheng, Luo, Yu, Cui, Li, Zhang and Sun. This is an open-access article distributed under the terms of the Creative Commons Attribution License (CC BY). The use, distribution or reproduction in other forums is permitted, provided the original author(s) and the copyright owner(s) are credited and that the original publication in this journal is cited, in accordance with accepted academic practice. No use, distribution or reproduction is permitted which does not comply with these terms.

frontiers in Earth Science

ORIGINAL RESEARCH
published: 12 November 2020
doi: 10.3389/feart.2020.527493

Records of Inorganic Ions and Dust Particles in Snow at Yushugou Glacier No. 6 in the Desert Belt of Northwestern China

Feng Liu[1,2], Zhongqin Li[3,4,5], Jianan Hao[6], Xi Zhou[6], Fanglong Wang[4], Hui Zhang[2,4], Panpan Wang[3], Xin Zhang[4], Mengyuan Song[4] and Taotao Chen[3]*

[1]Institute of International Rivers and Eco-security, Yunnan University, Kunming, Yunnan, China, [2]Yunnan Key Laboratory of International Rivers and Transboundary Eco-security, Kunming, China, [3]College of Geography and Environmental Sciences, Northwest Normal University, Lanzhou, China, [4]State Key Laboratory of Cryospheric Science, Northwest Institute of Eco-Environment and Resources, Chinese Academy of Sciences, Lanzhou, China, [5]College of Sciences, Shihezi University, Xinjiang, China, [6]College of Earth and Environmental Sciences, Lanzhou University, Lanzhou, China

OPEN ACCESS

Edited by:
Khanghyun Lee, Korea Polar Research Institute, South Korea

Reviewed by:
Yong Zhang, Hunan University of Science and Technology, China
Jizu Chen, Chinese Academy of Sciences (CAS), China
Parmanand Sharma, National Centre for Polar and Ocean Research (NCPOR), India

***Correspondence:**
Zhongqin Li
lizq@lzb.ac.cn

Specialty section:
This article was submitted to Cryospheric Sciences, a section of the journal Frontiers in Earth Science

Received: *16 January 2020*
Accepted: *30 September 2020*
Published: *12 November 2020*

Citation:
Liu F, Li Z, Hao J, Zhou X, Wang F, Zhang H, Wang P, Zhang X, Song M and Chen T (2020) Records of Inorganic Ions and Dust Particles in Snow at Yushugou Glacier No. 6 in the Desert Belt of Northwestern China. Front. Earth Sci. 8:527493. doi: 10.3389/feart.2020.527493

Chemical ions and dust particles deposited in snow can be used as indicators of climatic and environmental processes. Understanding their sources, energy transfer, and evolutionary mechanisms is extremely important in tracking regional climate and environmental changes. We collected snow samples from three pits at different altitudes and from the surface of Yushugou Glacier No. 6, Tian Shan Mountains, China, in the summers of 2017 and 2018. Sea-salt tracing, correlation analysis, and factor analysis were used to determine the characteristics and sources of the major ions and mineral dust particles in the snow. We found obvious seasonal variations, with high concentrations of dust particles and major ions deposited during the dust period, and relatively low concentrations deposited during the non-dust period. The concentrations peaked within two distinct dust layers in the snow pits. There was a significant correlation between the peak values and the dust layer. The ionic concentrations were ranked from highest to lowest as $Ca^{2+} > SO_4^{2-} > Cl^- > Na^+ > NO_3^- > NH_4^+ > Mg^{2+} > K^+$. Therefore, SO_4^{2-} was the dominate anion and Ca^{2+} was the dominate cation. The major ions in the snow at Yushugou Glacier No. 6 are mainly derived from terrestrial mineral dust but also include limited inputs from human activities and sea salt.

Keywords: Yushugou Glacier No. 6, accumulated snow, chemical characteristics, seasonal variation, ionic sources

INTRODUCTION

The cryosphere is a part of the Earth's surface where temperatures are continuously below the freezing point of water. It can be divided into continental, marine, and aerial components, consisting of glaciers, ice sheets, frozen ground, snow, sea ice, etc. (Qin et al., 2017). It is well known that the cryosphere is very sensitive to climate change and is therefore considered a barometer of it (Qin et al., 2006; Koven et al., 2013; Kraaijenbrink et al., 2017). Snow and ice in alpine glaciers contain a record of the chemistry of the atmosphere (Fuhrer et al., 1996; Olivier et al., 2006). Chemical studies on ice and snow in alpine glaciers are important because snow and glaciers can provide crucial information about climatic and environmental change as they are sites where atmospheric chemical components are deposited; for example, chemical ions, aerosol dust particles, trace metals, $\delta^{18}O$, greenhouse gases, and black carbon (Ming et al., 2009; Massling et al., 2015; Sugimoto et al., 2015; Du et al., 2016;

Van der A. et al., 2017). Identification of the origins and seasonal changes of the chemical components in snow may provide information about changes in the atmosphere, lithosphere, hydrosphere, and cryosphere (Prospero et al., 2002). Generally, chemical ions and dust particles deposited in snow reflect the influences of both atmospheric circulation patterns and the regional environment (Eichler et al., 2001; Li et al., 2007; Ming et al., 2009). Taking the Tibetan Plateau as an example, under the influence of a southwest monsoon climate and northwest drought climate, distinct regional climate patterns are formed. Similarly, differences in the geographical environment are also reflected in the snow and ice on the Tibetan Plateau (Liu et al., 2010; Wu et al., 2011). For example, the amount of dust particles in snow tends to decrease from north to south.

There has been comprehensive research on dust particles, their chemical compositions, and related topics in the snow and ice of the Tian Shan Mountains. Wu and Yao (2005) used HYSPLIT back-trajectory modeling to suggest that westerly winds, the arctic air mass, and local prevailing winds are the main ways that dust is brought to the eastern Tian Shan Mountains. Wang et al. (2013) studied the distribution and environmental significance of nitrate and ammonium in snow on glaciers in the Tian Shan Mountains. They proposed that the spatial distribution of nitrogen-containing ions is influenced by long-distance pollution and atmospheric dust, local anthropogenic outputs such as industry and agriculture, as well as the sampling conditions. You et al. (2019) studied the relationship between ion leaching and meteorological elements on Urumqi Glacier No. 1, finding that the ionic concentration in snow cover decreased with increases in temperature, while precipitation had a relatively weak influence. In addition, some scholars have achieved useful results by studying other glaciers in the Tian Shan Mountains, such as Bogda Glacier (Zhang and Edwards, 2011), Haxilegen Glacier No. 51 (Dong et al., 2011), and Miaoergou Glacier in Hami Prefecture (Chen et al., 2015). These achievements have laid a foundation for the study of snow and ice chemistry in the western alpine mountains of China.

Dust particles are also an important indicator of atmospheric changes associated with changes in temperature, precipitation, and atmospheric circulation (Dong et al., 2011). Central Asia is a major dust source region of the Northern Hemisphere (Dong et al., 2013), from which large amounts of dust are transported to North China, Japan, Korea, the North Pacific, North America, and even the Arctic Greenland ice sheet by atmospheric circulation such as westerly winds (Dong et al., 2014; Wang et al., 2014). The dust concentrations observed in ice or snow result from a combination of interrelated mechanisms, ranging from dust mobilization in source areas by uplift and long-range transport, to deposition onto ice sheets (Ruth et al., 2003; Niu et al., 2017). Long-range transport of contaminants via atmospheric circulation is an important pathway for the accumulation of environmental pollutants in remote regions (Jackson, 1997; Fitzgerald et al., 1998; Niu et al., 2017).

The study area was located in the center of an arid region surrounded by many deserts, such as the Gulbantonggu Desert, Kumtag Desert, and other desertified regions, where dust storms are the main atmospheric phenomenon. Regional differences in the distribution of the geographical environment and atmospheric circulation system determine regional differences in the chemical composition of snow and ice. Dust particles in snow and ice can change the albedo of glaciers, thus affecting their energy balance, accelerating melting and, ultimately, affecting regional water cycles. Therefore, research into the characteristics of dust deposition and its seasonal changes in glacierized regions has become an urgent scientific mission. So far, there has been little in-depth study of the dust layer formation process and variations in particles in the snow of Yushugou Glacier No. 6. Furthermore, the connections between dust storm activity and the deposition mechanisms of particles and ions in snow remain unclear. Therefore, it is necessary to conduct research on particles and ions in snow and ice in Yushugou Glacier No. 6 and compare the results with existing research on other glacierized regions in Tian Shan. This will have two main benefits. 1) It has important theoretical significance for improving models of atmospheric dust circulation and deposition in arid regions of northwest China. 2) It will have extremely important practical significance for exploring regional climate change, water resource dynamics, and ecology construction. This study analyses the chemical characteristics of and seasonal variations in dust particles and major ions in snow collected from Yushugou Glacier No. 6 in the eastern Tian Shan Mountains in the summers of 2017 and 2018. Furthermore, backward trajectory analysis is employed to examine the air mass transport processes relevant to this glacier.

MATERIALS AND METHODS

Study Area and Sampling Strategy

The eastern Tian Shan Mountains lie in the center of arid and semi-arid areas in northwest China. They are surrounded by many deserts, which are source areas for dust activity in central Asia. Yushugou Glacier No. 6 (43°03′N, 94°57′E) is located on the southern slope of Harrick Mountain at the end of eastern Tian Shan (**Figure 1**). It is a typical alpine glacier with an area of 4.06 km^2 (Wang et al., 2017). According to meteorological data from Yushugou Station, the annual maximum temperature in Yushugou Basin is 34.2°C and the annual minimum temperature is −25.8°C, with an average annual temperature of 5.9°C (Ming et al., 2009). Affected by westerly winds, the precipitation in this area is mainly concentrated in summer (79.6% of annual precipitation). From October to March, precipitation is rare (14.5% of annual precipitation) and mainly falls as snow (Luo et al., 1999).

Three snow pits were excavated at different altitudes in Yushugou Glacier No. 6. Samples were collected from Snow pit 1 (Sp-1) in August 2017, Snow pit 2 (Sp-2) in August 2018, and Snow pit 3 (Sp-3) in early June 2018. The sampling depths were Sp-1 = 1.2 m, Sp-2 = 1.2 m, and Sp-3 = 1.0 m. A total of 102 snow samples were obtained from the three snow pits. Additionally, 42 surface snow samples were taken at altitudes of 3,800–4,500 m in August 2018. The sampling process was carried out in strict accordance with snow and ice sampling procedures (Wake et al., 1994; Niu et al., 2013). The selection of snow pit sampling points is very important. We selected relatively flat,

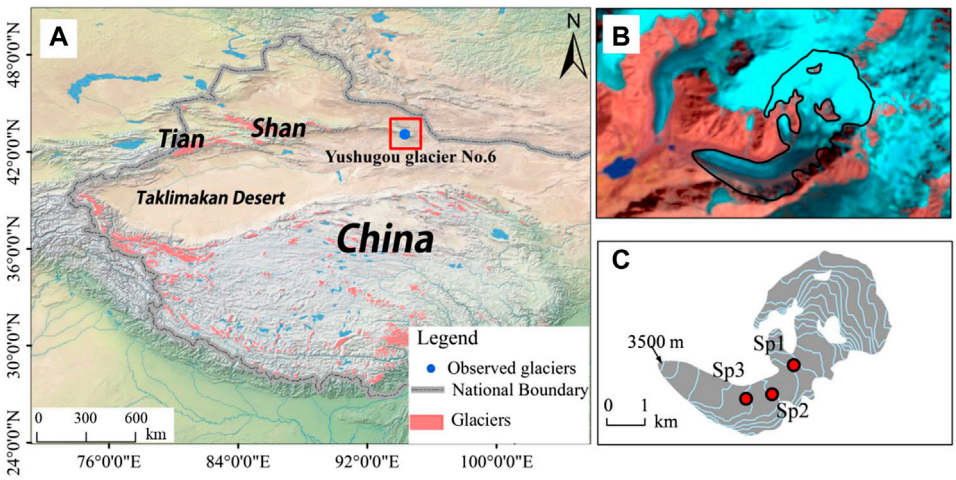

FIGURE 1 | Regional setting of Yushugou Glacier No. 6: **(A)** location in China; **(B)** satellite image with the glacier outlined; **(C)** topographic map of the glacier and the sampling sites in 2017 and in 2018, contour interval = 100 m.

shaded surfaces receiving low sunshine, as such conditions benefit the preservation of snow records (Wang et al., 2017). Sample collection was carried out in strict accordance with purification and pollution prevention requirements. Before sampling, all sample bottles, sampling tools, processing equipment, work clothes, and other equipment were cleaned with deionized water. Polyethylene gloves and face masks were used to avoid contamination of samples. Operators wore cleanroom clothes and the sampling tubes were inserted and removed manually. The sampling tubes had been previously acid-washed (0.05% HNO_3) and individually checked by inductively coupled plasma mass spectrometry (ICP-MS) to ensure there was no significant contamination. Immediately after sample collection, the tubes were sealed inside polypropylene bags and stored at −18°C until analysis. In addition, records were made of the weather conditions, snow pit depth, sampling interval, snow layer characteristics (e.g., dust layer, snow grain size, and hardness), etc. (Qin et al., 1999; Zhang et al., 2007; Wang et al., 2008).

Sample Transportation and Instrument Analysis

Alpine glaciers are mostly distributed in inaccessible mountainous areas. Care must be taken to ensure the integrity of snow samples, particularly in relation to maintaining a constant temperature. Samples were transported in an incubator containing ice cubes. The temperature in the incubator was checked every 4 h and ice cubes were added as necessary to avoid temperature increases. Transport of samples from the field to the laboratory freezer usually took 1–3 days. All samples were analyzed at the State Key Laboratory of Cryospheric Science. Particle analysis was performed using an optical particle detector (Accusizer 780 A) equipped with a 120-orifice by the single-particle optical sensing (SPOS) method (Zhu et al., 2006; Li et al., 2010). Measurements were performed under class 100 conditions on sample aliquots diluted with a pre-filtered NaCl solution to obtain a 2% vol. electrolyte concentration. The range of measurable diameters was 0.57–400 μm. Routine analysis of filtered deionized water blanks showed background counts to be, on average, 10 times lower than those in samples. Background counts were subtracted from the sample data. All samples were analyzed in triplicate in random order. Results were then averaged for individual samples, yielding an estimated error in particle concentration of ≤10% (Steffensen, 1997; Li et al., 2010). The concentrations of cations (Ca^{2+}, Mg^{2+}, Na^+, K^+, and NH_4^+) were detected by an ion chromatograph (Dionex-600) and the concentrations of anions (SO_4^{2-}, NO_3^-, and Cl^-) were detected by a similar machine (Dionex-300) with a measurement accuracy of 10^{-9} g ml^{-1} and a measurement error of <5%.

Research Methods

Factor analysis is a multivariate statistical method. A mathematical model of factor analysis is established on the basis of mass conservation. The basic idea is as follows: According to the analysis of the loading of each factor on each variable, the main factor is determined and the source of the load ion is judged according to its chemical properties (Blifford and Meeker, 1967). The study area was located downwind of the Central Asian sand and dust area, which is strongly affected by westerly winds. Therefore, this study used sea-salt tracer methods to explore the sources of ions. The core of this method is the selection of sea-salt tracer ions (Church et al., 1982; Keene et al., 1986). The determination principle is as follows:

(1) If the equivalent ratios of Mg^{2+}/Cl^- and Na^+/Cl^- concentrations are greater than those of standard seawater (Na^+/Cl^- = 0.859, Mg^{2+}/Cl^- = 0.195), then Cl^- can be used as the sea-salt tracing ion.
(2) If the equivalent ratios of Na^+/Mg^{2+} and Cl^-/Mg^{2+} concentrations are greater than those of standard seawater (Na^+/Mg^{2+} = 4.403, Cl^-/Mg^{2+} = 5.126), then Mg^{2+} can be used as the sea-salt tracing ion.

TABLE 1 | Properties of dust, pH, EC, and main ionic concentrations in snow pits and surface snow at Yushugou Glacier No. 6.

Sampling site	Altitude (m)	pH	EC ($\mu s\ cm_{-1}$)	Dust ($10_3\ ml_{-1}$)	Ion concentrations ($\mu g \cdot L^{-1}$)							
					Ca^{2+}	SO_4^{2-}	Cl^-	Na^+	NO_3^-	K^+	Mg^{2+}	NH_4^+
Snow pit 1	4,200	5.6	3.3	302	74.7	62.1	50.4	52.1	36.5	26.5	24.7	37.1
Snow pit 2	4,000	5.7	3.5	425	135.7	126.1	80.2	55.5	49.0	27.0	26.5	48.8
Snow pit 3	3,900	5.7	3.3	894	172.7	158.2	107.6	85.4	64.8	29.6	28.1	66.6
Mean value	4,033	5.6	3.4	540	132.5	124.6	85.2	69.8	56.4	28.7	27.4	51.4
Surface snow	3,800–4,500	5.5	2.9	342	142.0	72.7	51.2	45.1	42.6	23.1	27.3	58.5
Non-marine source (%)					99	96	66	59	95	91	90	89
Marine source (%)					1	4	34	41	5	9	10	11

(3) If the equivalent ratios of Cl^-/Na^+ and Mg^{2+}/Na^+ concentrations are greater than those of standard seawater ($Cl^-/Na^+ = 1.165$, $Mg^{2+}/Na^+ = 0.227$), then Na^+ can be used as the sea-salt tracing ion.

After selecting a sea-salt tracer ion, we use the formula:

$$N_{NNA} = C_A - R \cdot C_M, \quad (1)$$

where N_{NNA} is the non-marine source part of A, C_A represents the measured concentration of A, M is the sea salt tracer ion, C_M represents the measured concentration of M, and R is the ratio of A to M in standard sea salt.

In addition, the HYSPLIT back-trajectory model was used to simulate the trajectories of air masses reaching Yushugou Glacier No. 6. This model has been widely used in source analyses of aerosols, dust particles, and ions (Mukai and Suzuki, 1996; Lammel et al., 2003; Ming et al., 2009). The analysis is based on the HYSPLIT 4.8 model, which includes the vertical motion pattern of the atmosphere. The backward transport trajectory of the atmospheric air mass at the glacier sampling sites was analyzed and calculated within 3 days.

RESULTS AND DISCUSSION

Characteristics of Ions and Dust Particles

Table 1 shows the pH, EC (electrical conductivity), dust, and concentration values for the major ions found in Yushugou Glacier snow pits and surface snow, as well as their composition characteristics. The ranking of ionic concentrations was, from high to low, $Ca^{2+} > SO_4^{2-} > Cl^- > Na^+ > NO_3^- > NH_4^+ > Mg^{2+} > K^+$, in which SO_4^{2-} and Ca^{2+} were the main anions and cations, respectively. Dibb et al. (2007) found that the main cations and anions in snow on the Greenland Ice Sheet were NH_4^+ and NO_3^-. This is quite different from our result, reflecting regional differences in the chemical ions deposited in snow. Alkaline Ca^{2+} in glacial snow is an indicator of Asian dust, and its concentration usually has a good correlation with the concentration of mineral dust in snow. In particular, the concentrations of SO_4^{2-} and Ca^{2+} in glacial snow in the Asian dust source area are higher than those in marine glaciers and polar regions. The average concentrations of ions in the snow pits were higher than those in the surface snow. Similarly, the conductivity of the snow pits was higher than that of the surface snow. This is most probably because the surface snow contains the recent snowfall in the glacier area, while the snow in pits represents the accumulation of snow and atmospheric chemicals over a long period of time (Niu et al., 2013).

The concentrations of ions and dust particles in different snow pits also differed. According to **Table 1** and **Figure 2**, the elevations of the three snow pits were different. Sp-1 was highest (4,200 m) and its concentrations of ions and dust particles were the lowest. Sp-2 was at the middle elevation (4,000 m) and its concentrations were moderate. Sp-3 had the lowest elevation (3,900 m) and the highest concentrations of ions and dust particles. This phenomenon shows an obvious altitude-related effect. Generally, the ions and dust particles in snow pits are deposited by a combination of precipitation and dry deposition. According to the analysis, the concentrations of dust particles and ions from the Earth's surface and ions carried by vapor from the Atlantic and central Asian lakes will gradually decrease with increasing elevation of the glaciers. On the one hand, this may be related to the altitude that vapor transport can reach. Liu used TRMM precipitation data to calculate that the maximum precipitation on the south slope of Harrick Mountain occurred at elevations of 3,500–3,900 m (Liu et al., 2011). When vapor moves from Sp-3 (3,900 m) to Sp-1 (4,200 m), as the altitude increases, precipitation first increases and then decreases. On the other hand, dust and ions carried by the atmosphere are also affected by elevation as they fall to the surface of the glacier as dry deposition. Numerous studies have shown that the higher the altitude, the lower the concentration of dust particles. For instance, the concentration of dust particles in snow pits in Rongbuk Glacier in the Everest Mountains (6,000 m) is significantly lower than that of eastern Tian Shan (4,000 m), while the concentration of dust particles on glaciers of Tian Shan is much lower than that of Tateyama Mountain (2,100 m) in central Japan (Osada et al., 2004; Wu and Yao, 2005; Dong et al., 2009).

In addition, at different depths in the snow pits, the concentrations of dust particles and ions also showed obvious variation. The influencing factors may include the water vapor source for the glacier area, sand and dust activity, and meltwater leaching of the snow layer (Wake et al., 1994). Taking Sp-3 as an example (**Figure 3**), the concentration of dust particles and ions increased significantly from depths of 40–60 cm in the snow pit where it peaked. There was also an upward trend from 80 to 100 cm. Analysis suggests that this phenomenon must be closely related to the distribution of the dust layer in the snow pits.

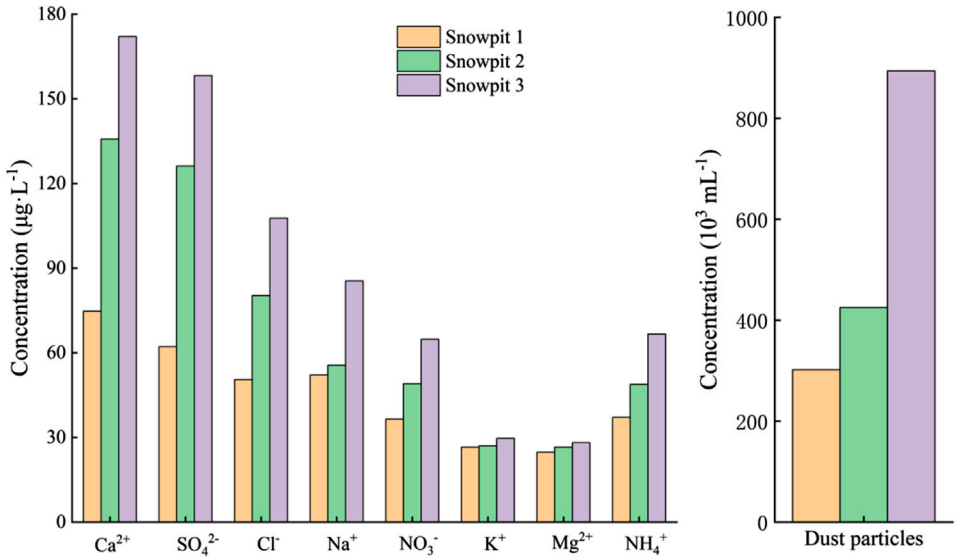

FIGURE 2 | Concentrations of ions and dust particles in snow pits at the study area.

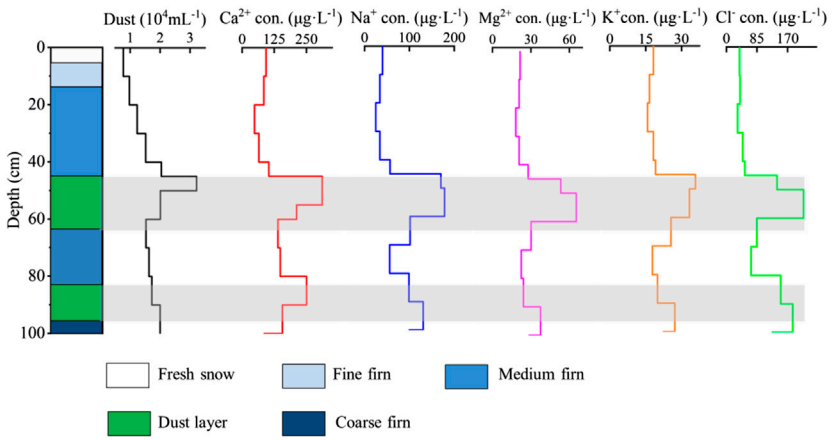

FIGURE 3 | Variations in dust and ions with depth in Snow pit 3.

During sampling in Sp-3, we found a thick fouling layer between 40 and 60 cm. There was also a dust layer at the bottom of Sp-3 that extended to the ice surface, which reflected the occurrence of atmospheric dust activity events. The annual period of sand and dust presence is from March to April each year in the Tian Shan Mountains, Xinjiang, with the frequency of sandstorms being highest in April (Li et al., 2014). Therefore, we suppose that the formation time of the dust layer at 80–100 cm depth in Sp-3 is likely to be the spring of 2017, while the 40- to 60-cm dust layer may well have formed in the spring of 2018. After the dust layer formed in spring 2017, the peak melting period occurred (July–August), and the concentrations of dust particles and ions in the snow layer were greatly depleted due to leaching. Because pit Sp-3 was excavated in early June 2018, the temperature had warmed, and the dust particles and ions in the upper layer (40–60 cm) were subject to some leaching, although the leaching effect was far less than that in the lower layer (80–100 cm). Although leaching of ions from the upper layer may also be a potential cause of the increased ion concentration in the lower layer, the contents of dust particles and ions in the upper layer (40–60 cm) were still higher than in the lower layer (80–100 cm). At the same time, we also analyzed the vertical gradient in dust particle concentration in pit Sp-3, which showed a trend of rising–falling–rising between 0 and 100 cm. Therefore, the vertical gradient in dust particles needs to be described in two stages: 1) from 0 to 40 cm, the concentration increased by 0.32 $ml^{-1} \times 10^4$ ml^{-1} for every 10–cm increase in depth, reaching a peak at 40–60 cm. 2) From 60 to 80 cm, the concentration increased by 0.15 $ml^{-1} \times 10^4$ ml^{-1} for every 10 cm, reaching a peak at 80–100 cm.

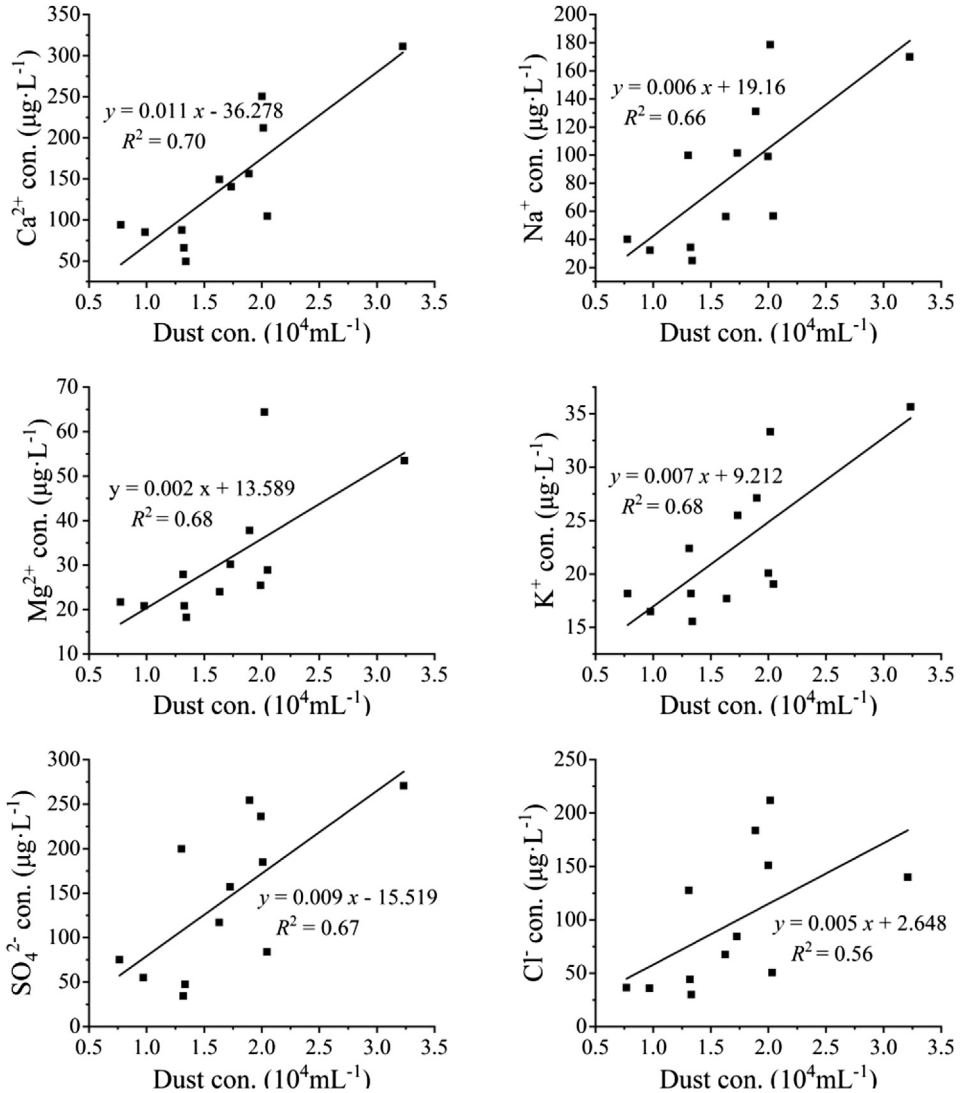

FIGURE 4 | Relationships between concentrations of dust and each of the major ions in snow, with linear models fitted.

In addition, we conducted a regression analysis on dust particle and major ion concentrations (**Figure 4**). Dust concentration was linearly related to the concentrations of Ca^{2+}, Na^{+}, K^{+}, Mg^{2+}, SO_4^{2-}, and Cl^{-} ions, most strongly for Ca^{2+} (R^2 = 0.70). Previous research has found that the concentrations of Ca^{2+}, Mg^{2+} and SO_4^{2-} in snow pits in Urumqi Glacier No. 1 (Tian Shan Mountains) vary seasonally and in relation to dust activity (Li et al., 2010). In this study, the concentrations of dust particles and major ions in pit Sp-3 peaked in the dust layer, and the dust particle concentrations were highly correlated with those of Ca^{2+}, Mg^{2+} and SO_4^{2-} (**Figure 4**). It also can be seen that the Na^{+} and dust particles varied in very similar ways in Sp-3. According to analyses of the environment surrounding the Tian Shan Mountains (Olivier, 2003; Wu and Yao, 2005; Zhang and Edwards, 2011), it was concluded that most Na^{+} in the snow comes from a sand-dust source area of inland Central Asia that is rich in salt mines. In addition, Ca^{2+} is a tracer of mineral particles from the deserts and loess regions of the Asian continent and an indicator of dust from the Asian source region (Kazuo et al., 2004). In addition, the concentrations and sizes of particles are greater in the dust layer and lesser in the non-dust layer. Meanwhile, the settling of particles in the dust layer brings many chemical components to the land surface and atmosphere, which makes the ionic concentration in the snow layer appear to be very high. The significant correlation between the high concentrations of dust particles and main ions. Therefore, seasonal variation in the regional atmospheric environment is the main reason why the concentrations of chemical ions and dust particles in snow at Glacier No. 6 vary with depth.

Seasonal Variation of Dust Particles

The study area is located in the center of the arid and semi-arid regions of northwest China and the source area for Central Asian

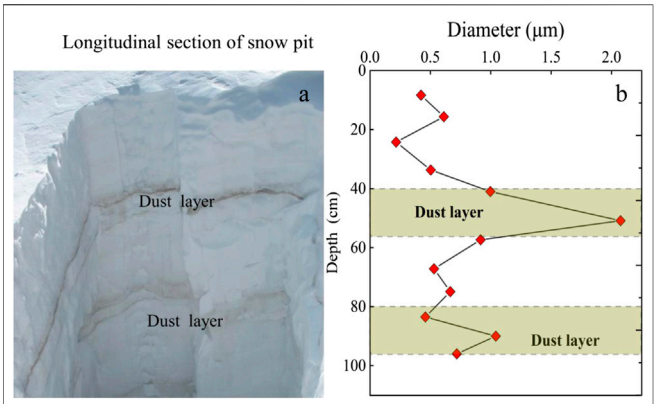

FIGURE 5 | Image of snow pit **(A)** and variation in dust diameter with depth **(B)**.

dust activity. Sandstorm activity is an important feature of the atmospheric environment in this area. Due to the geographical location, the ions and dust particles in high-altitude snow and ice differ significantly between the springtime dust period and the non-dust period. The mean diameter of dust particles in the dust layer always reflects the dust mass concentration, because greater mean diameters are associated with more coarse particles and a greater dust mass concentration. **Figure 5** shows the variation in dust diameter along the longitudinal section of the Sp-3. It can be seen that the dust diameter differs significantly with depth; that is, the mean diameter is high in the dust layer and low in the non-dust layer. This variation indicates that the Yushugou Glacier area is significantly affected by the dust activity of Central Asia.

Figure 6 shows that the mass–size distribution of dust particles in the snow can be approximated by a single model in the non-dust period and a multi-structure model in the dust period. The single distribution model reflects a single source, while the multi-structure distribution model indicates a complex source. Dust particle size distributions are not only related to the transporting winds but also the material sources. In snow samples collected in the non-dust period, dust particle sizes were concentrated in the range of 0.6–40.7 μm (mean = 10.8 μm); when the size is 9.5 μm, the particle mass tends to be the greatest (**Figure 6A**). It is concluded that particles in snow samples from the non-dust period are fine particles transported by westerly winds with long-distance transport. Some studies have proven that in the process of atmospheric dust transport, longer distances result in better particle size separation, causing lower particle concentration and deposition flux in snow and ice (Zdanowicz et al., 1998). For example, it takes a long time for dust to travel from the source to the North Pole, which causes atmospheric aerosol particle concentrations to drop to fairly low levels (Wake et al., 1994; Wei et al., 2005). The multi-structure distribution model refers to the samples taken during the dust period (Snow samples collected from dust layers; **Figure 6B**, in which particle diameters range from 0.3 to 72.6 μm). When the diameter is 10 and 40 μm, the concentration of dust particles reaches a peak. The results show that particles from the dust period samples were mainly coarse mineral dust (18.7–72.6 μm), which is mainly controlled by dust activity. The study area has high wind speeds during the dust period, which can bring a large number of dust particles. For example, the Taklimakan Desert and the Mongolian Desert near the Tian Shan Mountains provide material for the coarse particles found in snow and ice (Dong et al., 2009; Zhang and Edwards, 2011; Chen et al., 2015). In addition, there was a small amount of fine dust (0.3–18.7 μm), which comes from long-distance dust that is present year-round and is mainly controlled by westerly winds. In general, the snow of Yushugou Glacier No. 6 is significantly affected by Central Asian dust activity, and the particle size distributions of insoluble particles differ significantly between the dust and non-dust periods.

Source Analysis of Major Ions in Snow Pits

We used factor analysis to analyze the source of the major ions. The results show that the chemical composition of glacier No. 6 can be divided into three groups: group 1 (Cl^-, Na^+, and K^+), group 2 (NH_4^+, NO_3^-, and SO_4^{2-}), and group 3 (Ca^{2+}, Mg^{2+}, and dust; **Table 2**).

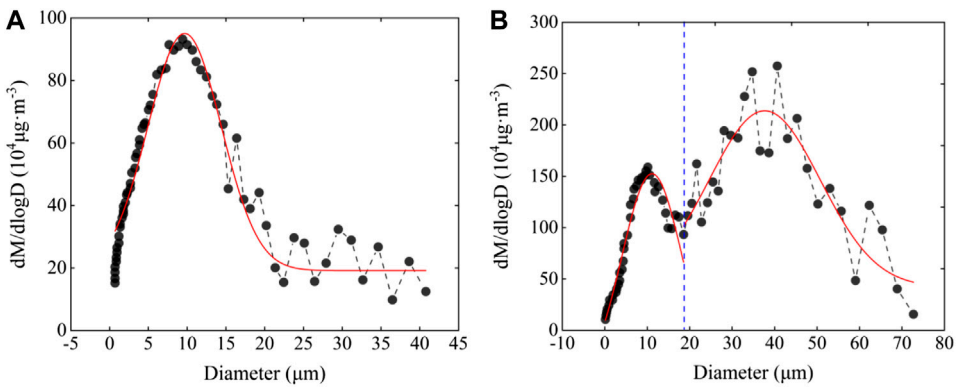

FIGURE 6 | Mass–size distributions of dust in snow at Yushugou Glacier No. 6 during the **(A)** non-dust and **(B)** dust periods.

TABLE 2 | Factor loading matrix for ions in snow pits at Yushugou Glacier No. 6.

Element	Communality	Factor loadings		
		Factor 1	Factor 2	Factor 3
Dust	0.922	0.376	0.345	**0.857**
Ca^{2+}	0.765	**0.714**	0.254	**0.789**
SO_4^{2-}	0.783	0.357	**0.736**	0.237
Cl^-	0.841	**0.784**	0.432	0.313
Na^+	0.862	**0.803**	0.238	0.341
NO_3^-	0.716	–0.065	**0.769**	0.283
Mg^{2+}	0.842	0.364	0.031	**0.836**
K^+	0.733	**0.745**	0.139	0.368
NH_4^+	0.751	0.522	**0.624**	0.031
Fraction of variance (%)		39.3	27.8	19.2
Cumulative (%)		86.3		

Notes: principal component loadings >0.6 shown in bold.

TABLE 3 | Correlations between ion and dust concentrations in snow pits at Yushugou Glacier No. 6 (Person correlation coefficient).

	Cl^-	NO_3^-	SO_4^{2-}	Na^+	NH_4^+	K^+	Mg^{2+}	Ca^{2+}
NO_3^-	0.75							
SO_4^{2-}	0.78**	0.9						
Na^+	0.91	0.53*	0.62					
NH_4^+	0.81	0.86	0.93	0.64				
K^+	0.71*	0.32	0.46*	0.75*	0.68			
Mg^{2+}	0.7**	0.34	0.65**	0.67**	0.82**	0.92**		
Ca^{2+}	0.55*	0.4*	0.82**	0.49*	0.86**	0.81**	0.94**	
Dust	0.78	0.47	0.76	0.58	0.55	0.71	0.77	0.93

*p < *0.05*.
**p < *0.01*.

Factor 1 loadings are the highest in Cl^-, Na^+, and K^+, which have good correlations with each other (**Table 3**). In the northwestern Tian Shan Mountains, there are large salt lakes (Alar Lake, Aibi Lake, Isek Lake, etc.) with high salt contents, and surrounding salt mineral resources are abundant. Under dry, high-temperature climatic conditions, salt lakes evaporate and salt particles rich in Na^+, Cl^-, and K^+ are carried to glacier areas by westerly winds. There are conflicting opinions on the sources of Na^+ and Cl^- in the typical glacier snow cover at the Tian Shan Mountains. One study suggests that the Na^+ and Cl^- ions are mainly derived from terrestrial dust and evaporation of surrounding salt lakes (Olivier, 2003). Other studies have found that at least half of the Na^+ and Cl^- originates from sea salt (Dong et al., 2011; Zhang and Edwards, 2011). In this study, the sea salt tracer method was used to calculate the marine sources of Na^+ and Cl^- (41 and 34%). It was concluded that the Na^+ and Cl^- in the snow at Yushugou Glacier No. 6 have not only terrestrial sources (terrestrial dust and salt lake evaporation) but also some sea salt input.

Factor 2 loadings were highest for NH_4^+, NO_3^-, and SO_4^{2-}, which also had good correlations with each other (**Table 3**). This factor is explained as a component with anthropogenic sources, including burning of fossil fuels and biomass, emissions from livestock and poultry waste, and natural fertilizers. Mineral dust is usually the carrier of such pollutants (Bernabe et al., 2005). Although the area is relatively sparsely populated, glacier No. 6 is only 80 km from Hami Prefecture in the Xinjiang Uygur Autonomous Region, which has more than 600,000 residents. Air pollutants in Hami Prefecture may have been transported to the glacier through low-level regional atmospheric circulation. According to the sea salt calculation formula, non-marine sources accounted for 85 and 89% of the NO_3^- and NH_4^+ in the snow cover at No. 6 glacier, respectively. Combined with the coefficient of correlation between NO_3^- and NH_4^+ (0.86), it can be inferred that the source of these ions is mainly terrestrial. It is generally believed that atmospheric NO_3^- and NH_4^+ are generally caused by the combustion of biological and fossil fuels (secondary reactions of NO_X), chemical fertilizers, motor vehicle exhaust, industrial emissions, and other human activities (Van der A. et al., 2017). The study area is located in the eastern Tian Shan Mountains, which is a typical continental climate area. The westerly winds play a leading role in this area. The air mass passes through central Asia and Xinjiang from west to east, carrying NO_3^-, NH_4^+, and SO_4^{2-} along the way, and eventually reaches the glacier area. In addition, natural pastures are widely distributed around the Tian Shan Mountains, which have a high livestock load, frequent agricultural and animal husbandry activities in summer and autumn, and high rates of biomass combustion (straw and firewood), decomposition of animal excreta and corpses, and fertilizer use, which all produce NO_X and NH_3. The ions SO_4^{2-}, Ca^{2+}, and NO_3^- were also significantly correlated. Moreover, the non-marine source accounted for 96% of the SO_4^{2-}, indicating that SO_4^{2-} in glacial snow is not only derived from input of sand and minerals (such as central Asian dust containing large amounts of $CaSO_4$ and other sulfates) but also from anthropogenic emissions of sulfur pollutants (such as from coal and oil combustion).

Factor 3 loadings were highest in Ca^{2+} and Mg^{2+}, which were also significantly correlated. Many studies have shown that the main chemical components in Asian dust are Ca^{2+} and Mg^{2+}, and their concentrations are closely related to the dust concentration. The analysis shows that Ca^{2+}, Mg^{2+}, K^+, and particles are transported by atmospheric circulation and, after reaching the glacier area, become attached to the snow layer by dry and wet sedimentation, finally forming a dust layer with obvious seasonal characteristics. This phenomenon is similar to the sandstorm weather process occurring in winter and spring, at which time the major chemical ions were observed to peak in the snow pits at glaciers No. 72 and No. 1 in the Tian Shan Mountains. The study area is mainly influenced by westerly winds and is surrounded by large deserts. As the westerly winds pass through the deserts and Gobi, sand, gravel, and dust particles are transported to the surfaces of glaciers by the airflow. Therefore, the Ca^{2+}, Mg^{2+}, and K^+ ions in the snow, which are attached to the dust layer, can be classified as having relatively remote sand and dust sources.

TABLE 4 | Concentrations of major ions (μeq L^{-1}) in snow at various glaciers in China.

Site	Yushugou Glacier No. 6 (this study)	Altai, Belukha Glacier (Olivier, 2003)	Tian Shan, Urumqi Glacier No. 1 (Li et al., 2010)	Himalayas, East Rongbuk Glacier (Gen et al., 2007)	Yu Long, Baishui Glacier No. 1 (Li et al., 2007)
Elevation (m a.m.l.)	4,177	3,800	4,130	6,450	4,600
Ca^{2+}	13.6	3.9	33.9	5.3	1.8
Na^{+}	3	1.6	4.2	0.5	0.02
Mg^{2+}	2.3	0.7	7.8	0.4	0.04
K^{+}	0.7	0.9	0.8	0.2	0.02
NH_4^{+}	2.6	4.7	8.1	3.0	
SO_4^{2-}	2.9	4.0	8.6	1.9	0.4
Cl^{-}	2.4	1.4	4.5	0.5	0.1
NO_3^{-}	0.91	3.5	4.0	0.7	0.3
Total	28.41	20.7	71.9	12.5	2.68

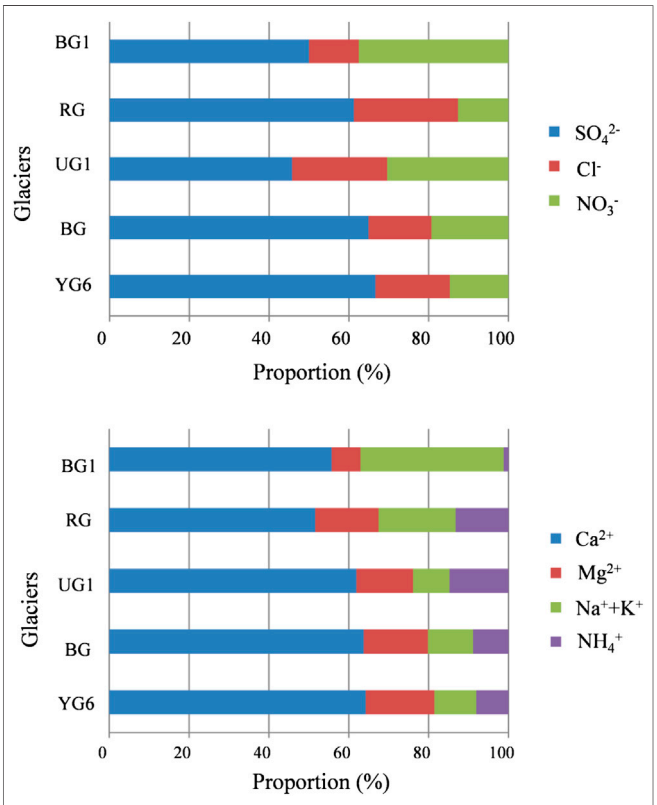

FIGURE 7 | Proportions of major ions in snow pits at various glaciers. YG6, Yushugou Glacier No. 6; BG, Belukha Glacier; UG1, Urumqi Glacier No. 1; RG, Rongbuk Glacier; BG1, Baishui Glacier No. 1.

DISCUSSION

Comparison of the Chemical Characteristics of Snow in Different Glacier Regions

To explain the regional characteristics of chemical ion deposition in the snow pits, this study compared and analyzed the ion contents and compositions of glaciers in other regions. **Table 4** shows that the concentrations of chemical ions in the snow cover of glaciers in the Tian Shan Mountains and Altai Mountains are generally higher, while those at the East Rongbuk Glacier (6,450 m) and Marine Baishui Glacier No. 1 are lower. This reflects spatial differences in chemical ion deposition in snow. In particular, the concentrations of ions in glacial snow cover within the Asian dust source area are generally higher, while those in the Marine Glaciers are lower. This indicates that land-sourced minerals may have a significant influence on the chemical characteristics of the snow cover. **Figure 7** shows the percentages of chemical ions in different glacier regions. The cationic percentage characteristics of Yushugou Glacier No. 6 are extremely similar to those of Urumqi Glacier No. 1 and Belukha Glacier. The percentages of Ca^{2+}, Mg^{2+}, and Na^{+} + K^{+} in the snow pits of Yushugou Glacier No. 6 are higher than those of East Rongbuk Glacier and Baishui Glacier No. 1, indicating that land minerals have a great influence on the chemical characteristics of glacier snow. In the anion composition diagram, the percentages of anions in the snow of different glaciers are significantly different. The percentages of SO_4^{2-} and Cl^{-} in the snow of Yushugou Glacier No. 6 are higher than those of other glaciers, while the percentage of NO_3^{-} in Yushugou Glacier No. 6 is lower and close to that of Rongbuk Glacier. This reflects the regional differences in the chemical compositions of snow in different glaciers. Overall, the proportions of NH_4^{+} and NO_3^{-} in the snow of Yushugou Glacier No. 6 are very low, which indicates that the glacier area is relatively unaffected by regional anthropogenic pollution (such as biomass combustion and fertilization).

Air Mass Transport Path During Dust Events

Figure 8 shows the results of the backward trajectory analysis of air mass transport to the sampling sites at Yushugou Glacier No. 6 during the dust period. According to the observational data of many meteorological stations (Hami Station, Alashan Station, Urumqi Station, etc.), we counted several large-scale sandstorm events from 2017 to 2018 and simulated their air mass transport paths to Yushugou Glacier No. 6. **Figure 8A** shows the track of the sandstorm air masses on August 30, 2017, in which the upper air mass from the southwest originated in Afghanistan, while the

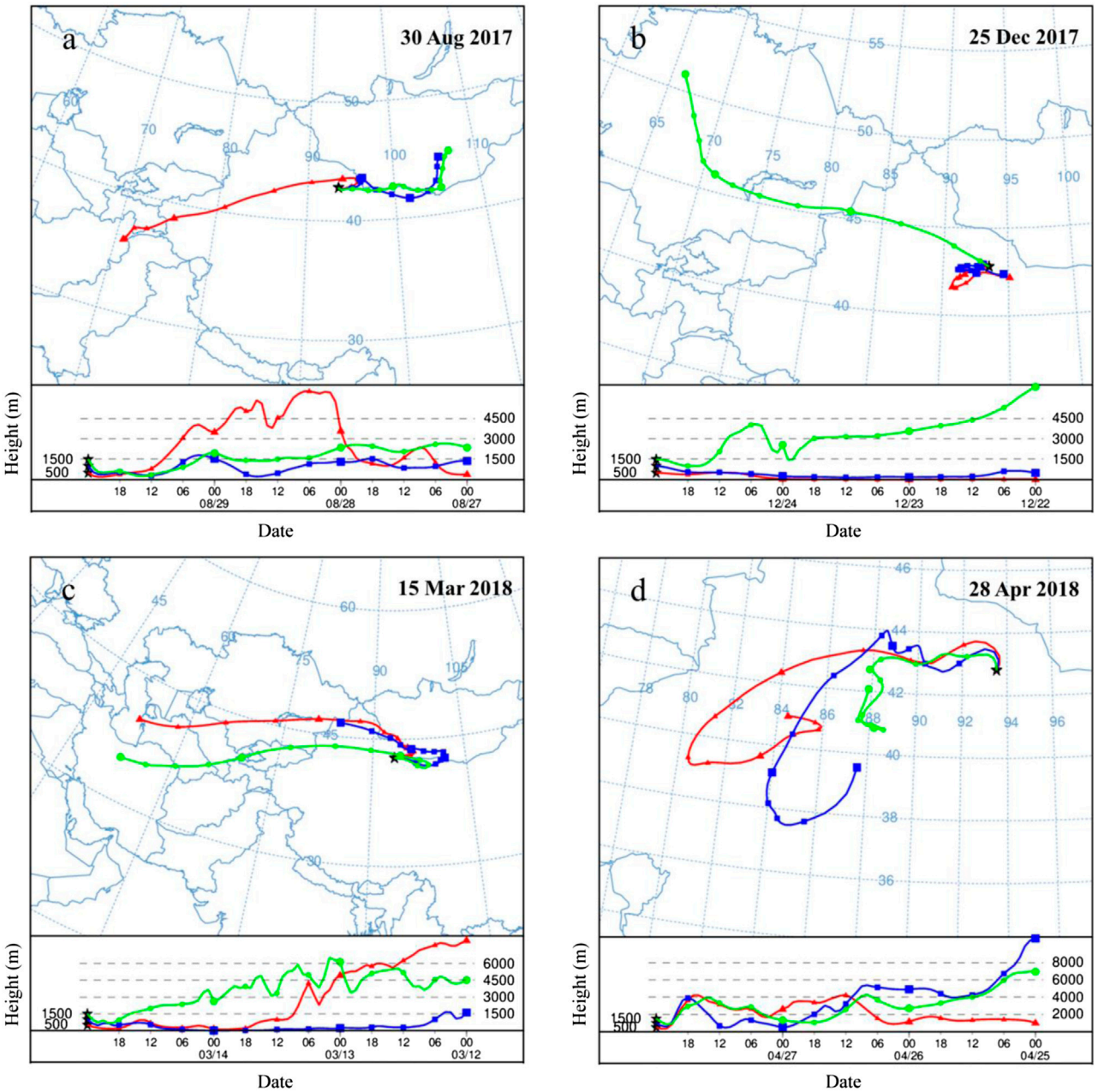

FIGURE 8 | Backward trajectory analysis of several large-scale sandstorm air masses that reached Yushugou Glacier No. 6 during the study period (2017 and 2018).

lower air mass from the east originated in Mongolia. In the sandstorm event on December 25, 2017, the long-path air mass originated in Kazakhstan, while the short-path air mass came from the local deserts and Gobi (**Figure 8B**). **Figure 8C** shows the dust storm air masses on March 15, 2018. These air masses originated from the Caspian Sea coast and crossed Central Asia from west to east until they reached glacier No. 6. The sandstorm air mass on December 25, 2017, originated from the Taklimakan Desert (**Figure 8D**). In conclusion, when sandstorms occurred at Yushugou Glacier No. 6, the air masses mainly came from Mongolia, the Tarim Basin, and Central Asia. It is surrounded by the Taklimakan Desert, Gulbantonggu Desert, and Kumtag Desert (Chen et al., 2015), which are important sources of the dust particles, Ca^{2+} and Mg^{2+}, found in the snow at Yushugou Glacier No. 6.

CONCLUSIONS

This study analyzed the chemical ion characteristics and environmental significance of snow samples from pits and the

surface of Yushugou Glacier No. 6, Tian Shan, based on field sampling, experimental detection, and data processing. We draw the following conclusions.

The ionic concentrations in snow at Yushugou Glacier No. 6 were ranked in order of highest to lowest as $Ca^{2+} > SO_4^{2-} > Cl^- > Na^+ > NO_3^- > NH_4^+ > Mg^{2+} > K^+$. Hence, SO_4^{2-} was the dominate anion and Ca^{2+} was the dominant cation. The major ionic average concentrations, pHs, and electrical conductivities in snow pits were higher than those in surface snow. This is because surface snow is formed from recent snowfall in the glacier area, while the snow in snow pits represents the accumulation of snowfall and atmospheric chemical deposition over a long period.

The concentrations of particles and ions in the snow had obvious seasonal variations, with high concentrations in spring (dust period) and low concentrations in summer (non-dust period). There was a significant difference in the mass–size distribution of particles in snow between the dust and non-dust periods, which indicates that sandstorm activity in Central Asia has a significant influence on the concentrations of chemical ions and dust particles in the snow at Yushugou Glacier No. 6.

The sources of the ions in the snow at Yushugou Glacier No. 6 were mainly land mineral dust and human activities, with a small influence of marine sources. The Ca^{2+}, Mg^{2+}, and K^+ ions in snow pits were generally classified as long-distance land-sourced mineral dust. The Na^+ and Cl^- ions had a terrestrial source with partial sea salt input. The NO_3^-, NH_4^+, and SO_4^{2-} ions were mainly sourced from human industrial and agricultural activities (combustion of biological and fossil fuels, industrial emissions). In addition, a small amount of SO_4^{2-} was sourced from sand and dust minerals.

DATA AVAILABILITY STATEMENT

All datasets generated for this study are included in the article/supplementary files.

AUTHOR CONTRIBUTIONS

All authors contributed to the development of the research question and general conceptual approach. PW, XZ, XZ, and MS developed and applied the statistical analysis and led the writing and production of the manuscript. FW and HZ assisted with access to collect data and precipitation sample.

FUNDING

This work was supported by The Second Tibetan Plateau Scientific Expedition and Research (2019QZKK0201), the Strategic Priority Research Program of Chinese Academy of Sciences (Class A) (XDA20060201; XDA20020102), the National Natural Science Foundation of China (41761134093; 41471058), and The SKLCS founding (SKLCS-ZZ-2020).

REFERENCES

Bernabé, J. M., Carretero, M. I., and Galán, E. (2005). Mineralogy and origin of atmospheric particles in the industrial area of Huelva (SW Spain). *Atmos. Environ.* 39 (36), 6777–6789. doi:10.1016/j.atmosenv.2005.07.073

Blifford, I. H., and Meeker, G. O. (1967). A factor analysis model of large scale pollution. *Atmos. Environ.* 1 (2), 147–157. doi:10.1016/0004-6981(67)90042-x

Chen, W., Li, Z., and Hu, B. (2015). The ionic concentration characteristics in snow pits of Miaoergou Glacier, Tian Shan, Hami Prefecture. *J. Environ. Chem.* 34 (12), 2307–2309 [in Chinese, with English summary].

Church, T. M., Galloway, J. N., Jickells, T. D., and Knap, A. H. (1982). The chemistry of western Atlantic precipitation at the mid-Atlantic coast and on Bermuda. *J. Geophys. Res.* 87 (C13), 11013–11018. doi:10.1029/jc087ic13p11013

Dahe, Q., Shiyin, L., and Peiji, L. (2006). Snow cover distribution, variability, and response to climate change in western China. *J. Clim.* 19 (9), 1820–1833. doi:10.1175/jcli3694.1

Dibb, J., Whitlow, S., and Arsenault, M. (2007). Seasonal variations in the soluble ion content of snow at Summit. Greenland: Constraints from three years of daily surface snow samples. *Atmos. Environ.* 41 (24), 5007–5019. doi:10.1016/j.atmosenv.2006.12.010

Dong, Z., Li, Z., Wang, F., and Zhang, M. (2009). Characteristics of atmospheric dust deposition in snow on the glaciers of the eastern Tien Shan, China. *J. Glaciol.* 55 (193), 797–804. doi:10.3189/002214309790152393

Dong, Z., Li, Z., Zhang, M., Wang, F., and Wu, L. (2011). Physico-chemical characteristics and environmental significance of snow deposition on Haxilegen glacier No. 51 in Tian Shan, China. *J. Mt. Sci.* 8 (3), 484–494. doi:10.1007/s11629-011-1012-3

Dong, Z., Qin, D., Chen, J., Qin, X., Ren, J., Cui, X., et al. (2014). Physicochemical impacts of dust particles on alpine glacier meltwater at the Laohugou Glacier basin in western Qilian mountains, China. *Sci. Total Environ.* 493, 930–942. doi:10.1016/j.scitotenv.2014.06.025

Dong, Z., Qin, D., and Ren, J. (2013). Characteristics of atmospheric dust deposition in snow on the glaciers of western Qilian Mountains. *Acta Geogr. Sin.* 68 (1), 25–35. doi:10.11821/xb201301005

Du, Y., Sun, X., and Adiguzel, O. (2016). Estimation of NOx emission from fossil fuel consumption in China for the period 1980–2012. *MATEC Web of Conferences.* 64, 601–609. doi:10.1051/matecconf/20166406001

Eichler, A., Schwikowski, M., and Gäggeler, H. W. (2001). Meltwater-induced relocation of chemical species in Alpine firn. *Tellus B* 53 (2), 192–203. doi:10.3402/tellusb.v53i2.16575

Fitzgerald, W. F., Engstrom, D. R., Mason, R. P., and Nater, E. A. (1998). The case for atmospheric mercury contamination in remote areas. *Environ. Sci. Technol.* 32 (1), 1–7. doi:10.1021/es970284w

Fuhrer, K., Neftel, A., Anklin, M., Staffelbach, T., and Legrand, M. (1996). High-resolution ammonium ice core record covering a complete glacial-interglacial cycle. *J. Geophys. Res.* 101 (D2), 4147–4164. doi:10.1029/95jd02903

Gen, Z., Hou, S., and Dong, Z. (2007). Major ions in ice cores and snow pits from the Himalayas: temporal and spatial variations and their sources. *J. Glaciol. Geocryol.* 29 (2), 191–200 [in Chinese, with English summary].

Jackson, T. A. (1997). Long-range atmospheric transport of mercury to ecosystems, and the importance of anthropogenic emissions-a critical review and evaluation of the published evidence. *Environ. Rev.* 5 (2), 99–120. doi:10.1139/a97-005

Kazuo, O., Hajime, I., and Mizuka, K. (2004). Mineral dust layers in snow at Mount Tateyama, Central Japan: formation processes and characteristics. *Tellus B* 56 (4), 382–392. doi:10.1111/j.1600-0889.2004.00108.x

Keene, W. C., Pszenny, A. A. P., Galloway, J. N., and Hawley, M. E. (1986). Sea-salt corrections and interpretation of constituent ratios in marine precipitation. *J. Geophys. Res.* 91 (D6), 6647. doi:10.1029/jd091id06p06647

Koven, C. D., Riley, W. J., and Stern, A. (2013). Analysis of permafrost thermal dynamics and response to climate change in the CMIP5 earth system models. *J. Clim.* 26 (6), 1877–1900. doi:10.1175/jcli-d-12-00228.1

Kraaijenbrink, P. D. A., Bierkens, M. F. P., Lutz, A. F., and Immerzeel, W. W. (2017). Impact of a global temperature rise of 1.5 degrees Celsius on Asia's glaciers. *Nature* 549 (7671), 257–260. doi:10.1038/nature23878

Lammel, G., Brüggemann, E., Gnauk, T., Müller, K., Neusüss, C., and Röhrl, A. (2003). A new method to study aerosol source contributions along the tracks of air parcels and its application to the near-ground level aerosol chemical composition in central Europe. *J. Aerosol Sci.* 34 (1), 1–25. doi:10.1016/s0021-8502(02)00134-9

Li, Z., He, Y., and Pang, H. (2007). Source of major anions and cations of snowpacks in the typical monsoonal temper ate glacial region of China. *Acta Geogr. Sin.* 62 (9), 992–1001.

Li, Z., Li, H., Dong, Z., and Zhang, M. (2010). Chemical characteristics and environmental significance of fresh snow deposition on Urumqi Glacier No. 1 of Tianshan Mountains, China. *Chin. Geogr. Sci.* 20 (5), 389–397. doi:10.1007/s11769-010-0412-6

Li, W., Chen, L., and He, Q. (2014). Analysis of sandstorm frequency variation tendency of Xinjiang in recent 50 years. *Environ. Protection of Xinjiang*, 36 (3), 20–24 [in Chinese, with English summary]. doi:10.3969/j.issn.1008-2301.2014.03.005

Liu, J., Chen, S., and Qin, W. (2011). Study on the vertical distribution of precipitation in mountainous regions using TRMM data. *Shuikexue Jinzhan/Adv. Water Sci.* 22 (4), 447–454 [in Chinese, with English summary]. doi:10.1007/s11589-011-0776-4

Liu, Y.-p., Geng, Z.-x., and Hou, S.-g. (2010). Spatial and seasonal variation of major ions in Himalayan snow and ice: a source consideration. *J. Asian Earth Sci.* 37 (2), 195–205. doi:10.1016/j.jseaes.2009.08.006

Luo, G., Liu, L., and Wu, L. (1999). Analysis of hydrological characteristics in the yiwu river basin. *Arid. Land Geogr.* 22 (1), 47–52 [in Chinese, with English summary]. doi:10.13826/j.cnki.cn65-1103/x.1999.01.007

Ma, X., and Luo, X. (2009). Analysis of the impact of climate change on runoff in the Yushugou basin. *China Water Transport.* 9 (10), 190–193 [in Chinese, with English summary]. doi:CNKI:SUN:ZSUX.0.2009-10-090

Massling, A., Nielsen, I., and Kristensen, D. (2015). Atmospheric black carbon and sulfate concentrations in northeast Greenland. *Atmos. Chem. Phys.* 15 (16), 11465–11493. doi:10.5194/acpd-15-11465-2015

Ming, J., Xiao, C., Cachier, H., Qin, D., Qin, X., Li, Z., et al. (2009). Black Carbon (BC) in the snow of glaciers in west China and its potential effects on albedos. *Atmos. Res.* 92, 114–123. doi:10.1016/j.atmosres.2008.09.007

Mukai, H., and Suzuki, M. (1996). Using air trajectories to analyze the seasonal variation of aerosols transported to the Oki Islands. *Atmos. Environ.* 30 (23), 3917–3934. doi:10.1016/1352-2310(96)00142-2

Niu, H., He, Y., Zhu, G., Xin, H., Du, J., Pu, T., et al. (2013). Environmental implications of the snow chemistry from Mt. Yulong, southeastern Tibetan Plateau. *Quat. Int.* 313-314, 168–178. doi:10.1016/j.quaint.2012.11.019

Niu, H., Kang, S., Zhang, Y., Shi, X., Shi, X., Wang, S., et al. (2017). Distribution of light-absorbing impurities in snow of glacier on Mt. Yulong, Southeastern Tibetan Plateau. *Atmos. Res.* 197, 474–484. doi:10.1016/j.atmosres.2017.07.004

Olivier, S. (2003). Glaciochemical investigation of an ice core from Belukha glacier, Siberian Altai. *Geophys. Res. Lett.* 30 (19), 21–24. doi:10.1029/2003gl018290

Olivier, S., Blaser, C., Brütsch, S., Frolova, N., Gäggeler, H. W., Henderson, K. A., et al. (2006). Temporal variations of mineral dust, biogenic tracers, and anthropogenic species during the past two centuries from Belukha ice core, Siberian Altai. *J. Geophys. Res.* 111 (D5). doi:10.1029/2005jd005830

Osada, K., Iida, H., Kido, M., Matsunaga, K., and Iwasaka, Y. (2004). Mineral dust layers in snow at Mount Tateyama, Central Japan: formation processes and characteristics. *Tellus B* 56 (4), 382–392. doi:10.3402/tellusb.v56i4.16436

Prospero, J. M., Ginoux, P., Torres, O., Nicholson, S. E., and Gill, T. E. (2002). Environmental characterization of global sources of atmospheric soli dust identified with the nimbus 7 total ozone mapping spectrometer (TOMS) absorbing aerosol product. *Rev. Geophys.* 40 (1), 4–30. doi:10.1029/2000rg000095

Qin, D., Ding, Y., Xiao, C., Kang, S., Ren, J., Yang, J., et al. (2017). Cryospheric Science: research framework and disciplinary system. *Natl. Sci. Rev.* 5 (2), 255–268. doi:10.1093/nsr/nwx108

Qin, D., Liu, S., and Li, P. (2006). Snow cover distribution, variability, and response to climate change in western China. *J. Clim.* 19 (9), 1820–1833. doi:10.1175/jcli3694.1

Qin, X., Qin, D., Huang, C., et al. (1999). Chemical characteristics of waters in rongbu glacier on mount everest. *Environ. Sci.* 20 (1), 1–6 [in Chinese, with English summary].

Ruth, U., Wagenbach, D., Steffensen, J. P., and Bigler, M. (2003). Continuous record of microparticle concentration and size distribution in the central Greenland NGRIP ice core during the last glacial period. *J. Geophys. Res.* 108 (D3), 4098. doi:10.1029/2002jd002376

Steffensen, J. P. (1997). The size distribution of microparticles from selected segments of the Greenland Ice Core Project ice core representing different climatic periods. *J. Geophys. Res.* 102 (C12), 26755–26763. doi:10.1029/97jc01490

Sugimoto, N., Nishizawa, T., Shimizu, A., Matsui, I., and Kobayashi, H. (2015). Detection of internally mixed Asian dust with air pollution aerosols using a polarization optical particle counter and a polarization-sensitive two-wavelength lidar. *J. Quant. Spectrosc. Radiat. Transf.* 150, 107–113. doi:10.1016/j.jqsrt.2014.08.003

Van der A, R. J., Mijling, B., Ding, J., Koukouli, M. E., Liu, F., and Li, Q. (2017). Cleaning up the air: effectiveness of air quality policy for SO_2 and NO_x emissions in China. *Atmos. Chem. Phys.* 17 (3), 1775–1789. doi:10.5194/acp-17-1775-2017

Wake, C. P., Mayewski, P. A., Li, Z., Han, J., and Qin, D. (1994). Modern eolian dust deposition in central Asia. *Tellus B* 46 (3), 220–233. doi:10.1034/j.1600-0889.1994.t01-2-00005.x

Wang, P., Yao, T., Tian, L., Wu, G., Li, Z., and Yang, W. (2008). Recent high-resolution glaciochemical record from a Dasuopu firn core of middle Himalayas. *Chin. Sci. Bull.* 53 (3), 418–425 [in Chinese, with English summary]. doi:10.1007/s11434-008-0098-7

Wang, S., Zhang, M.-J., Li, Z.-Q., Wang, F.-T., and Zhang, X.-Y. (2013). Distribution and its environmental significance of nitrate and ammonium in snowpack of glaciers in Chinese Tianshan Mountains. *Earth Sci.* 38 (1), 201–210. 10.3799/dqkx.2013.021

Wang, S., Zhang, M., Pepin, N. C., Li, Z., Sun, M., Huang, X., et al. (2014). Recent changes in freezing level heights in High Asia and their impact on glacier changes. *J. Geophys. Res. Atmos.* 119 (4), 1753–1765. doi:10.1002/2013jd020490

Wang, X., Xiao, C., and Gao, X. (2017). Matters needing attention in collection and pretreatment of snow and ice samples in chemical analysis. *J. Glaciol. Geocryol.* 39 (5), 1075–1083 [in Chinese, with English summary]. doi:10.7522/j.issn.1000-0240.2017.0119

Wang, X., Li, Z., and Jiang, C. (2017). Run-off analyses using isotopes and hydrochemistry in Yushugou River basin, eastern Tianshan Mountains. *J. Earth Syst. Sci.* 126 (6), 86. doi:10.1007/s12040-017-0858-3

Wei, J., Li, Y., and Tan, D. (2005). Review of research on insoluble micro-particles in the polar cores. *Adv. Earth Sci.* 20 (2), 216–222 [in Chinese, with English summary]. doi:10.3321/j.issn:1001-8166.2005.02.012

Wu, G., and Yao, T. (2005). Progress in studies on insoluble microparticle in ice cores. *J. Glaciol. Geocryol.* 27 (4), 528–538 [in Chinese, with English summary]. doi:CNKI:SUN:BCDT.0.2005-04-009

Wu, X., Li, Q., Wang, N., Pu, J. C., He, J. Q., and Zhang, C. W. (2011). Regional characteristics of ion concentration in glacial snow pits over the Tibetan Plateau and source analysis. *Environ. Sci.* 32 (4), 971–975. doi:10.1016/S1671-2927(11)60313-1

You, X., Li, Z., and Wang, L. (2019). The relationship between meteorological elements and ice core record forming process and its resolution on Glacier No. 1 in headwater of Urumqi River, eastern Tianshan Mountains. *J. Glaciol. Geocryol.* 41 (2), 259–267. doi:10.7522/j.issn.1000-0240.2019.0065

Zdanowicz, C. M., Zielinski, G. A., and Wake, C. P. (1998). Characteristics of modern atmospheric dust deposition in snow on the penny ice cap, baffin island, arctic Canada. *Tellus B* 50(5), 506–520. doi:10.3402/tellusb.v50i5.16234

Zhang, X., and Edwards, R. (2011). Anthropogenic sulfate and nitrate signals in snow from Bogda Glacier, eastern Tianshan. *J. Earth Sci.* 22 (4), 490–502. doi:10.1007/s12583-011-0196-3

Zhang, Y., Kang, S., and Zhang, Q. (2007). Snow ice records on Mt. Geladandong in the central Tibetan Plateau. *J. Glaciol. Geocryol.* 29 (5), 686–693 [in Chinese, with English summary].

Zhu, Y., Li, Z., and You, X. (2006). Application and technique in glacier by Accusizer 780A optical particle size. *Modern Sci. Apparatus.* 3, 81–84 [in Chinese, with English summary].

Conflict of Interest: The authors declare that the research was conducted in the absence of any commercial or financial relationships that could be construed as a potential conflict of interest.

Copyright © 2020 Liu, Li, Zhou, Wang, Zhang, Wang, Zhang and Song. This is an open-access article distributed under the terms of the Creative Commons Attribution License (CC BY). The use, distribution or reproduction in other forums is permitted, provided the original author(s) and the copyright owner(s) are credited and that the original publication in this journal is cited, in accordance with accepted academic practice. No use, distribution or reproduction is permitted which does not comply with these terms.

frontiers in Earth Science

ORIGINAL RESEARCH
published: 11 December 2020
doi: 10.3389/feart.2020.542557

Spatial Distribution of the Input of Insoluble Particles Into the Surface of the Qaanaaq Glacier, Northwestern Greenland

Sumito Matoba[1]*, *Ryo Hazuki*[1,2], *Yutaka Kurosaki*[1,2] and *Teruo Aoki*[3,4]

[1]Pan-Okhotsk Research Center, Institute of Low Temperature Science, Hokkaido University, Sapporo, Japan, [2]Graduate School of Environmental Science, Hokkaido University, Sapporo, Japan, [3]National Institute of Polar Research, Tachikawa, Japan, [4]Meteorological Research Institute, Japan Meteorological Agency, Tsukuba, Japan

From glaciological observations, we found spatial variation in the input of insoluble particles (ISP) on a glacier surface from atmospheric deposition and outcropping at the surface of the glacier by surface ablation at the ablation area of the Qaanaaq Ice Cap in northwestern Greenland. Possible sources of ISP input to the glacier surface were outcropping at the surface of the glacier by ablation at intermediate and low elevations, and from atmospheric deposition at high elevations. The annual atmospheric deposition of ISP was larger at high elevations than at intermediate and low elevations. The annual abundance of outcropping ISP was larger at intermediate elevations than at low elevations, where the annual ablation rate of the glacier surface was 1.5 times larger than at intermediate elevations. The ISP concentration in the glacier ice at intermediate sites was approximately 10 times larger than at low sites. The water stable isotopes of glacier ice at intermediate sites indicated that glacier ice at the intermediate sites did not form since the last glacial maximum, possibly the Holocene Thermal Maximum. Therefore, the accumulation of the ISP, which is outcropping at the intermediate site, occurred at high elevations after Holocene Thermal Maximum.

Keywords: Greenland, insoluble particles, Qaanaaq, dark ice, albedo reduction

OPEN ACCESS

Edited by:
Helle Astrid Kjær,
Niels Bohr Institute, Denmark

Reviewed by:
Zhiwen Dong,
Chinese Academy of Sciences (CAS), China
David F. Porter,
Columbia University, United States

***Correspondence:**
Sumito Matoba
matoba@lowtem.hokudai.ac.jp

Specialty section:
This article was submitted to Cryospheric Sciences, a section of the journal Frontiers in Earth Science

Received: *13 March 2020*
Accepted: *22 September 2020*
Published: *11 December 2020*

Citation:
Matoba S, Hazuki R, Kurosaki Y and Aoki T (2020) Spatial Distribution of the Input of Insoluble Particles Into the Surface of the Qaanaaq Glacier, Northwestern Greenland. Front. Earth Sci. 8:542557. doi: 10.3389/feart.2020.542557

INTRODUCTION

Ice loss from the Greenland Ice Sheet (henceforth referred to as ice sheet) and local glaciers and ice caps surrounding Greenland (henceforth referred to as glaciers) is one of the largest contributors to the current global sea level rise (Meier et al., 2007; Rignot et al., 2011). Bolch et al. (2013) estimated that the mass loss of glaciers from 2003 to 2008 is responsible for 10% of the global sea level rise. Glaciers are sensitive to recent climate change because they are at relatively low elevations (Hanna et al., 2012). The mass loss of an ice sheet and glaciers is driven mainly by rising air temperature and a reduction in surface albedo (Box et al., 2012). Remote sensing data show the reduction in albedo in recent decades (e.g., Tedesco et al., 2011; Shimada et al., 2016). As the albedo of the ice surface decreases, the absorption of solar radiation at the glacier surface increases, and surface melting is enhanced. The albedo of the surface of glaciers and ice sheets is controlled by snow grain size and the concentration of light-absorbing impurities in snow (henceforth referred to as LAI), such as mineral dust, black carbon, and organic compounds. Snow grain size has increased via accelerated snow metamorphism under recent warm conditions, and coarse snow grains reduce the albedo in the near-

infrared range. LAI reduce the albedo in the visible range. If LAI exist with coarse snow grains, the albedo reduction is enhanced (Warren and Wiscombe, 1980; Aoki et al., 2011; Aoki et al., 2003).

LAI are added to a glacier surface via 1) atmospheric deposition, 2) outcropping at the surface of the glacier during glacier surface ablation, and 3) microbial products and metabolites, and is reduced by 4) meltwater run-off and 5) the decomposition of organic substances via microbial activities and chemical reactions, such as photo-oxidation (e.g., Takeuchi et al., 2018). The main constituent of atmospheric deposition is mineral dust, with a minor contribution of black carbon in Greenland (Aoki et al., 2014a). Several papers show that atmospheric mineral dust deposited on the interior of the ice sheet is mainly transported from Asian deserts by long-distance transport and that atmospheric mineral dust deposited on the ablation area of the ice sheet and glaciers is from local windblown sediment or englacial debris. Asian dust, generated when the surface soil in the arid region of the Asian continental landmass is lifted by winds into the free troposphere, can be transported a long distance (e.g., Uno et al., 2001; Sasaki et al., 2016). Bory et al. (2002) showed that mineral dust in the snow in the last decade at the North GRIP in the central ice sheet was originated from eastern Asia using mineralogical analyses and isotopic analyses of Sr and Nd, which are used for tracer of mineral dust sources. Svensson et al. (2000) showed that the predominant source of mineral dust deposited at Summit of the ice sheet for Younger Dryas, Bølling, Last Glacier Maximum, and the cold and mild glacial periods back to 44 kyr B.P. is found most likely to be eastern Asia. Nagatsuka et al. (2016) showed that mineral dust in the snow at the ablation area of the glacier and the ice sheet in the Qaanaaq region in northwestern Greenland, and the Kangerlussuaq area in western Greenland is originated from moraines and around each glacier using isotopic analyses of Sr and Nd. Windblown sediment or englacial debris in the coastal region of Greenland cannot be lifted up to high elevation where aerosol can be transported a long distance, because the strength of air convection is not enough in the cold region. Moreover, the stability of the atmosphere over the ice sheet developed by anticyclone restricts the transportation of substances from the coastal region of Greenland to inland (e.g., Davidson et al., 1993; Matoba et al., 2014). Therefore, the dominant source of mineral dust in the inland of the ice sheet is a remote area such as Asian deserts. On the other hand, the ablation area of the ice sheet and glaciers locate the coastal region of Greenland and the elevation is low. Thus, the windblown sediment or englacial debris, even coarse particles, can be transported to the low elevation site. Therefore, dominant sources of mineral dust in the ablation area of the ice sheet and glaciers are the windblown sediment or englacial debris in the coastal region of Greenland. Wientjes et al. (2011) indicated that the contribution of outcropping dust to albedo reduction is comparable to that of atmospheric dust.

The spatiotemporal variation in surface albedo and its effects on surface melting in the ablation zone of the ice sheet and glaciers are complex. Field data are insufficient to discuss the regional variation in Greenland, especially for glaciers. Several studies in northwestern Greenland have examined the mass balance and variation in surface albedo at the Qaanaaq Glacier and Ice Cap. Aoki et al. (2014b) installed an automatic weather station at site SIGMA-B (944 m elevation) on the Qaanaaq Ice Cap in 2012 and made glaciological observations; they reported temporal changes in snow height, air temperature, and surface conditions. In 2012, the surface at site SIGMA-B was slushy and was covered with snow or ice grains containing dark material, whereas the surface of large areas at elevations higher than about 700 m a.s.l. was covered with snow in 2013. Sugiyama et al. (2014) observed the surface melt rate, ice flow velocity, and ice thickness along a survey route on an outlet glacier (Qaanaaq Glacier) from the Qaanaaq Ice Cap, and showed that the degree-day factor was larger on the dark surface in the middle of the glacier than on relatively clean surfaces at lower and higher parts of the glacier. They suggested the importance of darkening on the increased surface melting of glaciers. Tsutaki et al. (2017) reported the surface mass balance, ice velocity, and ice temperature along the flow line of the Qaanaaq Glacier and site SIGMA-B. Takeuchi et al. (2018) showed the mechanisms for the development and collapse of cryoconite holes based on observations on the Qaanaaq Ice Cap. Nagatsuka et al. (2014) indicated that mineral dust in cryoconite on the Qaanaaq Glacier was supplied from englacial dust and moraines near the glaciers rather than from distant areas based on analyses of strontium and neodymium isotopes in mineral dust in the cryoconite. Søndergaad et al. (2019) reported the glacier history of the Qaanaaq Ice Cap using geomorphological mapping, ^{10}Be exposure dating of boulders, and lake sediment cores and suggested that the Qaanaaq Ice Cap survived the Holocene Thermal Maximum, although the ice cap was smaller than at present between 3.3 ± 0.1 and 0.9 ± 0.1 kcal BP, and it advanced again at the Little Ice Age.

Uncertainty about the spatiotemporal variation in dark material on the Qaanaaq Ice Cap and the processes that increase or decrease these materials persists. Here, we focused on the processes inputting materials to the surface of the Qaanaaq Ice Cap and report the spatial variation in the input of materials from atmospheric deposition and outcropping from the inside of the glacier at the ice cap based on investigations conducted on the glacier in 2017.

METHOD

The Qaanaaq Ice Cap (77°28′N, 69°14′W), located in northwestern Greenland, covers an area of 312 km^2 and an elevation range of 30–1,110 m a.s.l. over the central part of a peninsula (**Figure 1**). Since 2012, several field campaigns have been conducted on the Qaanaaq Glacier, which flows southwest from the southern part of the Qaanaaq Ice Cap, and six observation sites were established along the flowline of the Qaanaaq Glacier (Aoki et al., 2014b; Sugiyama et al., 2014; Tsutaki et al., 2017) (**Table 1**). We conducted field observations at these sites and the SIGMA-B site, where an automatic weather station was installed in 2012 (Aoki et al., 2014b). We made snow pit observations at each observation site, observed stratigraphic features by eye using a loupe, and

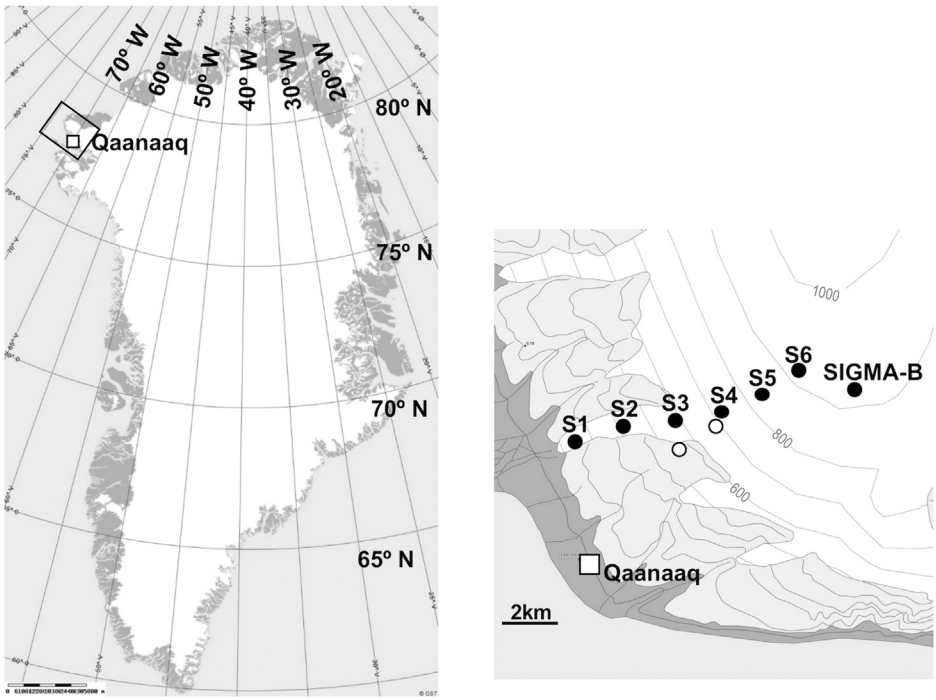

FIGURE 1 | Locations of the study area and the observation sites showing measurement sites (solid circles) and places of atmospheric deposition sampling (white circle). A square indicates Qaanaaq village. The contour interval is 100 m.

measured snow density using a 100-cm^3 snow sampler and an electric balance, and snow temperature using a PT100 sensor. The observations were conducted on June 12, 2017, at sites 1 and 2, June 14 at site 3, June 9, and 14 at site 4, June 17 at sites 5 and 6, and June 9 at the SIGMA-B site.

We collected snow samples from full depth seasonal snowpack at each site to estimate the amount of atmospheric deposition during snow season. We also collected ice samples from the glacier under the seasonal snowpack at each site to estimate the amount of outcropping substance by surface ablation of the glacier. We took snow and ice samples using a stainless sampler and then stored them in polyethylene bags, melted the samples in the bags at ambient temperature, and decanted the sample into polypropylene bottles. In this research, we did not consider the increase in the mass of the concentration of insoluble particles (ISP) due to biological activity on the glacier surface. To avoid contamination by material that covered the glacier surface the previous summer, we collected only ice underneath the glacier surface of the previous summer. To confirm that the ice sampled could be collected from the inside of the glacier, and not from superimposed ice formed within the past few years or glacier surface in last summer, we measured the tritium concentration using a liquid scintillation counter (LSC-LB1, Aloka). If the ice had formed within a few decades, tritium from natural sources produced by the reaction with cosmic rays should be detected. We examined only samples in which no tritium was detected. To determine whether the sampled ice had formed in the Holocene or last glacial period, we measured the stable isotopes of water in ice samples using wavelength-scanned cavity ring-down spectroscopy (L2130i, Picarro).

We also collected atmospheric depositional materials using buckets filled with pure water tied to wooden stakes. The bucket samplers were set at site 4 and on a moraine near site 3, where surface albedo reduction by LAI had been observed by Sugiyama et al. (2014), from June 6 to July 4, 2017. The diameter of the open mouth of each bucket was 0.2 m. After the sampling period, we recovered the materials and liquid in the buckets. To avoid contaminations from the snow surface and ground surface, the buckets were set 1.5 m height.

We measured the ISP concentration in both snowpack and bucket samples using a Coulter counter (Multisizer 3, Beckman Coulter) using standard analytical conditions.

TABLE 1 | Elevation, surface mass balance (SMB), and annual abundance of atmospheric deposition and outcropping of ISP.

Site	Elevation m a.s.l.	SMB m w.e. yr^{-1}	Annual atm. dep	Annual outcropping
			$mm^3\ m^{-2}\ yr^{-1}$	
1	243	–1.65	5.0	1,585.7
2	427	–1.67	62.1	5,589.4
3	584	–1.07	211.5	48,810.8
4	739	–0.86	223.2	13,109.7
5	839	–0.49	2382.4	1,501.0
6	968	–0.05	1013.6	5.0
Bucket	739		44.5	

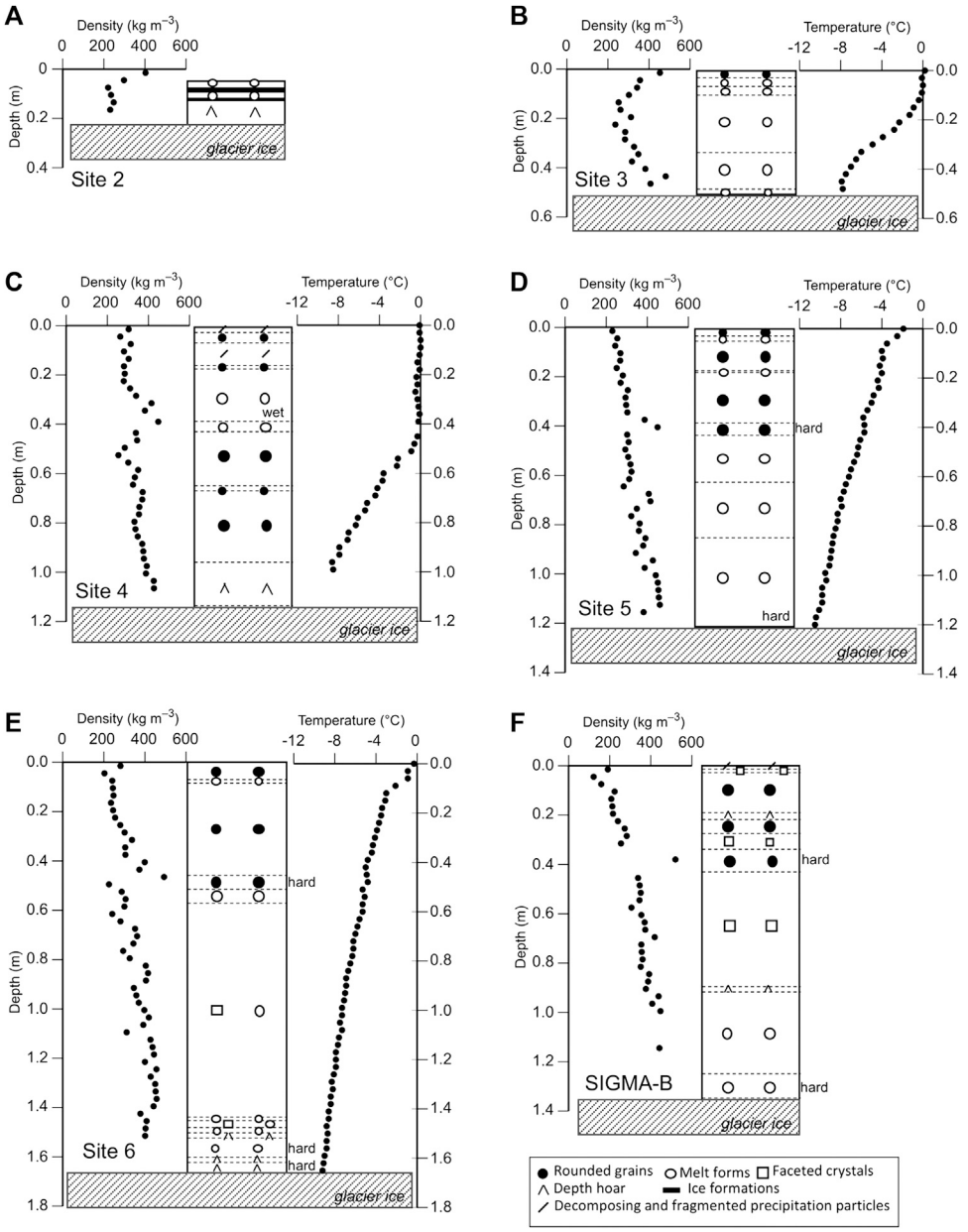

FIGURE 2 | Snow stratigraphy and vertical profiles of snow density and snow temperature in snow pits at sites 2–6 **(A–E)** and SIGMA-B site **(F)**. The characters showing snow classification of stratigraphy are following by the snow classification by Fierz et al. (2009). Shading areas represent glacier ice under seasonal snow layer. "hard" represents relatively hard snow layer. "wet" in figure c represents a snow layer containing liquid water.

RESULTS AND DISCUSSIONS

Figure 2 shows the vertical profiles of snow density, snow stratigraphy, and snow temperature of the seasonal snowpack at sites 2–6 and SIGMA-B on the Qaanaaq Glacier. Most of the snowpack of seasonal snow at sites 3 and 4 consisted of melt forms. At site 3, the snow density exceeded 300 kg m^{-3} at the surface, decreased with snow depth to 0.2 m, and then increased with snow depth below 0.4 m. The snow temperature was 0°C from the surface to 0.1 m depth and below 0°C at greater depths. At site 4, the snow density above 2.5 m was approximately 300 kg m^{-3}, increased with snow depth to 0.4 m, and then decreased with snow depth to 0.55 m. The snow temperature was 0°C from the surface to 0.4 m depth and below 0°C at greater depths. These profiles from sites 3 and 4 indicate that the upper parts of the snowpack had already melted but that the amount of melting was not remarkable, and no meltwater had been washed out of the snowpack. At sites 5, 6, and SIGMA-B, most of the

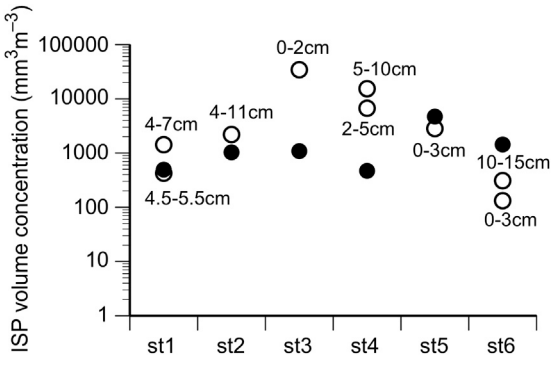

FIGURE 3 | Mass concentrations of ISP in snowpack **(solid circle)** and the glacial ice **(open circle)** at site 1–6.

seasonal snow snowpack consisted of rounded grains. The snow temperature at all depths was below 0°C. These profiles indicate that the snowpack at sites 5, 6, and SIGMA-B had not melted before the observations. We calculated the snow water equivalent (SWE) depth of seasonal snow at each site from the snow depth and density.

Figure 3 shows the ISP concentrations in seasonal snow and glacier ice at each site. The ISP concentration in seasonal snow ranged from 490 to 4,710 $mm^3\ m^{-3}$ and was highest at site 5. The ISP concentrations were higher in glacial ice than in the seasonal snow and had a wider range from 1,320 to 34,300 $mm^3\ m^{-3}$. The glacial ice ISP concentrations were highest at intermediate elevations (sites 3 and 4) on the Qaanaaq Glacier.

We calculated the annual flux of atmospheric deposition of ISP from the ISP concentrations in the snowpack as:

$$F_{air\,(snow)} = C_{snow} \cdot H_{snow} / t_{snow},$$

where $F_{air(snow)}$ is the annual flux of atmospheric ISP, C_{snow} is the ISP concentration in the snowpack, H_{snow} is the SWE at the site, and t_{snow} is the period from the first day of snow accumulation in this season to the day of the observation. We set August 17, 2016, as the first day of snow accumulation in this season based on the variation in snow height at site SIGMA-B recorded by the automatic weather station (Aoki et al., 2014b; Aoki et al., 2014c).

We also calculated the annual flux of the atmospheric deposition of ISP with the amount of ISP collected by the bucket samplers as:

$$F_{air\,(bucket)} = C_{bucket} \cdot V_{bucket} / S_{bucket} \cdot t_{bucket},$$

where $F_{air(bucket)}$ is the annual flux of atmospheric ISP, C_{bucket} is the measured concentration of ISP in the water in a bucket, V_{bucket} is the volume of water in the bucket at the end of sampling, S_{bucket} is the area of the open mouth of the bucket, and t_{bucket} = 0.071 years (26 days) is the period of bucket sampling from June 6 to July 4, 2017. **Table 1** shows the calculated annual fluxes. $F_{air(bucket)}$ was comparable to $F_{air(snow)}$, although the period of bucket sampling differed from the snow cover period used for the $F_{air(snow)}$ calculations.

The annual abundance of ISP outcropped from the glacier surface is the abundance of ISP contained in the glacier ice which melts in an ablation season at each site. We calculated the annual abundance of outcropping ISP at glacier surface at each site as:

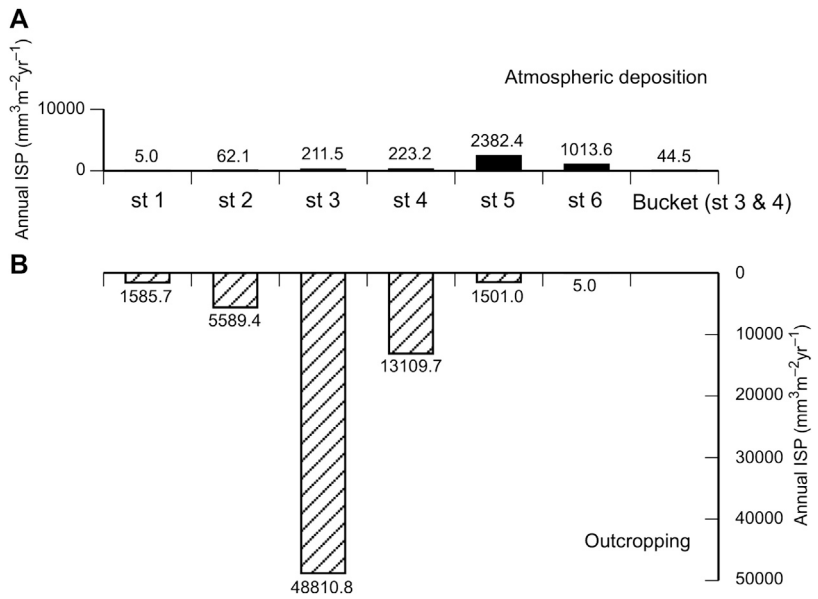

FIGURE 4 | (top) Annual flux of atmospheric ISP estimated from ISP concentration in seasonal snowpack in site 1–6 (st1 - st6), and from ISP concentration collected by bucket samplers set in sites 3 and 4 (right most). Value estimated by the bucket samplers is average of those in site 3 and site 4. Numbers of bar graphs indicate the estimated annual flux of atmospheric ISP ($mm^3\ m^{-2}\ yr^{-1}$). **(bottom)** Annual abundance of outcropping ISP at the surface of the glacier estimated by ISP concentrations in the glacier ice and annual surface mass balance at each site 1–6. Numbers of bar graphs indicate the estimated annual abundance of outcropping ISP ($mm^3\ m^{-2}\ yr^{-1}$) in each site.

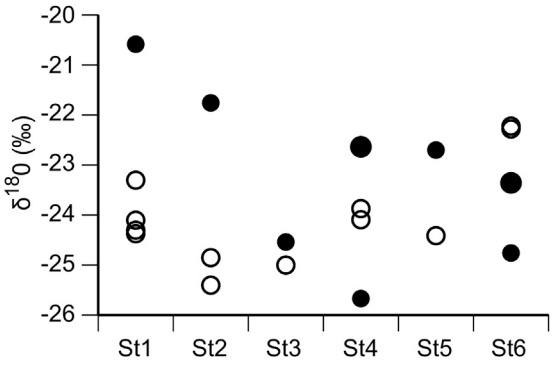

FIGURE 5 | $\delta^{18}O$ of snow of the seasonal snow (solid circle) and the glacial ice (open circle) at site 1–6.

$$F_{out} = C_{ice} \cdot A_{ice},$$

where F_{out} is the annual abundance of outcropping ISP, C_{ice} is the ISP concentration in glacial ice, and A_{ice} is the annual ablation rate of the glacier surface at the site. We used the A_{ice} averages of the annual surface mass balance from 2012/13 to 2015/16 reported by Tsutaki et al. (2017). Table 1 shows the calculated annual values of the outcropped ISP.

Figure 4 shows the annual flux of atmospheric ISP and the annual abundance of outcropping ISP at each site. The dominant source of ISP input to the glacier surface was atmospheric deposition at sites 5 and 6 and outcropping from glacial ice at sites 1–4, where it exceeded 97%. The annual flux of atmospheric ISP was higher at sites 5 and 6. The annual abundance of outcropping ISP was higher at sites 3 and 4.

We consider the cause of the spatial distribution of atmospheric deposition of ISP, which was higher at sites 5 and 6. Hashimoto et al. (2018, 2019) reported that occasional events of intense winds in winter and early spring in this region. Numerical simulation results show that the intense wind is driven by a northerly lee side downward wind from the ice sheet when low pressure exists over the northern Baffin Bay. We speculate that the northerly intense wind from the ice sheet to the Qaanaaq Ice Cap can blow up mineral dust from glacier moraine between the ice sheet and the Qaanaaq Ice Cap, and transport the mineral dust over the Qaanaaq Ice Cap from north to south. Therefore, the ISP concentrations in the snowpack at the more northern and higher elevation sites (5 and 6) are higher than at lower sites (1–4) (Hashimoto et al., 2018).

Next, we considered the cause of the spatial distribution of outcropping ISP, which was very high at sites 3 and 4, where dark material covered the glacier surface (Sugiyama et al., 2014). Although the annual ablation rate of the glacier surface was 1.5 times higher at sites 1 and 2 than at sites 3 and 4, the abundance of outcropping ISP at sites 1 and 2 was lower because the ISP concentrations in the glacial ice at sites 3 and 4 were approximately 10 times higher than those at sites 1 and 2.

We consider why the ISP concentrations in the glacial ice at sites 3 and 4 were higher than those at sites 1 and 2. The equilibrium line altitude (ELA) of the Qaanaaq Glacier is approximately 900 m a.s.l. (Tsutaki et al., 2017). The ice in the present ablation zone formed in a higher accumulation zone in the past and flowed to the present position with the glacier dynamics. Therefore, the ISP at sites 1, 2, 3, and 4 accumulated at high elevation areas in the past. One possible mechanism to accumulate the high ISP concentration at higher elevation areas is the high atmospheric deposition of mineral dust in the past. During the glaciation period, water circulation in the atmosphere weakens, and airborne dust can be transported over long distances. Therefore, the mineral dust concentration in the upper troposphere increases (e.g., Lambert et al., 2008). The rate of mineral dust deposition on land and ocean also increased in the glaciation period (e.g., Lambert et al., 2008). The concentration of mineral dust in an ice core obtained from the Greenland Ice Sheet was more than 10 times higher during the glaciation period than in the Holocene (e.g., Ruth et al., 2003). To identify whether glacier formation and ISP deposition, which is occurring at sites 3 and 4 at present, had occurred at higher elevations in the glaciation period, we measured the water stable isotopes of the glacial ice sample at sites 3 and 4. Generally, the water stable isotope ratio is smaller at cold temperatures. In Greenland ice cores, $\delta^{18}O$ was 5–8‰ lower during the glaciation period than at present (Svensson et al., 2008). However, the $\delta^{18}O$ in the glacial ice sample was comparable with that in seasonal snow at present (**Figure 5**). Therefore, we concluded that ISP contained in the inside of the glacier at sites 3 and 4 was deposited in the Holocene. We postulated the following mechanism for the high ISP concentrations deposited on the glacier surface at higher elevations in the Holocene (**Figure 6**). In a warmer period, the ELA was higher than at present, and the ablation zone expanded to higher areas. In this higher ablation zone, ISP accumulated annually via atmospheric deposition, outcropping substances at the surface of the glacier by ablation, and microbe activities. Then, the air temperature decreased, and ELA descended to the present elevation. The area where the ISP had accumulated became the accumulation zone, and the ISP was transported into the inside of the glacier with accumulated snow. Then, the ISP flowed up to the glacier surface at sites 3 and 4 at present. Søndergaad et al. (2019) believed that the Qaanaaq Ice Cap survived the Holocene Thermal Maximum, but was smaller from 3.3 ± 0.1 to 0.9 ± 0.1 kcal BP than at present, before expanding in the Little Ice Age. The ISP accumulation in higher areas may have occurred in the warm period before the Little Ice Age. To verify this mechanism, further studies need to include glacier flow dynamics and quantitative evaluation of the contribution of microbe activities.

CONCLUSION

We conducted glaciological observations in the ablation zone of the Qaanaaq Glacier in northwestern Greenland to reveal the spatial variation in the input of insoluble particles (ISP)

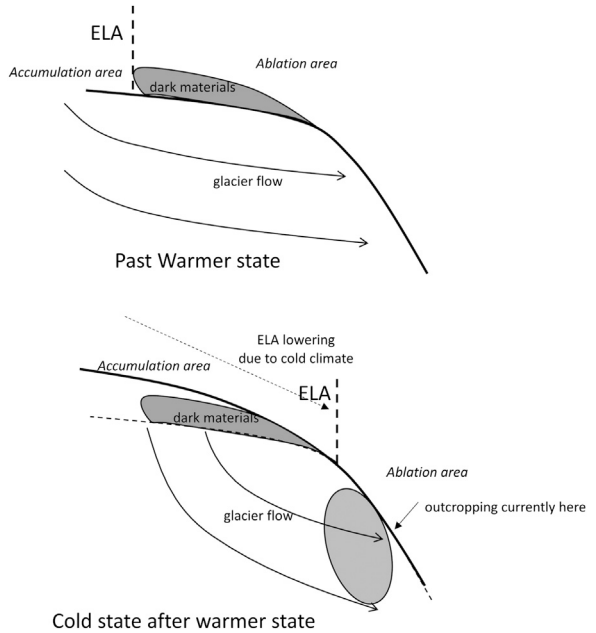

FIGURE 6 | Schematic drawing of accumulation of dark materials in warmer state and outcropping of dark materials in current state. Dark materials accumulated in Past Warmer state is conveyed with glacier flow in Cold States inside glacier, then is outcropping currently at intermediate of the glacier.

on the glacier surface from atmospheric deposition and outcropping at the surface of the glacier by ablation. The annual abundance of atmospheric depositions of ISP was estimated from ISP concentrations in the seasonal snowpack before the snowmelt season at low (sites 1 and 2), intermediate (sites 3 and 4), and high (sites 5 and 6) elevation sites. ISP was collected by bucket samplers at site 4 and a side moraine. The annual abundance of atmospheric ISP at site 4 estimated using the seasonal snowpack was comparable to that based on bucket sampling. The annual atmospheric ISP was higher at sites 5 and 6 because the intense wind from the Greenland Ice Sheet blows over the Qaanaaq Ice Cap and transports mineral dust to higher areas on the Qaanaaq Ice Cap. The annual abundance of outcropping ISP was higher at sites 3 and 4 because the ISP concentrations in the glacial ice at sites 3 and 4 were higher, although the annual ablation rate was higher at sites 1 and 2 than at sites 3 and 4. Because the water stable isotopes of the glacial ice at sites 3 and 4 were not the values found in the glaciation period, we propose that concentrated ISP, which accumulated at higher elevations in a warmer Holocene period, is flowing up at sites 3 and 4 at present.

DATA AVAILABILITY STATEMENT

All datasets generated for this study are included in the article.

AUTHOR CONTRIBUTIONS

SM: Designed research, conducted field research, and wrote the paper. RH: Conducted field researches and laboratory analyses and wrote this paper. YK: conducted field researches. TA: Gave technical supports.

FUNDING

This study was supported by MEXT/JSPS KAKENHI (18H05292, 17H01156, 16H01772, and 15H01733), ArCS (Arctic Challenge for Sustainability), ArCS II (JPMXD1420318865), grant from the Joint Research Program of the Institute of Low Temperature Science, Hokkaido University (18S007 and 19G043), and Okhotsk Network Program from the Pan-Okhotsk Research Center, Institute of Low Temperature Science, Hokkaido University.

ACKNOWLEDGMENTS

We thank Navarana K'avigak, Toku Ohshima, Kim Petersen, and Sofie Jensen for their support in Qaanaaq. We also thank Tetsuhide Yamasaki, Yoshinori Iizuka, Naga Ohshima, Tomonori Tanikawa, and Masashi Niwano for support of field observations. We also appreciate reviewers and a scientific editor Dr. Helle Astrid Kjær for their helpful comments.

REFERENCES

Aoki, T., Aoki, T., Fukabori, M., Hachikubo, A., Tachibana, Y., and Nishio, F. (2000). Effects of snow physical parameters on spectral albedo and bidirectional reflectance of snow surface. *J. Geophys. Res.* 105, 10219–10236. doi:10.1029/1999JD901122

Aoki, T., Hachikubo, A., and Hori, M. (2003). Effects of snow physical parameters on shortwave broadband albedos. *J. Geophys. Res.* 108, 4616. doi:10.1029/2003JD003506

Aoki, T., Kuchiki, K., Niwano, M., Kodama, Y., Hosaka, M., and Tanaka, T. (2011). Physically based snow albedo model for calculating broadband albedos and the solar heating profile in snowpack for general circulation models. *J. Geophys. Res.* 116, D11114. doi:10.1029/2010JD015507

Aoki, T., Matoba, S., Yamaguchi, S., Tanikawa, T., Niwano, M., Kuchiki, K., et al. (2014a). Light-absorbing snow impurity concentrations measured on Northwest Greenland Ice Sheet in 2011 and 2012. *Bull. Glacier Res.* 32, 21–31. doi:10.5331/bgr.32.21

Aoki, T., Matoba, S., Uetake, J., Takeuchi, N., and Motoyama, H. (2014b). Field activities of the "snow impurity and glacial microbe effects on abrupt warming in the Arctic" (SIGMA) project in Greenland in 2011-2013. *Bull. Glacier Res.* 32, 3–20. doi:10.5331/bgr.32.3

Aoki, T., Matoba, S., Yamaguchi, S., Fujita, K., Yamasaki, T., Tanikawa, T., et al. (2014c). SIGMA-AWS dataset, 1.10, arctic data archive system (ADS), Japan. Available at: http://ads.nipr.ac.jp/dataset/A20140714-002.

Bolch, T., Sandberg Sørensen, L., Simonsen, S. B., Mölg, N., Machguth, H., Rastner, P., et al. (2013). Mass loss of Greenland's glaciers and ice caps 2003-2008

revealed from ICESat laser altimetry data. *Geophys. Res. Lett.* 40, 875–881. doi:10.1002/grl.50207010.1002/grl.50270

Bory, A. J.-M., Biscaye, P. E., Svensson, A., and Grousset, F. E. (2002). Seasonal variability in the origin of recent atmospheric mineral dust at NorthGRIP, Greenland. *Earth Planet Sci. Lett.* 196, 123. doi:10.1016/S0012-821X(01)00609-4.

Box, J. E., Fettweis, X., Stroeve, J. C., Tedesco, M., Hall, D. K., and Steffen, K. (2012). Greenland ice sheet albedo feedback: thermodynamics and atmospheric drivers. *Cryosphere* 6, 821–839. doi:10.5194/tc-6-821-2012

Davidson, C. I., Jaffrezo, J.-L., Small, M. J., Summers, P. W., Olson, M. P., and Borys, R. D. (1993). Trajectory analysis of source regions influencing the south Greenland Ice Sheet during the Dye 3 gas and aerosol sampling program. *Atmos. Environ A* 27, 2739–2749. doi:10.1016/0960-1686(93)90306-J.

Fierz, C., Armstrong, R. L., Durand, Y., Etchevers, P., Greene, E., MacClung, D. M., et al. (2009). "The international classification for seasonal snow on the ground," in *IHP-VII technical documents in hydrology No. 83, IACS contribution No.1* (Paris, France: UNESCO-IHP), 90.

Hanna, E., Mernild, S. H., Cappelen, J., and Steffen, K. (2012). Recent warming in Greenland in a long-term instrumental (1881-2012) climatic context: I. Evaluation of surface air temperature records. *Environ. Res. Lett.* 7 (4), 045404. doi:10.1088/1748-9326/7/4/045404

Hashimoto, A., Niwano, M., Yamaguchi, S., Yamasaki, T., and Aoki, T. (2018). Numerical simulation of lee-side downslope winds near Siorapaluk in northwest Greenland. *CAS/JSC WGNE Res. Act. Atmos. Oceanic Modell.* 48, 505–506.

Hashimoto, A., Yamasaki, T., Teruo, A., Masashi, N., and Yamaguchi, S. (2019). Occurrence frequency of strong winds at Siorapaluk and Qaanaaq in northwest Greenland. *Annu. Rep. Snow Ice Hokkaido.* 38, 81–84. (in Japanese with English abstract).

Lambert, F., Delmonte, B., Petit, J. R., Bigler, M., Kaufmann, P. R., Hutterli, M. A., et al. (2008). Dust-climate couplings over the past 800,000 years from the EPICA Dome C ice core. *Nature* 452, 616–619. doi:10.1038/nature06763

Matoba, S., Yamasaki, T., Miyahara, M., and Motoyama, H. (2014). Spatial variations of δ18O and ion species in the snowpack of the northwestern Greenland ice sheet. *Bull. Glacier Res.* 32, 79–84. doi:105331/bgr.32.79.

Meier, M. F., Dyurgerov, M. B., Rick, U. K., O'Neel, S., Pfeffer, W. T., Anderson, R. S., et al. (2007). Glaciers dominate eustatic sea-level rise in the 21st century. *Science* 317, 1064–1067. doi:10.1126/science.1143906.

Nagatsuka, N., Takeuchi, N., Uetake, J., and Shimada, R. (2014). Mineralogical composition of cryoconite on glaciers in northwest Greenland. *Bull. Glacier Res.* 32, 107–114. doi:105331/bgr.32.10710.5331/bgr.32.107

Nagatsuka, N., Takeuchi, N., Uetake, J., Shimada, R., Onuma, Y., Tanaka, S., et al. (2016). Variations in Sr and Nd isotopic ratios of mineral particles in cryoconite in western Greenland. *Front. Earth Sci.* 4, 93. doi:10.3389/feart.2016.00093

Rignot, E., Velicogna, I., van den Broeke, M. R., Monaghan, A., and Lenaerts, J. T. M. (2011). Acceleration of the contribution of the Greenland and Antarctic ice sheets to sea level rise. *Geophys. Res. Lett.* 38, 1–5. doi:10.1029/2011GL046583

Ruth, U., Wagenbach, D., Steffensen, J. P., and Bigler, M. (2003). Continuous record of microparticle concentration and size distribution in the central Greenland NGRIP ice core during the last glacial period. *J. Geophys. Res.* 108, 4098, doi:10.1029/2002JD002376

Sasaki, H., Matoba, S., Shiraiwa, T., and Benson, C. S. (2016). Temporal variation in iron flux deposition onto the northern North Pacific reconstructed from an ice core drilled at Mount Wrangell, Alaska. *SOLA* 12, 287–290. doi:10.2151/sola.2016-056.

Shimada, R., Takeuchi, N., and Aoki, T. (2016). Inter-annual and geographical variations in the extent of bare ice and dark ice on the Greenland Ice Sheet derived from MODIS satellite images. *Front. Earth Sci.* 4, 43. doi:10.3389/feart.2016.00043

Søndergaad, A. S., Larsen, N. K., Olsen, J., Strunk, A., and Woodroffe, S. (2019). Glacial history of the Greenland Ice Sheet and a local ice cap in Qaanaaq, northwest Greenlan. *J. Quaternary. Sci.* 34 (7), 536–547. doi:10.1002/jqs.3139

Sugiyama, S., Sakakibara, D., Matsuno, S., Yamaguchi, S., Matoba, S., and Aoki, T. (2014). Initial field observations on Qaanaaq ice cap, northwestern Greenland. *Ann. Glaciol.* 55, 25–33. doi:10.3189/2014AoG66A102

Svensson, A., Andersen, K. K., Bigler, M., Clausen, H. B., Dahl-Jensen, D., Davis, S. M., et al. (2008). A 60,000 year Greenland stratigraphic ice core chronology. *Clim. Past.* 4, 47–57. doi:10.5194/cp-4-47-2008

Svensson, A., Biscaye, P. E., and Grousset, F. E. (2000). Characterization of late glacial continental dust in the Greenland Ice Core Project ice core. *J. Geophys. Res.* 105 (D4), 4637–4656. doi:10.1029/1999JD901093

Takeuchi, N., Sakaki, R., Uetake, J., Nagatsuka, N., Shimada, R., Niwano, M., et al. (2018). Temporal variations of cryoconite holes and cryoconite coverage on the ablation ice surface of Qaanaaq Glacier in northwest Greenland. *Ann. Glaciol.* 59, 21–30. doi:10.1017/aog.2018.19

Tedesco, M., Fettweis, X., van den Broeke, M. R., van de Wal, R. S. W., Smeets, C. J. P. P., van de Berg, W. J., et al. (2011). The role of albedo and accumulation in the 2010 melting record in Greenland. *Environ. Res. Lett.* 6, 014005. doi:10.1088/1748-9326/6/1/014005

Tsutaki, S., Sugiyama, S., Sakakibara, D., Aoki, T., and Niwano, M. (2017). Surface mass balance, ice velocity and near-surface ice temperature on Qaanaaq Ice Cap, northwestern Greenland, from 2012 to 2016. *Ann. Glaciol.* 58, 181–192. doi:10.1017/aog.2017.7

Uno, I., Amano, H., Emori, S., Kinoshita, K., Matsui, I., and Sugimoto, N. (2001). Trans-Pacific yellow sand transport observed in April 1998: a numerical simulation. *J. Geophys. Res.* 106 (D16), 18331–18344. doi:10.1029/2000JD900748.

Warren, S. G., and Wiscombe, W. J. (1980). A model for the spectral albedo of snow. II: snow containing atmospheric aerosols. *J. Atmos. Sci.* 37, 2734–2745. doi:10.1175/1520-0469(1980)037<2734:amftsa>2.0.co;2

Wientjes, I. G. M., Van de Wal, R. S. W., Reichart, G. J., Sluijs, A., and Oerlemans, J. (2011). Dust from the dark region in the western ablation zone of the Greenland Ice Sheet. *Cryosphere* 5 (3), 589–601. doi:10.5194/tc-5-589-2011

Conflict of Interest: The authors declare that the research was conducted in the absence of any commercial or financial relationships that could be construed as a potential conflict of interest.

Copyright © 2020 Matoba, Hazuki, Kurosaki and Aoki. This is an open-access article distributed under the terms of the Creative Commons Attribution License (CC BY). The use, distribution or reproduction in other forums is permitted, provided the original author(s) and the copyright owner(s) are credited and that the original publication in this journal is cited, in accordance with accepted academic practice. No use, distribution or reproduction is permitted which does not comply with these terms.

frontiers in Earth Science

BRIEF RESEARCH REPORT
published: 14 January 2021
doi: 10.3389/feart.2020.538762

Seasonal and Spatial Differences in Metal and Metalloid Concentrations in the Snow Cover of Hansbreen, Svalbard

Krystyna Koziol[1], *Aleksander Uszczyk*[2], *Filip Pawlak*[1], *Marcin Frankowski*[3] *and Żaneta Polkowska*[1]*

[1]Department of Analytical Chemistry, Faculty of Chemistry, Gdańsk University of Technology, Gdańsk, Poland, [2]Department of Geomorphology, Faculty of Natural Sciences, Institute of Earth Sciences, University of Silesia, Sosnowiec, Poland, [3]Department of Analytical and Environmental Chemistry, Faculty of Chemistry, Adam Mickiewicz University Poznan, Poznań, Poland

Metals and metalloids in snow on glaciers, depending on the season of deposition, may come from various sources: local rock dust (erosion of the geological substratum), marine aerosol, local human activity (e.g., impurities in combusted fuel and waste incineration), and long-range atmospheric transport. Hansbreen, a glacier located close to the Polish Polar Station in southern Svalbard, is a perfect site to study metals and metalloids: it has a complex geological substratum, has a year-round presence of a small group of people, and is near the coast. We analyzed a snapshot of metal and metalloid concentrations in snow samples from shallow cores corresponding to autumn, winter, and spring deposition on Hansbreen. Eighteen cores of snow were collected across the glacier, revealing the influence of potential local sources of metals and metalloids. In these samples, we predominantly found Na, Mg, and K, followed by Zn, Ca, Al, and Fe. Heavy metals, such as Bi or Hg, were also detected. Cluster analysis of the determined elemental concentrations divided them into three distinct groups: Group 1: Ag, As, Bi, Cd, Hg, Mo, Sb, Se, and Zn—the most diverse cluster, representing mostly long-range transported volatile elements, with possible extra local geological sources; Group 2: Al, Fe, Cu, and Mn—elements with crustal sources; and Group 3: Na, Ca, Mg, K, and Sr—with the main source in sea spray aerosol. The latter interpretation was confirmed by the calculation of sea salt contribution based on the composition of mean seawater and the positive significant correlation between their concentrations and the electrical conductivity of snow samples. In the study site, snow was up to six times more efficient in bringing metal pollution into terrestrial environment, when compared to rain.

Keywords: Svalbard, Arctic, spatial distribution, snow, heavy metals, trace elements

OPEN ACCESS

Edited by:
Feiteng Wang,
Chinese Academy of Sciences, China

Reviewed by:
Janae Csavina,
National Ecological Observatory Network, United States
Giovanni Baccolo,
University of Milano-Bicocca, Italy

***Correspondence:**
Żaneta Polkowska
zanpolko@pg.edu.pl

Specialty section:
This article was submitted to Cryospheric Sciences, a section of the journal Frontiers in Earth Science

Received: *28 February 2020*
Accepted: *10 December 2020*
Published: *14 January 2021*

Citation:
Koziol K, Uszczyk A, Pawlak F, Frankowski M and Polkowska Ż (2021) Seasonal and Spatial Differences in Metal and Metalloid Concentrations in the Snow Cover of Hansbreen, Svalbard. Front. Earth Sci. 8:538762. doi: 10.3389/feart.2020.538762

INTRODUCTION

Metal and metalloid impurities in the Arctic snow may come from both local and distant sources, and only some are supplied by human activities (Kozak et al., 2015). Pollutants can be delivered to Svalbard along fast and slow transport routes, and the cold climate favors accumulation of some contaminants (Ruman et al., 2012). Metals and metalloids can occur from background to excessive levels in the Arctic environment and cause harmful effects in people and animals at the latter

(AMAP, 2005). Arctic snow captures atmospheric dust efficiently, through dry and wet deposition, and thus forms an archive of the seasonal contamination of the Arctic atmosphere. It transfers the pollutants to glacier surfaces, where they may be incorporated into ice (Lehmann-Konera et al., 2017) and cryoconite matter (Łokas et al., 2016). Snow upon glaciers in Svalbard has only rarely been sampled for metal and metalloid concentrations (beyond the major ion chemistry, as performed by, e.g., Virkkunen et al., 2007; Nawrot et al., 2016) and when it was sampled, the focus was either on one element, usually mercury (Ferrari et al., 2008; Larose et al., 2010), or on one location (Spolaor et al., 2020a). There has also been a study conducted on firn cores across one Svalbard glacier (Singh et al., 2015). Further studies report on the elemental composition of ice samples (Yevseyev and Korzun, 1985; Simoes and Zagorodnov, 2001; Drbal et al., 1992; Lehmann et al., 2016).

The spatial distribution of elemental deposition upon glacier surfaces may be modified by the influence of local sources of metals and metalloids, snow redeposition patterns (e.g., Grabiec et al., 2011), and other postdepositional processes (Larose et al., 2010; Avak et al., 2019). Here, we focus on the spatial distribution of elemental impurities in the snow on one glacier in southern Svalbard, in light with these processes. The site is located in the vicinity of the Polish Polar Station, a well-monitored area which may be considered a natural science laboratory for complex system observations. The area is subject to intensive glaciological research (Błaszczyk et al., 2019), especially Hansbreen (Kosiba, 1963; Pälli et al., 2003; Grabiec et al., 2006; Oerlemans et al., 2011; Petlicki et al., 2015; Laska et al., 2017; Decaux et al., 2019), which forms a perfect basis for the understanding of biogeochemical processes in glacial environments. This can be also enhanced through comparisons with metal and metalloid distribution, as was investigated in various environmental components of the area, such as surface waters (e.g., Kosek et al., 2019), plant tissue (e.g., Wojtuń et al., 2018), or fjord sediments (Frankowski and Zioła-Frankowska, 2014; Zaborska et al., 2017). In the context of glaciers, cryoconite matter has been subject to metal content studies (Łokas et al., 2016), as was the aluminum export from the nearby Werenskiöldbreen (Stachnik et al., 2019). Since the deposition of chemical elements may change seasonally (as was observed, e.g., for Ni and Pb by Berg et al. (2004)), additional temporal information is added in this study through the subdivision of the collected snow cores into layers. These correspond to a snapshot of autumn, winter, and spring deposition of metals and metalloids in the accumulation season of 2017/2018.

METHODS

Field Site

Hansbreen is a medium-sized tidewater glacier (56 km^2) located in SW Spitsbergen (Wedel Jarlsberg Land). It is approximately 16 km long and 2.5 km wide on average; it terminates into Hansbukta (Hornsund). Bordered by mountains, it is nevertheless linked to other glaciers (Paierlbreen, Vrangpeisbreen, and Werenskiöldbreen) (Szafraniec, 2002; Grabiec et al., 2011). Four tributary glaciers (Staszelisen, Deileggbreen, Tuvbreen, and Fuglebreen) are located in its western bank and one small tributary glacier in its eastern bank (**Figure 1**). The glacier's elevation range is ca. 550 m (Grabiec et al., 2012).

Every year on Hansbreen, new firn is built from the remaining snow cover (Błaszczyk et al., 2019; Uszczyk et al., 2019), yet the entire glacier records a negative mass balance due to the losses from ice melt and calving. The maximum depth of the snow cover at the end of accumulation season (April/May) occurs in the highest parts of the glacier (upglacier from H10, **Figure 1**). During the last 8 years, it reached 5.99 m in the accumulation season of 2010/2011. At the same point in the season, the minimum snow cover depth of 0.66 m was noted in 2012/2013 in the lower parts of Hansbreen (downglacier from H2, **Figure 1**). On average, the end-of-accumulation-season snow cover depth was 2.58, 2.01, and 2.22 m (in the 2010/2011, 2012/2013, and 2013/2014, respectively) (Grabiec, 2017). In general, the distribution of snow cover is linked to weather conditions (solid precipitation and temperature). Therefore, the altitude of the glacier determines the snow cover pattern and the snow cover thickness is modified further by the wind. As indicated by Grabiec et al. (2006), the eastern part of the glacier, which has relatively low accumulation, is the place where strong winds occur. Contrastingly, the west side (including tributary glaciers) is the typical place for the higher accumulation of snow cover.

The snow density on Hansbreen depends on snow depth (Uszczyk et al., 2019) and weather conditions (Grabiec et al., 2011; Łupikasza et al., 2019). The highest snowpack density occurred in the higher parts of the glacier, while the low density was nearer its front. A significant factor influencing the snow cover structure and its density is rain-on-snow events (Łupikasza et al., 2019). These events (more frequent than winter thaws) increase the density of snowpack through the formation of hard ice layers and may also leave a chemical footprint (Spolaor et al., 2020b). According to observations in 2010 and 2014 (Laska et al., 2016, 2017; Uszczyk et al., 2019), the snow cover density reached on average 398 kg/m^3 at the end of accumulation season and 528 kg/m^3 in the ablation season.

Hansbreen terminus lies approximately 3 km from the Polish Polar Station Hornsund, the only human settlement within a radius of 100 km (approximately 10 permanent staff live there). The biggest centre of human activity in Svalbard, Longyearbyen, is located about 140 km north from the study site. Its pollution sources include an airport, a functioning coal mine, local coal-fired power plant, a landfill and untreated sewage outflow (Granberg et al., 2017), a harbor, and local road and snowmobile traffic (e.g., Reimann et al., 2009). Barentsburg, another important settlement in Svalbard, lies over 120 km north from Hansbreen, harboring an active coal mine, a heliport, and a dumpsite where garbage has been burnt repeatedly (Granberg et al., 2017). The local human activity in Hornsund is from the small year-round team and up to 42 people during the peak research season (parts of the summer). It causes the following contamination sources: two arrivals of a supply

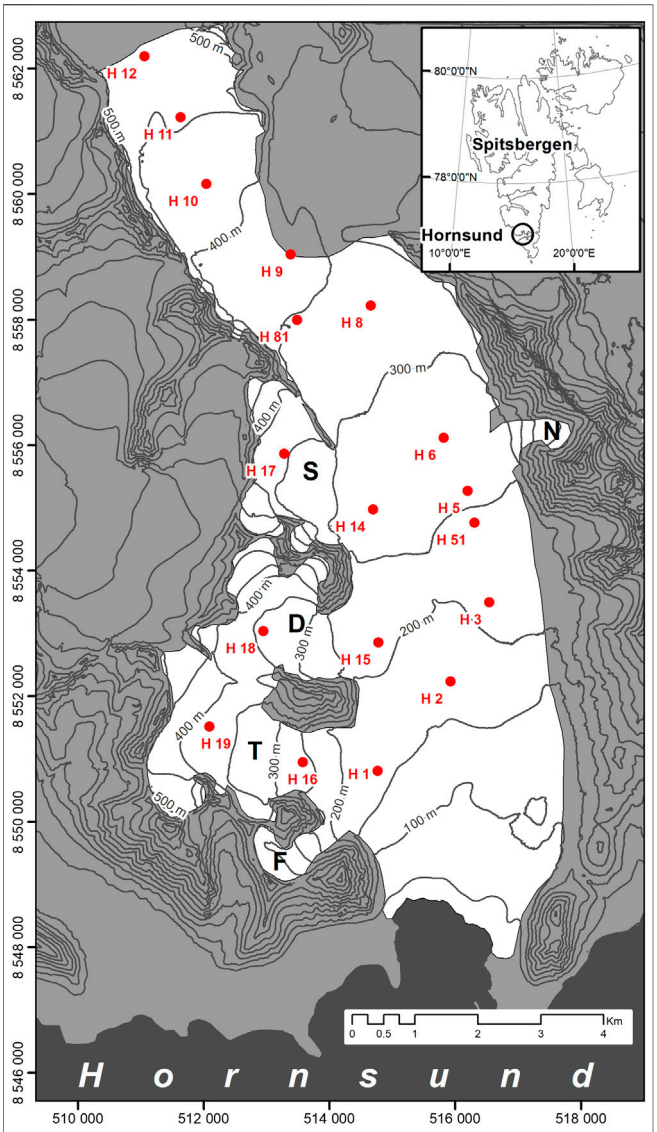

FIGURE 1 | Study area: Hansbreen. The snow sampling locations are marked with red dots. Capital letters indicate tributary glaciers: D, Deileggbreen; F, Fuglebreen; N, Nørdstebreen; S, Staszelisen; T, Tuvbreen. The map is plotted in transverse Mercator projection, WGS84 datum, UTM 33X zone, with northing and easting marked on the map frame.

ship, a diesel power plant, waste incineration, and sewage processing; ship traffic also exists in the nearby Hornsund fjord. In the spring, there is occasional local snowmobile traffic for research purposes.

The glacier is surrounded by diverse geological formations, with ore-bearing veins, which may be a source of metals and metalloids such as Al, As, Bi, Ca, Cd, Co, Cu, Fe, Mg, Mn, Ni, Pb, S, and Zn (Birkenmajer, 1990; Kieres and Piestrzyński, 1992; Czerny et al., 1993). In the wider area (within 15 km radius), there exist geological sources of Al, B, Ba, Be, Ca, Cr, Cs, Cu, Fe, K, Li, Mg, Mn, Na, Nb, Pb, Rb, Sn, Sr, Ta, Th, Ti, U, V, Zn, Zr, and rare-earth elements (cf. Koziol et al., 2020; Spolaor et al., 2020a).

Sampling

Snow samples were collected on 22nd and 25th April 2018. The air temperature during those field trips was approximately −5 and −10°C, respectively; on both days, there was a moderate wind speed of 5 m/s and little-to-no direct solar radiation. A snow core, with 9 cm diameter, was hand-drilled at each point shown on the map in **Figure 1**. To avoid external contamination entering the snow samples, an outer layer of the collected core was scraped with a precleaned polyethylene scraper. Only selected layers from the core were sampled, representing the bottom, middle, and top of the annual snowpack, which most likely belonged to the seasons autumn 2017, winter 2017/2018, and spring 2018, respectively. In particular, the autumn samples were characterized by an increased density (as compared to the rest of the snow core). The sampled layers spanned between 9 and 32 cm, averaging 17 cm (±4.3, 1 SD), while their density ranged from 0.287 to 0.655 g cm^{-3} (mean: 0.460 ± 0.0874 g cm^{-3}). Each sampled layer differed from its neighboring layers in terms of hardness and/or grain size. The total thickness of the snow cover has been measured at each sampling site with a graduated avalanche probe, averaging 202 cm (±51.7, 1 SD; full range: 115–337 cm).

Laboratory Analysis

We analyzed potassium, calcium, magnesium, and iron, with inductively coupled plasma optical emission spectrometry (ICP-OES 9820, Shimadzu, Japan). Twenty-one other elements (Ag, Al, As, Ba, Bi, Cd, Co, Cr, Cu, Hg, Li, Mn, Mo, Na, Ni, Pb, Sb, Se, Sr, V, and Zn) were analyzed using inductively coupled plasma mass spectrometry (ICP-MS 2030, Shimadzu, Japan). Before analysis, the samples were acidified with high-purity nitric acid and trace metal basis (Sigma-Aldrich). Analyses were run in triplicate (with a mean CV 3.82% and 6.43% for ICP-OES and ICP-MS measurements, respectively). The specific measurement conditions and parameters are listed in **Supplementary Table S1** (Supplementary Information). All measurements were quality-assured. The ICP-MS was calibrated with the ICP IV multielement standard (Merck) and the single-element standards of As, Sb, Se, Mo, and V (Sigma-Aldrich). Solutions of Sc, Rh, Tb, and Ge in suprapure 1% HNO3 (Merck) were applied as internal standards. Samples were diluted (if necessary) using deionized water (from Milli-Q Direct 8 Water Purification System, Merck Millipore). The ICP-OES was calibrated with single-element standards (Sigma-Aldrich) of 1000 mg L^{-1}. Analytical accuracy was verified with two certified reference materials (CRMs): Trace Metals ICP-Sample 1 and Trace Metals ICP-Sample 2 (Sigma-Aldrich). CRM recovery ranged from 96% to 104%. Further analytical parameters, including the detection and quantification limits of the method, are listed in **Supplementary Table S2** (Supplementary Information).

Total organic carbon (TOC) was determined through catalytic oxidation with oxygen at 680°C, with a nondispersive infrared spectroscopy detector (Analyser TOC-VCSH/CSN, Shimadzu). The pH and electrical conductivity were measured with a microcomputer pH meter and conductivity meter (inoLab® Multi 9310 IDS pH), fitted with a Tetra-Con® 925 conductivity sensor and a SenTix®940 electrodes. The

analytical qualitative parameters of the basic physicochemical characteristics are given in **Supplementary Table S3** (Supplementary Information). Metal and metalloid concentrations measured have been corrected by the subtraction of a mean blank value, calculated from five procedural blanks. In the rest of the assays, the blank correction was not required, as background contamination was negligibly low.

Statistical Procedures

Before statistical analyses, results below the limit of detection were assigned 1/3 of its value (to approximate their probable level according to the data distribution curve, approximated best as log-normal for most of the studied variables). All statistical analyses were performed using Statistica, version 13.3 (TIBCO). The first tool used to explore our data was cluster analysis applied to variables. The cluster analysis procedure links elements with concentrations of the most similar variability. In brief, concentrations of elements are standardized (transformed to have a mean of 0 and standard deviation of 1), which means that the concentrations of predominant and minor chemical components of the snow samples can be safely compared. Then, they are plotted upon a dendrogram, and the closer they are on the graph, the more similar is their distribution around their mean. Admittedly, the mean and standard deviation are parameters typical for normally distributed datasets, yet as an exploratory method, cluster analysis can also be used for non-normal data distributions. For the clustering, we used Ward's method, with squared Euclidean distance. The correlations mentioned further in the text were calculated using two nonparametric indices, Spearman rank ρ, and Kendall τ, due to the non-normal distribution of data.

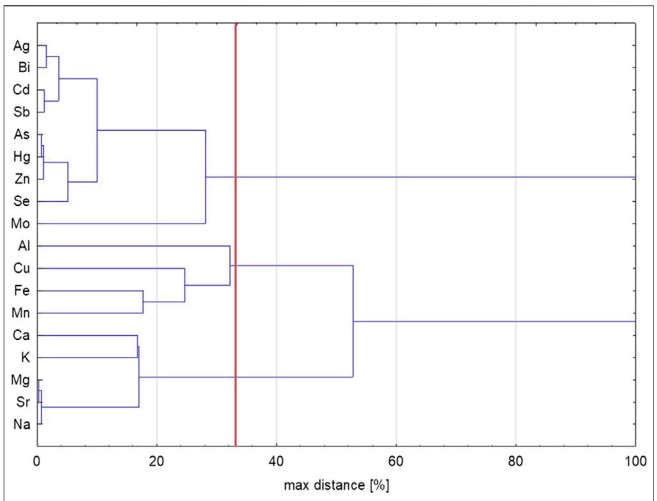

FIGURE 2 | Dendrogram resulting from cluster analysis of the metal and metalloid concentrations in the snow cover of the Hansbreen, based on the samples collected in spring 2018. Clustering was performed based on Ward's method, with squared Euclidean distance, on z-transformed (standardized) values.

RESULTS AND DISCUSSION

Cluster analysis results (**Figure 2**) show, at a 33% relative distance level (a typical cutoff point for the most similar items), there are three distinct groups of metals and metalloids: cluster 1: Ag, Bi, Cd, Sb, As, Hg, Zn, Se, and Mo; cluster 2: Al, Cu, Fe, and Mn; cluster 3: Ca, K, Mg, Sr, and Na. Since the snow in the area has been shown to contain a relatively high proportion of sea spray aerosols (Nawrot et al., 2016), cluster 3 is likely connected to this source. Cluster 2 is likely representing local geological substratum variability, with the local metamorphic rocks containing ore-bearing veins with Cu and Fe, while Al and Mn are also generally abundant elements of the Earth's crust (Birkenmajer, 1990; Kieres and Piestrzyński, 1992; Czerny et al., 1993). Cluster 1 is the most diverse, with elements at very low concentrations, some of which are typically transported to Svalbard from remote anthropogenic sources (e.g., Hg and Cd; Carlsson et al., 2016). Furthermore, the elements in this cluster have volatile forms, which are easily transported over long distances (especially Hg, Zn, As, Cd, Sb, and Se, and likely also Ag, Bi, and Mo; Steinnes and Friedland, 2006). However, in the Hansbreen surroundings, both Hg and Cd, as well as Ag, As, Bi, Sb, and Zn, all occur in ore-bearing veins on the western side of Hansbreen (Kieres and Piestrzyński, 1992), either as their minerals or as admixtures (Cd mainly in sphalerite, Ag in galena, Hg in sphalerite, pyrite, and pyrrhotite). Interestingly, Se occurred as an admixture in rock samples from ore-bearing veins (especially of pyrite, pyrrhotite, and galena), yet at a much lower content level (at least 10 times less than the other elements in the cluster). Furthermore, there was no significant mineral source of Mo found in those rocks, despite this element being included in the geological composition study (Kieres and Piestrzyński, 1992).

The spatial and temporal distribution of elements from each cluster is exemplified by one of the cluster members in **Figure 3**. Additional information on the seasonal distribution of elemental concentrations and on elemental fluxes calculated in this study is also given in **Supplementary Tables S4 and S5**, respectively (Supplementary Information). The sea spray cluster 3 was characterized by generally lower concentrations of its elements in the winter season layers (**Figure 3A**), while the highest concentrations of these elements were noted in the spring layers nearest to seawater (Burgerbukta to the east). The concentrations of elements from cluster 3 decreased also up the glacier, which could reflect a decreasing supply of sea spray from the Hornsund fjord. The rock dust in cluster 2 showed a more even distribution of concentrations across the glacier (**Figure 3B**). Occasionally, elevated concentrations of its elements could be found, especially in the autumn layer. Such concentrations could be interpreted as an effect of rock dust abundance in the period when snow cover only starts forming and does not cover fully the mountain slopes or the moraines. The volatile element cluster 1 (**Figure 3C**) was patchily distributed, with higher concentrations on the western side of the glacier, where the snow cover was accumulated by wind redeposition (Grabiec et al., 2006), and at higher elevations, perhaps due to the

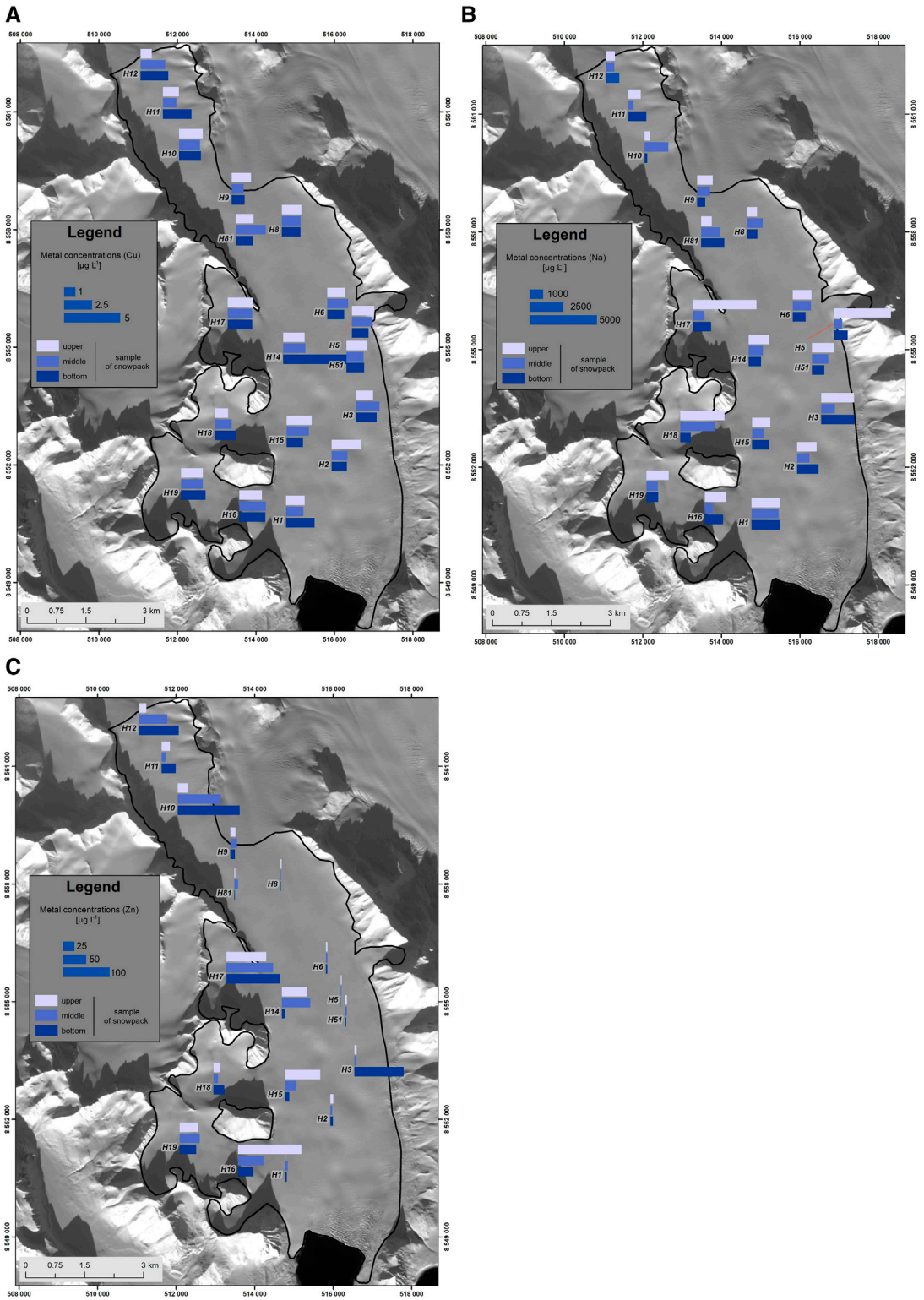

FIGURE 3 | Spatial and interlayer distribution of selected metal concentrations [µg L^{-1}] in the snow cover of Hansbreen in the accumulation season of 2017/2018. Each figure concerns a member of a different variable cluster in **Figure 2**: **(A)** Na, **(B)** Cu, and **(C)** Zn. All maps are plotted in the WGS84 datum, in transverse Mercator projection, UTM 33X zone, with northing and easting marked on the map frame.

TABLE 1 | Sea salt contribution (ssC) to the elemental composition of snow on Hansbreen, calculated from the proportional concentration of each element to sodium.

ssC [%]	Q_2	Q_1	Q_3	min	max
Ag	0.03	0.01	0.2	0	2.5
Al	0	0	0	0	0.01
As	0.11	0.04	0.23	0	1.04
Bi	0	0	0	0	0
Ca	308	236	395	61.5	763
Cd	0.02	0.01	0.03	0	0.07
Cu	0.01	0	0.01	0	0.02
Fe	0.01	0.01	0.01	0	0.03
Hg	0.04	0.02	0.06	0	7.1
K	26	18.1	39.7	6.2	58.7
Mg	61.3	57.6	66.4	46.3	103
Mn	0	0	0.01	0	0.02
Mo	0.28	0.16	0.78	0.03	22.5
Sb	0.01	0.01	0.02	0	0.11
Se	0.01	0.01	0.03	0	0.07
Sr	39.1	32	44.1	12.1	58.1
Zn	0.01	0	0.02	0	0.21

The data in the table describe the distribution of sea salt contribution across the whole glacier and seasons (vertically distributed samples within the snow core, i.e., n = 54 snow samples for each element). Q_{1-3} are quartiles, i.e., Q_2 = median; min and max show the full range of sea salt contribution calculation results. Values below the limit of detection were excluded from ssC calculations. Fractions >100% signify depletion in a certain element against the typical composition of seawater.

exposure to long-distance-transported air pollution. However, this side of the glacier is also closer to the elemental sources in rock dust, so their concentrations may only be elevated very near to such areas (due to the generally lower concentrations of these elements in the said rocks and their irregular spatial distribution as ore-bearing veins).

To further explore the possible sources of various elements in the snowpack, we calculated correlation coefficients between their concentrations and the pH, electrical conductivity, and total organic carbon (TOC) concentration in the collected samples. Both Spearman ρ and Kendall τ showed the same pairs of variables to correlate significantly at the p level <0.05 (and only the correlations with electrical conductivity were significant at $p < 0.01$). Electrical conductivity correlated positively and strongly with the concentrations of Ca, K, Mg, Na, and Sr, grouping again the sea salt-related elements in one cluster. Also, the concentration of Fe correlated negatively with pH of the samples, likely indicating the origin of Fe from sulphide minerals, which oxidate producing SO_4^{2-} ions which acidify the snow (Moses et al., 1987). If we assume that TOC concentration is a sign of likely pollution from snowmobile tracks, then this factor appears as unimportant in shaping the metal and metalloid composition of snow upon the glacier: the highest positive Spearman ρ between any metal concentration and TOC equaled 0.096 for Mo.

Multiple elements seem to be supplied from sea spray on this glacier, which merits the calculation of sea salt contribution (ssC) into the elemental concentrations in the snow cover. This has been performed assuming that all Na was derived from sea salt and that sea spray has the same salt composition as average seawater (Turekian, 1968) (**Table 1**). In this procedure, all data records with values below the detection limit were omitted. The occurrence of sea salt contributions exceeding 100% indicates either that there were extra sources of Na besides sea salt or that Na may be enriched in sea spray, as compared to mean seawater composition, or else that these elements' concentrations were depleted postdepositionally. The elements with the highest sea salt contributions were Ca, Mg, Sr, and K (median ssCs >25%), which confirms the origin of the first variable cluster in **Figure 2** from sea spray. In isolated cases (maximum ssCs >5%), sea spray seemed to be a significant source of also Mo and Hg.

Crustal fractions of elements were also estimated (**Supplementary Table S6**, Supplementary Information), assuming all Al was of crustal origin, and using geochemical background composition after the Geochemical Atlas of Svalbard (Ottesen, 2015). Whenever the Geochemical Atlas supplied two different values derived from two different analytical methods, we used the concentrations determined by the analytical method most similar to the one used here. The calculations highlighted the crustal origin of Fe in the collected samples; in certain samples, Mg and As could also be supplied from the general geochemical crustal background (max crustal fractions >5%). However, the very low crustal fractions of other elements calculated in this way do not exclude their origin from local ore-bearing veins. This is because the locally occurring veins would not influence the Svalbard-wide geochemical background concentrations, which were the basis for the calculations. The low crustal fractions of calcium support the interpretation that Ca from rock dust was negligible in the collected snow samples.

Since the deposition of impurities in snow is generally considered very efficient (Błaś et al., 2010), we compare the obtained median concentrations in the snow with the median concentrations measured in the rain at the nearby Polish Polar Station Hornsund (Kozak et al., 2015). Available for comparison were the concentrations of Al, As, Cu, Mn, Se, Sr, and Zn. All these elements were found at higher median concentrations in the snow on Hansbreen, exceeding the concentrations in rain from 1.02 to 5.88 times (for Zn and Al, respectively). The maxima of metal and metalloid concentrations in summer precipitation, published by Koziol et al. (2020), were also mostly lower than maximum concentrations in the snow studied here (for Al, Cu, Sb, and Se). Mn, Sr, and Zn showed the opposite proportion, but the difference between the two maxima was very small for Zn. Overall, the snow cover seems a more important medium than rain for the transfer of metal and metalloid impurities from the atmosphere to the terrestrial system on this glacier. The snow cover also holds such impurities for longer and may release them in different temporal patterns, depending on their abundance in the snowpack (Avak et al., 2019). Thus, snow appears to be a crucial component for the supply of metals and metalloids to

the surface waters of the area, which warrants its further investigations to understand the element mobility and long-term concentration changes.

CONCLUSION

Weinvestigated the concentrations of metal and metalloid impurities in the annual snowpack on a glacier in southern Svalbard, focusing on their spatial variability. We attempted to determine their main sources by the application of statistical analysis and a comparison to seawater and crustal composition. As a result, we found that Na, Mg, Ca, K, and Sr had a significant source in the sea spray aerosol. Al, Fe, Cu, and Mn could be attributed to crustal sources. Multiple elements likely come from long-range transport, with potential secondary sources in the local geological substratum (ore-bearing veins): Ag, As, Bi, Cd, Hg, Sb, Se, and Zn; however, Mo is likely to come from atmospheric transport alone. In comparison to summer rains, snowfall showed higher median concentrations of metals and metalloids (between one and six times higher). The studies on metal and metalloid admixtures in the Arctic snow are important means of measuring the supply of impurities to surface waters and downstream ecosystems, and their long-term changes should be studied in the future.

DATA AVAILABILITY STATEMENT

The datasets generated for this study can be found in the Open Science Framework repository [https://osf.io/ypskz] and in Supplementary Information.

AUTHOR CONTRIBUTIONS

KK and ŻP developed the concept of the paper. KK wrote the main body of the manuscript and prepared the sampling kit. AU collected the samples, prepared maps, and provided field site description. FP and MF analysed the samples (for basic parameters and metal/metalloid concentrations, respectively) and wrote the description of the analytical methods. All authors participated in the final discussion of the results and checked the final version of the manuscript.

FUNDING

Internal funding for the statutory activity at the Pedagogical University in Cracow has supported this research (project Spatial Variability of the Concentrations of Macro- and Microelements in the Snow Cover of the Arctic, PI: KK), as did the Leading National Research Centre (KNOW) project received by the Centre for Polar Studies of the University of Silesia, Poland. The article has been written as part of KK's employment and FP's scholarship within the National Science Centre of Poland, under research grant no. 2017/26/D/ST10/00630.

ACKNOWLEDGMENTS

Ł. Małarzewski is thanked for field assistance.

SUPPLEMENTARY MATERIAL

The Supplementary Material for this article can be found online at: https://www.frontiersin.org/articles/10.3389/feart.2020.538762/full#supplementary-material.

REFERENCES

AMAP (2005). AMAP assessment 2002: heavy metals in the arctic. Oslo, Norway: arctic monitoring and assessment programme (AMAP). Available at: http://www.amap.no/documents/doc/amap-assessment-2002-radioactivity-in-the-arctic/93 (Accessed April 1, 2006).

Avak, S. E., Trachsel, J. C., Edebeli, J., Brütsch, S., Bartels-Rausch, T., Schneebeli, M., et al. (2019). Melt-induced fractionation of major ions and trace elements in an alpine snowpack. *J. Geophys. Res. Earth Surf.* 124, 1647–1657. doi:10.1029/2019JF005026

Berg, T., Kallenborn, R., and Manø, S. (2004). Temporal trends in atmospheric heavy metal and organochlorine concentrations at zeppelin, Svalbard. Arctic. *Antarct. Alp. Res.* 36, 284–291. doi:10.1657/1523-0430

Birkenmajer, K. (1990). *Geological Map of the Hornsund area 1 : 75 000*. Katowice, Poland: University of Silesia.

Błaś, M., Cichała-Kamrowska, K., Sobik, M., Polkowska, Ż., and Namieśnik, J. (2010). Conditions controlling atmospheric pollutant deposition via snowpack. *Environ. Rev.* 18, 87–114. doi:10.1139/A10-003

Błaszczyk, M., Ignatiuk, D., Uszczyk, A., Cielecka-Nowak, K., Grabiec, M., Jania, J. A., et al. (2019). Freshwater input to the arctic fjord Hornsund (Svalbard). *Polar Res.* 38, 1–18. doi:10.33265/polar.v38.3506

Carlsson, P., Christensen, J. H., Borgå, K., Kallenborn, R., Aspmo Pfaffhuber, K., Odland, J. Ø., et al. (2016). *AMAP 2016. Influence of Climate Change on Transport, Levels, and Effects of Contaminants in Northern Areas-Part 2* (Oslo, Norway: AMAP).

Czerny, J., Kieres, A., Manecki, M., and Rajchel, J. (1993). *Geological Map of the SW Part of Wedel-Jarlsberg Land*. Spitsbergen.

Decaux, L., Grabiec, M., Ignatiuk, D., and Jania, J. (2019). Role of discrete water recharge from supraglacial drainage systems in modeling patterns of subglacial conduits in Svalbard glaciers. *Cryosphere* 13, 735–752. doi:10.5194/tc-13-735-2019

Drbal, K., Elster, J., and Komárek, J. (1992). Heavy metals in water, ice and biological material from Spitsbergen. *Svalbard. Polar Res.* 11, 99–101. doi:10.3402/polar.v11i2.6721

Ferrari, C. P., Padova, C., Faïn, X., Gauchard, P. A., Dommergue, A., Aspmo, K., et al. (2008). Atmospheric mercury depletion event study in Ny-Alesund (Svalbard) in spring 2005. Deposition and transformation of Hg in surface snow during springtime. *Sci. Total Environ.* 397, 167–177. doi:10.1016/j.scitotenv.2008.01.064

Frankowski, M., and Zioła-Frankowska, A. (2014). Analysis of labile form of aluminum and heavy metals in bottom sediments from Kongsfjord, Isfjord, Hornsund fjords. *Environ. Earth Sci.* 71, 1147–1158. doi:10.1007/s12665-013-2518-5

Grabiec, M., Jania, J. A., Puczko, D., Kolondra, L., and Budzik, T. (2012). Surface and bed morphology of Hansbreen, a tidewater glacier in Spitsbergen. *Pol. Polar Res.* 33, 111–138. doi:10.2478/v10183-012-0010-7

Grabiec, M., Leszkiewicz, J., Głowacki, P., and Jania, J. (2006). Distribution of snow accumulation on some glaciers of Spitsbergen. *Pol. Polar Res.* 27, 309–326

Grabiec, M., Puczko, D., Budzik, T., and Gajek, G. (2011). Snow distribution patterns on Svalbard glaciers derived from radio-echo soundings. *Pol. Polar Res.* 32, 393–421. doi:10.2478/v10183-011-0026-4

Grabiec, M. (2017). *Stan I Współczesne Zmiany Systemów Lodowcowych Południowego Spitsbergen W Świetle Badań Metodami Radarowymi [The State and Contemporary Changes of the Glacial Systems in Southern Spitsbergen in the Light of the Radar Methods]*. Katowice, Poland: University of Silesia.

Granberg, M. E., Ask, A., and Gabrielsen, G. W. (2017). *Local contamination in Svalbard. Overview and suggestions for remediation actions*. Tromsø: Norwegian Polar Institute.

Kieres, A., and Piestrzyński, A. (1992). "Ore-mineralisation of the hecla hoek succession (precambrian) around Werenskioldbreen, south Spitsbergen," in *Studia geologica polonica*. Editor K. Birkenmajer (Warsaw: Polish Academy of Sciences, Institute of Geological Sciences), 115–151.

Kosek, K., Kozioł, K., Luczkiewicz, A., Jankowska, K., Chmiel, S., and Polkowska, Ż. (2019). Environmental characteristics of a tundra river system in Svalbard. Part 2: chemical stress factors. *Sci. Total Environ*. 653, 1585–1596. doi:10.1016/j.scitotenv.2018.11.012

Kosiba, A. (1963). Changes in the Werenskiold glacier and Hans glacier in SW Spitsbergen. *Int. Assoc. Sci. Hydrol. Bull*. 8, 24–35. doi:10.1080/02626666309493294

Kozak, K., Kozioł, K., Luks, B., Chmiel, S., Ruman, M., Marć, M., et al. (2015). The role of atmospheric precipitation in introducing contaminants to the surface waters of the Fuglebekken catchment, Spitsbergen. *Polar Res*. 34, 24207. doi:10.3402/polar.v34.24207

Koziol, K., Ruman, M., Pawlak, F., Chmiel, S., and Polkowska, Ż. (2020). Spatial differences in the chemical composition of surface water in the hornsund fjord area: a statistical analysis with a focus on local pollution sources. *Water (MDPI)*. 12, 1–22. doi:10.3390/w12020496

Larose, C., Dommergue, A., De Angelis, M., Cossa, D., Averty, B., Marusczak, N., et al. (2010). Springtime changes in snow chemistry lead to new insights into mercury methylation in the Arctic. *Geochem. Cosmochim. Acta*. 74, 6263–6275. doi:10.1016/j.gca.2010.08.043

Laska, M., Grabiec, M., Ignatiuk, D., and Budzik, T. (2017). Snow deposition patterns on southern Spitsbergen glaciers, Svalbard, in relation to recent meteorological conditions and local topography. *Geogr. Ann. Phys. Geogr*. 99, 262–287. doi:10.1080/04353676.2017.1327321

Laska, M., Luks, B., and Budzik, T. (2016). Influence of snowpack internal structure on snow metamorphism and melting intensity on Hansbreen, Svalbard. *Polish Polar Res*. 37, 193–218. doi:10.1515/popore-2016-0012

Lehmann-Konera, S., Ruman, M., Kozioł, K., Gajek, G., and Polkowska, Ż. (2017). Glaciers as an important element of the world glacier monitoring implemented in Svalbard. *Glaciers Evol. A Chang. World*., 3–36. doi:10.5772/intechopen.69237

Lehmann, S., Gajek, G., Chmiel, S., and Polkowska, Ż. (2016). Do morphometric parameters and geological conditions determine chemistry of glacier surface ice? Spatial distribution of contaminants present in the surface ice of Spitsbergn glaciers (European Arctic). *Environ. Sci. Pollut. Res. Int*. 23, 23385–23405. doi:10.1007/s11356-016-7354-1

Łokas, E., Zaborska, A., Kolicka, M., Różycki, M., and Zawierucha, K. (2016). Accumulation of atmospheric radionuclides and heavy metals in cryoconite holes on an Arctic glacier. *Chemosphere* 160, 162–172. doi:10.1016/j.chemosphere.2016.06.051

Łupikasza, E. B., Ignatiuk, D., Grabiec, M., Cielecka-Nowak, K., Laska, M., Jania, J., et al. (2019). The role of winter rain in the glacial system on Svalbard. *Water* 11, 334. doi:10.3390/w11020334

Moses, C. O., Kirk Nordstrom, D., Herman, J. S., and Mills, A. L. (1987). Aqueous pyrite oxidation by dissolved oxygen and by ferric iron. *Geochem. Cosmochim. Acta*. 51, 1561–1571. doi:10.1016/0016-7037(87)90337-1

Nawrot, A. P., Migała, K., Luks, B., Pakszys, P., and Głowacki, P. (2016). Chemistry of snow cover and acidic snowfall during a season with a high level of air pollution on the Hans Glacier, Spitsbergen. *Polar Sci*. 10, 249–261. doi:10.1016/j.polar.2016.06.003

Oerlemans, J., Jania, J., and Kolondra, L. (2011). Application of a minimal glacier model to Hansbreen. *Svalbard. Cryosph*. 5, 1–11. doi:10.5194/tc-5-1-2011

Ottesen, R. T. (2015). "Geochemistry of superficial deposits," in *Geoscience atlas of Svalbard*. Editor W. K. Dallmann (Tromsø: Norsk Polarinstitutt, 241–248.

Pälli, A., Moore, J. C., Jania, J., Kolondra, L., and Głowacki, P. (2003). The drainage pattern of Hansbreen and Werenskioldbreen, two polythermal glaciers in Svalbard. *Polar Res*. 22, 355–371. doi:10.3402/polar.v22i2.6465

Petlicki, M., Cieply, M., Jania, J. A., Prominska, A., and Kinnard, C. (2015). Calving of a tidewater glacier driven by melting at the waterline. *J. Glaciol*. 61, 851–863. doi:10.3189/2015JoG15J062

Reimann, S., Kallenborn, R., and Schmidbauer, N. (2009). Severe aromatic hydrocarbon pollution in the Arctic town of Longyearbyen (Svalbard) caused by snowmobile emissions. *Environ. Sci. Technol*. 43, 4791–4795. doi:10.1021/es900449x

Ruman, M., Kozak, K., Lehmann, S., Kozioł, K., and Polkowska, Z. (2012). Pollutants present in different components of the Svalbard archipelago environment. *Ecol. Chem. Eng. S*. 19, 571–584. doi:10.2478/v10216-011-0040-9

Simoes, J. C., and Zagorodnov, V. S. (2001). The record of anthropogenic pollution in snow and ice in Svalbard, Norway. *Atmopsheric Environ*. 35, 403–413. doi:10.1016/S1352-2310(00)00122-9

Singh, S. M., Gawas-Sakhalkar, P., Naik, S., Ravindra, R., Sharma, J., Upadhyay, A. K., et al. (2015). Elemental composition and bacterial incidence in firn-cores at Midre Lovénbreen glacier, Svalbard. *Polar Rec*. 51, 39–48. doi:10.1017/S0032247413000533

Spolaor, A., Moroni, B., Luks, B., Nawrot, A., Roman, M., Larose, C., et al. (2020a). Investigation on the sources and impact of trace elements in the annual snowpack and the firn ice in the Hansbreen glacier (southwest Spitsbergen). *Front. Earth Sci*., doi:10.3389/feart.2020.536036

Spolaor, A., Varin, C., Pedeli, X., Christille, J. M., Kirchgeorg, T., Giardi, F., et al. (2020b). Source, timing and dynamics of ionic species mobility in the Svalbard annual snowpack. *Sci. Total Environ*. 751, 141640. doi:10.1016/j.scitotenv.2020.141640

Stachnik, L., Yde, J. C., Nawrot, A., Uzarowicz, Ł., Łepkowska (Majchrowska), E., and Kozak, K. (2019). Aluminium in glacial meltwater demonstrates an association with nutrient export (Werenskiöldbreen, Svalbard). *Hydrol. Process*. doi:10.1002/hyp.13426

Steinnes, E., and Friedland, A. J. (2006). Metal contamination of natural surface soils from long-range atmospheric transport: existing and missing knowledge. *Environ. Rev*. 14, 169–186. doi:10.1139/A06-002

Szafraniec, J. (2002). Influence of positive degree-days and sunshine duration on the surface ablation of Hansbreen, Spitsbergen glacier. *Pol. Polar Res*. 23, 227–240.

Turekian, K. K. (1968). *Oceans*. Upper Saddle River, NJ: Prentice-Hall.

Uszczyk, A., Grabiec, M., Laska, M., Kuhn, M., and Ignatiuk, D. (2019). Importance of snow as component of surface mass balance of Arctic glacier (Hansbreen, southern Spitsbergen). *Pol. Polar Res*. 40, 311–338. doi:10.24425/ppr.2019.130901

Virkkunen, K., Moore, J. C., Isaksson, E., Pohjola, V., Perämäki, P., Grinsted, A., et al. (2007). Warm summers and ion concentrations in snow: comparison of present day with Medieval Warm Epoch from snow pits and an ice core from Lomonosovfonna, Svalbard. *J. Glaciol*. 53, 623–634. doi:10.3189/002214307784409388

Wojtuń, B., Samecka-Cymerman, A., Kolon, K., and Kempers, A. J. (2018). Metals in racomitrium lanuginosum from arctic (SW Spitsbergen, Svalbard archipelago) and alpine (Karkonosze, SW Poland) tundra. *Environ. Sci. Pollut. Res. Int*. 25, 12444.doi:10.1007/s11356-018-1508-2

Yevseyev, A. V., and Korzun, A. V. (1985). On the chemical composition of ice cover on Nordaustlandet [in Russian]. *Mater. Glyatsologicheskikh Isledovaniy*. 52, 205–209.

Zaborska, A., Beszczyńska-Moeller, A., and Włodarska-Kowalczuk, M. (2017). History of heavy metal accumulation in the Svalbard area: distribution, origin and transport pathways. *Environ. Pollut*. 231, 437–450. doi:10.1016/j.envpol.2017.08.042

Conflict of Interest: The authors declare that the research was conducted in the absence of any commercial or financial relationships that could be construed as a potential conflict of interest.

Copyright © 2021 Koziol, Uszczyk, Pawlak, Frankowski and Polkowska. This is an open-access article distributed under the terms of the Creative Commons Attribution License (CC BY). The use, distribution or reproduction in other forums is permitted, provided the original author(s) and the copyright owner(s) are credited and that the original publication in this journal is cited, in accordance with accepted academic practice. No use, distribution or reproduction is permitted which does not comply with these terms.

frontiers in Earth Science

BRIEF RESEARCH REPORT
published: 19 January 2021
doi: 10.3389/feart.2020.536036

Investigation on the Sources and Impact of Trace Elements in the Annual Snowpack and the Firn in the Hansbreen (Southwest Spitsbergen)

Andrea Spolaor[1], Beatrice Moroni[2], Bartłomiej Luks[3], Adam Nawrot[3,4], Marco Roman[5], Catherine Larose[6], Łukasz Stachnik[7], Federica Bruschi[1,2], Krystyna Kozioł[8], Filip Pawlak[8], Clara Turetta[1], Elena Barbaro[1], Jean-Charles Gallet[9] and David Cappelletti[2]*

[1]Institute of Polar Sciences, ISP-CNR, Venice, Italy, [2]Dipartimento di Chimica, Biologia e Biotecnologie, Università degli Studi di Perugia, Perugia, Italy, [3]Institute of Geophysics, Polish Academy of Sciences, Warsaw, Poland, [4]forScience Foundation, Toruń, Poland, [5]Department of Environmental Sciences, Informatics and Statistics, Ca' Foscari University of Venice, Venice, Italy, [6]Environmental Microbial Genomics, Laboratoire Ampère, CNRS, University of Lyon, Lyon, France, [7]University of Wrocław, Faculty of Earth Sciences and Environmental Management, Wrocław, Poland, [8]Department of Analytical Chemistry, Chemical Faculty, Gdańsk University of Technology, Gdańsk, Poland, [9]Norwegian Polar Institute, Tromsø, Norway

OPEN ACCESS

Edited by:
Jing Ming,
Independent researcher, Melbourne, Australia

Reviewed by:
Zhiwen Dong,
Chinese Academy of Sciences, China
Sumito Matoba,
Hokkaido University, Japan

***Correspondence:**
Andrea Spolaor
andrea.spolaor@cnr.it

Specialty section:
This article was submitted to Cryospheric Sciences, a section of the journal Frontiers in Earth Science

Received: *18 February 2020*
Accepted: *30 November 2020*
Published: *19 January 2021*

Citation:
Spolaor A, Moroni B, Luks B, Nawrot A, Roman M, Larose C, Stachnik Ł, Bruschi F, Kozioł K, Pawlak F, Turetta C, Barbaro E, Gallet J-C and Cappelletti D (2021) Investigation on the Sources and Impact of Trace Elements in the Annual Snowpack and the Firn in the Hansbreen (Southwest Spitsbergen). Front. Earth Sci. 8:536036. doi: 10.3389/feart.2020.536036

We present a thorough evaluation of the water soluble fraction of the trace element composition (Ca, Sr, Mg, Na, K, Li, B, Rb, U, Ni, Co, As, Cs, Cd, Mo, Se, Eu, Ba, V, Ge, Ga, Cr, Cr, P, Ti, Mn, Zr, Ce, Zn, Fe, Gd, Y, Pb, Bi, Yb, Al, Nb, Er, Nd, Dy, Sm, Ho, Th, La, Lu, Tm, Pr, Tb, Fe, In, Tl) and their fluxes in the annual snowpack and the firn of the Hansbreen (a tidewater glacier terminating in the Hornsund fjord, southwest Spitsbergen). The trace element samples were obtained from a 3 m deep snow pit dug at the plateau of the glacier (450 m a.s.l.), and from a 2 m deep firn core collected from the bottom of the snow pit. The comparison of elemental fluxes and enrichment factors allowed us to constrain specific summer and wintertime deposition patterns of water soluble trace elements in the southern part of the Svalbard archipelago. Our results suggest that the chemical composition of the Hansbreen (and likely other glaciers where the summit is close to the equilibrium line) is mainly affected by summertime deposition of trace elements from local sources and some volatile elements, which may be transported into the Arctic when polar vortex is weak. The melting of the annual snowpack seems to have a minor influence on the overall chemical signature of the glacier ice.

Keywords: svalbard, snowpack, firn, trace element, transport

INTRODUCTION

The climate of the Svalbard archipelago is characterized by a marked thermal gap between summer and winter periods (Maturilli et al., 2013). As a consequence, high variability in snow accumulation between the coastline and the interior of the archipelago exists (Winther et al., 1998). The annual snowpack covers almost the entire archipelago between October and May, but the recent air temperature increase, estimated at 1.3°C per decade (Maturilli et al., 2013), is affecting its onset, evolution and duration. The snow season has been shortening from 250 to 220 days per year at Longyearbyen and Ny-Ålesund meteorological stations (www.mosj.no), with similar trends observed at Barentsburg (−4.6 days decade^{-1}) and Hornsund stations (−10.0 days decade^{-1}) (Osuch and

Wawrzyniak, 2017). Both the warming and the change in snow season duration have direct consequences for glacier mass balance, which has registered a constant decrease over the past years (Kohler et al., 2007; Aas et al., 2016; Van Pelt et al., 2019), despite the recorded rise in the amount of precipitation (from 400 to 600 mm; www.mosj.no) and a potential increase in the annual snowpack thickness. The decrease in glacier mass balance is shifting the equilibrium line altitude upwards, i.e. the altitude above which winter snow survives summer melting and can contribute to positive mass balance (Möller and Kohler, 2018). Besides being crucial for glacier mass balance, the annual snowpack is a sink and a reservoir for a wide range of inorganic and organic elements naturally present and/or released by human activities. The presence of impurities in the annual snowpack, in the form of either insoluble dust particles (Barbante et al., 2017), soluble chemical species (Barbaro et al., 2017b) or organic compounds (Vecchiato et al., 2018), can be used to study the transport processes from polluted source areas at mid-latitudes and constrain the potential impact of human activities on the Arctic environment (Barbante et al., 2001; Ezerinskis et al., 2014; Nawrot et al., 2016).

The chemical composition of the annual snow depends on various factors including the source of air masses (local, regional, long-range) and impurities (natural, anthropogenic) (Barbante et al., 2017; Vecchiato et al., 2018; Conca et al., 2019). Considering the location of Svalbard, marine processes and oceanic emissions contribute markedly to the deposition flux of multiple elements, next to the crustal components (Spolaor et al., 2013; Barbaro et al., 2017a). However, the long-range transport of atmospheric dust and wildfire emissions from Eurasia can significantly impact the elemental composition of the annual snowpack (Moroni et al., 2016; Feltracco et al., 2020). A recent study investigating the lead isotope composition of aerosol samples suggests a predominant contribution of air masses from North Eurasia during spring, and the main influence during summer coming from North America (Barbaro et al., 2016; Zielinski et al., 2020). Furthermore, the anticipated shortening of the snow season, combined with glacier retreat, will increase the time and extent of soil exposure locally, thus likely enhancing the impact of dust on snowpack composition. The annual snowpack is a critical component of the cryosphere and interfaces with most environmental spheres (hydrosphere, atmosphere, pedosphere and ecosphere) in Svalbard (Gallet et al., 2019). For example, the impact of the release of elements and compounds during the melting season, in particular biologically active elements such as iron and phosphorus, on the surface oceanic water composition, highlights the importance of snowmelt on ecosystems (Stachnik et al., 2019). Therefore, investigating the chemical composition of snow and the underlying processes controlling it is fundamental for constraining the impact of snowpacks on down-stream ecosystems. Trace elements could be a good indicator of human contamination of remote areas. As previously reported by Siudek et al. (2015), the major sources of trace elements are associated with natural processes (rock weathering, mineralization, dust storm, volcanic eruption), although industrial activities have also been shown to influence their abundance in the environment. Industrial processes such as fossil (As, Cu, Co, Cr, V, Ni, Sb, Fe, Mn, Zn, Sn) and oil combustion (Mn, Pb, Fe, Ni), motor vehicle exhausts (Pb, Cu, Cr, Sn, Sb), smelting (Ni, Cu, As, Pb, Cd), iron/steel manufacturing (Cr, Mn, Ni, Co), waste incineration (Pb, Zn), and cement production lead to the release of trace elements to the atmosphere. The Svalbard archipelago can almost be considered as a pristine environment since industrial activities are mostly limited to coal extraction and oil combustion through ship and snow mobile traffic. Therefore, potential sources of trace elements could also be ascribed to long-range transport in addition to natural emissions.

Few studies on the elemental composition of the Svalbard snowpack exist (Spolaor et al., 2013; Pedersen et al., 2015; López-Moreno et al., 2016; Nawrot et al., 2016; Spolaor et al., 2016; Barbaro et al., 2017a), and they are mostly geographically limited to the western side of the Archipelago. There is a general lack of data on trace element concentrations and their fluxes in the southern part of the Svalbard archipelago. Here, we present the first characterization of the water-soluble fraction of trace elements in the annual snowpack in the Hansbreen, a tidewater glacier terminating in the Hornsund fjord. We focused on the water-soluble fraction being that mostly affected by the melting episodes that occur in the Hansbreen. The element concentrations and deposition fluxes in both snow and ice were evaluated to better characterize their sources (marine, crustal or anthropogenic) and impacts. In addition, considering the moderate altitude of the summit of the Hansbreen (500 m a.s.l) and the glacier equilibrium line (370 m a.s.l., Laska et al., 2016) (Schuler et al., 2020), this study provides an important piece of information evaluating the effect of the annual snow pack chemical composition on the glacier firn trace element abundance in a low elevation Svalbard glacier.

CLIMATIC AND GEOLOGICAL SETTING OF HANSBREEN

The southern part of the Svalbard archipelago is characterized by higher winter snow accumulation and higher temperatures as compared to the Svalbard average and in particular to those measured in the northern territory of the archipelago. The Hansbreen covers an area of about 56 km^2 with a length of approximately 15 km (Laska et al., 2016). The glacier terminates in the Hornsund fjord and its summit is located approximately at 500 m a.s.l in connection with Vrangpeisbreen (**Figure 1**). Due to the moderate altitude of the glacier summit and the calculated glacier equilibrium line (370 m a.s.l., Laska et al., 2016), the annual snowpack covering the Hansbreen is strongly affected by summer melting. Hansbreen lies over a mosaic of metamorphic rocks. The eastern flank of the glacier laps the Sofiekammen (mainly calcitic and dolomitic marbles) and the Sørkapp Land group (quartzite-dominated) formations (Birkenmajer, 1990): Sofiekammen (mainly

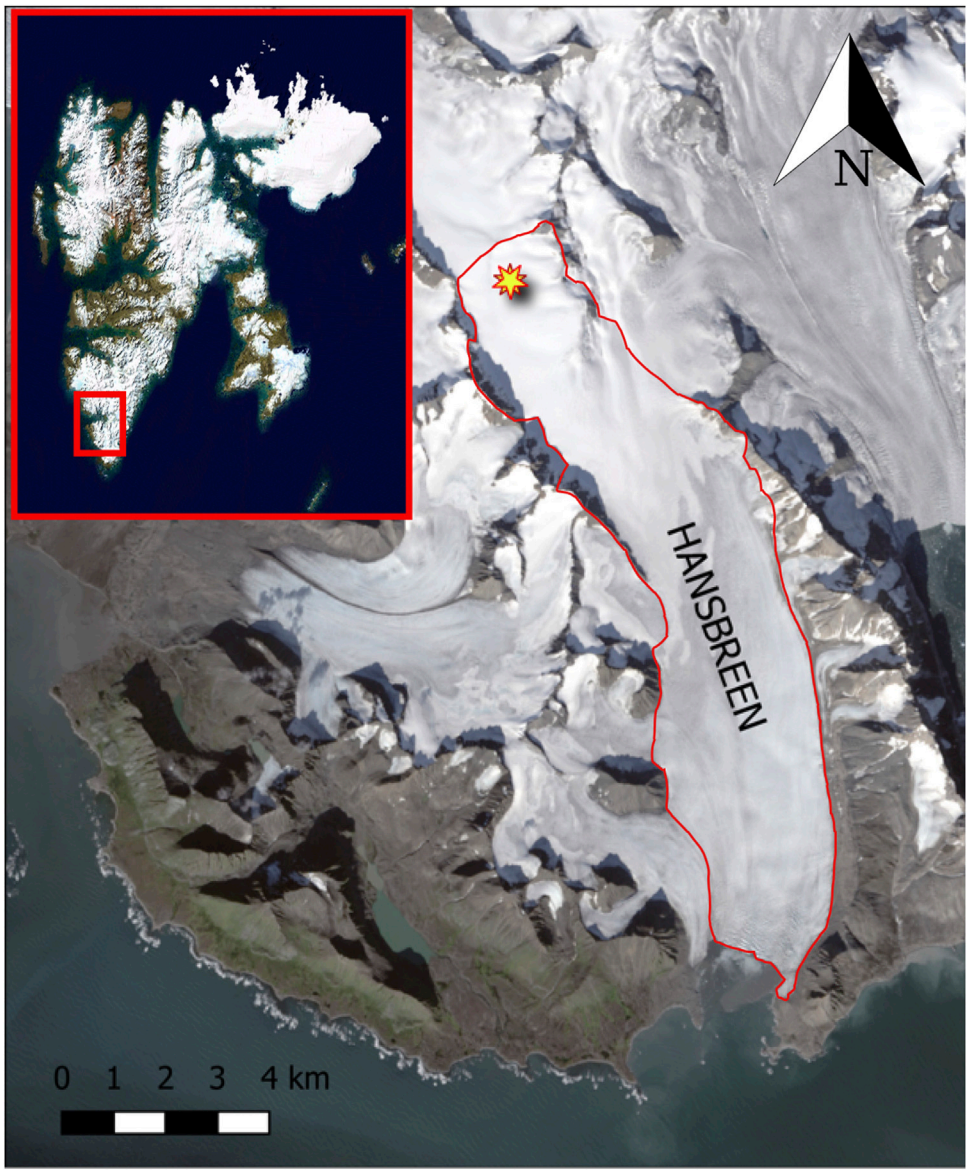

FIGURE 1 | Location of the Hansbreen (inset panel) and the sampling site during the summer season (both marked with a star marker) (Norwegian Polar Institute/ USGS Landsat). The red contour indicates the glacier basin (see https://toposvalbard.npolar.no/ for a detailed map).

carbonates: marbles and dolomites) and Sørkapp Land group (quartzite-dominated). The western side of the glacier (Czerny et al., 1993) is surrounded by the Deilegga and Eimfjellet groups. Deilegga is a formation built of metasedimentary rocks (phyllites, calcitic and dolomitic marbles). It contains pyrite, pyrrhotite, chalcopyrite, and subordinately, marcasite, galena, sphalerite, arsenopyrite, and chlorite accessory minerals. At Slyngfjellet (the mountain ridge to the side of the Hansbreen) siderite, ankerite and quartz veins have also been found (Kieres and Piestrzyński, 1992). This group can, thus, supply significant concentrations of major (Fe, S, Cu, Pb, Zn, As, Ca, Mg and Mn) and, likely, minor elements (e.g., Ni from chlorites) to the glacier. The Eimfjellet group, situated ~3 km west from Hansbreen, is built of quartzites, schists, and amphibolites. These rock types include the minerals pyrite, chalcopyrite, pyrrhotite, hematite, galena, arsenopyrite, marcasite, sphalerite, and mackinawite. Native bismuth has also been found in these rocks. Thus, it can be a source, besides the aforementioned elements, of Ni and Bi in atmospheric dust of the area. Some of the listed minerals were also found to contain Cd and Co as vicariant elements of Zn and Fe, respectively (Kieres and Piestrzyński, 1992).

Snow pack proprieties and methodological details on sample collection, preparation and analysis for the water-soluble fraction of the elements are detailed reported in the **Supplementary Material**.

TABLE 1 | Average elemental concentration order based on its sea spray contribution in the snowpack (SP Ave. Conc) and the firn core (FC. Ave Conc) expressed both as ng g^{-1}.

	ssC-SP (%)	ssC-FC (%)	SP-Ave. Conc	FC-Ave. Conc	Snowpack (flux)	Firn core (flux)	FC\SP flux ratio	Snowpack EF_{Ba}	Firn core EF_{Ba}
Ca	100.000	100.000	6.876	3.270	0.265	0.389	1.466	0.3	0.8
Sr	100.000	100.000	0.729	0.113	0.028	0.014	0.511	3.1	3.2
Mg	100.000	100.000	121.423	16.233	4.705	2.132	0.453	12.2	11.2
Na	100.000	100.000	1,061.465	297.278	41.058	40.596	0.989	55.8	139.1
K	87.406	49.129	44.079	21.963	1.706	2.912	1.707	2.1	7.1
Li	80.440	21.050	0.021	0.022	0.001	0.002	3.084	1.3	8.4
B	57.928	61.722	0.755	0.198	0.029	0.027	0.929	59.3	180.2
Rb	36.784	14.777	0.032	0.022	0.001	0.003	2.361	0.4	1.6
U	20.825	12.751	0.002	0.001	0.000	0.000	1.760	0.8	3.8
Ni	2.131	0.327	0.030	0.056	0.001	0.007	5.822	1.8	31.1
Co	1.861	0.437	0.002	0.002	0.000	0.000	3.567	0.2	1.7
As	1.836	2.236	0.014	0.003	0.001	0.000	0.831	9.4	18.3
Cs	1.600	1.508	0.002	0.001	0.000	0.000	1.078	0.4	1.1
Cd	0.805	<0.1	0.001	0.003	0.000	0.000	8.052	16.5	294.6
Mo	0.488	2.976	0.202	0.009	0.008	0.001	0.188	156.6	84.1
Se	0.408	0.361	0.022	0.007	0.001	0.001	1.274	354.2	1,112.5
Eu	0.370	0.369	0.000	0.000	0.000	0.000	1.042	0.1	0.3
Ba	0.333	0.549	0.620	0.105	0.024	0.015	0.643	1	1
V	0.313	0.330	0.060	0.016	0.002	0.002	0.980	1.4	3.8
Ga	0.119	<0.1	0.002	0.001	0.000	0.000	2.131	2.3	10.1
Cr	<0.1	<0.1	0.021	0.029	0.001	0.004	5.103	0.7	14.3
P	<0.1	0.134	14.952	1.807	0.567	0.235	0.415	27.6	32.3
Ti	<0.1	<0.1	0.181	0.050	0.007	0.007	1.036	0.1	0.2
Mn	<0.1	<0.1	0.090	0.173	0.003	0.017	5.132	0.2	1.9
Zr	<0.1	<0.1	0.006	0.004	0.000	0.001	2.356	0.0	0.2
Ce	<0.1	<0.1	0.099	0.028	0.004	0.004	1.068	1.8	4.2
Zn	<0.1	<0.1	2.004	3.330	0.078	0.427	5.476	42.0	459.0
Fe	<0.1	<0.1	2.550	0.760	0.097	0.101	1.049	0.1	0.3
Gd	<0.1	<0.1	0.007	0.002	0.000	0.000	1.157	2.8	5.6
Y	<0.1	<0.1	0.013	0.004	0.001	0.001	1.020	0.8	1.5
Pb	<0.1	<0.1	0.052	0.028	0.002	0.004	1.980	4.1	19.9
Bi	<0.1	<0.1	0.048	0.015	0.002	0.002	1.203	560.2	1,563.5
Yb	<0.1	<0.1	0.002	0.001	0.000	0.000	1.349	N\A	N\A
Al	<0.1	<0.1	4.235	0.672	0.162	0.087	0.539	0.1	0.1
Nb	<0.1	<0.1	0.102	0.012	0.004	0.002	0.488	4.4	6.9
Er	<0.1	<0.1	0.008	0.003	0.000	0.000	1.372	N\A	N\A
Nd	<0.1	<0.1	0.030	0.006	0.001	0.001	0.823	1.4	2.2
Dy	<0.1	<0.1	0.117	0.044	0.004	0.006	1.333	48.3	120.5
Sm	<0.1	<0.1	0.008	0.002	0.000	0.000	1.063	2.0	3.7
Ho	<0.1	<0.1	0.004	0.001	0.000	0.000	1.262	7.4	16.0
Th	<0.1	<0.1	0.010	0.001	0.000	0.000	0.492	1.1	1.2
La	<0.1	<0.1	0.077	0.018	0.003	0.003	0.859	3.3	6.3
Lu	<0.1	<0.1	0.007	0.003	0.000	0.000	1.406	29.9	77.4
Tm	<0.1	<0.1	0.009	0.004	0.000	0.000	1.403	N\A	N\A
Pr	<0.1	<0.1	0.176	0.034	0.007	0.005	0.733	33.4	49.1
Tb	<0.1	<0.1	0.044	0.015	0.002	0.002	1.179	105.1	224.2
In	<0.1	<0.1	0.001	0.001	0.000	0.000	3.573	19.1	198.5
Tl	<0.1	<0.1	0.001	0.001	0.000	0.000	3.025	2.1	18.5

Percentage of sea spray contribution (ssC-%) has been calculated using sodium as a reference element, based on the average elemental concentration in surface water (Millero et al., 2008). Average flux, expressed in mg m^{-2}, has been calculated using the snow\firn density from the snowpack and the shallow core samples. The last column shows the ratio between the average firn core (FC) flux and average snowpack (SP) flux. Enrichment factor (EF) for the analyzed elements calculated based on the UCC (Wedepohl, 1995) abundance and using barium as a reference element (EF_{Ba}) in both Snowpack and firn Core. The elements have been order based on the relative sea spray contribution in the snow samples.

RESULTS AND DISCUSSION

In the Hansbreen snowpack, Na concentration was the highest (1,016 ng g^{-1} on average), followed by Mg (122 ng g^{-1} on average), K (44 ng g^{-1} on average) and P (14 ng g^{-1} on average). Compared to the elements of marine origin (Millero et al., 2008; Weller et al., 2008), crustal element (Gabrielli et al., 2005) concentrations were at least one order of magnitude lower in the snow pack and firn samples (**Table 1**). For example, average Al, Fe and Zn concentrations in the snow pack were 4.2, 2.6, and 2.0 ng g^{-1}, respectively. Specific trace elements, that has already been associated with human activities such as Pb, Cr, Cd and As,

showed concentrations in the snow pit of 0.052, 0.021, 0.039, and 0.014 ng g^{-1}, respectively. Assuming that Na is primarily derived from sea spray aerosols (Rhodes et al., 2018) and using the average elemental concentration in seawater (Millero et al., 2008), we can distinguish the elements with predominant sea spray contribution (ssC) from those that are mainly of crustal origin (**Table 1** and **Supplementary Material**). In the Hansbreen snowpack, Mg, Ca and Sr were completely derived from sea spray emissions, while the sea-spray contribution rates for Li, K, B, Rb and U were 80, 87, 58, 37, and 20%, respectively (**Table 1**). Ca and Sr can also have crustal sources (e.g. Sofiebogen Ridge, Slyngfjellet peak, Deillega Ridge), but due to the high sea spray emission and the short distance between the sampling site and coastline (15 km), those seem completely overwhelmed by the marine contribution. The firn samples reveal an overall high ssC for elements such as Na, Mg and K (**Table 1**), however, the lower ssC for Li, U, K and Rb, in the firn with respect to annual snow pack suggests a rather likely increased contribution of dust deposition during snow-free season.

While the annual snowpack is representative of a single year, the firn is a result of several years of accumulation. In the Hansbreen, it is particularly difficult to date the firn, since percolation of liquid water might mix the layers and re-distribute the water-soluble fraction of chemical species across them. Therefore, in order to compare snow and firn, the elemental concentration in each snow and shallow core sample was multiplied by the water equivalent to obtain a deposition flux for each element expressed as mg m^{-2} (see **Supplementary Material** and **Supplementary Table S1**). This flux is representative of the mass deposition for each studied layer/sample (**Table 1**). We used the average flux per m^2 calculated from each sample instead of the annual flux to avoid the inaccurate dating problem.

Based on the firn\snow flux ratio, three main groups of elements can be distinguished. Snow pit and firn profile of representative elements for each group are reported in **Figure 2**. The first group includes Mo, P, Mg, Th, Sr, Al, Ba and As. These elements showed an average deposition flux that is higher in the annual snowpack than in the firn (firn\snow ratio <1). The second group includes B, V, Na, Ti, Fe and Ce, whose average depositional fluxes in the two compartments were not different (firn\snow ratio ≈1). The third group included Bi, Se, Ca, K, U, Pb, Rb, Tl, Li, Co, In, Cr, Mn, Zn, Ni and Cd; which had a higher average depositional flux in the firn samples (firn\snow ratio >1) (**Figure 3**).

Elements in the first and second group seem mainly related to sea spray aerosols and more water-soluble since they are mainly present in the salt form. However in this two groups exception are presence since Al, V, Ti and Mo are mainly crustal origin elements (Gabrielli et al., 2005). Snowmelt has an effect on the concentration of soluble elements (Brimblecombe et al., 1987; Spolaor et al., 2016) such as Na, P, Mg, Ca, K, Ba and B, by washing them out of the snowpack. For Mg, P and Ba, in particular, the lower average flux in the firn suggests a strong wash out from snowpack and likely a subsequent glacier surface run-off during melting season. The fact that Na and Ca do not show differences in the average deposition flux between firn and snow possibly indicates constant/similar deposition throughout the entire year. Molybdenum shows a significantly higher flux in the snowpack as compared to the firn (**Figure 3**). The natural presence of Mo is commonly associated with the occurrence of the mineral molybdenite (MoS_2). This latter mineral is typical of granitoid rocks outcropping in different Arctic regions (e.g, N-Norway and E-Greenland), and only small outcrops of these rocks were found in the northernmost Svalbard (Johansson et al., 2002). In coal mining regions, however, Mo is usually present in trace amounts in ore deposits, but it can be enriched due to exploitation (Frascoli and Hudson-Edwards, 2018). Also, Mo associated with over bank deposits from Triassic rocks has low content in sediments. In this respect, the lower average depositional flux of Mo in the firn compared to the snowpack suggests a medium to long-range transport of molybdenite to Svalbard. Mo can also be derived from coal combustion (Harkness et al., 2017). Therefore, its presence in the snowpack might be related to long-range or regional transport, since coal is used in the Svalbard archipelago for energy production since its marine contribution is less than 1% in the snow-samples (**Table 1**). Aluminum is a crustal element and the sea spray contribution is relatively low. Aluminum has a poor solubility, as supported by the EF << 1, and its total abundance could be determined only after complete mineralization of the particulate fraction. The lower amount of water-soluble fraction in the firn core compared to the snow pit (FC\SP < 1) could be the result of removing the soluble fraction during snow pack melting. The late spring melting could remove the soluble Al fraction (Stachnik et al., 2019), leaving the insoluble Al fraction trapped in the ice. This might also occur for Fe, which is abundant in the mineral particle lattice.

The third and largest group of elements (**Table 1**), suggests the occurrence of different specific processes which can strongly influence their concentrations in the firn as compared to the snowpack, such as 1) the retention of dust particles in the annual accumulated firn, 2) their increase weathering due to water presence during summer 3) the contribution of human activities, 4) the change in dust transport pathways, and 5) the activation of different, local sources during summer. The retention (hypothesis a) of the insoluble dust particles in firn due to snow mass reduction during summer can play an important role. If this were the main process contributing to elemental load, we would expect that their abundance should be similar to that of the snowpack. However as observed in **Table 1** and **Figure 3**, this is not the case, therefore the reduction of snow mass during the melting season cannot explain the observed difference alone. We should note that we are considering the water-soluble fraction of the investigated elements, and not the whole composition of insoluble dust particles. We cannot exclude that summer weathering process (hypothesis b) could act diversely for each element and partially contributing to the difference observed but crustal elements are present in the mineral lattice and only a minor fraction could be released\converted in the water-soluble fraction. Human activities can also impact elemental deposition in the Arctic/Svalbard region. As a first approximation, and with caution (Reimann et al., 2005), we used the Enrichment Factor (EF) approach to disentangle possible anthropogenic contributions

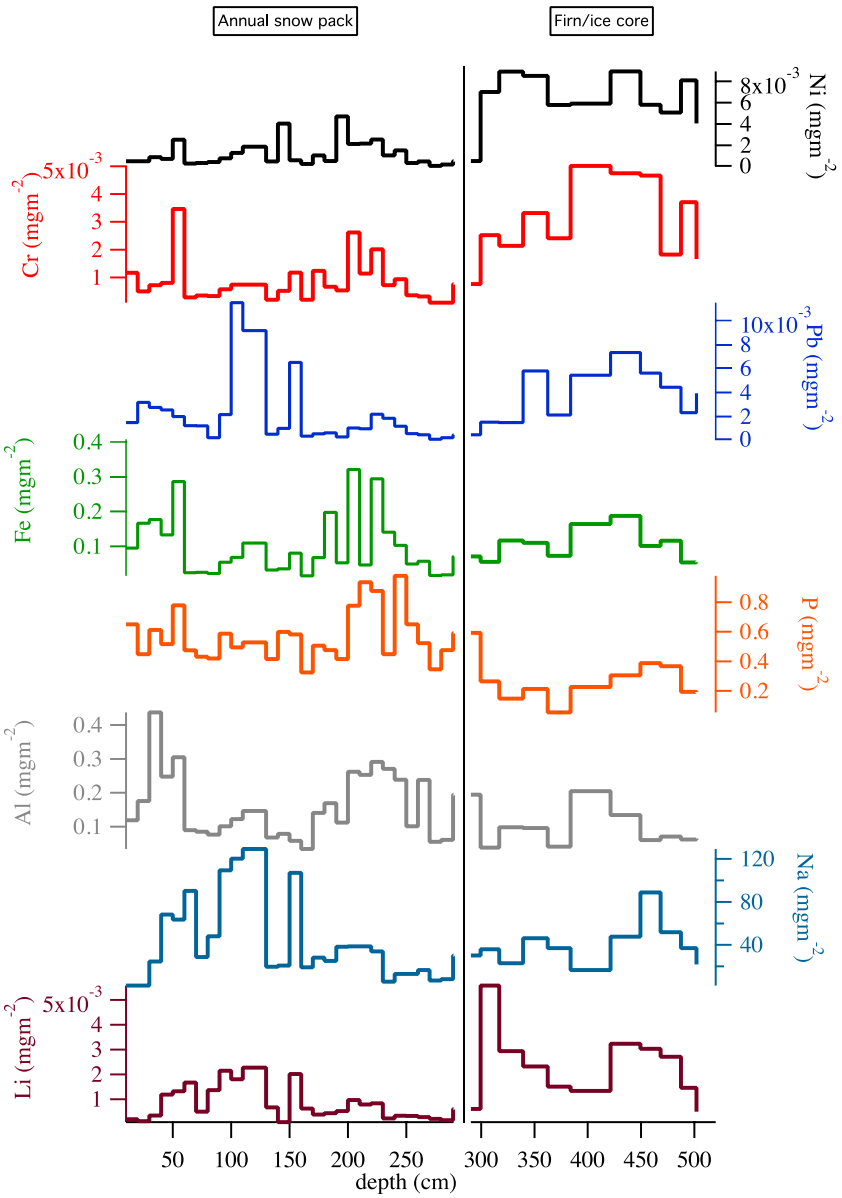

FIGURE 2 | Snowpack sample flux **(left panels)** versus firn sample flux **(right panels)** of selected elements for the three groups. Lithium, Ni, Cr, and Pb are representative of the third group (Bi, Se, Ca, K, U, Pb, Rb, Tl, Li, Co, In, Cr, Mn, Zn, Ni, and Cd), Fe and Na of the second (B, V, Na, Ti, Fe, and Ce) and Al and P of the third (Mo, P, Mg, Th, Sr, Al, Ba, and As). The left and right axis units are both mg m^{-2}, lower axis represents the depth (in cm) from the annual snowpack surface.

from natural ones. We calculated the EFs using barium as crustal tracer (EF_{Ba}) for its solubility, abundance and the negligible effect of sea spray emissions on its concentration. The enrichment factor was calculated based on the chemical element abundance in the Upper Continental Crust (UCC) as reported in (Wedepohl, 1995). Considering the low contribution of sea spray for almost all the crustal elements (no sea spray corrections were applied for the elements in this group), the EF was calculated for the average deposition flux in the snow pit and the firn samples (**Table 1**). Since only the soluble fraction of elements was determined, these values of EF might actually result from a combination of: 1) specific composition of the incoming material; 2) different *in situ* distribution between particulate and dissolved fraction due to different solubility; and 3) different mobility of the elements also due to their different solubility. Given that these processes cannot be disentangled with the available data, particular care must be taken in the interpretation of EFs. However, useful indications on the elemental sources can be extracted even so.

As a rule of thumb, an element is considered enriched when EF > 100. The enrichment factor is a method frequently adopted to evaluate possible extra sources, in addition to natural ones, that contribute to the deposition of a specific element. In this respect, Bismuth (Bi) is the most enriched element with values of 560 and ~1,560 in the annual snowpack and the firn samples, respectively.

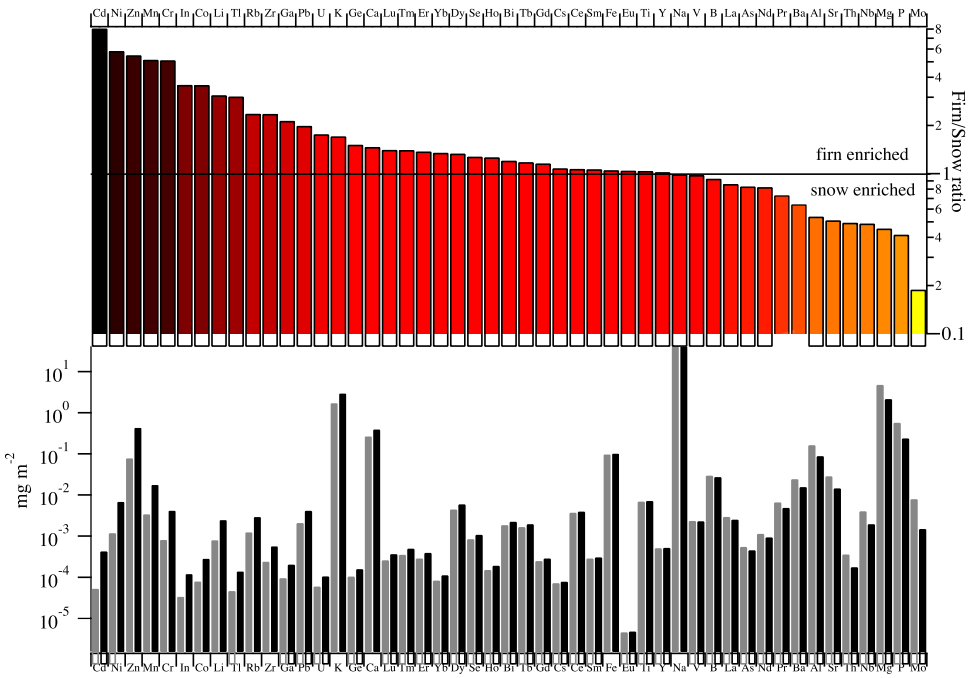

FIGURE 3 | Firn and snow flux and their ratio for the analyzed elements. The upper panel shows the firn\snow ratio for each element. The enrichment of elements in firn is represented on a color scale from light\yellow **(low)** to the dark red **(high)**. The lower panel shows the average flux in the annual snowpack (grey bars) and in the firn samples (black bars).

The higher EF_{Ba} of Bi is difficult to assess and additional investigation must be considered but, in the surrounding area of the Hansbreen, pegmatite outcrops might contribute to the snow\ice load (Majka and Kośmińska, 2017) and native bismuth was also found in mountain peaks (Kieres and Piestrzyński, 1992). However, the presence of such rocks might not explain fully the high EF_{Ba} determined. Bismuth might also have an anthropogenic contribution from coal and oil combustion, as well as from aluminum production (Ferrari et al., 2000). A higher enrichment was also found for Se, probably resulting from marine (Amouroux et al., 2001) and terrestrial (Aastrup et al., 2000) biological emissions, although anthropogenic influences cannot be excluded (Tan et al., 2016). Lead had an EF of 19.9 in the firn samples and 4.1 in the snow. The increase in EF_{Ba} for several elements in firn might suggest that during the summer period, the extent of air mass transport from lower latitudes increases due to the breakdown of the polar vortex. Another hypothesis is that the local ship emissions contribute significantly to the amount of these specific trace elements in the aerosol. However, we sampled close to the equilibrium line altitude that is surrounded by snow-free mountain peak in summer (e.g. Skilryggen, Strypegga), which contain galena (PbS) bearing rocks (Kieres and Piestrzyński, 1992; Czerny et al., 1993), therefore local dust might also be a non-negligible source and might become the most important source for impurities in the glacier. This last hypothesis is supported by the REEs relative abundance and specific ratios that do not show significant differences between snow and firn samples (**Supplementary Figure S1**) suggesting a negligible change of the long range transport mainly affecting this group of elements. Zinc and In both had a relatively high flux and EF_{Ba} in the firn as compared to the snowpack (five and three times higher, respectively). This increased depositional flux in the firn can be associated with the common presence of sphalerite (ZnS) in the metamorphic basement outcropping in the Hornsund region (Kieres and Piestrzyński, 1992; Czerny et al., 1993). Nickel, Cr and Co, which had higher firn/snow flux ratios (**Figure 3**; **Table 1**), are frequently associated with minerals such as iron sulphides, sphalerite, magnetite found in Svalbard bedrock, including the study area (Kieres and Piestrzyński, 1992). This could suggest that the activation of local rock dust sources during summer significantly impacts the glacier firn elemental concentrations. The other elements with a positive firn/snow ratio are associated with several minerals that are widespread in Svalbard and other geological regions, thus rendering the identification of specific source regions difficult. However, out of fifteen elements in this third type of EF behavior, seven were found in rocks in the direct vicinity of Hansbreen, and further five could be sourced from rock erosion within 15 km radius from there (Kozak et al., 2015; Kosek et al., 2019a; Kosek et al., 2019b).

The highest difference between firn and annual snowpack depositional flux was determined for Cd, with firn values eight times higher than in the snow. Although we cannot exclude a local contribution (e.g. in range of 0.3–3% in sphalerite), Cd is generally considered a marker for long-range dust transport, since it is mainly anthropogenically produced from the smelting of non-ferrous metals (Łokas et al., 2019). Its increase in the firn samples might be associated with transport from North

America and Siberia during the summer, following the breakdown of the polar vortex.

CONCLUSION

The results obtained in the present work suggest that the Hansbreen snowpack is strongly influenced by marine emissions with a higher depositional flux of marine-related elements as compared to crustal elements. Significant differences between the composition of the annual snowpack and the firn samples were observed. In particular, elements present in the sediment\rocks in the Hornsund region and characterizing the Svalbard geology showed a higher depositional flux in the firn as compared to the annual snowpack.

The annual snowpack showed higher depositional flux for a few elements (for instance, Mo) not abundant in the mineralogy of the area and might associate with local human activities or long-range transport. The higher depositional flux for a large number of crustal elements in the firn and, in particular, for Ni, Cr and Co are likely associated with minerals and rocks abundant in the Hornsund region. The higher abundance of the latter elements suggests that, during the summer periods, the local dust sources are predominant, although some anthropogenic contamination (such as for Cd), derived from long-range transport, might influence the total deposition.

The results presented suggest that Svalbard glaciers, like Hansbreen, whose summit is close to the equilibrium line, are prone to predominant local dust deposition during summer (late) when some freezing is possible after summer melting. Local dust deposition may, thus, affect the chemical composition of the glacier ice. On the other hand, elements released from annual snowpack during the melt season seem to have minor influence on the overall chemical signature. Quantitative evaluation of the whole composition compared to the water-soluble fraction is necessary to obtain a clear picture of deposition versus melting effects. In addition, the impact of cryoconite as a trap for dust and on the efficiency of dust particle transfer from surface to the glacier ice should also be considered in future studies.

DATA AVAILABILITY STATEMENT

The datasets generated for this study are available on request to the corresponding author.

AUTHOR CONTRIBUTIONS

AS, BL, AN, CL, KK, FP, and DC conceived the experiment and collected the samples, AS and MR. measured the samples, AS, BM, CL, and DC: wrote the paper with inputs from CT, EB, J-CG, LS, BL, AN, and KK.

ACKNOWLEDGMENTS

The field activities of AS, CL, and DC at the Polish Polar Station in Hornsund were supported by the INTERACT Transnational Access (H2020, BC-HOR project, Grant Agreement No. 730938); of KK and FP-by the National Science Centre of Poland, grant no. 2017/26/D/ST10/00630. We thank also the Norwegian Research Council which supported BL's and AN's field activities through the Svalbard Strategic Grant BC-3D "Spatial Distributions of Black Carbon and Mineral Dust in Air and Snow Surface Layers upon Svalbard Glaciers". This project has also received funding from the European Union's Horizon 2020 research and innovation programme under grant agreement no. 689443 via project iCUPE (Integrative and Comprehensive Understanding on Polar Environments). AN and BL were also supported by the Institute of Geophysics, Polish Academy of Sciences within statutory activities no. 3841/E-41/S/2020 of the Ministry of Science and Higher Education of Poland.

SUPPLEMENTARY MATERIAL

The Supplementary Material for this article can be found online at: https://www.frontiersin.org/articles/10.3389/feart.2020.536036/full#supplementary-material.

REFERENCES

Aas, K. S., Dunse, T., Collier, E., Schuler, T. V., Berntsen, T. K., Kohler, J., et al. (2016). The climatic mass balance of svalbard glaciers: a 10-year simulation with a coupled atmosphere–glacier mass balance model. *The Cryosphere* 10, 1089–1104. 10.5194/tc-10-1089-2016

Aastrup, P., Riget, F., Dietz, R., and Asmund, G. (2000). Lead, zinc, cadmium, mercury, selenium and copper in Greenland caribou and reindeer (rangifer tarandus). *Sci. Total Environ.* 245, 149–159. doi:10.1016/s0048-9697(99)00440-4

Amouroux, D., Liss, P. S., Tessier, E., Hamren-Larsson, M., and Donard, O. F. X. (2001). Role of oceans as biogenic sources of selenium. *Earth Planet Sci. Lett.* 189, 277–283. doi:10.1016/S0012-821X(01)00370-3

Barbante, C., Veysseyre, A., Ferrari, C., Van De Velde, K., Morel, C., Capodaglio, G., et al. (2001). Greenland snow evidence of large scale Atmospheric contamination for platinum, palladium, and rhodium. *Environ. Sci. Technol.* 35, 835–839. doi:10.1021/es000146y

Barbante, C., Spolaor, A., Cairns, W. R. L., and Boutron, C. (2017). Man's footprint on the Arctic environment as revealed by analysis of ice and snow. *Earth Sci. Rev.* 168, 218–231. doi:10.1016/j.earscirev.2017.02.010

Barbaro, E., Spolaor, A., Karroca, O., Park, K. T., Martma, T., Isaksson, E., et al. (2017a). Free amino acids in the Arctic snow and ice core samples: potential markers for paleoclimatic studies. *Sci. Total Environ.* 607-608, 454–462. doi:10.1016/j.scitotenv.2017.07.041

Barbaro, E., Zangrando, R., Padoan, S., Karroca, O., Toscano, G., Cairns, W. R. L., et al. (2017b). Aerosol and snow transfer processes: an investigation on the behavior of water-soluble organic compounds and ionic species. *Chemosphere* 183, 132–138. doi:10.1016/j.chemosphere.2017.05.098

Barbaro, E., Zangrando, R., Kirchgeorg, T., Bazzano, A., Illuminati, S., Annibaldi, A., et al. (2016). An integrated study of the chemical composition of Antarctic aerosol to investigate natural and anthropogenic sources. *Environ. Chem.* 13 (5) 867–876. doi:10.1071/EN16056

Birkenmajer, K. (1990). *Hornsund Spitsbergen 1:75 000 Geology*. Katowice, Poland: University of Silesia.

Brimblecombe, P., Clegg, S. L., Davies, T. D., Shooter, D., and Tranter, M. (1987). Observations of the preferential loss of major ions from melting snow and laboratory ice. *Water Res*. 21, 1279–1286. doi:10.1016/0043-1354(87)90181-3

Conca, E., Abollino, O., Giacomino, A., Buoso, S., Traversi, R., Becagli, S., et al. (2019). Source identification and temporal evolution of trace elements in PM10 collected near to Ny-Ålesund (Norwegian Arctic). *Atmos. Environ*. 203, 153–165. doi:10.1016/j.atmosenv.2019.02.001

Czerny, J., Kieres, A., Manecki, M., and Rajchel, J. (1993). "Geological map of the SW part of wedel-jarlsberg land, spitsbergen," in *Institute of geology and mineral deposits*. Editor A. Manecki (Kraków, Poland: University of Mining and Metallurgy).

Ezerinskis, Z., Spolaor, A., Kirchgeorg, T., Cozzi, G., Vallelonga, P., Kjær, H. A., et al. (2014). Determination of 129I in Arctic snow by a novel analytical approach using IC-ICP-SFMS. *J. Anal. At. Spectrom*. 29, 1827–1834. doi:10.1039/C4JA00179F

Feltracco, M., Barbaro, E., Tedeschi, S., Spolaor, A., Turetta, C., Vecchiato, M., et al. (2020). Interannual variability of sugars in arctic aerosol: biomass burning and biogenic inputs. *Sci. Total Environ*. 706, 136089. doi:10.1016/j.scitotenv.2019.136089

Ferrari, C. P., Hong, S., Van de Velde, K., Boutron, C. F., Rudniev, S. N., Bolshov, M., et al. (2000). Natural and anthropogenic bismuth in central greenland. *Atmos. Environ*. 34, 941–948. doi:10.1016/S1352-2310(99)00257-5

Frascoli, F., and Hudson-Edwards, K. A. (2018). Geochemistry, mineralogy and microbiology of molybdenum in mining-affected environments. *Minerals* 8 (4), 42. 10.3390/min8020042

Gabrielli, P., Planchon, F. A. M., Hong, S., Lee, K. H., Hur, S. D., Barbante, C., et al. (2005). Trace elements in Vostok Antarctic ice during the last four climatic cycles. *Earth Planet Sci. Lett*. 234, 249–259. 10.1016/j.epsl.2005.03.001

Gallet, J.-C., Björkman, M., Borstad, C. P., Hodson, A. J., Jacobi, H.-W., Larose, C., et al. (2019). "Snow research in Svalbard: current status and knowledge gaps," in *SESS report 2018*. Editors E. Orr, G. Hansen, H. Lappalainen, C. Hübner, and H. Lihavainen (Longyearbyen, Norway: Svalbard Integrated Arctic Earth Observing System), 82–107.

Harkness, J. S., Darrah, T. H., Moore, M. T., Whyte, C. J., Mathewson, P. D., Cook, T., et al. (2017). Naturally occurring versus anthropogenic sources of elevated molybdenum in groundwater: evidence for geogenic contamination from southeast Wisconsin, United States. *Environ. Sci. Technol*. 51, 12190–12199. doi:10.1021/acs.est.7b03716

Johansson, Å., Larionov, A. N., Tebenkov, A. M., Ohta, Y., and Gee, D. G. (2002). Caledonian granites of western and central Nordaustlandet, northeast Svalbard. *GFF* 124 (3), 135–148. doi:10.1080/11035890201243135

Kieres, A., and Piestrzyński, A. (1992). Ore-mineralization of the hecla hoek succession (precambrian) around werenskioldbreen, South Spitsbergen. *Stud. Geol. Pol*. 98, 115–151.

Kohler, J., James, T. D., Murray, T., Nuth, C., Brandt, O., Barrand, N. E., et al. (2007). Acceleration in thinning rate on western Svalbard glaciers. *Geophys. Res. Lett*. 34, L18502. doi:10.1029/2007GL030681

Kosek, K., Luczkiewicz, A., Kozioł, K., Jankowska, K., Ruman, M., and Polkowska, Ż. (2019a). Environmental characteristics of a tundra river system in Svalbard. Part 1: bacterial abundance, community structure and nutrient levels. *Sci. Total Environ*. 653, 1571–1584. doi:10.1016/j.scitotenv.2018.11.378

Kosek, K., Kozioł, K., Luczkiewicz, A., Jankowska, K., Chmiel, S., and Polkowska, Ż. (2019b). Environmental characteristics of a tundra river system in Svalbard. Part 2: chemical stress factors. *Sci. Total Environ*. 653, 1585–1596. doi:10.1016/j.scitotenv.2018.11.012

Kozak, K., Kozioł, K., Luks, B., Chmiel, S., Ruman, M., Marć, M., et al. (2015). The role of atmospheric precipitation in introducing contaminants to the surface waters of the Fuglebekken catchment. *Spitsbergen. Polar Res*. 34, 24207. doi:10.3402/polar.v34.24207

Laska, M., Luks, B., and Budzik, T. (2016). Influence of snowpack internal structure on snow metamorphism and melting intensity on Hansbreen. *Svalbard, Polish Polar Research* 37 (2), 193–218. doi:10.1515/popore-2016-0012

Łokas, E., Zaborska, A., Sobota, I., Gaca, P., Milton, J., Kocurek, P., et al. (2019). Airborne radionuclides and heavy metals in high Arctic terrestrial environment as the indicators of sources and transfers of contamination. *The Cryosphere* 13, 2075–2086. doi:10.5194/tc-2019-34

López-Moreno, J. I., Boike, J., Sanchez-Lorenzo, A., and Pomeroy, J. W. (2016). Impact of climate warming on snow processes in Ny-Ålesund, a polar maritime site at Svalbard. *Global Planet. Change* 146, 10–21. doi:10.1016/j.gloplacha.2016.09.006

Majka, J., and Kośmińska, K. (2017). Magmatic and metamorphic events recorded within the southwestern basement province of svalbard. *Arktos* 3 (5), 1–7. doi:10.1007/s41063-017-0034-7

Maturilli, M., Herber, A., and König-Langlo, G. (2013). Climatology and time series of surface meteorology in Ny-Älesund, Svalbard. *Earth Syst. Sci. Data* 5, 155–163. doi:10.5194/essd-5-155-2013

Millero, F. J., Feistel, R., Wright, D. G., and McDougall, T. J. (2008). The composition of standard seawater and the definition of the reference-composition salinity scale. *Deep Sea Res. Oceanogr. Res. Pap*. 55, 50–72. doi:10.1016/j.dsr.2007.10.001

Möller, M., and Kohler, J. (2018). Differing climatic mass balance evolution across Svalbard glacier regions over 1900–2010. *Front. Earth Sci*. 6, 128. doi:10.3389/feart.2018.00128

Moroni, B., Cappelletti, D., Ferrero, L., Crocchianti, S., Busetto, M., Mazzola, M., et al. (2016). Local vs. long-range sources of aerosol particles upon Ny-Ålesund (Svalbard Islands): mineral chemistry and geochemical records. *Rendiconti Lincei*. 27, 115–127. doi:10.1007/s12210-016-0533-7

Nawrot, A. P., Migała, K., Luks, B., Pakszys, P., and Głowacki, P. (2016). Chemistry of snow cover and acidic snowfall during a season with a high level of air pollution on the Hans Glacier, Spitsbergen. *Polar Sci*. 1 (3), 249–261. doi:10.1016/j.polar.2016.06.003

Osuch, M., and Wawrzyniak, T. (2017). Variations and changes in snow depth at meteorological stations Barentsburg and Hornsund (Spitsbergen). *Ann. Glaciol*. 58 (75), 11–20. doi:10.1017/aog.2017.20

Pedersen, C. A., Gallet, J. C., Ström, J., Gerland, S., Hudson, S. R., Forsström, S., et al. (2015). *In situ* observations of black carbon in snow and the corresponding spectral surface albedo reduction. *J. Geophys. Res.: Atmosphere* 120, 1476–1489. doi:10.1002/2014JD022407

Reimann, C., and de Caritat, P. (2005). Distinguishing between natural and anthropogenic sources for elements in the environment: regional geochemical surveys versus enrichment factors. *Sci. Total Environ*. 337, 91–107. doi:10.1016/j.scitotenv.2004.06.011

Rhodes, R. H., Yang, X., and Wolff, E. W. (2018). Sea ice versus storms: what controls sea salt in arctic ice cores?. *Geophys. Res. Lett*. 45, 5572–5580. doi:10.1029/2018GL077403

Schuler, T. V., Glazovsky, A., Hagen, J. O., Hodson, A., Jania, J., Kääb, A., et al. (2020). "New data, new techniques and new challenges for updating the state of Svalbard glaciers (SvalGlac)," in *SESS report 2019*. Editors F. van den Heuvel, C. Hübner, M. Błaszczyk, M. Heimann, and H. Lihavainen (Longyearbyen, Norway: Svalbard Integrated Arctic Earth Observing System), 108–134.

Siudek, P., Frankowski, M., and Siepak, J. (2015). Trace element distribution in the snow cover from an urban area in central Poland. *Environ. Monit. Assess*. 187, 225. doi:10.1007/s10661-015-4446-1

Spolaor, A., Barbaro, E., Christille, J. M., Kirchgeorg, T., Giardi, F., Cappelletti, D., et al. (2016). Evolution of the Svalbard annual snow layer during the melting phase. *Rendiconti Lincei*. 2016, 1–8. doi:10.1007/s12210-015-0500-8

Spolaor, A., Gabrieli, J., Martma, T., Kohler, J., Björkman, M. B., Isaksson, E., et al. (2013). Sea ice dynamics influence halogen deposition to Svalbard. *The Cryosphere* 7, 1645–1658. doi:10.5194/tcd-7-1075-2013

Stachnik, Ł., Yde, J. C., Nawrot, A., Uzarowicz, Ł., Łepkowska, E., and Kozak, K. (2019). Aluminium in glacial meltwater demonstrates an association with nutrient export (Werenskiöldbreen, Svalbard). *Hydrol. Process*. 33, 1638–1657. doi:10.1002/hyp.13426

Tan, L. C., Nancharaiah, Y. V., van Hullebusch, E. D., and Lens, P. N. L. (2016). Selenium: environmental significance, pollution, and biological treatment technologies. *Biotechnol. Adv*. 34, 886–907. doi:10.1016/j.biotechadv.2016.05.005

Van Pelt, W., Pohjola, V., Pettersson, R., Marchenko, S., Kohler, J., Luks, B., et al. (2019). A long-term dataset of climatic mass balance, snow conditions and runoff in Svalbard (1957–2018). *The Cryosphere* 13, 2259–2280. doi:10.5194/tc-13-2259-2019

Vecchiato, M., Barbaro, E., Spolaor, A., Burgay, F., Barbante, C., Piazza, R., et al. (2018). Fragrances and PAHs in snow and seawater of Ny-Ålesund (Svalbard): local and long-range contamination. *Environ. Pollut*. 242, 1740–1747. doi:10.1016/j.envpol.2018.07.095

Wedepohl, K. H. (1995). The composition of the continental crust. *Geochem. Cosmochim. Acta* 59, 1217–1232. doi:10.1016/0016-7037(95)00038-2

Weller, R., Wöltjen, J., Piel, C., Resenberg, R., Wagenbach, D., König-Langlo, G., et al. (2008). Seasonal variability of crustal and marine trace elements in the aerosol at Neumayer station, Antarctica. *Tellus B.* 60, 742–752. doi:10.1111/j.1600-0889.2008.00372.x

Winther, J. G., Bruland, O., Sand, K., Killingtveit, Å., and Marechal, D. (1998). Snow accumulation distribution on spitsbergen, svalbard, in 1997. *Polar Res.* 17, 155–164. doi:10.1111/j.1751-8369.1998.tb00269.x

Zielinski, T., Bolzacchini, E., Cataldi, M., Ferrero, L., Graßl, S., Hansen, G., et al. (2020). Study of chemical and optical properties of biomass burning aerosols during long-range transport events toward the arctic in summer 2017. *Atmosphere* 11 (1), 84. doi:10.3390/atmos11010084

Conflict of Interest: The authors declare that the research was conducted in the absence of any commercial or financial relationships that could be construed as a potential conflict of interest.

Copyright © 2021 Spolaor, Moroni, Luks, Nawrot, Roman, Larose, Stachnik, Bruschi, Kozioł, Pawlak, Turetta, Barbaro, Gallet and Cappelletti. This is an open-access article distributed under the terms of the Creative Commons Attribution License (CC BY). The use, distribution or reproduction in other forums is permitted, provided the original author(s) and the copyright owner(s) are credited and that the original publication in this journal is cited, in accordance with accepted academic practice. No use, distribution or reproduction is permitted which does not comply with these terms.

frontiers in Earth Science

ORIGINAL RESEARCH
published: 28 January 2021
doi: 10.3389/feart.2020.527663

Physicochemical Impacts of Dust Storms on Aerosol and Glacier Meltwater on the Northern Margin of the Taklimakan Desert

Cunying Zheng[1,2], *Zhongqin Li*[1,3,4]*, *Ping Zhou*[1], *Xin Zhang*[1], *Xi Zhou*[1,5] *and Shan Ma*[5]

[1]State Key Laboratory of Cryospheric Sciences, Northwest Institute of Eco-Environment and Resources, Lanzhou, China, [2]University of Chinese Academy of Sciences, Beijing, China, [3]College of Geography and Environmental Sciences, Northwest Normal University, Lanzhou, China, [4]College of Sciences, Shihezi University, Xinjiang, China, [5]Key Laboratory of Western China's Environmental Systems (Ministry of Education), College of Earth and Environmental Sciences, Lanzhou University, Lanzhou, China

To analyze the impacts of dust storms on the atmospheric and meltwater environment, intensive and simultaneous sampling for aerosols and meltwater on the terminal moraine (41°73′ N, 79°88′ E, 3,789 m a.s.l.) of Qingbingtan Glacier No. 72 (Glacier No. 72) on the northern margin of the Taklamakan Desert were conducted during the summer of 2008. Aerosol and meltwater chemistry (including the species of Na^+, K^+, Mg^{2+}, Ca^{2+}, NH_4^+, Cl^-, SO_4^{2-}, and NO_3^-) was analyzed by ion chromatography. The results indicated that the major anions and cations in the samples were SO_4^{2-} and Ca^{2+}, respectively. In the dust event, the average value of aerosol ions was 566.91 neq·m^{-3}, which was nearly five times that under nondust conditions (115.58 neq·m^{-3}). In addition, in the meltwater samples, the sum of ion concentrations ranged from 31.26 to 180.98 mg·L^{-1}, with an average of 76.40 mg·L^{-1}. When a dust storm occurred, the ion concentrations in these two media increased significantly and simultaneously, but with different trends due to the different influencing factors. That is, the atmospheric environment was significantly affected by the dust storm. According to the correlation analysis and principal component analysis, the water-soluble ions, such as SO_4^{2-}, Cl^-, Na^+, K^+, Mg^{2+}, and Ca^{2+}, originated from natural sources, while NH_4^+ and NO_3^- originated from anthropogenic sources. The results of the air mass trajectory suggested that the regional dust storms caused by the air masses originating from Eastern Europe and Siberia had a significant influence on the glacial environment.

Keywords: qingbingtan glacier No 72, dust storms, atmospheric aerosol, meltwater, sources

OPEN ACCESS

Edited by:
Khanghyun Lee,
Korea Polar Research Institute,
South Korea

Reviewed by:
Zhiwen Dong,
Chinese Academy of Sciences (CAS), China
Jizu Chen,
Chinese Academy of Sciences (CAS), China
Ramanathan Alagappan,
Jawaharlal Nehru University, India

***Correspondence:**
Zhongqin Li
lizq@lzb.ac.cn.com

Specialty section:
This article was submitted to Cryospheric Sciences, a section of the journal Frontiers in Earth Science

Received: *17 January 2020*
Accepted: *16 December 2020*
Published: *28 January 2021*

Citation:
Zheng C, Li Z, Zhou P, Zhang X, Zhou X and Ma S (2021) Physicochemical Impacts of Dust Storms on Aerosol and Glacier Meltwater on the Northern Margin of the Taklimakan Desert. Front. Earth Sci. 8:527663. doi: 10.3389/feart.2020.527663

INTRODUCTION

Dust aerosols contribute nearly 75% of the global aerosol mass load and 30% of the global aerosol optical thickness. It is highly emphasized that dust aerosols play an important role in connecting the atmosphere, biosphere, and lithosphere, making them a critical factor in global mass circulation (Tang et al., 2018). The Earth's radiation budget can be perturbed by dust aerosols through their direct (scattering as well as absorbing solar and terrestrial thermal radiation), semidirect (changing the evaporation rate of cloud droplets), and indirect (modification of cloud optical properties and lifetimes) effects (Seinfeld et al., 2016; Kedia et al., 2018). Dust aerosols also have a significant impact

on global climate change (Wang et al., 2015), deterioration of air quality, visibility reduction and human health (Goudie, 2014), marine ecosystems, and biogeochemical cycles through their transportation mechanisms. The transportation mechanisms are highly dependent on the composition, concentration, and particle size distribution of dust aerosols (Ramanathan et al., 2001; Chow et al., 2008; Seinfeld and Pandis, 2012). The radiative forcing of aerosols is considered to be especially important at the regional scale because their lifetime is relatively short, which is different from the radiative forcing of greenhouse gases. Aerosols are removed from the atmosphere through dry and wet deposition. Dust aerosols can also mix with anthropogenic aerosols while they are being transported hundreds to thousands of kilometers away, which play a crucial role in the atmospheric chemistry and biogeochemical cycles in the Northern Hemisphere (Duce et al., 1991; Arimoto et al., 1996; Griffin, 2007). Dust aerosols deposited on glacial surfaces can decrease snow albedo by enhancing lighting absorption, which is a vital factor influencing glacial melt (Wang et al., 2013; Kaspari et al., 2015). Dust particles also have a significant impact on the chemistry of glacial meltwater. The hydrochemical characteristics of meltwater runoff will be affected by dust particles. Analyzing meltwater chemistry is of great significance to studying dramatic glacial change influences on meltwater (Dong et al., 2014). Moreover, glacial meltwater is an essential water resource in arid and semiarid areas of Northwestern China. Some dust particles stored in glaciers will be released with glacial meltwater into glacial runoff and eventually incorporated into downstream aquatic ecosystems (Zhang et al., 2019).

The Tianshan area is located in the arid and semiarid region of Central Asia, which is in a significant dust source region of the Northern Hemisphere (Li et al., 2011; Dong et al., 2014); a great quantity of dust has been transported to the North Pacific and the western coast of America or even globally under the action of strong winds each year. The information of aerosol dust can be recorded in the snow and ice of high mountains and polar regions. During the past few decades, dust particles in glaciers of Central Asia have been of widespread concern. In the early stage, the studies of dust storms in the glacial region mainly focused on the properties of dust particles in snow and ice. Wake et al. (1994) analyzed the concentrations and size distributions of insoluble particles in snow and ice samples and discussed the spatial and seasonal distributions of eolian dust deposition in Central Asia. Subsequently, Dong et al. (2009) measured the deposition of atmospheric dust in snow deposited on Haxilegen Glacier No. 51 in Kuitun, Glacier No.1 at the headwater of Urumqi River, and Miaoergou Glacier in Hami in East Tianshan Mountains. Dong et al. (2010) researched the characteristics of aerosol dust in fresh snow during Asian dust and nondust periods at Urumqi Glacier No. 1 of eastern Tian Shan. Dong and Li, (2011) and Dong et al. (2013) analyzed the characteristics of atmospheric dust deposition in snow on Glacier No. 72 and Glacier No. 4, Mt Bogeda. Dong et al. (2014a) studied and compared the deposition of atmospheric dust in snow deposited on Glacier No. 12 at the Laohugou River, Shiyi Glacier in Yeniugou of the western Qilian Mountains, China. In recent years, Asia dust provenance in snow and ice of glacier regions was analyzed by researchers (Xu et al., 2012; Yu et al., 2013; Du et al., 2015; Dong et al., 2016; Du et al.,2017). These studies mainly focus on the characteristics of Asia dust particles in snow and ice, as well as the spatial and temporal distribution and source analysis. However, there are few studies on the impact of dust storms on aerosols and meltwater. You and Dong (2011) also studied samples collected from aerosols, fresh snow, and snow pits on Urumqi Glacier No. 1 and determined the deposition processes and characteristics of mineral dust microparticles from aerosols to fresh snow and then the evolution to snow pits. Little research has been carried out regarding dust particle effects on the physicochemistry of glacial meltwater runoff. Dong et al. (2014b) discussed the temporal variations in various physicochemical species in the meltwater runoff of Laohugou Glacier No. 12 in Central Asia and their correlation with dust particles based on two-year field observations in the summers of 2012 and 2013.

However, there are few studies on the coupling relationship between the atmospheric environments and meltwater environments of glaciers during dust storms. In addition, there has been little research on aerosols of Glacier No. 72. Therefore, aerosol samples and meltwater samples were collected on Glacier No. 72 during 2008. The purposes of this research were to comprehend the water-soluble ion chemical characteristics of aerosols in the region and the coupling relationship between aerosols and meltwater on both dust and nondust days. Although the field experiment was carried out for only seven days, inorganic ion chemistry and individual analyses of aerosols were investigated in this study for the first time. Thus, it is essential to investigate the chemical characteristics of aerosols and glacial meltwater at Glacier No. 72 in the southern Tianshan Mountains.

MATERIALS AND METHODS

Site Description

Glacier No. 72 (41°45.51′N, 79°54.43′E) is a compound valley glacier located in the southern foot of the Tianshan Mountains and the southern part of Tomur peak in the northern margin of the Tarim Basin in Xinjiang. This glacier is representative of many other glaciers on Mount Tomur, with the highest elevation of 5,986 m a.s.l. The glacier is surrounded by vast deserts and Gobi (**Figure 1**). The climate in this area is typical of the continental climate and mainly affected by the westerlies. The aerosol sampling point is located at the lateral moraine at the east end of Glacier No. 72 at an altitude of 3,789 m. The bedrock is exposed without vegetation coverage. The salt contents of crystalline rocks, such as granite and metamorphic rocks, in the alpine zone, are difficult to dissolve. The soluble salt is mainly bicarbonate, some of which included marble and limestone. The low mountain zone is composed of the salt bearing rock series of the Tertiary system, with soluble salts. The area of mobile sand dunes in the Taklimakan Desert is as high as 85%. Evaporites such as the gypsum layer, Glauber's salt, halite, and sylvite are widely developed in the underlying strata.

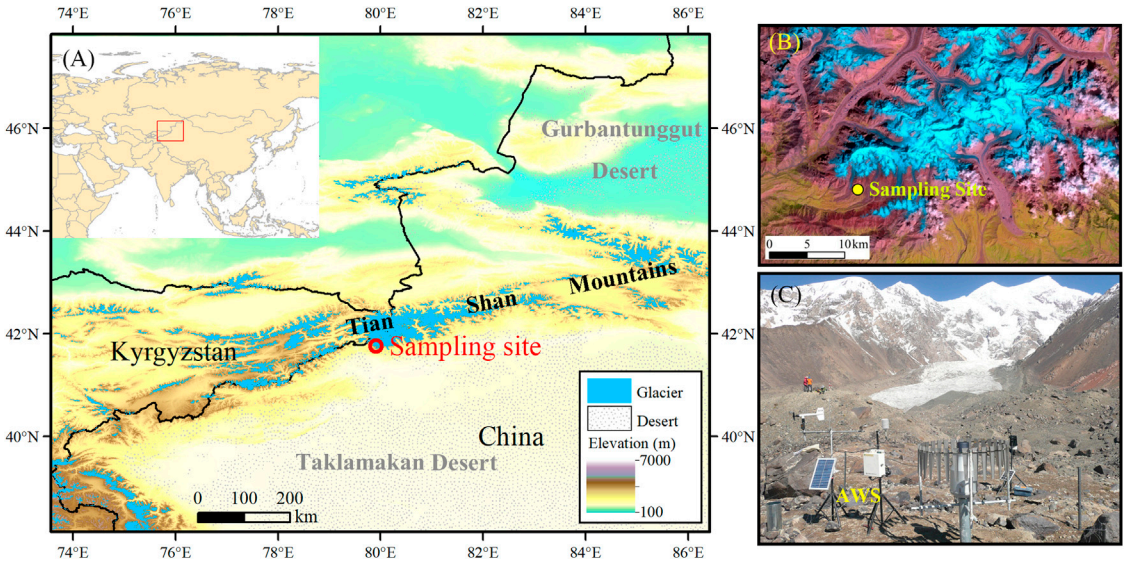

FIGURE 1 | Map showing the location of Qingbingtan Glacier No. 72 **(A,B)** and automatic weather station at the end of glacier 72 **(C)**.

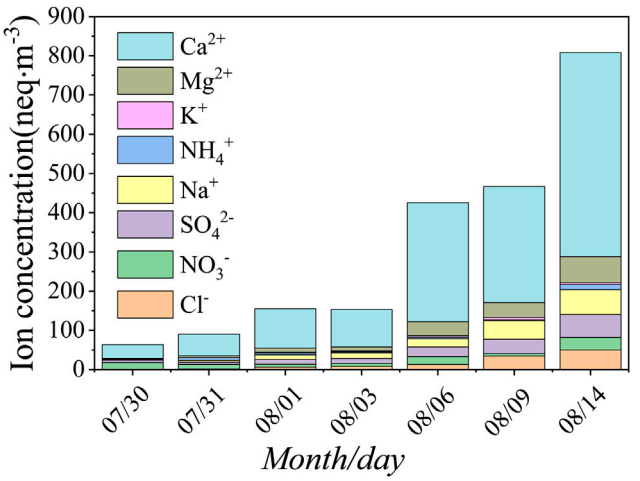

FIGURE 2 | Temporal variation in the concentration of soluble ions in aerosol samples in 2008.

Sample Collection and Analyses

Aerosol samples were collected for seven days from July 30 to August 14, 2008 (**Figure 2**). Four samples were collected on July 30, July 31, August 1, and August 3 before the dust storm on August 5. Three samples were collected after the dust storm on August 6, 9, and 14, respectively. Zefluor™ Teflon filters, 47 mm diameter with 2.0 μm pore size (Gelman Sciences), were used to collect the aerosol samples. The sampler was driven by a 24 V diaphragm pump powered by solar cells. The filters were mounted face-down approximately 1.5 m above the ground surface. Sampling usually started at 11:00 in the morning (Beijing time). No samples were collected during rainy or foggy weather. The air extraction volumes of aerosol samples varied from 2.71 to 6.25 m^3; for details, see (Zhao et al., 2011). The air volume through the filter was measured by an in-line meter and then converted into standard conditions according to local environmental pressure and temperature. Based on the average flow rate of 1.27 $m^3 \cdot h^{-1}$ on the filter, the particle collection efficiency was greater than 97% for aerosol particles with the diameter larger than 0.035 μm (Liu et al., 1984; Li et al., 2011). After sampling, the filters were removed from the filter holder and placed into cleaned airtight plastic containers and stored at 4°C before analysis. When loading and unloading the filters, the operator should wear plastic gloves and face the upwind side to minimize pollution.

Nine days of meltwater samples were collected from July 30 to August 9, 2008. The sampled hydrological section was 1.1 km away from the end of the No.72 glacier. The SWY-20 type monthly self-metering water level and water gauge were adopted to measure the water level and flow rate, and there was an automatic weather station in the area to measure wind speed and direction, air temperature, air pressure, precipitation, and relative humidity. Meltwater samples were collected at 14:00 every day. All samples were kept frozen and transported in the condition of −18°C until laboratory measurement at the State Key Laboratory of Cryospheric Science of Chinese Academy of Sciences. Before testing and analyzing, the sample melted naturally at room temperature.

Both samples and field blank filters were analyzed in a class 100 clean room at the State Key Laboratory of Cryosphere Sciences, Chinese Academy of Sciences (Lanzhou). In order to efficiently extract the water-soluble species from the filters, the sample and blank filters were first wetted with 200 μL ultra-pure methanol. The soluble components were then extracted with 25 ml of deionized water for about 30 min using an ultrasonic water bath device (Zhao and Li, 2004; Zhao et al., 2011; Zhang et al., 2016). Dionex model 320 ion chromatograph (Thermo Fisher Scientific, Inc.) was used to determine the major ion

TABLE 1 | Correlation coefficients of the soluble ions in aerosol samples.

	Cl^-	NO_3^-	SO_4^{2-}	Na^+	NH_4^+	K^+	Mg^{2+}	Ca^{2+}
Cl^-	1.00	0.51	0.99**	0.99**	0.56	0.79*	0.95**	0.93**
NO_3^-		1.00	0.62	0.48	0.73	0.09	0.65	0.68
SO_4^{2-}			1.00	0.99**	0.60	0.78*	0.98**	0.98**
Na^+				1.00	0.53	0.83*	0.95**	0.94**
NH_4^+					1.00	0.05	0.62	0.62
K^+						1.00	0.77*	0.76*
Mg^{2+}							1.00	0.99**
Ca^{2+}								1.00

*indicates correlation significant at p = 0.05; ** indicates correlation significant at p = 0.01.

concentrations in the aqueous extracts. Zhao and Li (2004) and Zhao et al. (2011) have described the detailed experimental methods. Mean concentrations of five field blank filters were Cl^- (3.66 ng/g), NO_3^- (17.31 ng/g), SO_4^{2-} (2.60 ng/g), Na^+ (2.61 ng/g), NH_4^+ (3.35 ng/g), K^+ (0.04 ng/g), Mg^{2+} (2.44 ng/g), and Ca^{2+} (6.41 ng/g). These were obviously lower than the concentrations detected in the aerosol samples. The average blank values were subtracted from the sample concentrations.

In addition, the scanning electron microscopy-energy dispersive X-ray spectrometer (SEM-EDX) was used to analyze individual particles. For each membrane, a part of the total filter was cut and mounted on an electron microprobe stub, and a thin gold film (16 nm) was coated to obtain a high-quality secondary electron image. The operating conditions were listed as follows: the accelerating voltage is in the range of 5–10 kV; and the spectral acquisition time is 60 s. Noran TM System software (Thermo Fisher Scientific Inc.) for energy dispersive microanalysis was used for the quantitative analysis of individual particles. The morphological characteristics of aerosol samples were classified, and the detailed analytical techniques of aerosols are described in the literature (Zhao et al., 2011).

RESULTS AND DISCUSSION

Impact of Dust Storms on the Atmospheric Environment of Glacial Areas

On August 5, 2008, there was a strong dust storm event in southern Xinjiang, http://www.duststorm.com.cn/. According to the field records obtained during sampling, there was strong dusty weather at Glacier No. 72 on the afternoon of August 5, and there was floating dust in the air all day on August 6. Therefore, the three aerosol samples collected from August 6 to August 14 were affected by dust storms with varying degrees, which was helpful for understanding the impact of dust storms on the atmospheric environments in high-altitude areas. According to the sampling time, the seven aerosol samples were divided into two parts: before the dust storm event of July 30 to August 3 and after the dust storm event of August 6 to August 14. **Supplementary Table S1** presents the mean concentrations of the water-soluble primary inorganic ions (Cl^-, NO_3^-, SO_4^{2-}, Na^+, NH_4^+, K^+, Mg^{2+}, and Ca^{2+}). Of all seven samples, the sum of anions and cations in the aerosols ranged from 63.66 to 808.29 neq·m^{-3}, with an average of 309.01 neq·m^{-3}. **Table 1** showed that the total number of cations measured in the aerosols [$\sum^+ = (Na+) + (NH_4^+) + (K^+) + (Mg^{2+}) + (Ca^{2+})$] was 4.82 times the total number of anions measured [$\sum^- = (Cl^-) + (NO_3^-) + (SO_4^{2-})$]. This phenomenon existed in all samples, indicating that aerosol particles on that day were more alkaline (Yang et al., 2016). Most of the excess cations in the samples could be balanced by carbonate ions ($HCO_3^-/CO_3^{2-} = \sum^+ - \sum^- = \Delta C$) that were not detected in the experiment (Zhao et al., 2008). Ca^{2+} and ΔC were the main ions in the aerosols, accounting for 78.88% of the total measured anions and cations.

Before the dust storm occurred, the sum of anions and cations in the aerosols ranged from 63.66 to 154.99 neq·m^{-3}, with an average of 115.58 neq·m^{-3}. The order of ion concentrations was $Ca^{2+} > NO_3^- > SO_4^{2-} > Na^+ > Mg^{2+} > Cl^- > NH_4^+ > K^+$, which represented the background value of the atmospheric environment in the region. However, after the dust storm, the sum of anions and cations in the aerosols ranged from 425.35 to 808.29 neq·m^{-3}, with the average of up to 566.91 neq·m^{-3}, which was 4.9 times the average before the dust storm. The order of ion concentrations was $Ca^{2+} > Mg^{2+} > Na^+ > SO_4^{2-} > Cl^- > NO_3^- > NH_4^+ > K^+$. According to the orders of ion concentrations, Ca^{2+} and SO_4^{2-} were the most important cations and anions in this area, whether affected by dust storms or not. Dust storm events could bring much Mg^{2+} and Na^+, so that the relative positions of the two ions in the sequence were advanced. During the sampling period, except for the nonobvious change in K^+, the other seven ions showed a significant increasing trend, especially after the occurrence of the dust storm on August 5. In particular, with Ca^{2+}, the average ion concentration after the dust storm event was 5.21 times that before the dust storm event, which showed that the dust storm event had a great impact on the atmospheric environment in the glacial area.

In previous studies, Ca^{2+} and Mg^{2+} were thought to be the index of dust substitution in studies of crustal sources on snow and ice chemistry (Wake et al., 1994; Dong et al., 2009; Zhang et al., 2016). Glacier No. 72 was surrounded by desert and located in the source area of Asian dust. There were many minerals, such as quartz, feldspar, calcite, yellow flash, and black mica, in the sand of the desert, which was also rich in $CaCO_3$, $CaSO_4$, and NaCl. When dust storms occurred, a large amount of dust was carried to the glaciers. Therefore, the concentrations of Ca^{2+} and Mg^{2+} increased significantly. Simultaneously, the debris at the southern foot of Mt. Tomur was rich in limestone, amphibole, and other minerals, and these minerals were also abundant in Ca, Mg, Na, and other substances. In addition, the concentrations of Na^+, Cl^-, and K^+ also increased significantly. This was because the air masses that passed by the salty sea and Issky Kul Lake could bring more salt particles with high concentrations. These factors contributed to the concentrations of water-soluble ions increases in the atmospheric environment of the glacial area after a dust storm.

To calculate the relative contributions of each ion to aerosols before and after the dust storm, the percentage value was calculated based on each sample. Then the average value was calculated (**Figure 3**). In general, Ca^{2+} and HCO_3^-/CO_3^{2-} were the most abundant ions in aerosols, accounting for 39.26% and

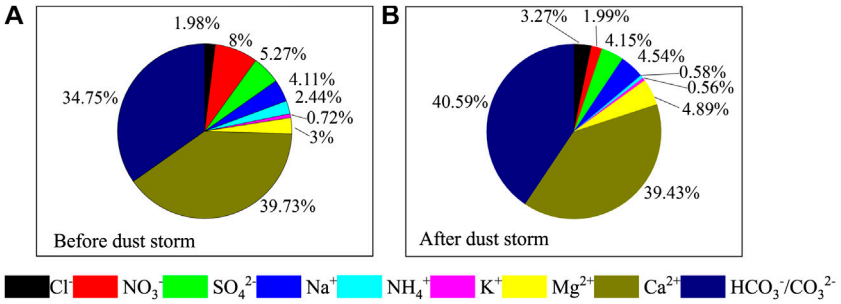

FIGURE 3 | (A) Before and **(B)** after dust storms.

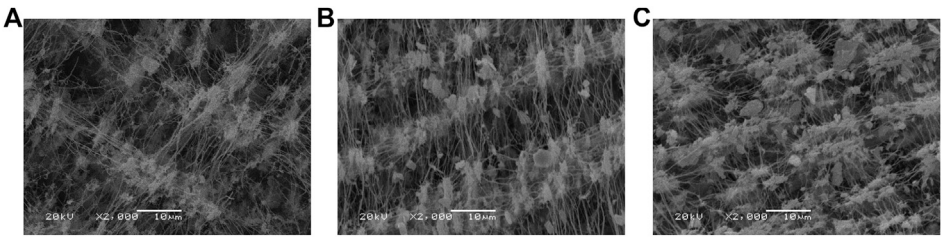

FIGURE 4 | Scanning electron microscope (SEM) images of typical aerosol samples. **(A)** 3 August 2008 before the dust storm; **(B)** 6 August 2008 after the dust storm; **(C)** 14 August 2008 after the dust storm.

39.62%, respectively, of the ion balance. The contributions of Ca^{2+}, HCO_3^-/CO_3^{2-}, NO_3^-, and SO_4^{2-} to the ion balance were 39.73%, 34.75%, 7.99%, and 5.27%, respectively, from July 30 to August 3 (nondust days). The contributions of HCO_3^-/CO_3^{2-}, Ca^{2+}, Mg^{2+}, Na^+, and SO_4^{2-} to the ion balance were 40.59%, 39.43%, 4.89%, 4.54%, and 4.15%, respectively, from August 6 to August 14 (dust days). Based on the contributions of the above ions, $CaCO_3$/Ca $(HCO_3)_2$ was the main dust material during the sampling period.

The SEM-EDX technique is an important method to analyze the characteristics of aerosol particles, which can supply detailed information about the shape and size of particulate matter, such as morphology, element composition, surface load, and agglomeration (Li et al., 2011; Zhang et al., 2016), and this method used to analyze aerosol samples is able to more intuitively understand the effects of dust storms on the atmospheric environment. The single-particle analysis for aerosols at Urumqi Glacier No. 1 and Mt. Bogda indicated that natural sources of dust and mineral particles usually appeared irregular, and then, the particles produced by artificial sources of pollution usually appeared as surface light sliding spherical or floc aggregates (Li et al., 2011; Zhao et al., 2011). According to **Figure 4**, most of the particles enriched on Teflon sampling filters were irregular, mainly minerals and dust particles. There may be aluminosilicate, quartz, feldspar, gypsum, and calcite in these particles. This indicated that the atmospheric environment of the glacier area was mainly affected by natural sources. By comparing the samples for August 6, August 14, and August 3, it could be found that the particles attached to the membrane showed an increasing tendency due to the August 5 dust storm incident. Thus, the occurrence of dust storms could bring large quantities of mineral particles, causing the concentrations of water-soluble ions in the atmosphere of the glacier area to increase sharply.

For comparison, the average soluble ion concentrations of aerosols in this work and other glaciered areas are summarized in **Supplementary Table S2**. When analyzing the spatial difference in aerosol chemical composition, the average concentration of the four samples before the dust storm event at Glacier No. 72 represented the background concentration of aerosols. Bogda glacier is close to Glacier No.72; both of them are affected by the prevailing westerly. The sampling period was the same, all in summer; thus it had certain comparability. In general, the ion concentration of Glacier No. 72 was higher than that of Bogda glacier, especially Ca^{2+} and Mg^{2+}. Compared with Bogda glacier, the average temperature (5.4°C) and humidity (72%) of Glacier No. 72 were higher than those of Bogda glacier (4.7°C, 57%), but the average wind speed (2.6 $m{\cdot}s^{-1}$) was lower than that of Bogda glacier (4.8 $m{\cdot}s^{-1}$). Wake et al. (1990) and Sun et al. (1998) have also pointed out that Na^+ and Cl^- originated from the extensive evaporate deposits in the arid regions surrounding these mountain ranges. When the temperature was higher, it contributed to evaporating the sediment; thus the concentrations of Na^+ and Cl^- were relatively high. When the wind velocity was low, it was not conducive to the local emission of dust (Dong et al., 2013). The concentrations of Ca^{2+} and Mg^{2+} should be lower, but the ion concentrations of Glacier No. 72 were much higher than that of Bogda glacier. The main reason was that

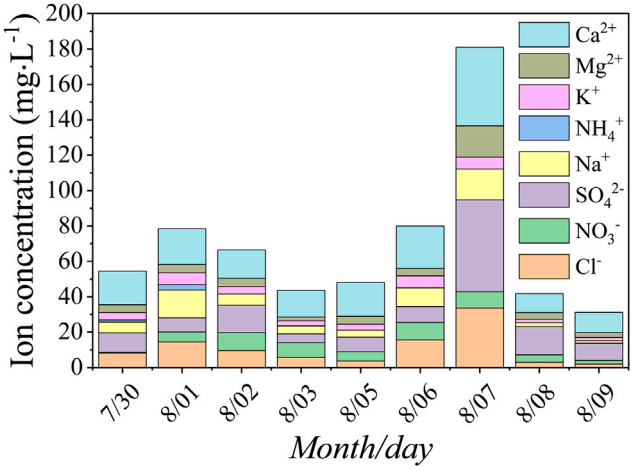

FIGURE 5 | Temporal variations in the concentrations of chemical ions in meltwater samples in 2008.

Glacier No.72 was located in the northern edge of the desert, which was closest to the Taklimakan Desert, and was greatly affected by the Taklimakan Desert.

Impact of Dust Storms on Meltwater in Glacial Areas

Glacial meltwater is an important part of the terrestrial hydrosphere, and the change is the result of the water-energy balance in the basin, which can accurately reflect the river basin information on climate change at different time scales and human activities in the region. The sum of ions in the samples from Glacier No. 72 ranged from 43.65 to 78.48 $mg{\cdot}L^{-1}$, with an average of 60.77 $mg{\cdot}L^{-1}$ (**Supplementary Table S3**). Ca^{2+} was the main ion in the measured samples, with a mean value of 17.62 $mg{\cdot}L^{-1}$, followed by SO_4^{2-}, with a mean value of 9.89 $mg{\cdot}L^{-1}$. Besides, the standard deviation also showed that the change in the concentration of these two ions was very large, while the concentrations of K^+ and NH_4^+ were low and relatively stable. In general, the meltwater ions were mainly composed of the sulfate-calcium type, which was consistent with the characteristics of the atmospheric environment of the glacial area. The order of ion concentration was $SO_4^{2-} > Ca^{2+} > Cl^- > NO_3^- > Na^+ > Mg^{2+} > K^+ > NH_4^+$. After the dust storm, ion concentrations significantly increased; the sum of ion concentrations ranged from 31.26 to 180.98 $mg{\cdot}L^{-1}$, with an average of 76.40 $mg{\cdot}L^{-1}$, the mean concentration of Ca^{2+} was approximately 21.94 $mg{\cdot}L^{-1}$, and SO_4^{2-} was approximately 18.95 $mg{\cdot}L^{-1}$, which were 1.25 and 1.92 times greater, respectively, than before. Dust storms could bring more Ca^{2+}, SO_4^{2-}, Mg^{2+}, and so on. **Figure 5** also showed that the concentrations of various meltwater ions increased significantly on August 6 and August 7, especially Ca^{2+}, Mg^{2+}, and SO_4^{2-}. According to the field records of sampling, there was strong dust weather on Glacier No. 72 in the afternoon of August 5, and there was floating dust all day on August 6. After the dust storm, the dust particles fell onto the surface of the glacier and meltwater through a dry and wet deposition. The dust composition changes from one chemical state to another. Different chemical substances dissolved into the meltwater, which led to the higher ion concentration in meltwater. We find that the higher concentration of cations and anions is of Ca^{2+}, Mg^{2+}, Na^+, and SO_4^{2-}, Cl^- in meltwater samples, respectively. The total ion concentration also increased on the sixth and seventh. Considering the dust storm on August 5, we can infer that the chemical constituents mainly reflect the apparent effects of mineral dust input on glacier meltwater.

As for the concentration of ions in glacial meltwater, it was not only affected by the dry and wet deposition of glacial dust but also affected by the erosion effect of glacial meltwater on the channel bed, namely, the water-rock interaction. Water-rock interaction is related to geological conditions and flow velocity, and various ions in rocks and weathering materials around the river bed are brought into the meltwater mainly through the erosion of the water. The geological conditions are relatively stable in a long time series, so it has little effect on the ion species in the river water (Zhang and Chen, 2000). The higher discharge of meltwater will affect the erosion rate, thereby affecting the process of physical and chemical weathering, making it higher than the continental average (Kumar et al., 2019). The discharge of meltwater mainly depends on meteorological factors. Due to the increase in temperature or precipitation, the discharge volume increases (Li et al., 2019). After the dust storm occurred on August 5, the temperature dropped, there was no significant precipitation, the flow velocity tended to decrease, the water-rock interaction weakened, and the ion concentration in the sample would not increase rapidly. Therefore, after excluding relevant factors that may cause ion changes in meltwater, it is concluded that the sudden increase in ion concentrations during this period is mainly related to the occurrence of dust storms.

After the dust storm, the temperature rose, the glacier melted faster, the runoff increased, and the flow velocity increased. The contact time between the water and the channel bed was relatively short; the soluble salts in the soil and rocks less dissolved in the water. At the same time, during the sampling period, there was precipitation on August 9. Atmospheric precipitation is one of the water bodies with the lowest soluble matter content. Therefore, when there was more precipitation replenishment to the river, due to the dilution of precipitation, there is a negative correlation between the total amount of meltwater ions and the corresponding regional rainfall (Zhang and Chen, 2000). After the ninth, the amount of precipitation increased, and the runoff of river water recharged from atmospheric precipitation increased, which could lead to increased erosion of glacial moraine and lateral moraine, and increased interaction of river water and rock, resulting in increased river water ion concentration.

Coupling Relationship of Typical Dust Concentrations in Aerosol and Meltwater Samples

The effect of dust storms on the glacial environment was based on dry and wet deposition. To observe the effect of the dust storm on

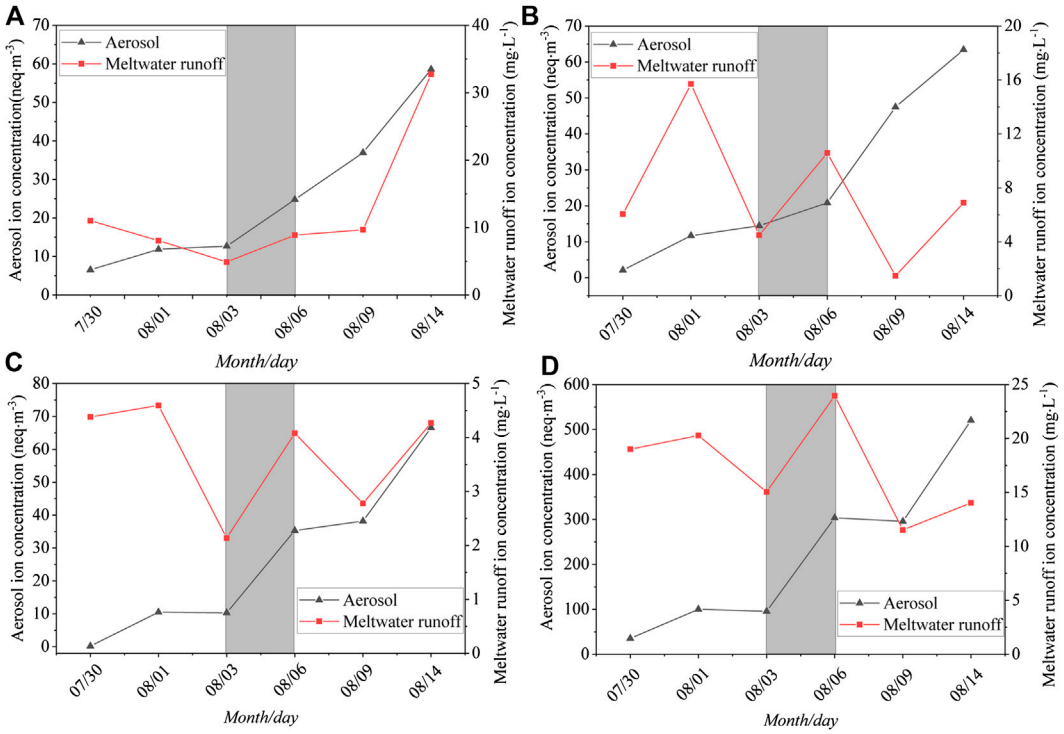

FIGURE 6 | Temporal variations in typical ions in aerosol and meltwater runoff samples in 2008. **(A)** SO_4^{2-}; **(B)** Na^+; **(C)** Mg^{2+}; **(D)** Ca^{2+}.

the atmospheric environment and water environment in the glacial area, the four main ions carried in the dust (SO_4^{2-}, Na^+, Mg^{2+}, and Ca^{2+}) were selected as the research objects. There was a significant increase between August 3 and August 6 (**Figure 6**) in both the aerosol samples and meltwater samples. The concentrations of SO_4^{2-}, Na^+, Mg^{2+}, and Ca^{2+} increased by 1.95, 1.44, 3.42, and 3.17 times in the aerosol samples and increased by 1.82, 2.35, 1.91, and 1.59 times in the meltwater samples, respectively. The increases in Mg^{2+} and Ca^{2+} in the aerosol samples were the largest, indicating that dust storms largely influenced the chemical composition of the atmosphere and water environment of the glacial area, especially in the atmospheric environment.

In the process of a dust storm, if there was no precipitation, a large amount of dust would remain in the atmosphere, and the horizontal diffusion rate would be extremely slow. Approximately one week after the end of the dusty weather, the air cleanliness could be restored to the level it was before the dust storm, so the ion concentration in the atmosphere would not decrease over a short time (Shen and Wen, 1994). However, due to the limited collection of samples, we did not observe that the aerosol returned to the normal levels, and the ion concentration was still high on the 14th.

However, the trend in ion concentration in the meltwater runoff was inconsistent with the change in ion concentration in atmospheric aerosols because of the different factors affecting ion concentration in the two media. The flow of meltwater gradually weakened the effect of dust storms on the water environment, so the ion concentration decreased in a stepwise manner. Also, the sampling point was surrounded by a large number of moraines composed of rocks and sand, and the erosion of the meltwater would continuously bring a large amount of sulfate, such as calcium sulfate, dissolved in the water, which hydrolyzed into Ca^{2+} and SO_4^{2-}, so there was no significant reduction in SO_4^{2-}. After August 9, the temperature rose, the upstream glaciers ablated dramatically, the amount of meltwater increased, the flow rate also increased, and the river water erosion on the riverbed strengthened; those caused the ions in the river to increase again. The concentrations of SO_4^{2-}, Na^+, Mg^{2+}, and Ca^{2+} increased by 3.38, 4.68, 1.54, and 1.22 times, respectively. Among them, the increases in SO_4^{2-} and Na^+ were greater than when the dust storm occurred. This result indicated that when the dust storm event occurred, although the chemical compositions of both the atmospheric environment and water environment in the glaciers were greatly affected by dust storms, the effect of the dust storm on the atmospheric environment was strong, and the impact on the water environment mainly because of temperature rise would cause more glacier melting and then more dust deposited on glacier surface was moved to glacial river by meltwater.

Source Analysis of Water-Soluble Ions in Aerosols

Dust storms had a substantial impact on the atmospheric environment of the glacial area because the materials in the area would be carried to the glacial area by air masses, including some sources of anthropogenic pollution, such as

NO_3^- and NH_4^+. Subsequently, the chemical composition of the water environment in the glacial area was affected by the dry and wet deposition of dust aerosols. Therefore, the primary sources of dust aerosols were analyzed by correlation analysis and principal component analysis.

Correlation coefficients among the main water-soluble ions are presented in **Table 1**. Significant positive correlation coefficients were found between Ca^{2+} and Mg^{2+} (r = 0.99) and Ca^{2+} and SO_4^{2-} (r = 0.98), which indicated that these two species might come from the same source. High Ca^{2+} was a tracer of dust from desert and loess areas in Asia (Dong and Li, 2011; Zhao et al., 2011). For Ca^{2+} and SO_4^{2-}, because the Tianshan Mountains were surrounded by a large number of deserts and Gobi, the calcium-rich minerals in the desert were usually $CaCO_3$, $CaSO_4$, or a mixture of $CaCO_3$, $CaSO_4$, and silicates. Meanwhile, when the air masses passed from west to east or from south to north through the desert, these air masses would bring a large amount of sand and stone grains rich in Ca^{2+} and Mg^{2+} (Okada and Kai, 2004). In addition to the surrounding desert and soil, the soil in the middle of the Caspian Sea and the Aral Sea west of the Tianshan Mountains may also be one of the primary sources of Ca^{2+} in this area (Claquin et al., 1999). Furthermore, there were many evaporite sedimentary zones between the Aral Sea and Kuzul Kum Desert in the Western Tianshan Mountains, in which the sulfate (including gypsum) content was relatively rich (Kreutz and Sholkovitz, 2000). Besides, the oxidation of sulfur dioxide from coal combustion for industrial production was another possible source of SO_4^{2-}. The equivalent concentration ratio of SO_4^{2-}/Ca^{2+} described by Ming et al. (2007) was calculated to distinguish SO_4^{2-} from anthropogenic sources or natural sources. The values of SO_4^{2-}/Ca^{2+} in our study only ranged from 0.08 to 0.19. Thus, the SO_4^{2-} in our samples mainly originated from natural processes.

In addition, significant positive correlation coefficients were also found among Ca^{2+}, Na^+ and Cl^-, Ca^{2+}, and Cl^- (r = 0.93), Ca^{2+} and Na^+ (r = 0.99), and Na^+ and Ca^{2+} (r = 0.94), suggesting that they may have had the same desert source as Ca^{2+}. An analysis of aerosol samples collected in the Taklimakan Desert found that halite (NaCl) particles were more commonly discovered in sand and dust (Okada and Kai 2004). Early research also showed that Na^+ and Cl^- rich dust originated from extensive evaporate deposits from surrounding salt lakes. K^+ might also be derived from the same source because it was more highly correlated with Na^+ (r = 0.83).

NH_4^+ and NO_3^- showed significant positive correlation coefficients (r = 0.73) but had a weak correlation with other ions. NH_4^+ came from wet or dry deposited gaseous NH_3 or was neutralized with sulfuric acid, nitric acid, and hydrochloric acid to form ammonium hydrogen sulfate (NH_4HSO_4), ammonium nitrate (NH_4NO_3), and ammonium chloride (NH_4Cl). The neutralization progress was accomplished by particle gas formation and gas-to-particle conversion (Ianniello et al., 2011). The potential sources for NH_4^+ near the glacier areas were human agriculture activities such as fertilizer use, animal farming, and organic matter decomposition (Verma et al., 2010). NO_3^- was almost the reaction product of NOx emissions, while NOx emissions were mainly caused by biomass burning and fossil fuel combustion (Wang et al., 2006; Wu et al., 2006). Wensu County, where Qingbingtan Glacier No. 72 is located, was dominated by agriculture, and animal husbandry was the second most important factor. NOx and NH_3 were produced by frequent farming and animal husbandry activities, strong decomposition of animal excreta, the use of chemical fertilizers, and traffic emissions. Therefore, in this study, the weaker correlation between the two and other ions may indicate that they had different sources compared to other ions, mainly related to anthropogenic pollution.

TABLE 2 | Rotated component matrix for soluble ions in aerosol samples.

Ions	Factor 1	Factor 2
Cl^-	*0.90*	0.39
NO_3^-	0.22	*0.90*
SO_4^{2-}	*0.88*	0.47
Na^+	*0.93*	0.35
NH_4^+	0.21	*0.91*
K^+	*0.98*	-0.16
Mg^{2+}	*0.86*	0.50
Ca^{2+}	*0.84*	0.52
Initial eigenvalue	6.25	1.35
Variance explained	78%	17%
Cumulative variance explained	78%	95%

Note: PCA loadings >0.6 are shown in italics.

To further determine the possible sources of various ions, the principal component analysis (PCA) was performed. SPSS 22.0 software was used to conduct PCA analysis for water-soluble ions for Glacier No. 72. Detailed information is presented in **Table 2**. Principal components (PCs) extracted with Varimax rotation provided a clearer variable loading mode in factors, making data easier to interpret (Xu et al., 2017). Two PCs were extracted from the rotated component matrix for the PCA. The first factor displayed high loadings of Ca^{2+}, Mg^{2+}, K^+, Na^+, Cl^-, and SO_4^{2-}, with a total variance of 78%. Studies have shown that these soluble ions may come from natural sources such as deserts and loess soils (Zhang and Edwards, 2011). The second factor was related to NO_3^- and NH_4^+, with a total variance of 17%. The result indicated that the two ions were derived from anthropogenic activities and had a strong correlation coefficient. This finding was consistent with the correlation analysis results.

Transport Path and Potential Sources of Aerosols

Hybrid Single-Particle Lagrangian Integrated Trajectory from the Air Resources Lab of National Oceanic and Atmospheric Administration has been widely used (Draxler and Rolph, 2003; Zhang et al., 2016) to identify potential source regions and transport pathways of aerosols. To interpret the source of water-soluble ions in aerosols before and after the dust storm in this study, the five-day backward trajectory analysis started at 500 m from the sampling site was performed by using GIS-based software TrajStat model (Wang et al., 2009). The backward air trajectories were simulated with a daily resolution. Trajectories were calculated at the end of 00:00, 06:00, 12:00, and 18:00 (UTC)

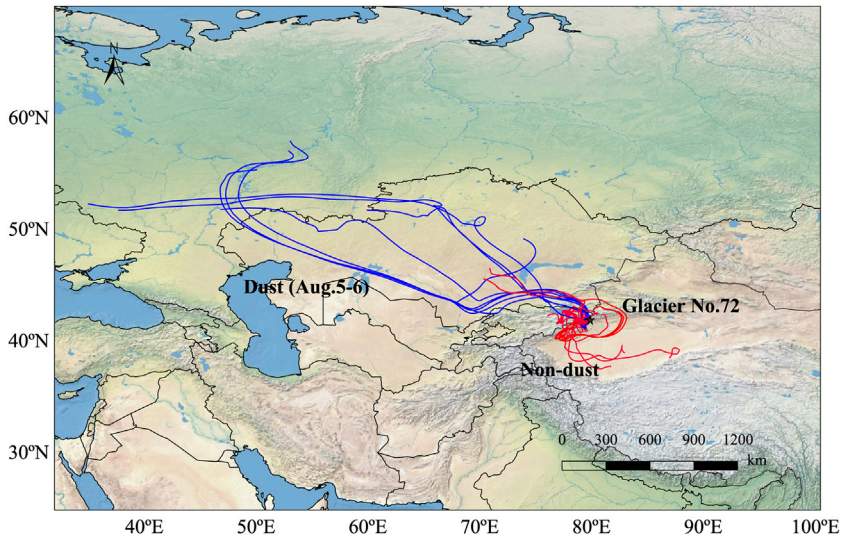

FIGURE 7 | Analysis of the 5-day air mass back trajectories with beginning heights at 500 m above ground level at Glacier No. 72 during the sampling periods (July 2008 to August 2008).

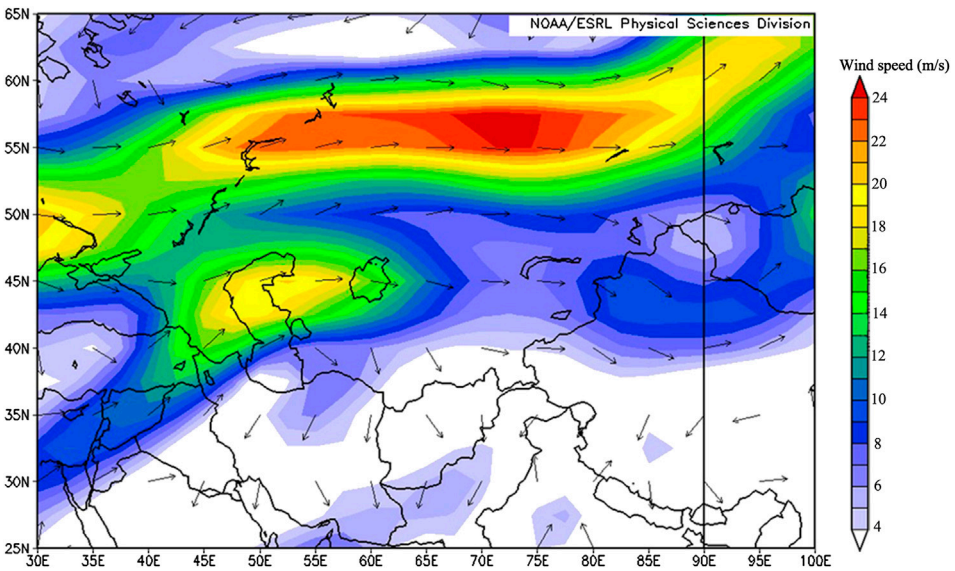

FIGURE 8 | The wind stream of the 700 hPa isobaric surface (August 5–7, 2008) over Glacier No. 72 and the surrounding regions, based on NCEP/NCAR reanalysis (shadowing indicates the wind speed, and arrows indicate the wind direction).

each day. The Global Data Assimilation System (GDAS) date (1.0° × 1.0°) of the corresponding time period provided by NCEP was adopted to simulate the daily backward trajectories. The trajectories for air masses reaching the sampling site are plotted in **Figure 7**. During the dust event, air masses originated from the arid regions of the Eastern European plains, Kazakhstan and Kyrgyzstan. Affected by the westerlies, the cold air masses that were further developed by the low pressure in the southern Xinjiang basin invaded from the Eastern European Plain to the southeast. This meteorological condition led to the occurrence of the dust storm event (Yang et al., 2006). In addition to dust storms, the air masses descended from the northwest could bring more sand and dust to the glacial area. This was because there were a large number of deserts in the area where the air masses passed, including the Muyunkum desert and Sary Ishkotrau desert. In addition, the pollutants produced by human activities could be carried to the Tomur peak glacial area, including Glacier No. 72, by the air masses. Thus, the concentrations of Ca^{2+}, Mg^{2+}, SO_4^{2-}, and NO_3^- were very high. To corroborate the inference, the variation of wind

direction on different isobaric surfaces was calculated in **Figure 8**. **Figure 8** indicated that the prevailing wind at Glacier No. 72 was northwesterly with a higher wind speed, which further confirmed the impact of Central Asia on the glacier.

In the nondust period, according to their origins and paths, all the trajectories could be divided into two categories: northwest and southeast. The northwest route mainly originated from Kazakhstan, and the deserts were widely distributed in the route area. The air masses mainly transported a lot of dust particles to the glacial area of Mount Tomur through low-altitude transmissions. The southeast route was mainly affected by the summer monsoon. Although the water vapor carried by the northward movement of the summer monsoon decreased gradually, the dust from the Taklimakan Desert could still be brought to the glacier area during the northward movement of the summer monsoon. Moreover, when they passed through some areas with intensive human activities and heavy industries, such as Kashi, Karamay, and the other regions, some anthropogenic pollutants in these areas could still be carried to the surfaces of the glaciers at high altitudes, which would lead to increases in the concentrations of SO_4^{2-}, NO_3^-, and Ca^{2+}. However, overall, the impact on the glacial environment was relatively nonsignificant.

In this study, the backward air mass trajectory analysis indicated that, in both dust and nondust periods, although the origins of the air mass trajectories were different, they mainly originated from both the northwest and southeast directions, which was consistent with the prevailing westerly circulation in the region.

CONCLUSION

In situ and intensive measurements of aerosol and meltwater samples conducted from July 31 to August 14, 2008, provide the first information of aerosols over Glacier No. 72 on Mount Tomur in southern Tianshan and further our understanding of the characteristics of dust aerosol in this region. Although Dong and Li, (2011) and Zhang et al. (2012) studied the chemical composition of the snowpack at Glacier No. 72, no aerosols data in Mount Tomur were found. Dust storms caused the ion concentrations in both the atmosphere and meltwater of Glacier No. 72 to increase significantly, but the subsequent change trends were different, mainly because of the various influencing factors. The change of ion concentration in atmospheric aerosol was mainly affected by dust storm, while the change of ion concentration in glacial meltwater was mainly affected by the change of temperature. When the dust storm event occurred, although the chemical compositions of both the atmospheric environment and the water environment in the glaciers were affected, the atmospheric environment was more affected by dust storms. During the dust storm period, the backward trajectory analysis showed that air masses originated from Eastern Europe and Siberia. Strong wind and cold weather could not only bring dust and anthropogenic pollutants from Central Asia to the glacial areas but also cause regional dust storms due to the formation of unstable temperature stratification in southern Xinjiang, which would lead to the further increase in natural source ions in the glacial areas. During the nondust storm period, the air masses originated from Kazakhstan and Kyrgyzstan in Central Asia. These air masses could bring part of the dust material to the glacial area, but the extent was not large and could not cause strong regional dust storm events.

DATA AVAILABILITY STATEMENT

The datasets generated for this study are available on request to the corresponding author.

AUTHOR CONTRIBUTIONS

ZL designed the experiments; the intensive and simultaneous sampling for aerosol and meltwater were conducted by PZ; CZ wrote the manuscript in consultation with XZ (4th author), SM, and XZ (5th author).

FUNDING

This work was supported by The Second Tibetan Plateau Scientific Expedition and Research (2019QZKK0201), the Strategic Priority Research Program of Chinese Academy of Sciences (Class A) (XDA20060201; XDA20020102), the National Natural Science Foundation of China (41761134093; 41471058), and The SKLCS founding (SKLCS-ZZ-2020).

ACKNOWLEDGMENTS

The authors would like to thank PZ for the sampling and YuMan Zhu, QiuFang Bao, and YaPing Liu for the chemical analyses.

SUPPLEMENTARY MATERIAL

The Supplementary Material for this article can be found online at: https://www.frontiersin.org/articles/10.3389/feart.2020.527663/full#supplementary-material.

REFERENCES

Arimoto, R., Duce, R. A., Savoie, D. L., et al. (1996). Relationships among aerosol constituents from Asia and the North Pacific during PEM-West A. *J. Geophys. Res.* 101, 2011–2023. doi:10.1029/95JD01071

Chow, J. C., Watson, J. G., Lowenthal, D. H., and Magliano, K. L. (2008). Size-resolved aerosol chemical concentrations at rural and urban sites in Central California, USA. *Atmos. Environ.* 90, 243–252. doi:10.1016/j.atmosres.2008.03.017

Claquin, T., Schulz, M., and Balkanski, Y. J. (1999). Modeling the mineralogy of atmospheric dust sources. *J. Geophys. Res.: Atmosphere.* 104 (D18), 22243–22256. doi:10.1029/1999JD900416

Dong, Z., and Li, Z. (2011). Characteristics of atmospheric dust deposition in snow on Glacier No. 72, Mt. Tuomuer, China. *Arctic Antarct. Alpine Res.* 43 (4), 517–526. doi:10.1657/1938-4246-43.4.517

Dong, Z., Li, Z., Wang, F., and Zhang, M. (2009). Characteristics of atmospheric dust deposition in snow on the glaciers of the Eastern Tien Shan, China. *J. Glaciol.* 55 (193), 797–804. doi:10.3189/002214309790152393

Dong, Z., Li, Z., Xiao, C., Zhang, M., and Wang, F. (2010). Characteristics of aerosol dust in fresh snow in the Asian dust and non-dust periods at Urumqi Glacier No. 1 of eastern Tian Shan, China. *Environ. Earth Sci.* 60, 1361–1368. doi:10.1007/s12665-009-0271-6

Dong, Z., Li, Z., Wang, W., Li, K., and Zhou, P. (2013). Characteristics of atmospheric dust deposition in snow on Glacier No. 4, Mt Bogeda, China. *Environ. Earth Sci.* 70, 1423–1433. doi:10.1007/s12665-013-2228-z

Dong, Z., Qin, D., Chen, J., Qin, X., Ren, J., Cui, X., et al. (2014a). Physicochemical impacts of dust particles on alpine glacier meltwater at the Laohugou Glacier basin in western Qilian Mountains, China. *Sci. Total Environ.* 493, 930–942. doi:10.1016/j.scitotenv.2014.06.025

Dong, Z., Qin, D., Kang, S., Ren, J., Chen, J., Cui, X., et al. (2014b). Physicochemical characteristics and sources of atmospheric dust deposition in snow packs on the glaciers of western Qilian Mountains, China. *Tellus B.* 66 (1), 20956. doi:10.3402/tellusb. v66.20956

Dong, Z., Kang, S., Qin, D., Li, Y., Wang, X., Ren, J., et al. (2016). Provenance of cryoconite deposited on the glaciers of the Tibetan Plateau: new insights from Nd-Sr isotopic composition and size distribution. *J. Geophys. Res.: Atmosphere.* 121 (12), 7371–7382. doi:10.1002/2016JD024944

Draxler, R. R., and Rolph, G. (2003). *HYSPLIT (HYbrid single-particle Lagrangian integrated trajectory) model access via NOAA ARL READY*. Silver Spring, Maryland: NOAA Air Resources Laboratory

Du, Z., Xiao, C., Liu, Y., and Wu, G. (2015). Geochemical characteristics of insoluble dust as a tracer in an ice core from Miaoergou Glacier, east Tien Shan. *Global Planet. Change.* 127, 12–21. doi:10.1016/j.gloplacha.2015.01.011

Du, Z., Xiao, C., Liu, Y., Yang, J., and Li, C. (2017). Natural vs. anthropogenic sources supply aeolian dust to the Miaoergou Glacier: evidence from Sr-Pb isotopes in the eastern Tienshan ice core Part B. *Quat. Int.* 430, 60–70. doi:10.1016/j.quaint.2015.11.069

Duce, R. A., Liss, P. S., Merrill, J. T., Atlas, E. L., Buat-Menard, P., Hicks, B. B., et al. (1991). The atmospheric input of trace species to the world ocean. *Global Biogeochem. Cycles.* 5, 193–259. doi:10.1029/91GB01778

Goudie, A. S. (2014). Desert dust and human health disorders. *Environ. Int.* 63, 101–113. doi:10.1016/j.envint.2013.10.011

Griffin, D. W. (2007). Atmospheric movement of microorganisms in clouds of desert dust and implications for human health. *Clin. Microbiol. Rev.* 20 (3), 459–477. doi:10.1128/CMR.00039-06Clin

Ianniello, A., Spataro, F., Esposito, G., Allegrini, I., Hu, M., and Zhu, T. (2011). Chemical characteristics of inorganic ammonium salts in PM2.5 in the atmosphere of Beijing (China). *Atmos. Chem. Phys.* 11, 10803–10822. doi:10.5194/acp-11-10803-2011

Kaspari, S., McKenzie Skiles, S., Delaney, I., and Dixon, D. A. (2015). Accelerated glacier melt on snow Dome, Mt. Olympus, Washington, USA due to deposition of black carbon and mineral dust from wildfire. *J. Geophys. Res.: Atmosphere.* 120, 2793–2807. doi:10.1002/2014JD022676

Kedia, S., Kumar, R., Islam, S., Sathe, Y., and Kaginalkar, A. (2018). Radiative impact of a heavy dust storm over India and surrounding oceanic regions. *Atmos. Environ.* 185, 109–120. doi:10.1016/j.atmosenv.2018.05.005

Kreutz, K. J., and Sholkovitz, E. R. (2000). Major element, rare earth element, and sulfur isotopic composition of a high elevation firn core: sources and transport of mineral dust in Central Asia. *G-cubed.* 1, 2000GC000082. doi:10.1029/2000GC000082

Kumar, A., Bhambri, R., Tiwari, S. K., Verma, A., Gupta, A. K., and Kawishwar, P. (2019). Evolution of debris flow and moraine failure in the Gangotri Glacier region, Garhwal Himalaya: hydro-geomorphological aspects. *Geomorphology* 333, 152–166. doi:10.1016/j.geomorph.2019.02.015

Li, X. Y., Ding, Y. J., Liu, Q., Zhang, Y., Han, T. D., et al. (2019). Intense chemical weathering at glacial meltwater-dominated Hailuogou basin in the southeastern Tibetan plateau. *Water.* 11, 1209. doi:10.3390/w11061209

Li, Z., Zhao, S., Edwards, R., Wang, W., and Zhou, P. (2011). Characteristics of individual aerosol particles over Ürümqi Glacier No.1 in eastern Tianshan, central Asia, China. *Atmos. Res.* 99 (1), 57–66. doi:10.1016/j.atmosres.2010.09.001

Liu, B., Pui, D., and Rubow, K. (1984). "Characteristics of air sampling filter media," In Aerosols in the mining and industrial work environments. Editors V. A. Marple and B. Y. H. Liu (Instrumentation, Butterworth-Heinemann, Newton, Mass), 3, 989–1038.

Ming, J., Zhang, D., Kang, S., and Tian, W. (2007). Aerosol and fresh snow chemistry in the east Rongbuk Glacier on the northern slope of Mt. Qomolangma (Everest). *J. Geophys. Res.* 112, D15307. doi:10.1029/2007JD008618

Okada, K., and Kai, K. J. (2004). Atmospheric mineral particles collected at Qira in the Taklamakan Desert, China. *Atmos. Environ.* 38, 6927–6935. doi:10.1016/j.atmosenv.2004.03.078

Ramanathan, V., Crutzen, P. J., Kiehl, J. T., and Rosenfeld, D. (2001). Aerosols, climate, and the hydrological cycle. *Science.* 294, 2119–2124. doi:10.1126/science.1064034

Seinfeld, J. H., Bretherton, C., Carslaw, K. S., Coe, H., DeMott, P. J., Dunlea, E. J., et al. (2016). Improving our fundamental understanding of the role of aerosol-cloud interactions in the climate system. *Proc. Natl. Acad. Sci. U.S.A.* 113 (21), 5781–5790. doi:10.1073/pnas.1514043113

Seinfeld, J. H., and Pandis, S. N. (2012). Atmospheric chemistry and physics: from air pollution to climate change. *Environment.* 40 (7), 26. doi:10.1080/00139157.1999.10544295

Shen, Z. B., and Wen, J. (1994). The atmospheric turbidity and the influence of the dust atmosphere on the surface radiation balance in desert in region spring. *Plateau Meteorol.* 13 (3), 330–338.

Sun, J., Qin, D., Mayewski, P. A., Dibb, J. E., Whitlow, S., Li, Z., et al. (1998). Soluble species in aerosol and snow and their relationship at Glacier 1, Tien Shan, China. *J. Geophys. Res.* 103 (D21), 28021–28028. doi:10.1029/98JD01802

Tang, Y., Han, Y., Ma, X., and Liu, Z. (2018). Elevated heat pump effects of dust aerosol over northwestern China during summer. *Atmos. Res.* 23, 95–104. doi:10.1016/j.atmosres.2017.12.004

Verma, S. K., Deb, M. K., Suzuki, Y., and Tsai, Y. I. (2010). Ion chemistry and source identification of coarse and fine aerosols in an urban area of eastern central India. *Atmos. Environ.* 95, 65–76. doi:10.1016/j.atmosres.2009.08.008

Wake, C. P., Mayewski, P. A., and Spencer, M. J. (1990). A review of central Asian glaciochemical data. *Ann. Glaciol.* 14, 301–306. doi:10.1017/S026030550000879X

Wake, C. P., Mayewski, P. A., Li, Z., Han, J., and Qin, D. (1994). Modern eolian dust deposition in central Asia. *Tellus Ser. B Chem. Phys. Meteorol.* 46 (3), 220–223. doi:10.1034/j.1600-0889. 1994.t01-2-00005.x

Wang, Y., Zhuang, G., Zhang, X., Huang, K., Xu, C., Tang, A., et al. (2006). The ion chemistry, seasonal cycle, and sources of PM 2.5 and TSP aerosol in Shanghai. *Atmos. Environ.* 40, 2935–2952. doi:10.1016/j.atmosenv.2005.12.051

Wang, Y., Zhang, X., and Draxler, R. (2009). TrajStat: GIS-based software that uses various trajectory statistical analysis methods to identify potential sources from long-term air pollution measurement data. *Environ. Model. Software.* 24, 938–939. doi:10.1016/j.envsoft.2009.01.004

Wang, X., Doherty, S. J., and Huang, J. (2013). Black carbon and other light-absorbing impurities in snow across northern China. *J. Geophys. Res.: Atmosphere.* 118, 1471–1492. doi:10.1029/2012JD018291

Wang, W., Sheng, L., Jin, H., and Han, Y. (2015). Dust aerosol effects on cirrus and altocumulus clouds in northwestern China. *J. of Meteoro. Res.* 29, 793–805. doi:10.1007/s13351-015-4116-9

Wu, D., Tie, X., and Deng, X. (2006). Chemical characterizations of soluble aerosols in southern China. *Chemosphere.* 64, 749–757. doi:10.1016/j.chemosphere.2005.11.066

Xu, J., Yu, G., Kang, S., Hou, S., Zhang, Q., Ren, J., et al. (2012). Sr-Nd isotope evidence for modern aeolian dust sources in mountain glaciers of western China. *J. Glaciol.* 58 (211), 859–865. doi:10.3189/2012JoG12J006

Xu, J., Xu, M., Snape, C., He, J., Behera, S. N., Xu, H., et al. (2017). Temporal and spatial variation in major ion chemistry and source identification of secondary inorganic aerosols in northern Zhejiang Province, China. *Chemosphere.* 179, 316–330. doi:10.1016/j.chemosphere.2017.03.119

Yang, L., Zhang, G., and Yang, Q. (2006). Circulation dynamical structure of sand-storm caused by cold air crossing mountains in southern Xinjiang. *J. Desert Res.* 26 (1), 71–76.

Yang, Y., Zhou, R., Yan, Y., Yu, Y., Liu, J., Du, Z., et al. (2016). Seasonal variations and size distributions of water-soluble ions of atmospheric particulate matter at Shigatse, Tibetan Plateau. *Chemosphere.* 145, 560–567. doi:10.1016/j.chemosphere.2015.11.065

You, X., and Dong, Z. (2011). Deposition process of dust microparticles from aerosol to snow-firn pack on glacier No. 1 in eastern Tianshan mountains, China. *J. Earth Sci.* 22 (4), 460–469. doi:10.1007/s12583-011-0200-y

Yu, G., Xu, J., Kang, S., Zhang, Q., Huang, J., Ren, Q., et al. (2013). Lead isotopic composition of insoluble particles from widespread mountain glaciers in western China: natural vs. anthropogenic sources. *Atmos. Environ.* 75 (4), 224–232. doi:10.1016/jorg/.atmosenv.2013.04.018

Zhang, L. T., and Chen, J. S. (2000). The relationship between the composition of the major ion of river of China and regional natural factors. *Sci. Geogr. Sin.* 20 (3), 236–240. doi:10.13249/j.cnki.sgs.2000.03.007

Zhang, N., Cao, J., Ho, K., and He, Y. (2012). Chemical characterization of aerosol collected at Mt. Yulong in wintertime on the southeastern Tibetan Plateau. *Atmos. Res.* 107, 76–85. doi:10.1016/j.atmosres.2011.12.012

Zhang, X., and Edwards, R. (2011). Anthropogenic sulfate and nitrate signals in snow from glacier of Mt. Bogda, eastern Tianshan. *J. Earth Sci.* 22 (4), 490–502. doi:10.1007/s12583-011-0196-3

Zhao, S. H., Li, Z. Q., and Zhou, P. (2011). Ion chemistry and individual particle analysis of atmospheric aerosols over Mt. Bogda of eastern Tianshan Mountains, Central Asia. *Environ. Monit. Assess.* 180, 409–426. doi:10.1007/s10661-010-1796-6

Zhang, X., Li, Z., Zhou, P., Wang, S. J., et al. (2016). Characteristics and source of aerosols at Shiyi Glacier, Qilian mountains, China. *Sciences in Cold and Arid Regions.* 8 (2), 0135–0146. doi:10.3724/SP.J.1226.2016.00135

Zhang, Q., Sun, X., Sun, S., Yin, X., Huang, J., Cong, Z., et al. (2019). Understanding mercury cycling in Tibetan glacierized mountain environment: recent progress and remaining gaps. *Bull. Environ. Contam. Toxicol.* 102, 672–678. doi:10.1007/s00128-019-02541-0

Zhao, Z., and Li, Z. (2004). Determination of soluble ions in atmospheric aerosol by ion chromatography. *Mod. Sci. Instrum.* 5, 46–49.

Zhao, Z., Tian, L., Fischer, E., Li, Z., and Jiao, K. (2008). Study of chemical composition of precipitation at an alpine site and a rural site in the Urumqi River Valley, Eastern Tien Shan, China. *Atmos. Environ.* 42, 8934–8942. doi:10.1016/j.atmosenv.2008.08.003

Disclaimer: Frontiers Media SA remains neutral with regard to jurisdictional claims in published maps and institutional affiliations.

Conflict of Interest: The authors declare that the research was conducted in the absence of any commercial or financial relationships that could be construed as a potential conflict of interest.

Copyright © 2021 Zheng, Li, Zhou, Zhang, Zhou and Ma. This is an open-access article distributed under the terms of the Creative Commons Attribution License (CC BY). The use, distribution or reproduction in other forums is permitted, provided the original author(s) and the copyright owner(s) are credited and that the original publication in this journal is cited, in accordance with accepted academic practice. No use, distribution or reproduction is permitted which does not comply with these terms.

frontiers in Earth Science

ORIGINAL RESEARCH
published: 08 October 2021
doi: 10.3389/feart.2021.524963

Light-Absorbing Impurities on Urumqi Glacier No.1 in Eastern Tien Shan: Concentrations and Implications for Radiative Forcing Estimates During the Ablation Period

Xin Zhang[1], Zhongqin Li[1], Xiaoni You[2], Yuanyang She[3], Mengyuan Song[1] and Xi Zhou[4]*

[1]State Key Laboratory of Cryospheric Sciences, Northwest Institute of Eco-Environment and Resources, Chinese Academy of Sciences, Lanzhou, China, [2]College of Resources and Environmental Engineering, Tianshui Normal University, Tianshui, China, [3]School of History Culture and Tourism, Longnan Teachers College, Longnan, China, [4]College of Earth and Environment Sciences, Lanzhou University, Lanzhou, China

Light-absorbing impurities (LAIs) in surface snow and snow pits together with LAIs' concentrations and their impacts on albedo reduction and sequent radiative forcing (RF) have been investigated in the past. Here, we focused on temporal–spatial distributions of LAIs, especially on the albedo reduction and radiative forcing caused by the LAIs in Urumqi Glacier No.1. Various snow samples, including fresh snow, aged snow, and granular ice were collected between 3,770 and 4,105 m a.s.l of Urumqi Glacier No.1 during the snowmelt season of 2015. For the surface snow samples, BC and OC concentrations were 582 and 1,590 ng g^{-1}, respectively. Mineral dust (MD) concentrations were 110 μg g^{-1}. Due to the different ablation status of the glacier surface, LAIs accumulate at the lower altitude of the glacier. The estimation by the Snow, Ice, and Aerosol Radiative (SNICAR) model indicated that BC and MD could reduce the albedo by 12.8 and 10.3% in fresh snow, aged snow by 23.3 and 5.9%, and granular ice by 22.4 and 26.7%, respectively. The RF of MD was higher than that of BC in fresh snow and granular ice, whereas the RF of BC exceeded MD in aged snow. These findings suggested that BC was the main forcing factor in snow melting and dust was the main forcing factor in accelerating glacier melt.

Keywords: Urumqi Glacier No.1, surface snow, radiative forcing (RF), albedo, light-absorbing impurities (LAIs)

OPEN ACCESS

Edited by:
Michael Lehning,
École Polytechnique Fédérale de Lausanne, Switzerland

Reviewed by:
Cenlin He,
National Center for Atmospheric Research (UCAR), United States
Helle Astrid Kjær,
Niels Bohr Institute, Denmark

****Correspondence:***
Xiaoni You
176639648@qq.com

Specialty section:
This article was submitted to Cryospheric Sciences, a section of the journal Frontiers in Earth Science

Received: *07 January 2020*
Accepted: *23 August 2021*
Published: *08 October 2021*

Citation:
Zhang X, Li Z, You X, She Y, Song M and Zhou X (2021) Light-Absorbing Impurities on Urumqi Glacier No.1 in Eastern Tien Shan: Concentrations and Implications for Radiative Forcing Estimates During the Ablation Period. Front. Earth Sci. 9:524963. doi: 10.3389/feart.2021.524963

INTRODUCTION

Light-absorbing impurities (LAIs) play a vital role in melting snow and glaciers in High Asia (Ming et al., 2012; Qian et al., 2015) and across the globe (Warren and Wiscombe, 1980; Hansen and Nazarenko, 2004; Flanner et al., 2007; Painter et al., 2013). LAIs include black carbon (BC), organic carbon (OC; in this study, only water-insoluble OC is considered), and mineral dust (MD). As for BC, it is derived from the incomplete combustion of fossil fuels and biomass (natural and anthropogenic). BC can influence global warming and change cloud formation processes in the atmosphere (Jacobson, 2001; Ramanathan et al., 2007; Gertler et al., 2016), which is a significant agent of climate warming (Ramanathan and Carmichael, 2008; Bond et al., 2013). LAIs deposited on glacier surface via precipitation and dry deposition may accelerate

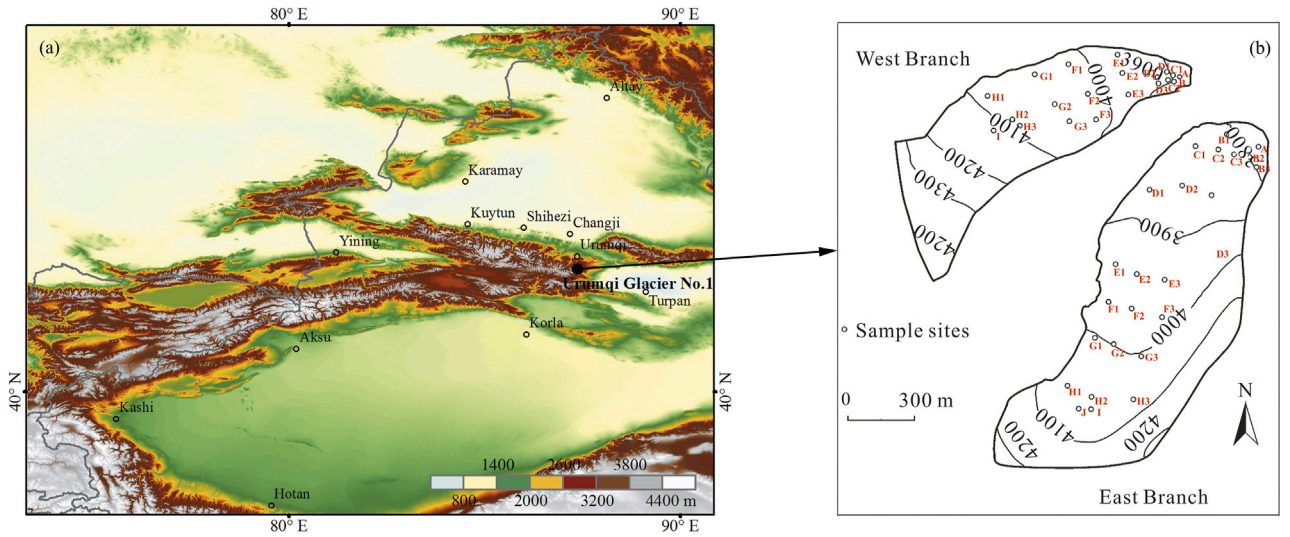

FIGURE 1 | Location and sampling sites on Urumqi Glacier No.1.

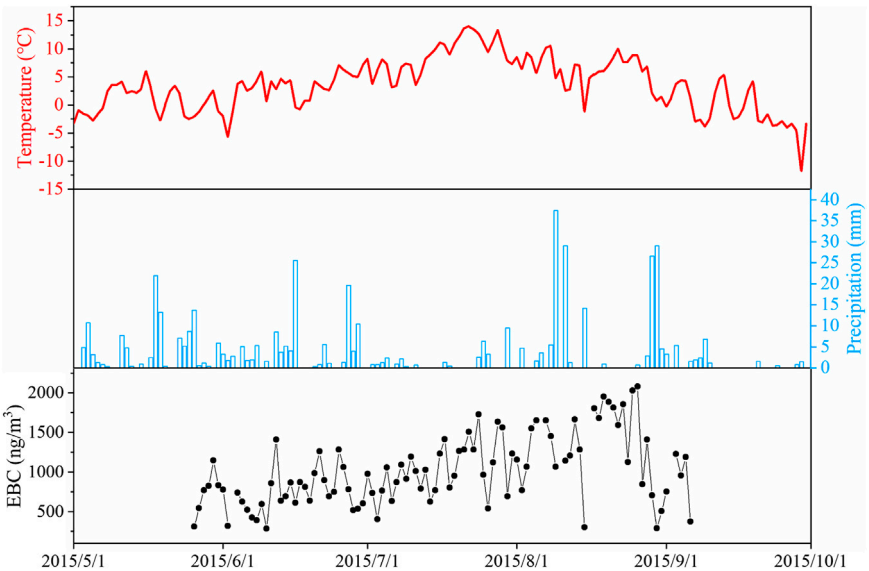

FIGURE 2 | Time series of daily-averaged temperature, precipitation, and equivalent black carbon (EBC) concentrations. EBC data came from the Tian Shan Glacier Station (43°12′N, 87°07′E, 2,100 m), about 30 km northeast of Urumqi Glacier No.1.

glacier melting by absorbing solar radiation (Bond et al., 2013; Gabbi et al., 2015). Therefore, it is critical to assess their contributions to glacier melting and get a picture of glacier runoff and water resources in glacierized catchments.

Glacier and snow cover are important water resources on the earth. There are nearly 8,000 glaciers in Tien Shan, which are the life-depending water sources maintaining both human living and the ecosystem. However, a large number of glaciers in Tien Shan are influenced by human activities (Schmale et al., 2017). Prior studies have reported LAIs record in surface snow, ice cores, and snow pits of glaciers, including the Tibetan Plateau and Tien Shan (Ming et al., 2013a; Zhao et al., 2013; Qu et al., 2014; Yang et al., 2015; Ming et al., 2016; Schmale et al., 2017). However, *in situ* data of LAIs on glacier surface during the melt season in Tien Shan are still scarce, which is important for understanding the temporal variability and spatial distribution of LAIs of glacier surface and essential for evaluating the contribution of LAIs to glacier melting. Furthermore, studies paid little attention to quantify the LAIs' effect on albedo reduction in different melting conditions (fresh snow, aged snow, and granular ice) in Tien Shan.

TABLE 1 | Input parameter of the SNICAR model.

Date	Code	Site	BC (ng g^{-1})	Density (kg/m^3)	Solar zenith angle (°)	Snow grain (mm)	MD (μg g^{-1})
2015/8/12	TS2015-04	C1	79	268	59	50	2
2015/8/12	TS2015-06	D1	26	296	62	50	3
2015/8/12	TS2015-07	D3	25	292	38	50	21
2015/8/12	TS2015-08	E1	10	291	62	50	3
2015/8/12	TS2015-09	E3	18	200	41	50	3
2015/8/12	TS2015-10	F1	5	266	61	50	1
2015/8/12	TS2015-11	F2	9	223	45	50	9
2015/8/12	TS2015-12	F3	13	242	43	50	5
2015/8/12	TS2015-13	G1	14	219	60	50	2
2015/8/12	TS2015-14	G2	13	213	46	50	2
2015/8/12	TS2015-15	G3	15	232	49	50	2
2015/8/12	TS2015-16	H1	5	209	57	50	0
2015/8/12	TS2015-17	H2	25	200	55	50	0
2015/8/12	TS2015-18	H3	19	203	50	50	0
2015/8/12	TS2015-19	I	11	222	51	50	4
2015/8/12	TS2015-20	J	13	199	53	50	12
2015/9/12	TS2015-29	A	212	270	35	200	10
2015/9/12	TS2015-30	B2	153	270	35	200	6
2015/9/12	TS2015-31	C1	229	270	36	200	3
2015/9/12	TS2015-32	C3	210	270	36	200	10
2015/8/12	TS2015-01	A	274	379	35	200	44
2015/8/12	TS2015-02	B1	88	374	35	500	11
2015/8/12	TS2015-03	B2	90	363	35	500	16
2015/8/12	TS2015-05	C3	30	342	36	500	10
2015/8/2	TS2015-48	E3	681	480	45	800	681
2015/8/2	TS2015-49	F1	510	480	43	800	735
2015/8/2	TS2015-50	F2	927	480	60	800	878
2015/8/2	TS2015-51	F3	475	480	46	800	784
2015/8/2	TS2015-52	G1	342	480	49	800	453
2015/8/2	TS2015-53	G2	289	480	57	800	439
2015/8/2	TS2015-54	G3	414	480	55	800	402
2015/8/2	TS2015-55	H1	284	480	50	800	517
2015/8/2	TS2015-56	H2	254	480	51	800	222
2015/8/2	TS2015-57	H3	224	480	53	800	687
2015/8/2	TS2015-58	I	193	480	53	800	158

Much work so far has focused on variability of LAIs' concentrations and the effect of LAIs on snow albedo (Ming et al., 2013b; Yasunari et al., 2013; Kaspari et al., 2014; Qu et al., 2014; Zhao et al., 2014; Li et al., 2017; Niu et al., 2017; Wang et al., 2017). Flanner et al. (2007) used the Snow, Ice, and Aerosol Radiative (SNICAR) model and suggested that BC could cause the RF more than 20 W m^{-2} on TP in spring. Using the same model, it was found that BC could cause an average RF of 6 W m^{-2} in High Asia glaciers (Ming et al., 2013b). Ming et al. (2009), suggesting that black carbon deposited on the surface may accelerate the melting of these glaciers by analyzing BC concentrations from seven glaciers in west China. Qu et al. (2014) studied the spatial distribution of BC and MD on Zhadang Glacier and estimated the RF caused by BC and MD. Xu et al. (2012) analyzed snow samples in Tien Shan and indicated that BC could influence glacier melting when BC concentrations were as much as 400 ng g^{-1} in the summer. Ming et al. (2016) indicated that snow aging, BC, and dust could reduce albedo by 44, 25, and 7%, respectively, in the accumulation zone of Urumqi Glacier No.1. These recent results suggest that LAIs have great variations in quantity and are critical for albedo reduction and glacier melting, and further studies need to reveal the spatial–temporal variability and spatial distribution of LAIs on the glacier surface and quantify the contribution of LAIs to albedo reduction and glacier melting. He et al. (2018) updated the SNICAR model and quantified the effects of snow grain shape and BC–snow mixing state on BC–snow albedo effects over the TP, which advanced the understanding of BC effects on snow albedo reduction and associated uncertainties in the TP. In addition, many recent studies have shown that snow grain shapes and BC–/dust–snow mixing states have important effects on snow albedo and radiative effects (Flanner et al., 2012; He et al., 2014; Dang et al., 2016; He et al., 2019), and this may lead to a large change in the value of the estimates of the albedo reduction caused by LAI.

Here, snow and ice samples were collected from the ablation and accumulation zones of Urumqi Glacier No.1. Meanwhile, the physical characteristics were also *in situ* observed, such as spectral albedo and snow density. The objectives of this study were 1) to depict the spatial–temporal variation of BC and other LAIs' concentrations in the snow and ice of Urumqi Glacier No.1, 2) to investigate the changes of the OC/BC ratios,

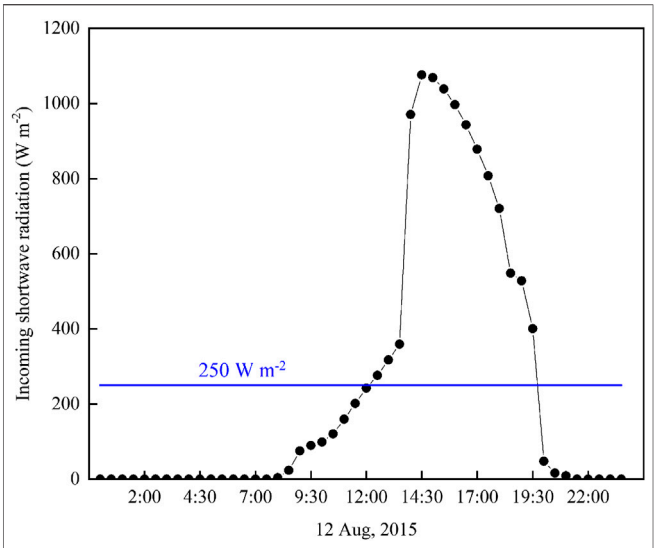

FIGURE 3 | The diurnal variations of incoming shortwave radiation at Urumqi Glacier No.1.

and 3) to simulate snow albedo reduction and RF caused by measured BC and MD, using the SNICAR model.

EXPERIMENT AND METHODS

Site Description

Urumqi Glacier No.1 (43°08′N, 86°82′E) is located in the headwaters of the Urumqi River in Tien Shan (**Figure 1**). Urumqi Glacier No.1 is the best monitored glacier with the longest data series in China and one of the reference glaciers in the World Glacier Monitoring Service (WGMS). Urumqi Glacier No.1 represents a large number of glaciers in northwest China (Che et al., 2019). This glacier is a northwest-facing valley glacier and has an elevation ranging from 3,743 to 4,484 m a.s.l. Urumqi Glacier No.1 consists of the east branch (1.086 km^2) and the west branch (0.591 km^2), and the total area is 1.667 km^2.

The total annual precipitation was 549 mm, and the daily mean air temperature was −3.6°C in 2015. During the ablation period (May–September), the daily average temperature was 3.6°C. The precipitation was 454 mm, which accounts for 83% of the yearly total (**Figure 2**). For the past decades, the air temperature caused the glacier ablation to exceed accumulation. Urumqi Glacier No.1 was melting rapidly and separated into two branches in 1993 (Xu et al., 2011). Equivalent black carbon (EBC) was measured with a seven-wavelength Aethalometer (AE-31) at the Tian Shan Glaciological Station (43°12′N, 87°07′E, 2,100 m) located at the northeast of Urumqi Glacier No.1, approximately 30 km from Urumqi Glacier No.1. Daily mean EBC was in the range of 287–2080 ng/m^3 with a mean of 1,011 ng/m^3 during the study period.

Sampling and Field Observations

A total of 96 surface samples were collected from Urumqi Glacier No.1 cover 9 days during the ablation period (May–September) in 2015. Sample collections and spectral albedo measurements were carried out at 23 sites on the east branch and 22 sites on the west branch (**Figure 1**). The snow line was approximately 4,050 m on the east branch during the study period. Whirl-Pak™ bags were used to collect 5 cm surface snow and ice samples on the surface of the glacier in a 50 cm × 50 cm square. All the samples were kept frozen and transported to the State Key Laboratory of Cryospheric Science (SKLCS) of Northwest Institute of Eco-Environment and Resources in Lanzhou. Furthermore, to simulate the radiative effect of LAIs with the SNICAR model, the physical characteristics of the snow were also observed. It should be noted that it was hard to distinguish the grain size for snow and ice by lens-based methods, so we assumed 50 μm for fresh snow (Nolin and Dozier, 2000) and 200–800 μm for aged snow and granular ice in central estimates (Schmale et al., 2017).

A spectroradiometer (Model ASD® Handheld 2) was used for spectral albedo observation of the glacier, which covers a radiative wavelength of 325–1,075 nm with a 1 nm spectral resolution. The accuracy of this spectroradiometer was ±1 nm. The spectroradiometer was held at the height of approximately 50 cm above the surface of the glacier to measure spectral reflectance. We used a whiteboard for whiteboard reflection correction and to calibrate every 10 min to prevent the sensor from responding to the drift of the system and the influence of changes in the sun's incident angle. We calculated the broadband albedo of the snow ice surface by dividing the sum of the reflected irradiances of all spectral wavelengths as follows:

$$\alpha = \frac{\int_{325nm}^{1075nm} a(\lambda) i(\lambda) d\lambda}{\int_{325nm}^{1075nm} i(\lambda) d\lambda}, \quad (1)$$

where α denotes the broadband albedo, λ denotes the wavelength, and i denotes the reference incoming solar irradiance. A more detailed description of albedo could be seen in former work (Ming et al., 2013a; Ming et al., 2015). The incoming shortwave radiation was measured from the radiometer (Kipp & Zonen NR LITE; spectral range, 305–2,800 nm) with 10 $\mu V/Wm^{-2}$ sensitivity, which was mounted on the automatic weather station (AWS) at 3,782 m.

Sample Analysis

In the laboratory, snow and ice samples were placed at room temperature and melted in a clean room. When the samples were completely melted, we used the quartz fiber filters (0.45 μm pore size, 47 mm in diameter, Whatman) to filter the samples. A vacuum pump was used to accelerate melting, and the Whirl-Pak bag and filter devices were flushed to allow full filtration (Xu et al., 2006; Wang et al., 2012). We dried the filter in a desiccator at 550°C for 6 h and washed the filter and samples twice with ultrapure water during the filtration process to remove the possible carbonaceous matters. The MD was weighed by using a microbalance (Liang You FA2104, accuracy: 0.1 mg). We calculated the difference between the weight before filtering

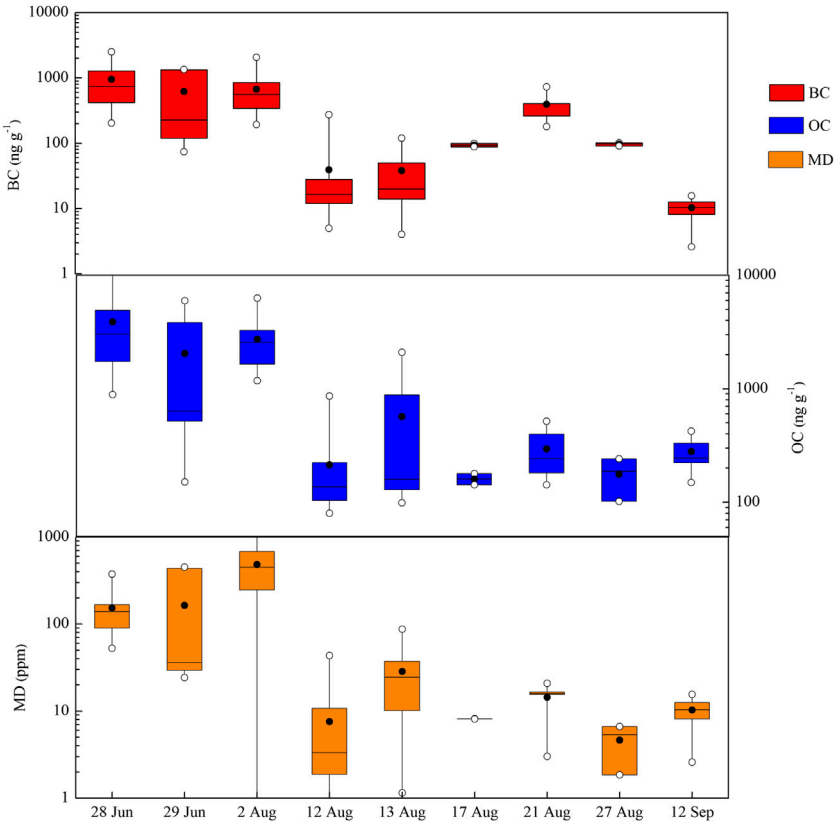

FIGURE 4 | Temporal variations of LAIs' concentrations during the snowmelt period, 2015.

and the weight after filtering. The sample deposited on each filter covered an area of approximately 12.56, and 0.5 cm^2 punches of the filter were used for BC and OC analysis. We used the thermal/optical reflectance carbon analyzer (Desert Research Institute Model 2001) to measure BC and OC at the Institute of Arid Meteorology in Lanzhou. This analyzer followed the Interagency Monitoring of Protected Visual Environments (IMPROVE) protocol and used the thermal/optical reflectance (TOR) method (Chow et al., 2004). The OC was gradually heated in a nonoxidizing atmosphere at 120, 250, 450, and 550°C, and BC was heated in an oxidizing atmosphere of 98% He and 2% oxygen at 550, 700, and 800°C. The uncertainty of analysis was approximately 15% for BC and 16% for OC (Xu et al., 2009).

SNICAR Model and Radiative Forcing

We evaluated BC and MD in the snow of glaciers using the Snow, Ice, and Aerosol Radiative (SNICAR) model (Flanner et al., 2007; Zhao et al., 2014; Wang et al., 2017), which can simulate the change of snow albedo for a given BC and MD concentration. Details concerning the simulations of albedo have been introduced in the previous work (Yasunari et al., 2010; Ming et al., 2013a). Snowpack depth was considered as 0.05 m. The solar zenith angle was calculated according to the local sampling time and geographic locations. The albedo of the underlying ground was taken as 0.2–0.6 in the visible band and 0.1–0.4 in the near-infrared band *in situ*. The mass absorption cross section (MAC) of BC was set as 11.3 (Ming et al., 2016), the median of typical MAC values (Hadley and Kirchstetter, 2012). The modeling results cover the spectral albedo from 350 to 2,500 nm. Here, we are only concerned with the range of 325–1,075 nm. Snow densities and snow grain size were taken as measured. Clear sky and direct radiation were chosen for the very low cloud amount (~1).

To research the RF and the role in climate change of LAIs, the SNICAR model was used to simulate the varying of snow albedo induced by BC and MD. It should be noted that the SNICAR model could not simulate the effect of OC in snow because the optical properties of OC cannot be reliably estimated (Flanner et al., 2007). The detailed input parameter of the SNICAR model is listed in **Table 1**.

The sensitive analysis was as follows: 1) The concentrations of BC and MD in the model were set to 0, to simulate albedo of snow and ice without the effect of BC and MD; 2) BC data were input into the model, and the MD concentrations were set to 0 to simulate the effect of BC on snow and ice albedo; and 3) BC and MD data were input into the model to simulate the effect of BC and dust on albedo. The contribution of BC and MD to the reduction of albedo was calculated by a series of sensitivity analyses.

Based on the albedo simulations, RF was defined using the following equation:

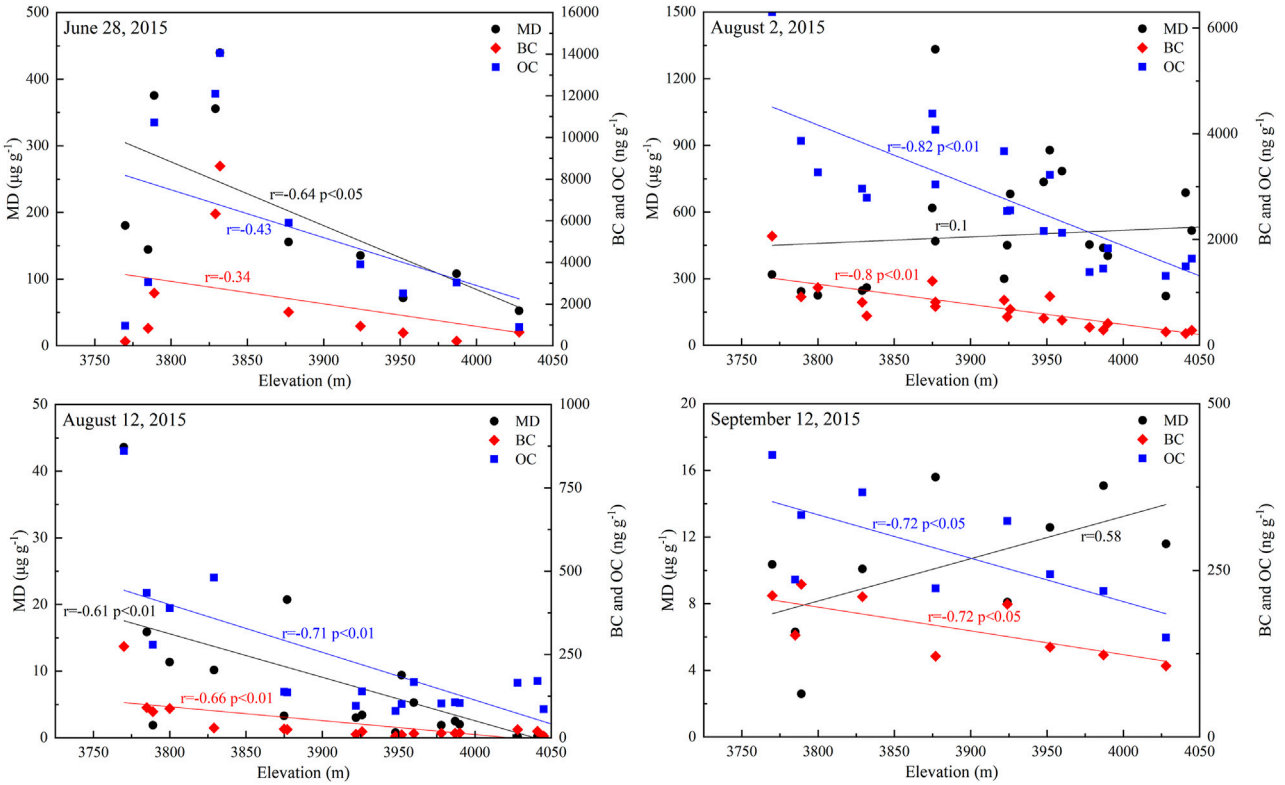

FIGURE 5 | Correlations between LAIs and the sampling elevations on the east branch of Urumqi Glacier No.1. Note that the scales were different for different sampling dates.

$$RF = R_{in-short}\Delta\alpha, \quad (2)$$

where $R_{in\text{-}short}$ denoted the incident solar radiation observed by using the radiometer and $\Delta\alpha$ denoted the reduction of albedo. For example, the highest incoming shortwave radiation was observed at the noon on 12th August, and the average incoming shortwave radiation was 250 W m^{-2} (**Figure 3**).

RESULTS

Temporal Variability of LAIs

As can be seen from **Figure 4**, LAIs' concentrations of surface snow had obvious changes with time. BC concentrations were in the range of 32–2,258 ng g^{-1} with an average of 582 ng g^{-1}, while OC concentrations were in the range of 102–5,712 ng g^{-1} with an average of 1,590 ng g^{-1}. For MD, concentrations were in the range of 2–484 μg g^{-1} with an average of 110 μg g^{-1}. The highest BC concentrations were associated with the areas of strong glacier melt.

On 28 June, BC concentrations were 2,258 ± 2,887 ng g^{-1} and OC concentrations were 5,712 ± 4,820 ng g^{-1} on the east branch. These relatively high values could be associated with the pollutants from cities and deserts and the glacier surface melting conditions of the glacier (Dong et al., 2016). BC and OC concentrations on the east branch were larger than those on the west branch due to the lower elevation. However, the west branch of Urumqi Glacier No.1 is enriched with more dust at 3,900 m due to the local dust. In July, the pollution from the atmosphere was getting worse and LAIs could deposit on the glacier surface. The glacier surface was covered with aged snow and granular ice. The scarce precipitation and higher temperature have further enriched the LAIs in the surface snow (**Figure 2**). On 2 August, the glacier surface was dominated by granular ice, and LAIs were easily removed by melt water. On 12 August, the glacier surface was buried by fresh snow, and the mean BC concentrations were 39 ± 61 ng g^{-1} and then increased to 94 ± 9 ng g^{-1} after 5 days of melting. Snow fell again on 27 August, and BC concentrations were 97 ng g^{-1}. In September, snowmelt weakened, and LAIs stayed at a low level. Even though no more data were taken afterward, combined with the prior results, we could infer that LAIs were still present at a low level due to a lower temperature and fewer emissions until the next melt period in 2016 (Xu et al., 2012). Therefore, the temporal variability of LAIs in surface snow was mainly dependent on the melting state of the glacier surface.

The highest OC/BC ratio was 8.77 on the east branch and 19.99 on the west branch in mid-August. Higher OC/BC ratio indicated that local emissions were mainly caused by biomass combustion, not fossil fuel combustion. By the end of August, the OC/BC ratio gradually decreased, which suggested OC accounted for a large proportion of fresh snow, but with the process of snow

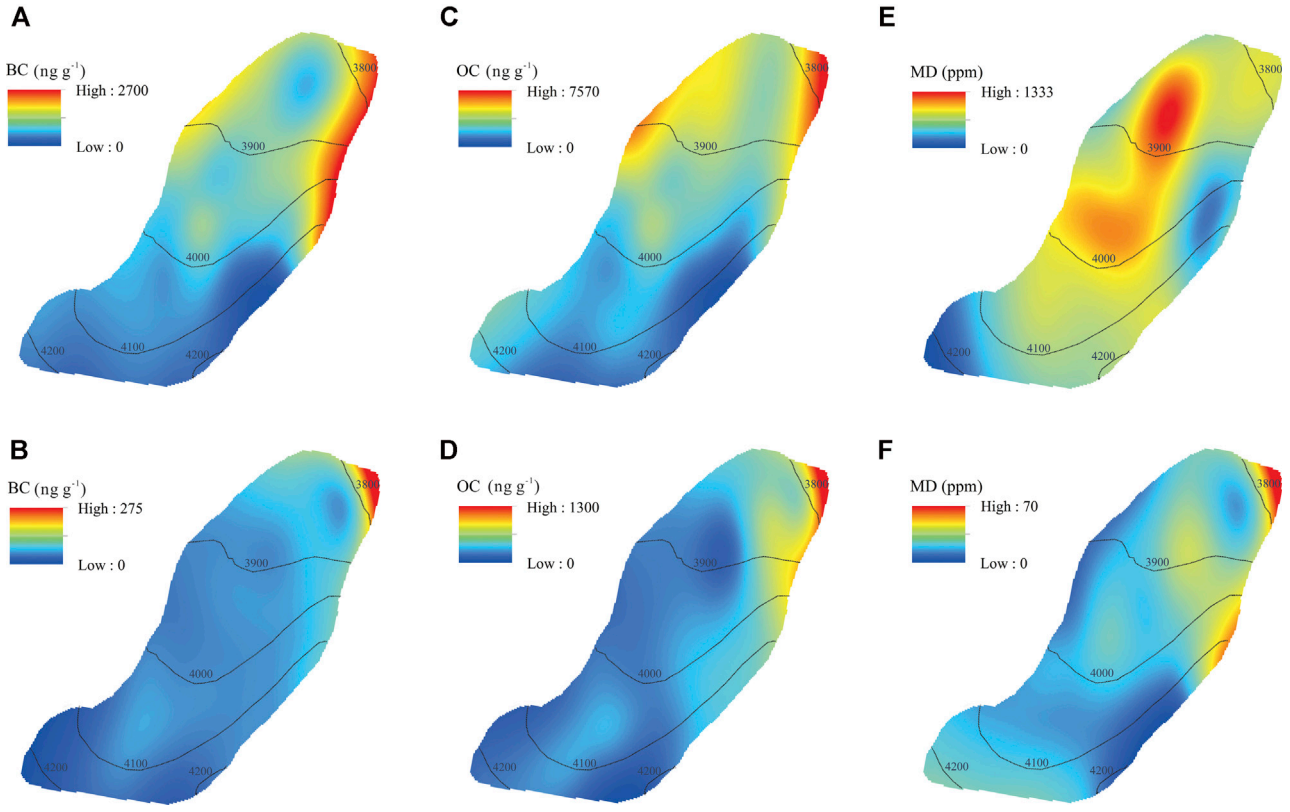

FIGURE 6 | Spatial variations of BC in the surface snow/ice. **(A)**, **(C),** and **(E)** BC, OC, and MD concentrations on 2 August, glacier surface mainly covered by granular ice; **(B)**, **(D)**, and **(F)** BC, OC, and MD concentrations on 12 August, glacier surface mainly covered by fresh snow.

TABLE 2 | Concentrations of BC, OC, and dust in Urumqi Glacier No.1.

Date	Site	Number of samples	BC (ng g^{-1})	OC (ng g^{-1})	Dust (μg g^{-1})	OC/BC
2015/6/28	East branch	10	2,258 ± 2,887	5,712 ± 4,820	202 ± 137	3.67
2015/6/29	West branch	8	1,479 ± 2,501	4,255 ± 5,214	239 ± 278	3.11
2015/8/2	East branch	21	676 ± 435	2,726 ± 1,270	484 ± 299	4.47
2015/8/12	East branch	20	39 ± 61	214 ± 193	8 ± 10	8.77
2015/8/13	West branch	20	32 ± 38	567 ± 634	29 ± 22	19.99
2015/8/17	East branch	2	94 ± 9	161 ± 26	8	1.69
2015/8/21	East branch	5	397 ± 208	296 ± 157	14 ± 7	0.78
2015/8/27	East branch	1	97	102	2	1.05
2015/9/12	East branch	9	166 ± 47	280 ± 87	10 ± 4	1.69

melting, OC was easier to be removed than BC by meltwater (Xu et al., 2012; Yang et al., 2015). OC/BC ratios held steady at about 1.69 during the first half of September, which suggested that the scavenging efficiency of BC and OC both remained stable.

Spatial Variability of LAIs

Figure 5 shows the correlations between LAIs and the sampling elevations on the east branch of Urumqi Glacier No.1. Note that LAIs and the sampling elevations have a poor correlation on the west branch during June 29 and August 13 due to the special terrain of Urumqi Glacier No.1. On June 28, LAIs enriched at the elevations of 3,800 m–3,850 m causing a negative correlation between the MD and elevations (r = −0.64, $p < 0.05$). On August 2, enriched LAIs were found towards the terminal of the glacier, and the glacier surface was mainly granular ice. Since more intense melting was likely to occur at lower elevations, there is a strong negative correlation between the BC and OC concentration and the sampling elevations. On August 12, the glacier surface was mainly fresh snow. LAIs decreased with the increasing elevation,

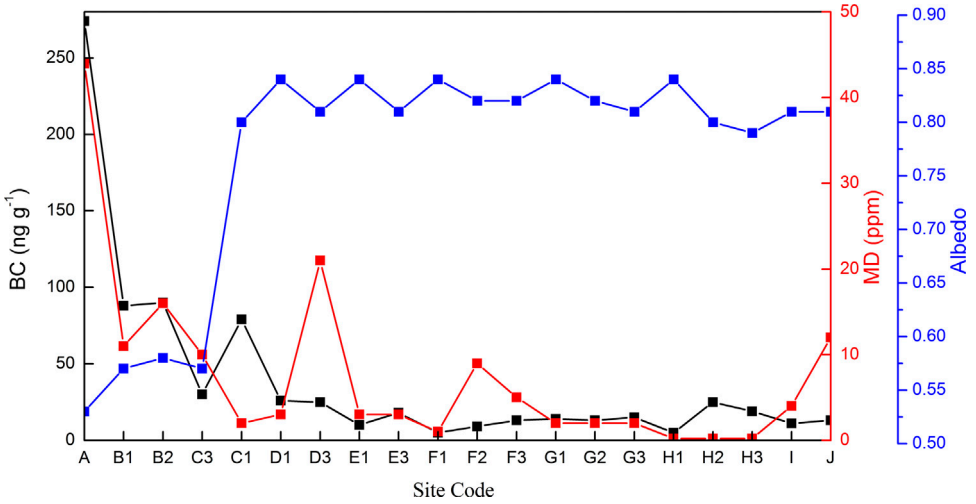

FIGURE 7 | The mean albedo of surface snow/ice measured by the Analytical Spectral Devices (ASD) on 12 August, along with BC and dust concentrations at the sampling sites.

with a significant negative correlation. On September 12, the glacier melting slowed down, and LAIs began to accumulate on the glacier surface. The BC and OC concentrations were still negatively correlated with elevations. The correlation between MD and elevations was poor during autumn, which was different from that on August 12. This is due to the weakening of melting in autumn, while MD was gradually decreased.

To investigate the distribution of LAIs on glacier specifically, we used sites of stakes for measuring mass balance as sample points, and LAIs' concentrations were analyzed over the glacier area of east branch on Glacier No.1 by using spline interpolation method. BC concentrations varied significantly with elevations, and the maximum concentrations depended on the glacier front (**Figure 6**). On 2 August, a large number of LAIs were exposed on the surface of the glacier in low-altitude areas, and the LAIs' concentration was higher. OC and BC were removed by melt water in the main stream line of glacier, which might restrict the effect of LAIs on the melting of the glacier, although a darkening on glacier terminus was observed. On 12 August, the glacier was covered by fresh snow and BC concentrations were the lowest ($39 \pm 61\ ng\ g^{-1}$), which could be considered as typical BC concentrations for fresh snow.

As for the entire glacier, a strong elevation gradient was observed, and the LAIs' concentrations were significantly higher at altitudes below 4,000 m than above 4,000 m. LAIs' enrichment mainly occurred on the central part of the glacier and the terminus of the glacier, and the enrichment was weak at the top of the glacier. There was a decreasing trend in LAIs with increasing elevation, which suggested that LAIs' concentrations were mainly dependent on the melting state of the glacier surface. In general, when elevation decreased, the ablation of the glacier increased. In addition, the elevation gradient has significant implications for spatial variations in LAIs' deposition, thus resulting in spatial variations of RF with glacier melting.

Comparison of BC Concentrations in Snow and Ice

We compared our observed BC, OC, and MD concentrations in Urumqi Glacier No.1 (**Table 2**) with previous research from snow and ice in High Asia. For fresh snow, BC concentrations of Urumqi Glacier No.1 were similar to those of Muji Glacier ($25\ ng\ g^{-1}$) in the western Tibetan Plateau; OC concentrations were higher than those for Xiao Dongkemadi Glacier ($157.97\ ng\ g^{-1}$); and MD concentrations were also higher than those for Xiao Dongkemadi Glacier ($1.89\ \mu g\ g^{-1}$) (Yang et al., 2015; Li et al., 2017). For aged snow, BC and MD concentrations of Urumqi Glacier No.1 were similar to those of glaciers at the edge of Tibetan Plateau (e.g., Laohugou Glacier No.12 and Baishui Glacier No.1) and significantly higher than those of glaciers in the Tibetan Plateau hinterland (e.g., Zhadang Glacier) (Qu et al., 2014; Niu et al., 2017; Zhang et al., 2017a). It may be due to the relatively low altitude of glaciers at the edge of TP. As the temperature rises, ice and snow melt more easily, and LAIs are concentrated on the glacier surface. In addition, these glaciers are more susceptible to the spread of pollutants over long distances. By comparison, it could be concluded that BC concentrations of Urumqi Glacier No.1 were at a relatively high level in High Asia, and this might be attributed to regional and local emissions (Dong et al., 2016b; Zhang et al., 2017b).

Previous research has suggested that local emissions and long-distance transported pollutants from Central Asia could also be potential contributors to black carbon and dust in Urumqi River Valley (Dong et al., 2016a; Zhang et al., 2020). BC concentrations in this work showed a small difference relative to the reported concentrations on Urumqi Glacier No.1; for example, BC concentrations were in the range of $250–500\ ng\ g^{-1}$ in the

TABLE 3 | Parameters for sensitivity analysis with the SNICAR model for Urumqi Glacier No.1.

Date	Code	Site	Observed albedo	Pure snow	Pure snow + BC	Pure snow + BC + dust	BC%	MD%
2015/8/12	TS2015-04	C1	0.805	0.847	0.839	0.838	19.106	1.454
2015/8/12	TS2015-06	D1	0.837	0.851	0.848	0.847	21.575	8.078
2015/8/12	TS2015-07	D3	0.810	0.828	0.824	0.815	20.660	48.892
2015/8/12	TS2015-08	E1	0.837	0.851	0.850	0.849	8.744	8.850
2015/8/12	TS2015-09	E3	0.813	0.826	0.824	0.823	15.695	8.849
2015/8/12	TS2015-10	F1	0.838	0.849	0.849	0.848	5.114	3.609
2015/8/12	TS2015-11	F2	0.818	0.831	0.830	0.826	8.406	27.609
2015/8/12	TS2015-12	F3	0.818	0.830	0.828	0.826	13.814	17.781
2015/8/12	TS2015-13	G1	0.835	0.846	0.845	0.844	12.445	6.085
2015/8/12	TS2015-14	G2	0.823	0.833	0.829	0.829	30.320	7.777
2015/8/12	TS2015-15	G3	0.806	0.835	0.833	0.832	6.010	2.739
2015/8/12	TS2015-16	H1	0.840	0.842	0.842	0.841	23.214	4.357
2015/8/12	TS2015-17	H2	0.802	0.839	0.837	0.837	6.301	0.083
2015/8/12	TS2015-18	H3	0.794	0.834	0.832	0.832	4.883	0.612
2015/8/12	TS2015-19	I	0.807	0.836	0.835	0.834	4.211	5.169
2015/8/12	TS2015-20	J	0.808	0.837	0.836	0.832	4.353	13.017
2015/9/12	TS2015-29	A	0.610	0.730	0.701	0.698	24.316	2.717
2015/9/12	TS2015-30	B2	0.650	0.774	0.756	0.754	14.432	1.627
2015/9/12	TS2015-31	C1	0.660	0.774	0.748	0.747	22.453	0.806
2015/9/12	TS2015-32	C3	0.691	0.774	0.750	0.747	28.564	3.707
2015/8/12	TS2015-01	A	0.534	0.653	0.604	0.587	41.350	13.681
2015/8/12	TS2015-02	B1	0.574	0.652	0.634	0.629	22.375	6.914
2015/8/12	TS2015-03	B2	0.583	0.649	0.632	0.625	25.977	11.292
2015/8/12	TS2015-05	C3	0.567	0.646	0.640	0.636	7.073	6.079
2015/8/2	TS2015-48	E3	0.230	0.626	0.514	0.416	28.147	24.874
2015/8/2	TS2015-49	F1	0.200	0.622	0.531	0.414	21.563	27.635
2015/8/2	TS2015-50	F2	0.190	0.661	0.537	0.444	26.327	19.663
2015/8/2	TS2015-51	F3	0.220	0.628	0.543	0.421	20.763	30.049
2015/8/2	TS2015-52	G1	0.280	0.634	0.570	0.515	18.037	15.724
2015/8/2	TS2015-53	G2	0.290	0.653	0.601	0.509	14.372	25.286
2015/8/2	TS2015-54	G3	0.420	0.648	0.577	0.498	31.290	34.725
2015/8/2	TS2015-55	H1	0.400	0.636	0.582	0.475	22.980	45.492
2015/8/2	TS2015-56	H2	0.350	0.639	0.590	0.529	16.987	20.836
2015/8/2	TS2015-57	H3	0.450	0.646	0.600	0.468	23.500	67.249
2015/8/2	TS2015-58	I	0.350	0.643	0.605	0.557	12.950	16.390

summer of 2004 (Xu et al., 2012). The discrepancy was mostly mainly due to previous studies focusing on snow pits in the accumulation zone of glaciers and less attention to the ablation zones. The differences in concentrations of BC and dust among different glaciers may indicate the differences of deposition, enrichment, and reexposure of impurities over different regions.

Effects of LAIs on Albedo

The albedo in different sample sites on August 12 is shown in **Figure 7**. For fresh snow (C1-J), the albedo showed smaller variability. For aged snow (A-C3), the albedo was increased with the decrease in LAIs' concentrations. As for the entire glacier, the albedo was higher at a higher elevation. It should be noted that the albedo at C1 was much higher than the albedo at C3, and the main cause was the different air temperatures at the different sampling time. With the increase in temperature, snow grain size gradually increased, which could change the albedo of snow. Parameters for sensitivity analysis with the SNICAR model for Urumqi Glacier No.1 are listed in **Table 3**. Given the current data, uncertainties by BC measurements were estimated to be about 3–6%.

Based on the melting conditions of the glacier surface, the samples were divided into three types: fresh snow, aged snow, and granular ice. The influence of BC and MD on reducing albedo of Urumqi Glacier No.1 in three melting conditions is shown in **Figure 8**. The sensitivity analysis suggested that BC and MD in fresh snow could reduce the albedo by 12.8 and 10.3%, in aged snow could reduce the albedo by 23.3 and 5.9%, and in granular ice could reduce the albedo by 21.5 and 29.8%. BC exceeded MD which contributed a major portion of the albedo reduction in fresh snow and aged snow. BC played a vital role in the process of snow melting on Urumqi Glacier No.1. However, with the disappearance of snow on the glacier surface, most of the glacier surface was covered with MD, which played a key role in glacier melting (Takeuchi and Li, 2008). Therefore, the reduction of albedo by surface BC and MD was the main factor that accelerated glacier retreating in the context of global warming.

DISCUSSION

We calculated the RF in three scenarios, only BC, only MD, and both MD and BC on Urumqi Glacier No.1, using **Eq. 2**. As shown in **Figure 9**, the RF induced by BC only in fresh

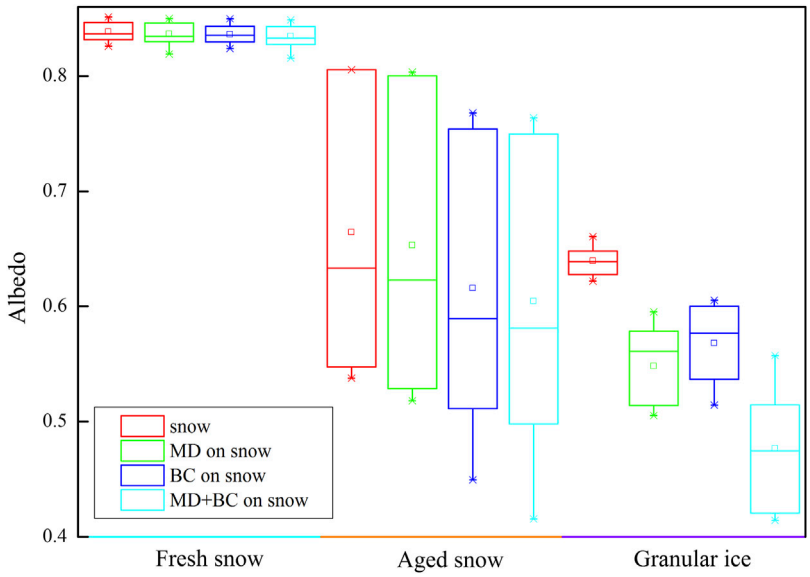

FIGURE 8 | The reduction of albedo by BC and MD on Urumqi Glacier No.1 under three different melting conditions: fresh snow, aged snow, and granular ice.

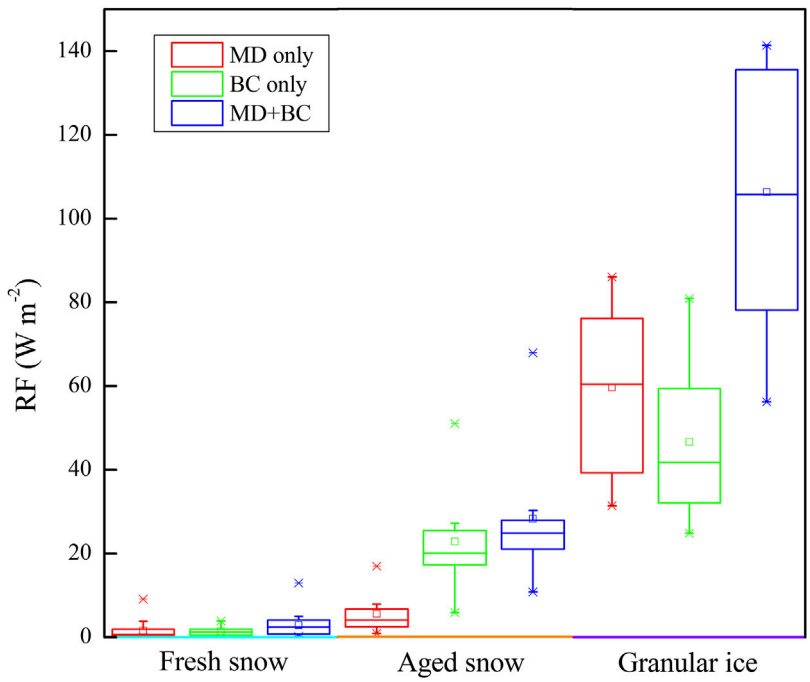

FIGURE 9 | The contribution of RF of BC and MD on Urumqi Glacier No.1 under three different melting conditions: fresh snow, aged snow, and granular ice.

snow, aged snow, and granular ice was 1.38, 22.76, and 46.66 W m^{-2}, respectively. The RF induced by MD only in fresh snow, aged snow, and granular ice was 1.52, 5.47, and 59.63 W m^{-2}, respectively. The RF induced by BC and MD in the granular ice and aged snow was higher than that in fresh snow. The RF of MD was higher than that of BC in fresh snow and granular ice, whereas the RF of BC exceeded MD in aged snow, which indicated that BC was the dominant factor in the melting of snow and MD caused higher RF when the glacier surface was without snow distribution.

Many studies of RF caused by BC have been conducted in High Asia (Qu et al., 2014; Yang et al., 2015; Li et al., 2017; Niu et al., 2017). For surface snow from glaciers in High Asia, RF induced by the effect of BC and dust ranged from several W m^{-2} to more than 100 W m^{-2} (Zhang and Kang, 2017). The RF caused by BC in Urumqi Glacier No.1 was higher than that in a large number of glaciers in High Asia, such as Dongkemadi Glacier, Qiyi Glacier, and Laohugou No.12 Glacier (Ming et al., 2013b; Zhang et al., 2017). This was because the concentrations of BC and MD over Urumqi Glacier No.1 in the atmosphere were much higher than those over other glaciers in High Asia.

CONCLUSION

This study provides the observational data of LAIs' concentrations of the glacier surface on Urumqi Glacier No.1 during the ablation season of 2015. BC concentrations ranged between 32 and 2,258 ng g^{-1}, and the concentrations of OC and MD were 1,590 and 110 μg g^{-1}, respectively. Temporal distributions of LAIs suggested that LAIs' concentrations gradually increased as the snow melting progressed. Temporal distributions of LAIs were mainly dependent on the different melting state of the glacier surface. LAIs were early enriched at lower elevations of the glacier. BC and MD could significantly reduce the albedo of snow at the glacier surface, and we found BC and MD at the glacier surface reduced the albedo 12.8 and 10.3% in fresh snow, reduced the albedo 23.3 and 5.9% in aged snow, and reduced the albedo 21.5 and 29.8% in granular ice, respectively. BC played a vital role in the process of snow melting on Urumqi Glacier No.1. MD may play a key role in glacier melting when the snow disappears. The calculated result showed that the average RF induced by BC in fresh snow, aged snow, and granular ice was 1.38, 22.76, and 46.66 W m^{-2}, respectively. Average RF induced by MD only was 1.52 W m^{-2} for fresh snow, 5.47 W m^{-2} for aged snow, and 59.63 W m^{-2} for granular ice. It was suggested that BC played an important role in snow melting and dust was the main forcing factor in accelerating glacier melt.

DATA AVAILABILITY STATEMENT

The datasets generated for this study are available on request to the corresponding author.

AUTHOR CONTRIBUTIONS

ZL designed the experiment. XY performed the experiments. YS collected the samples. XZ (1st author) and XY wrote the manuscript. MS and XZ (5th author) reviewed and edited the manuscript.

FUNDING

This work was supported by the SKLCS founding (SKLCS-ZZ-2019), the Strategic Priority Research Program of Chinese Academy of Sciences (Class A) (XDA20020102; XDA20060201), the Innovative Research Group Project of the National Natural Science Foundation of China (41721091), and the National Natural Science Foundation of China (41761134093; 41471058).

ACKNOWLEDGMENTS

The authors thank the staff working in the Tian Shan Glaciological Station for helping collect data. They also gratefully thank the reviewers for their constructive comments.

REFERENCES

Bond, T. C., Doherty, S. J., Fahey, D. W., Forster, P. M., Berntsen, T., DeAngelo, B. J., et al. (2013). Bounding the Role of Black Carbon in the Climate System: A Scientific Assessment. *J. Geophys. Res. Atmos.* 118 (11), 5380–5552. doi:10.1002/jgrd.50171

Che, Y., Zhang, M., Li, Z., Wei, Y., Nan, Z., Li, H., et al. (2019). Energy Balance Model of Mass Balance and its Sensitivity to Meteorological Variability on Urumqi River Glacier No.1 in the Chinese Tien Shan. *Sci. Rep.* 9, 13958. doi:10.1038/s41598-019-50398-4

Chow, J. C., Watson, J. G., Chen, L.-W. A., Arnott, W. P., Moosmüller, H., and Fung, K. (2004). Equivalence of Elemental Carbon by thermal/optical Reflectance and Transmittance with Different Temperature Protocols. *Environ. Sci. Technol.* 38, 4414–4422. doi:10.1021/es034936u

Dang, C., Fu, Q., and Warren, S. G. (2016). Effect of Snow Grain Shape on Snow Albedo. *J. Atmos. Sci.* 73 (9), 3573–3583. doi:10.1175/jas-d-15-0276.1

Dong, Z., Kang, S., Qin, D., Li, Y., Wang, X., Ren, J., et al. (2016a). Provenance of Cryoconite Deposited on the Glaciers of the Tibetan Plateau: New Insights From Nd-Sr Isotopic Composition and Size Distribution. *J. Geophys. Res. Atmos.* 121, 7371–7382. doi:10.1002/2016JD024944

Dong, Z., Qin, D., Kang, S., Liu, Y., Li, Y., Huang, J., et al. (2016b). Individual Particles of Cryoconite Deposited on the Mountain Glaciers of the Tibetan Plateau: Insights into Chemical Composition and Sources. *Atmos. Environ.* 138, 114–124. doi:10.1016/j.atmosenv.2016.05.020

Flanner, M. G., Liu, X., Zhou, C., Penner, J. E., and Jiao, C. (2012). Enhanced Solar Energy Absorption by Internally-Mixed Black Carbon in Snow Grains. *Atmos. Chem. Phys.* 12 (10), 4699–4721. doi:10.5194/acp-12-4699-2012

Flanner, M. G., Zender, C. S., Randerson, J. T., and Rasch, P. J. (2007). Present-day Climate Forcing and Response from Black Carbon in Snow. *J. Geophys. Res.* 112 (D11202), 1–17. doi:10.1029/2006JD008003

Gabbi, J., Huss, M., Bauder, A., Cao, F., and Schwikowski, M. (2015). The Impact of Saharan Dust and Black Carbon on Albedo and Long-Term Glacier Mass Balance. *Cryosphere Discuss.* 9 (1), 1385–1400. doi:10.5194/tcd-9-1133-2015

Gertler, C. G., Puppala, S. P., Panday, A., Stumm, D., and Shea, J. (2016). Black Carbon and the Himalayan Cryosphere: A Review. *Atmos. Environ.* 125, 404–417. doi:10.1016/j.atmosenv.2015.08.078

Hadley, O. L., and Kirchstetter, T. W. (2012). Black-carbon Reduction of Snow Albedo. *Nat. Clim Change* 2 (6), 437–440. doi:10.1038/nclimate1433

Hansen, J., and Nazarenko, L. (2004). Soot Climate Forcing via Snow and Ice Albedos. *Proc. Natl. Acad. Sci.* 101 (2), 423–428. doi:10.1073/pnas.2237157100

He, C., Flanner, M. G., Chen, F., Barlage, M., Liou, K.-N., Kang, S., et al. (2018). Black Carbon-Induced Snow Albedo Reduction over the Tibetan Plateau: Uncertainties from Snow Grain Shape and Aerosol-Snow Mixing State Based on an Updated SNICAR Model. *Atmos. Chem. Phys.* 18 (15), 11507–11527. doi:10.5194/acp-18-11507-2018

He, C., Li, Q., Liou, K. N., Takano, Y., Gu, Y., Qi, L., et al. (2014). Black Carbon Radiative Forcing over the Tibetan Plateau. *Geophys. Res. Lett.* 41 (22), 7806–7813. doi:10.1002/2014gl062191

He, C., Liou, K. N., Takano, Y., Chen, F., and Barlage, M. (2019). Enhanced Snow Absorption and Albedo Reduction by Dust-Snow Internal Mixing: Modeling and Parameterization. *J. Adv. Model. Earth Syst.* 11, 3755–3776. doi:10.1029/2019ms001737

Jacobson, M. Z. (2001). Strong Radiative Heating Due to the Mixing State of Black Carbon in Atmospheric Aerosols. *Nature* 409 (6821), 695–697. doi:10.1038/35055518

Kaspari, S., Painter, T. H., Gysel, M., Skiles, S. M., and Schwikowski, M. (2014). Seasonal and Elevational Variations of Black Carbon and Dust in Snow and Ice in the Solu-Khumbu, Nepal and Estimated Radiative Forcings. *Atmos. Chem. Phys.* 14 (15), 8089–8103. doi:10.5194/acp-14-8089-2014

Li, X., Kang, S., He, X., Qu, B., Tripathee, L., Jing, Z., et al. (2017). Light-absorbing Impurities Accelerate Glacier Melt in the Central Tibetan Plateau. *Sci. Total Environ.* 587-588 (3), 482–490. doi:10.1016/j.scitotenv.2017.02.169

Ming, J., Du, Z., Xiao, C., Xu, X., and Zhang, D. (2012). Darkening of the Mid-himalaya Glaciers since 2000 and the Potential Causes. *Environ. Res. Lett.* 7 (1), 014021–014033. doi:10.1088/1748-9326/7/1/014021

Ming, J., Wang, P., Zhao, S., and Chen, P. (2013a). Disturbance of Light-Absorbing Aerosols on the Albedo in a winter Snowpack of Central Tibet. *J. Environ. Sci.* 25 (8), 1601–1607. doi:10.1016/S1001-0742(12)60220-4

Ming, J., Wang, Y., Du, Z., Zhang, T., Guo, W., Xiao, C., et al. (2015). Widespread Albedo Decreasing and Induced Melting of Himalayan Snow and Ice in the Early 21st century. *Plos One* 10 (6), e0126235–13. doi:10.1371/journal.pone.0126235

Ming, J., Xiao, C., Cachier, H., Qin, D., Qin, X., Li, Z., et al. (2009). Black Carbon (BC) in the Snow of Glaciers in West China and its Potential Effects on Albedos. *Atmos. Res.* 92 (1), 114–123. doi:10.1016/j.atmosres.2008.09.007

Ming, J., Xiao, C., Du, Z., and Yang, X. (2013b). An Overview of Black Carbon Deposition in High Asia Glaciers and its Impacts on Radiation Balance. *Adv. Water Resour.* 55 (3), 80–87. doi:10.1016/j.advwatres.2012.05.015

Ming, J., Xiao, C., Wang, F., Li, Z., and Li, Y. (2016). Grey Tienshan Urumqi Glacier No.1 and Light-Absorbing Impurities. *Environ. Sci. Pollut. Res.* 23 (10), 9549–9558. doi:10.1007/s11356-016-6182-7

Niu, H., Kang, S., Shi, X., Paudyal, R., He, Y., Li, G., et al. (2017). *In-situ* Measurements of Light-Absorbing Impurities in Snow of Glacier on Mt. Yulong and Implications for Radiative Forcing Estimates. *Sci. Total Environ.* 581-582, 848–856. doi:10.1016/j.scitotenv.2017.01.032

Nolin, A. W., and Dozier, J. (2000). A Hyperspectral Method for Remotely Sensing the Grain Size of Snow. *Remote Sens. Environ.* 74 (2), 207–216. doi:10.5194/tc-12-2371-201810.1016/s0034-4257(00)00111-5

Painter, T. H., Seidel, F. C., Bryant, A. C., Skiles, M., and Rittger, K. (2013). Imaging Spectroscopy of Albedo and Radiative Forcing by Light-Absorbing Impurities in Mountain Snow. *J. Geophys. Res. Atmos.* 118 (18), 9511–9523. doi:10.1002/jgrd.50520

Qian, Y., Yasunari, T. J., Doherty, S. J., Flanner, M. G., Lau, W. K. M., Ming, J., et al. (2015). Light-absorbing Particles in Snow and Ice: Measurement and Modeling of Climatic and Hydrological Impact. *Adv. Atmos. Sci.* 32 (1), 64–91. doi:10.1007/s00376-014-0010-0

Qu, B., Ming, J., Kang, S.-C., Zhang, G.-S., Li, Y.-W., Li, C.-D., et al. (2014). The Decreasing Albedo of the Zhadang Glacier on Western Nyainqentanglha and the Role of Light-Absorbing Impurities. *Atmos. Chem. Phys.* 14 (20), 11117–11128. doi:10.5194/acp-14-11117-2014

Ramanathan, V., and Carmichael, G. (2008). Global and Regional Climate Changes Due to Black Carbon. *Nat. Geosci* 1 (1), 221–227. doi:10.1038/ngeo156

Ramanathan, V., Ramana, M. V., Roberts, G., Kim, D., Corrigan, C., Chung, C., et al. (2007). Warming Trends in Asia Amplified by Brown Cloud Solar Absorption. *Nature* 448 (7153), 575–578. doi:10.1038/nature06019

Schmale, J., Flanner, M., Kang, S., Sprenger, M., Zhang, Q., Guo, J., et al. (2017). Modulation of Snow Reflectance and Snowmelt from Central Asian Glaciers by Anthropogenic Black Carbon. *Sci. Rep.* 7, 40501. doi:10.1038/srep40501

Takeuchi, N., and Li, Z. (2008). Characteristics of Surface Dust on Ürümqi Glacier No. 1 in the Tien Shan Mountains, China. *Arctic Antarctic Alpine Res.* 40, 744–750. doi:10.1657/1523-043010.1657/1523-0430(07-094)[takeuchi]2.0.co;2

Wang, M., Xu, B., Zhao, H., Cao, J., Joswiak, D., Wu, G., et al. (2012). The Influence of Dust on Quantitative Measurements of Black Carbon in Ice and Snow when Using a Thermal Optical Method. *Aerosol. Sci. Techn.* 46 (1), 60–69. doi:10.1080/02786826.2011.605815

Wang, X., Pu, W., Ren, Y., Zhang, X., Zhang, X., Shi, J., et al. (2017). Observations and Model Simulations of Snow Albedo Reduction in Seasonal Snow Due to Insoluble Light-Absorbing Particles during 2014 Chinese Survey. *Atmos. Chem. Phys.* 17 (1-3), 2279–2296. doi:10.5194/acp-17-2279-2017

Warren, S. G., and Wiscombe, W. J. (1980). A Model for the Spectral Albedo of Snow. II: Snow Containing Atmospheric Aerosols. *J. Atmos. Sci.* 37 (12), 2734–2745. doi:10.1175/1520-0469(1980)037<2734:amftsa>2.0.co;2

Xu, B., Cao, J., Hansen, J., Yao, T., Joswia, D. R., Wang, N., et al. (2009). Black Soot and the Survival of Tibetan Glaciers. *Proc. Natl. Acad. Sci. U S A* 106 (52), 22114–22118. doi:10.1073/pnas.0910444106

Xu, B., Cao, J., Joswiak, D. R., Liu, X., Zhao, H., and He, J. (2012). Post-depositional Enrichment of Black Soot in Snow-Pack and Accelerated Melting of Tibetan Glaciers. *Environ. Res. Lett.* 7 (1), 014022–014035. doi:10.1088/1748-9326/7/1/014022

Xu, B., Yao, T., Liu, X., and Wang, N. (2006). Elemental and Organic Carbon Measurements with a Two-step Heating-Gas Chromatography System in Snow Samples from the Tibetan Plateau. *Ann. Glaciol.* 43 (1), 257–262. doi:10.3189/172756406781812122

Xu, X., Pan, B., Hu, E., Li, Y., and Liang, Y. (2011). Responses of Two Branches of Glacier No. 1 to Climate Change from 1993 to 2005, Tianshan, China. *Quat. Int.* 236, 143–150. doi:10.1016/j.quaint.2010.06.013

Yang, S., Xu, B., Cao, J., Zender, C. S., and Wang, M. (2015). Climate Effect of Black Carbon Aerosol in a Tibetan Plateau Glacier. *Atmos. Environ.* 111, 71–78. doi:10.1016/j.atmosenv.2015.03.016

Yasunari, T. J., Bonasoni, P., Laj, P., Fujita, K., Vuillermoz, E., Marinoni, A., et al. (2010). Estimated Impact of Black Carbon Deposition during Pre-monsoon Season from Nepal Climate Observatory - Pyramid Data and Snow Albedo Changes over Himalayan Glaciers. *Atmos. Chem. Phys.* 10 (14), 6603–6615. doi:10.5194/acp-10-6603-2010

Yasunari, T. J., Tan, Q., Lau, K.-M., Bonasoni, P., Marinoni, A., Laj, P., et al. (2013). Estimated Range of Black Carbon Dry Deposition and the Related Snow Albedo Reduction over Himalayan Glaciers during Dry Pre-monsoon Periods. *Atmos. Environ.* 78 (7), 259–267. doi:10.1016/j.atmosenv.2012.03.031

Zhang, X., Li, Z., Ming, J., and Wang, F. (2020). One-Year Measurements of Equivalent Black Carbon, Optical Properties, and Sources in the Urumqi River Valley, Tien Shan, China. *Atmosphere* 11, 478. doi:10.3390/atmos11050478

Zhang, Y., Kang, S., Li, C., Gao, T., Cong, Z., Sprenger, M., et al. (2017a). Characteristics of Black Carbon in Snow from Laohugou No. 12 Glacier on the Northern Tibetan Plateau. *Sci. Total Environ.* 607-608, 1237–1249. doi:10.1016/j.scitotenv.2017.07.100

Zhang, Y., and Kang, S. (2017b). Research Progress of Light-Absorbing Impurities in Glaciers of the Tibetan Plateau and its Surroundings. *Chin. Sci. Bull.* 62, 4151–4162. doi:10.1360/N972017-00505

Zhao, C., Hu, Z., Qian, Y., Ruby Leung, L., Huang, J., Huang, M., et al. (2014). Simulating Black Carbon and Dust and Their Radiative Forcing in Seasonal Snow: a Case Study over North China with Field Campaign Measurements. *Atmos. Chem. Phys.* 14 (20), 11475–11491. doi:10.5194/acp-14-11475-2014

Zhao, S., Ming, J., Sun, J., and Xiao, C. (2013). Observation of Carbonaceous Aerosols during 2006-2009 in Nyainqêntanglha Mountains and the Implications for Glaciers. *Environ. Sci. Pollut. Res.* 20 (8), 5827–5838. doi:10.1007/s11356-013-1548-6

Conflict of Interest: The authors declare that the research was conducted in the absence of any commercial or financial relationships that could be construed as a potential conflict of interest.

Publisher's Note: All claims expressed in this article are solely those of the authors and do not necessarily represent those of their affiliated organizations, or those of the publisher, the editors, and the reviewers. Any product that may be evaluated in this article, or claim that may be made by its manufacturer, is not guaranteed or endorsed by the publisher.

Copyright © 2021 Zhang, Li, You, She, Song and Zhou. This is an open-access article distributed under the terms of the Creative Commons Attribution License (CC BY). The use, distribution or reproduction in other forums is permitted, provided the original author(s) and the copyright owner(s) are credited and that the original publication in this journal is cited, in accordance with accepted academic practice. No use, distribution or reproduction is permitted which does not comply with these terms.

Advantages of publishing in Frontiers

OPEN ACCESS
Articles are free to read for greatest visibility and readership

FAST PUBLICATION
Around 90 days from submission to decision

HIGH QUALITY PEER-REVIEW
Rigorous, collaborative, and constructive peer-review

TRANSPARENT PEER-REVIEW
Editors and reviewers acknowledged by name on published articles

Frontiers
Avenue du Tribunal-Fédéral 34
1005 Lausanne | Switzerland

Visit us: www.frontiersin.org
Contact us: frontiersin.org/about/contact

REPRODUCIBILITY OF RESEARCH
Support open data and methods to enhance research reproducibility

DIGITAL PUBLISHING
Articles designed for optimal readership across devices

FOLLOW US
@frontiersin

IMPACT METRICS
Advanced article metrics track visibility across digital media

EXTENSIVE PROMOTION
Marketing and promotion of impactful research

LOOP RESEARCH NETWORK
Our network increases your article's readership